Selective Fluorescent Chemosensors and Iodinated Contrast Agents: Biological Evaluation for Cellular Zinc detection, Microdamage Detection and Imaging

By

Raman Parkesh, M. Sc.

November 2003

University of Dublin
Trinity College

A thesis submitted to the Department of Chemistry, University of Dublin, Trinity College in fulfillment of the requirements for the degree of Doctor of Philosophy.

DECLARATION

This thesis has not been submitted as an exercise for a degree at any other university. Except where stated, the work described therein was carried out by me alone.

I give permission for the Library to lend or copy this thesis upon request.

Signed: 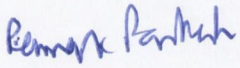

Dedicated to my Family

Acknowledgements

First and formost I wish to express my deep sense of gratitude to my supervisors Dr. Thorfinnur Gunnlaugsson and Prof. T. Clive Lee for their invaluable guidance and encouragement during the course of my research. My sincere thanks to Dr. Wolfgang Gowin and Dr. Michael Giehel at Free University Berlin for fruitful discussion and help with micro-CT imaging studies. A very Big thank you to Dr. Hugh Byrne, Dublin Institute of Technology ,for allowing me to use Raman spectroscopy and for discussions. 'Thank you' Neal (Centre for Microscopy and Analysis) for assisting me with SEM work. Special thanks to Dr. John O'Brien for all the help with NMR. Thanks to Dr. Sahar Mosin for providing bone samples and also in assisting with epifluorescence imaging. I am also thankful to Dr. K.N. Ganesh, National Chemical Laboratory (NCL) India for invaluable lessons in chemistry. Thanks to Peter Kellegan for assisting me in zinc staining work. Very special thanks to Fred, Ed, Brendan, Paul, Patsy, Martin, Teresa, Seamus, Keiran, Doherty, Peggy, Brendan and Colm for their much appreciated support and friendship.

I am also thankful to all the lab mates for their support and encouragement, especially in the last two months. I would like to take this opportunity to show my appreciation to my labmates, Mark, Sinead, Clair, Caroline, Aoife, Romain, Joe, Jilly, Julie, Celine, Fred, Susan, Andrew, Lin, Katell, Cidalia, Flo, Ann-Marie, Lisa and Emma, for providing a friendly atmosphere in the lab. Big 'thank you' to Joe, Julie, Jilly, Fred, Lin, Ann Marie, and Celine for much needed editing work. Also thanks to bone group members: David Taylor, Fergal, Matt, Jan, David, Matt, Paul, John, Nick and Vincent for research discussions.

I would like to take this opportunity to thank all the members of museum team for wonderful cricket experience. Special thanks to my friends Rohit, Kirti, Sushil, Rajeshkant, Sunil, Tarun and Raveiah, Nicole, Liz, Sivakumar and Suresh for all the support and help. Very special thanks to Aviansh Tejpal for introducing me to art of life and all the encouragement. Thanks to Prof. Satish Gupta, Prof. Y.P.Gupta, Prof. H.K.Kher for introducing to the wonderful world of science.

Mittu, Shanky, Ronak, Jjanu, Ashu, Nishu, Achu, Sambhu, Deepti, Sacchu - thanks for keeping me cheerful. This thesis would not have taken full form without the help of chnnu, chotu and sonnu. Mere words cannot express my gratitude to Mummy, Daddy and Tony and Rethi-the wonderful family. There was no way I could have completed this work without my girl friend, Rethi. She is the love of my life.

Finally I would like to thank health research board, Ireland and Trinity college-postgraduate fellowship for supporting my research and me.

Through Zeal, Knowledge is gotten; through lack of zeal knowledge is lost; let a man who knows the double path of gain and loss thus place himself that knowledge may grow

Buddha

Abstract

This thesis entitled "*Selective Fluorescent Chemosensors and Iodinated Contrast Agents: Biological Evaluation for Cellular Zinc detection, Microdamage Detection and Imaging*" has been divided into six Chapters. Chapter 1 highlights advances made in the field of fluorescent chemosensors. Examples discussed have been critically evaluated in terms of their photophysical properties, selectivity, sensitivity and binding ability. To introduce the relevance of supramolecular systems for microdamage detection in bone, a brief introduction to the characteristics of bone and X-rays are also provided.

Chapter 2 presents in detail the design, synthesis and photophysical evaluation of two water soluble and selective Zn(II) fluoroprobes **92** and **93**. The key feature of these sensors is their stability under simulated physiological conditions. The fluorescence titrations of **92** demonstrated its ability to detect nanomolar free Zn(II). Preliminarily studies carried out using pancreatic tissue have shown the ability of **92** to label the areas, which contain chelatable zinc.

Chapter 3 presents in details two aqueous soluble, anthracene based fluorescent PET sensors **125** and **126** for selective recognition of Zn(II) and Cd(II). The evaluation of the photophysical response of these sensors demonstrated their ability to distinguish between Zn(II) and Cd(II).

Chapter 4 details a critical investigation of microdamage in bone using histological methods, SEM and EDXA. A set of fluoroprobes, **135**, **136**, **138**, **140**, **141**, **142**, **143**, **92**, **93** and **125** were used to investigate the selective labelling of the microcrack in the bone. The scratched and unscratched surfaces of the bone were studied using Raman spectroscopy, SEM and EDXA. The selective labelling of scratches observed can be attributed to the interaction of dyes *via* binding at the free lattice sites, ionic interactions with the free lattice sites or incorporation in the broken lattice sites.

Chapter 5 outlines the synthesis and preliminary evaluation of three chelatable iodinated contrast agents **160**, **161** and **162** for microdamage detection in bone. Preliminary imaging studies of these agents on bovine cortical bone specimens, using cone-beam μ-CT, demonstrated their ability to provide good contrast in solid state.

Chapter 6 presents the experimental procedures for synthesis, photophysical evaluations and histological studies.

Publications

Highly selective and sensitive fluorescent PET (photoinduced electron transfer) chemosensor for Zn(II). Thorfinnur Gunnlaugsson, T. Clive Lee and **Raman Parkesh**, *Organic & Biomolecular Chemistry*, **2003**, *19*, 3265.

Cd(II) Sensing in Water Using Novel Aromatic Iminodiacetate Based Fluorescent Chemosensors. Thorfinnur Gunnlaugsson, T. Clive Lee and Raman Parkesh, *Organic Letters,* **2003**, *22*, 4065.

Detection of microdamage in Bone. T. Clive Lee, S. Mohsin, D. Taylor, **Raman Parkesh**, T. Gunnlaugsson, F. J. O'Brien, M. Giehl, W. Gowin, *Journal of Anatomy*, **2003**, *203*, 159.

Dual Responsive Chemosensors for Anions: the Combination of Fluorescent PET (Photoinduced Electron Transfer) and Colorimetric Chemosensors in a Single Molecule. Thorfinnur Gunnlaugsson, Paul E. Kruger, T. Clive Lee, **Raman Parkesh**, Frederick M. Pfeffer and Gillian M. Hussey, *Tetrahedron letters*, **2003**, *44*, 6575.

Detection of microdamage in Bone. T. Clive Lee, S. Mohsin, D. Taylor, Raman Parkesh, T. Gunnlaugsson, F. J. O'Brien, M. Giehl, W. Gowin. Proceedings of the 3rd Joint meeting of Anatomical Society of Great Britain & Ireland, **2003**, Dresden (Abstract).

Synthesis and Micro-CT Imaging Studies of Novel Iodinated X-ray Contrast Agent for Microdamage Detection in Bone. **Raman Parkesh**, T. Clive. Lee, Thorifinnur. Gunnlaugsson , Michel. Giehl, Wolfgang. Gowin.

Histological Evaluation of Microdamage In bone using Calcium Specific Chelating Fluorescent Chemosensors. **Raman Parkesh**, Thorfinnur Gunnlaugsson, Thomas C. Lee, Sahar Mohsin

Abbreviations

abs.	Absorbance
AcOH	Acetic acid
AcO^-	Acetate ions
CH_3CN	Acetonitrile
β	Binding constant
Boc	*tert*-Butyloxycarbonyl
br s	Broad singlet
$BaSO_4$	Barium sulphate
Cbz	Benzyloxycarbonyl
$CdCl_2$	Cadmium chloride
Cd(II)	Cadmium ions
Ca^{2+}	Calcium cation
CHEF	Chelation-Enhanced Fluorescence
CT	Charge Transfer
CD_3OD	Deuterated methanol
$CDCl_3$	Deuterated chloroform
CH_2Cl_2	DCM – Dichloromethane
$CHCl_3$	Chloroform
CT	Computed Tomography
μ-CT	micro-CT
DCC	Dicyclohexylcarbodiimide
D_2O	Deuterated water
DMSO-d_6	Deuterated dimethylsulphoxide
DEPT	Distortionless Enhancement by Polarization Transfer
DMA	Dimethylacetamide
DMSO	Dimethylsulfoxide
DNA	Deoxyribonucleic acid
EDCI	1-(3-dimethylaminopropyl)-3-ethyl-carbodiimide hydrochloride
ESMS	Electro spray mass spectroscopy
EtOAc	Ethyl acetate

EDTA	Ethylene diamine tetraacetic acid
EGTA	Ethylene glycol tetracetic acid
EtOH	Ethanol
FMO	Frontal Molecular Orbital
Φ_F	Quantum yield (fluorescence)
Gd	Gadolinium
Yb	Ytterbium
HMPT	Hexamethylphosphorotriamide
HOMO	Highest Occupied Molecular Orbital
HBr	Hydrogen bromide
HCl	Hydrochloric acid
HOBt	N-Hydroxybenzotriazole
HEPES	[N-[2-hydroxyethyl]piperazine-N'-(2-ethane sulphonic acid
ICI	Iodine Monochloride
ICT	Internal charge transfer
IR	Infrared spectroscopy
ISC	Inter system crossing
IC	Internal conversion
Li^+	Lithium cation
LiOH	Lithium hydroxide
ε	Molar absorptivity (Molar extinction coefficient) (cm^{-1} M^{-1})
MeOH	Methanol
$MgSO_4$	Magnesium sulfate
m.p.	Melting point
MRI	Magnetic Resonance Imaging
$HgCl_2$	Mercuric chloride
Hg(II)	Mercury ions
MTT	[3-[4,5-Dimethylthiazol-2-yl]-2,3-diphenyl] tetrazolium bromide
NaOH	Sodium hydroxide
$NaHCO_3$	Sodium hydrogen carbonate
NiO_2	Nickel peroxide
NMR	Nuclear magnetic resonance
NOE	Nuclear overhauser effect

NEt_3	Triethylamine
Pd/C	Palladium on carbon catalyst
P_2O_5	Phosphorus pentoxide
K_2HPO_4	Pottasium hydrogen phosphate
K_2CO_3	Pottasium carbonate
K^+	Potassium cation
ppm	Parts per million
PET	Photoinduced electron transfer
%	Percentage
pH	-log $[H_30^+]$
pCd	-log[Cd(II)]
pZn	-log[Zn(II)]
pCa	-log$[Ca^{2+}]$
pM	-log[M]
SN^2	Substitution, nucleophilic, bimolecular
H_2SO_4	Sulphuric acid
TRIS	Tris (hydroxymethyl)-aminomethane
TFA	Trifluoroacetic acid
THF	Tetrahydrofuran
TLC	Thin layer chromatography
UV	Ultraviolet
$ZnCl_2$	Zinc Chloride
Zn(II)	Zinc ions

CONTENTS

CHAPTER -1

Introduction

1.1 Introduction

The Nobel Prize awarded to Charles Pedersen, Donald Cram and Jean-Marie Lehn announced the arrival of Supramolecular Chemistry.[1] J. M. Lehn coined the term supramolecular chemistry in 1969 and defined it as "*the chemistry of the intermolecular bond*".[2] Supramolecular compounds are built by linking molecules through intermolecular interactions, such as covalent, electrostatic, hydrogen bonding and van der Waals forces.[3] Supramolecular structures are the result of not only of additive but also of cooperative interactions. Supramolecules are important in both material sciences where their uses includes sensors[4], optoelectronic devices[4] and switches[5] and also in biology for monitoring of the complex cellular processes such as small-molecule-messenger dynamics, enzyme activation, protein-protein interaction, receptor-protein binding, drug design and protein folding.[6,7,8] An important concept that is closely associated with the supramolecular chemistry is that of molecular recognition.[9] Molecular recognition not only involves interaction between the various supramolecular components of the molecules but the compatibility of this interaction is also of extreme importance. In other words, the recognition function is highly specific between the interacting components. This process is analogous to the "lock and key" hypothesis of enzymes proposed by Fischer.[10] Supramolecular synthesis, which can allow for the interaction of the host with specific guests, is still an emerging field.

The main theme of this thesis is how tuned supramolecules can be applied for selective signalling. The phenomenon of molecular recognition is used for the judicious design of highly desired, guest-specific, fluorescent probes and selective X-ray contrast agents. The introduction will touch briefly on all the aspects detailed throughout this research. This chapter firstly highlights the basic principle involved in the interaction of fluorescent probes with the appropriate guest, followed by recent advances in this area with particular emphasis on the recognition of biologically important ions. Another objective of this chapter is to address a well-known bone related disease, osteoporosis,[11] to establish the application possibilities of fluorescent probes as a prognostic tool. The anatomy and biology of bones will be outlined, followed by a short account of iodine based contrast agents.

1.2 Fluorescent chemosensors

The design of ligands for the selective complexation of suitable guests such as metal cations and anions has been an important goal of supramolecular chemistry.[4,5,6,9,12,13,14,15]

In both chemical and biological systems, ions and molecules occur in abundance. Monitoring their concentration *in vitro* as well as *in vivo* is critical as many of these ions are involved in important biological and chemical processes.[12] For example, Na^+, K^+, Ca^{2+}, and Zn(II) are involved in biological processes such as nerve impulses, muscle contraction, cell activity regulation, apoptosis, and nerve transmission.[12] Monitoring molecules such as carbon monoxide in the air and measuring blood glucose levels in diabetic patients is of great importance. Historically, batch processes carried out by conventional techniques were used to monitor the levels of ions and small molecules.[15] The main drawbacks to these methods include inaccuracy and more importantly a substantial time delay. The use of sensors, in particular chemosensors overcomes these drawbacks. The optical signalling methods based on sensors offer sensitivity, selectivity, real-time response and local observation.[14] Considerable research is being directed towards the development of selective sensors for cations[12], molecules[6,9] and more recently for anion detection.[13] Sensors are divided broadly into two classes:

- biosensors[16]
- chemosensors.[14]

Sensors incorporating biological receptor such as antibodies, aptamers or large biopolymers fall into the category of biosensors.[17] Biosensors often have a limited stability, which limits their practicaility.[17] Chemosensors utilise the abiotic or synthetic receptor for analyte recognition and have received increased attention as superior alternatives to biosensors.[14,15,18] However, in order to synthesise molecules to bind a specific guest selectively is often synthetically challenging and time consuming. Even with these limitations, fluorescent chemosensors are promising and occupy a prominent position in active research.[18]

A fluorescent chemosensor can be defined as a molecular machine capable of signalling the presence of an analyte such as ions and molecules.[19] Synthesis is conducted at a molecular level by linking a signalling moiety (fluorophore) to a recognition moiety (receptor) either directly or through a spacer.[20] The signalling moiety acts as a signal transducer, converting the information (recognition event) into an optical response. The optical response results due to the change in the photophysical characteristics of the fluorophore such as absorption, fluorescence, lifetime, quantum yield and wavelength.[21]

These changes are due to the perturbation (by the bound analyte) of photoinduced processes such as electron transfer, charge transfer, energy transfer, excimer or exciplex formation (Figure 1.1).[21] These aspects are relevant to the field of photophysics.[21]

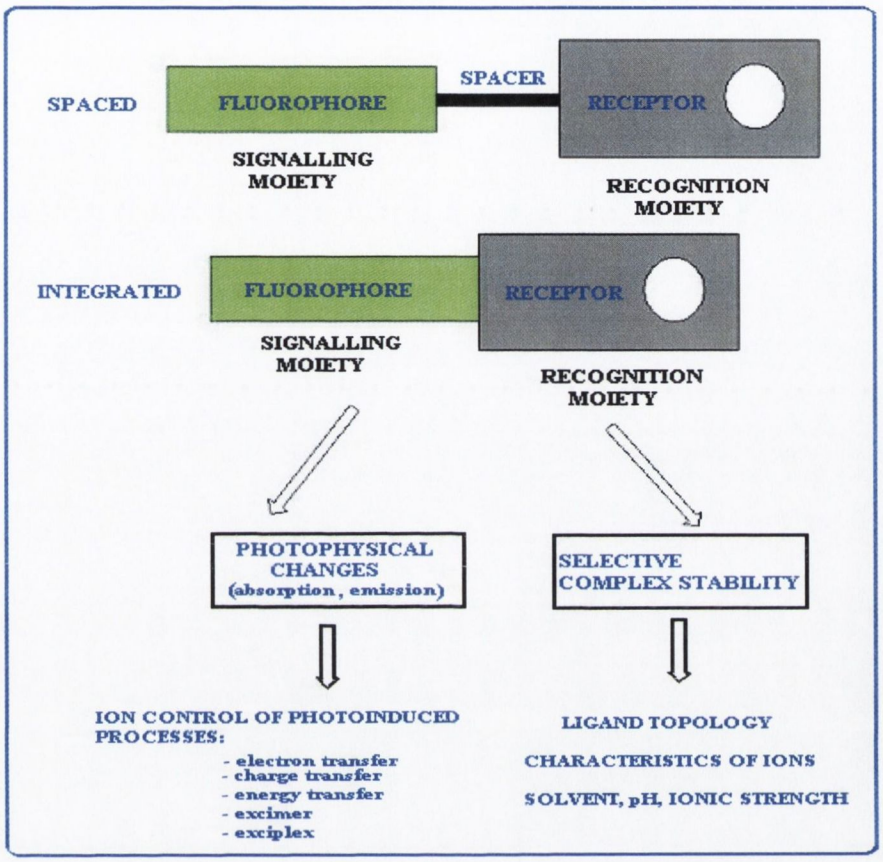

Figure 1.1 ***Supramolecular nature of a fluorescent chemosensors and various processes involved during recognition of ions and molecules.***[21]

The recognition moiety is responsible for selectivity and efficient binding of the guest/analyte, which depend on ligand topology, characteristics of the target cation or anion (ionic radius, charge, coordination number and hardness, *etc.*) and the nature of the solvent (pH, ionic strength, polarity).[21] From the above discussion, prerequisite for the formation of a fluorescent chemosensor are:

- selective binding of the molecular entity
- fluorescent changes as a result of binding.

Fluorescence detection can be achieved at a low concentration (~ 10^{-6} M) with most fluorometers. This offers the advantage of using the sensors directly within fibre optic systems.[12,21,22] The criteria for *"ideal"* sensors are:

- thermal and photochemical stability
- target selectivity
- kinetically rapid sensitisation and reversible response
- ease of delivery to target system
- real-space response (down to the micrometer level)
- ready availability or ease of synthesis.

According to the principle of fluorescent signal response, fluorescent chemosensors can be divided into the following categories:

- photoinduced electron transfer (PET) based chemosensors
- internal charge transfer (ICT) based chemosensors.

1.2.1 Fluorescent chemosensors based on photoinduced electron transfer (PET)

PET sensors are based on the *'fluorophore-spacer-receptor'* format developed by de Silva *et al.* (Figure 1.2).[23]

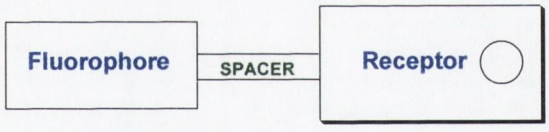

Figure 1.2 ***Schematic representation of PET sensor.***

A fluorophore module is the site where both photonic transactions of excitation and emission take place.[23] The receptor unit is responsible for guest complexation and decomplexation. The supramolecular characteristics of this combination are better conserved if a spacer unit is placed between them.[23] The spacer moiety maintains the integrity of the fluorophore and receptor, while also providing means for inducing a change in the fluorescence of attached fluorophore.[23] The spacer can be real or integrated (

as shown in Figure 1.1).[23] Feasibility of the electron transfer depends on the redox properties of the donor and acceptor coupled together with the singlet energy, and can be estimated by the Rahm-Weller[24,25] equation (Equation 1.1)

$$\Delta G_{ET} = -E_s - E_{red\ flour} + E_{ox\ amine} - e^2/\varepsilon r \qquad (1.1)$$

Where E_s = singlet energy

$E_{red\ fluor}$ = reduction potential of fluorophore (in electron volt, eV)

$E_{ox\ amine}$ = oxidation potential of amine (eV)

$e^2/\varepsilon r$ = columbic interaction energy between donor and the acceptor

e = electronic charge

ε = dielectric constant of the solvent and

r = distance between donor and acceptor.

These aspects of PET sensing can be rationalised by studying a simple molecule **1** (Figure 1.3), where anthracene fluorophore is covalently linked *via* a methylene spacer to tertiary amine, which acts as proton receptor.[20,23,26] The unprotonated amine [Figure 1.3 (A)] is capable of transferring electrons to the excited state of the anthracene. In the unprotonated state, fluorescence quantum yields approaching zero are achievable as the excited state of the fluorophore is quenched. Protonation of the amine moiety lowers its reduction potential; hence PET becomes strongly inhibited, resulting in switching *'on'* of the fluorescence of the anthracene [Figure 1.3 (B)]. Switching the fluorescence sensor *'off-on'* become possible with these *'fluorophore-spacer-receptor'* assemblies. This can be understood by using the frontal molecular orbital (FMO) approach (Figure 1.4).[26] On excitation of the fluorophore, an electron from the highest occupied molecular orbital (HOMO) is promoted to the lowest unoccupied molecular orbital (LUMO), which enables electron transfer (ET) from the HOMO of the donor (amine) to that of the fluorophore, inducing fluorescence. On binding of a cation, the reduction potential of the donor is decreased, so the relevant HOMO (amine) becomes lower in energy than that of the fluorophore.[26,27] As a result PET is not possible and fluorescence quenching is suppressed. In other words, the fluorescence intensity and quantum yield are enhanced upon cation recognition.

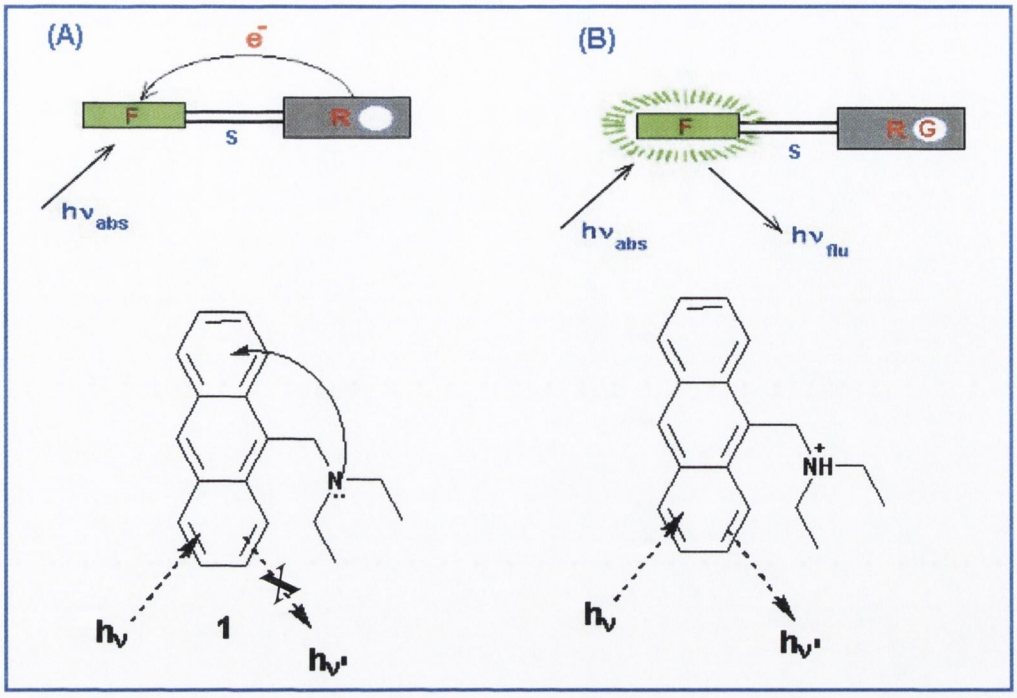

Figure 1.3 *Schematic representation of PET action of a representative proton sensor 1: (A) guest free receptor; (B) guest bound receptor. F = fluorophore; R = receptor; S = spacer; G = guest (H^+).*[23,26]

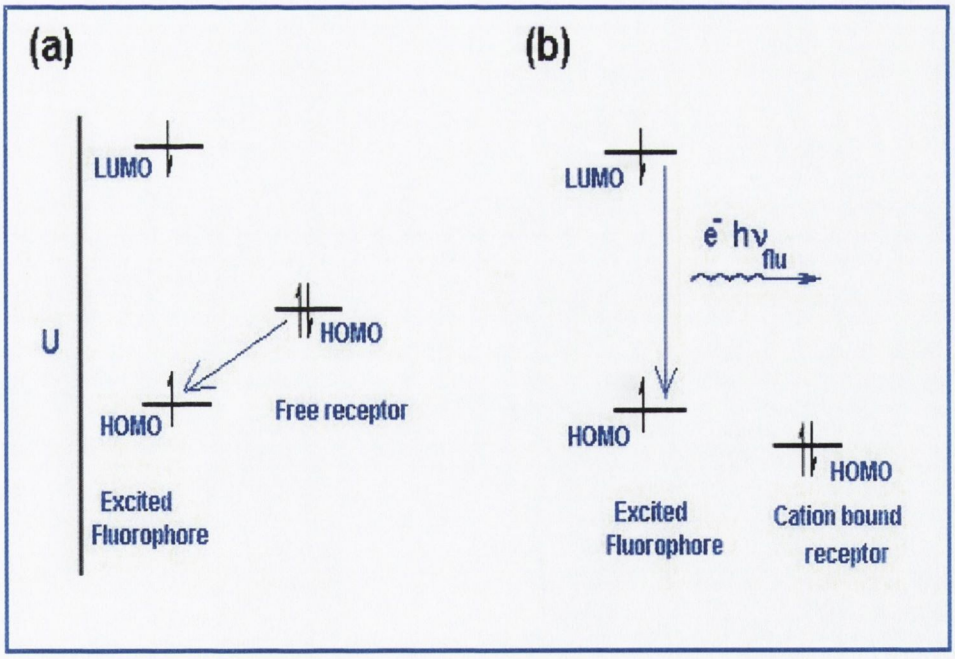

Figure 1.4 *FMO approach of PET sensor action:(A) guest free receptor; (B) guest bound receptor.*[26]

1.2.1.1 Literature survey on PET sensors

In 1985 de Silva *et al.* reported the development of PET based sensors **2** - **7**.[28] This was the first reported work of pH indicators based on PET. The excited state ionisation constants for all of the compounds were identical to those of the ground state. In addition, the spectral parameters were independent of pH (except for quantum yield). These characteristics are in contrast with conventional fluorescent pH indicators as the acid-base sites and the chromophore are well separated. The methylene spacer ensures no ground state interaction and thus independence of the absorption and emission spectra. The PET principle is similar as discussed for **1**.

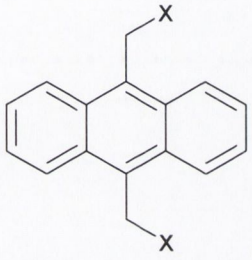

2: X = NEt_2
3: X = NHPh
4: X = $N(CH_2)_4O$

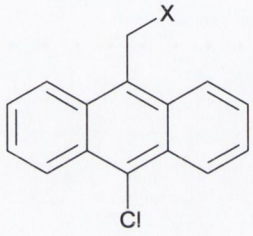

5: X = NEt_2
6: X = NHPh
7: X = $N(CH_2)_4O$

Although only simple pH indicators were reported initially, this pioneering work encouraged researchers to actively pursue the development of PET sensors in particular.[29] Group 1, 2 and transition metal ions attracted large interest and consequently cation recognition is now a well-developed and somewhat mature area of supramolecular chemistry.[30] Although anion coordination chemistry has received less attention than cation chemistry, in recent years the field of anion sensing is making huge progress.[13,31] Researchers are now realising the importance of the role of anions in a wide range of biological processes[32,33], in catalysis[34] and carcinogenesis[35]

1.2.1.2 PET chemosensors for group 1 metal ions

Extending the PET-based H^+ sensors further lead to the development of molecules capable of signalling metal cations. The crown ether containing PET sensor, **8**[36], exhibited a remarkable increase in its fluorescence upon K^+ binding. However, the fluorescence was pH dependent as a result of the basic nitrogen in the aza crown ether. This sensitivity towards pH was overcome by the development of sensor **9**[37], where the aromatic alkoxy groups can participate in an electron transfer process to the anthracene fluorophore.

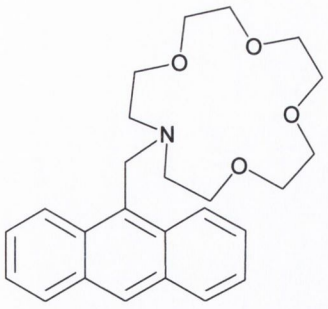

8

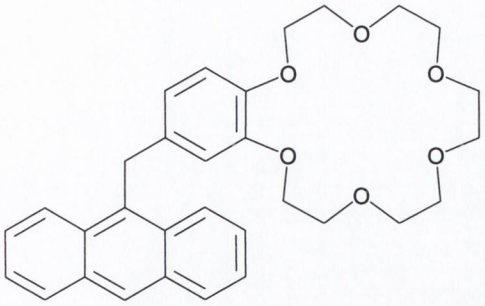

9

Cryptand based PET sensors **10-13** were developed to achieve increased selectivity for K^+.[37, 38, 39] Sensor **10** is well known for its use in monitoring K^+ level in blood and across biological membranes. The major drawback of **10** is its pH sensitivity due to the presence of the basic nitrogen atom. This problem was overcome in **11** by positioning this nitrogen atom in the receptor as a part of the aromatic system. In all of these cryptand based PET sensors, the attached crown ether acts as electron donors. Compound **11** was constructed for the measurement of intracellular alkali metal ions. In the case of **11** cation binding was clearly observed by NMR and UV-VIS as well as fluorescence spectroscopy. A downfield shift of δ 0.25 in the ^{1}H-NMR of **11** was observed upon cation binding. This shift can be attributed to the deconjugation of the nitrogen electron pair into the aromatic system. The fluorescence quantum yield showed a dramatic increase in the cation-bound complex, *e.g.* the Φ_F increases from 0.018 (cation free) to 0.17 upon K^+ binding in methanol. Sensors **12** and **13** also form well-defined excited state complexes (exciplex) upon ion recognition. This was characterised by an additional band at higher wavelengths, thus allowing the ratiometric measurement at two different observational wavelengths.

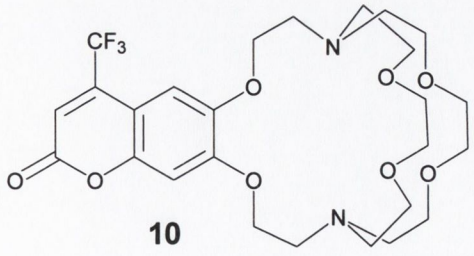

10

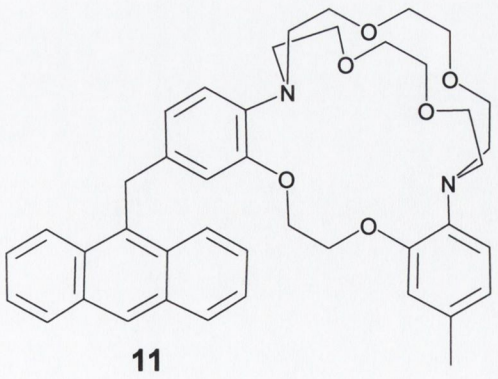

11

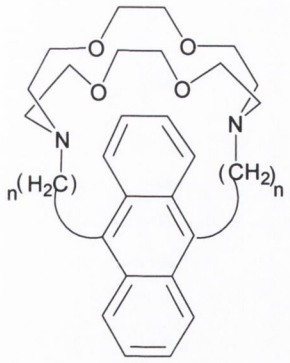

12: n = 2
13: n = 3

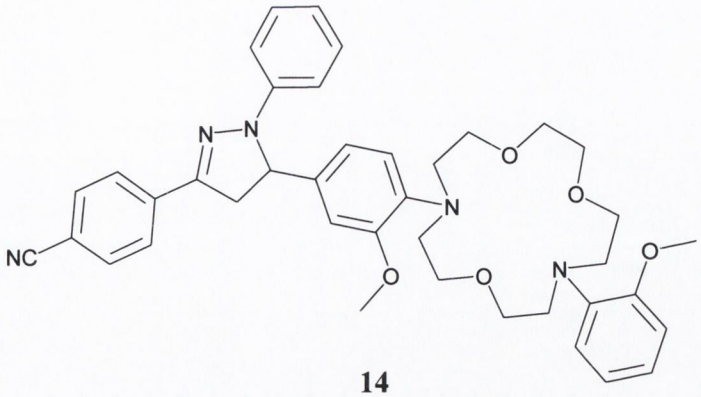

14

Sensor **14** was developed for the selective sensing of Na^+ over K^+.[40] In **14**, the methoxy group in the ortho position (with respect to the nitrogen atom) of the crown ether participates in the complexation of Na^+ which causes fluorescence to be switched *'on'*. The sensor also detects Li^+ but is 10 times less sensitive compared to Na^+. Other ions such as K^+, Mg^{2+} and Ca^{2+} did not lead to any significant enhancement in the fluorescence emission.

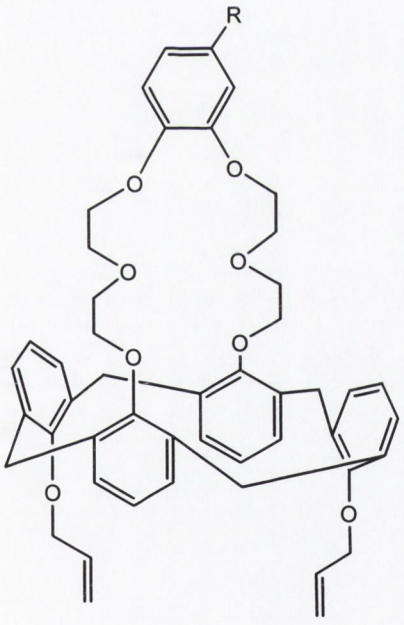

15

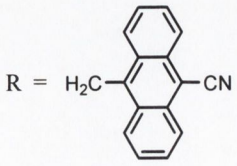

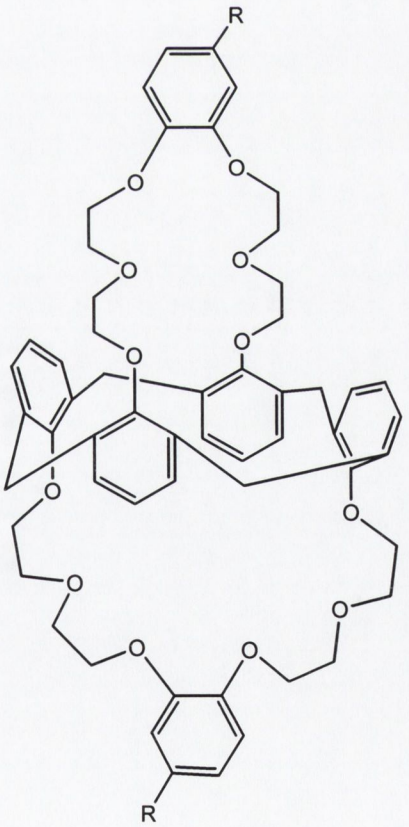

16

Calixarene based sensors **15** and **16** are designed as Cs^+ selective optical sensors.[41] The fluorescent enhancement of **15** and **16** upon Cs^+ recognition were *ca.*12 and 8 fold respectively. The sensitivity of both sensors towards various alkali metal ions decreases in the order, $Cs^+ > Rb^+ > K^+ > Li^+$ in CH_2Cl_2:MeOH (1:1, *v/v*) rendering them remarkable sensors for Cs^+. These sensors emit weakly as a result of electron transfer from the oxygen lone pair of the benzocrown ether moiety to the singlet-excited state of 9-cyanoanthracene. Upon Cs^+ complexation the oxygen lone pair electrons are involved in binding and hence no longer participate in PET, resulting in increased emission.

Gunnlaugsson *et al.* synthesised a novel sodium selective PET sensor **17** for the detection of Na^+ in blood at physiological pH (pH~ 7).[42] The sensing action was in the form of *'off-on'* switching with no other spectral change. The sensitivity of **17** was evaluated using Li^+ Na^+, K^+, Ca^{2+} and Mg^{2+} acetate salts in methanol: water (1:1, *v/v*) solution. The results indicated high selectivity for Na^+ over these ions. This selectivity may be due to the size of aza crown moiety and the steric effect enforced by the *ortho*-methoxy groups. A pK_a value of 5.3 for the receptor was observed from the fluorescence emission titration studies with pH, which eliminates protonation problems in the physiological environment. A binding constant (log β) of 2.5 was determined upon titration with Na^+. These facts combined indicate that **17** is suitable for sensing Na^+ in blood or serum.

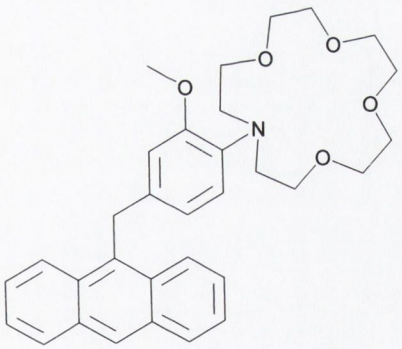

17

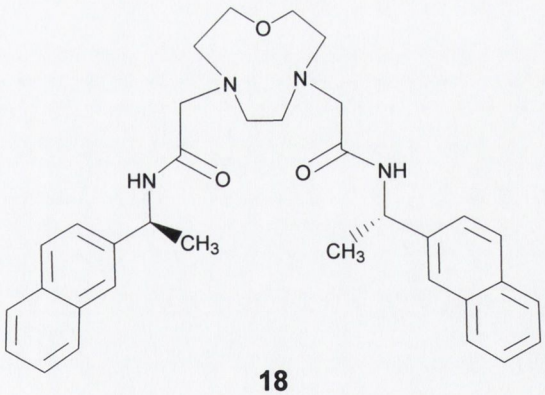

18

Gunnlaugsson *et al.* have also designed **18** as a Li^+ selective sensor.[43] The receptor in this sensor introduces a smaller crown ether moiety in order to increase the selectivity of Li^+ over Na^+. A naphthalene fluorophore is attached to the receptor by a chiral methyl substituted amide spacer, which further improves the selectivity for Li^+. The pK_a of the

sensor was determined to be 7.2 in MeOH:CH_3CN (1:1, *v/v*). The Li^+ sensing ability of **18** was investigated in CH_3CN and a 5-fold fluorescence enhancement was observed. No changes in fluorescence were observed with Na^+, K^+, Ca^{2+} and $Mg.^{2+}$ Simple 1:1 binding equilibrium with a log β= 5.4 was observed on Li^+ recognition.

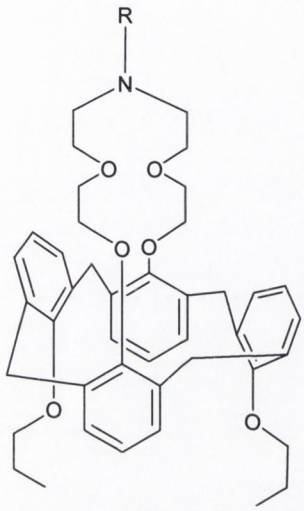

19

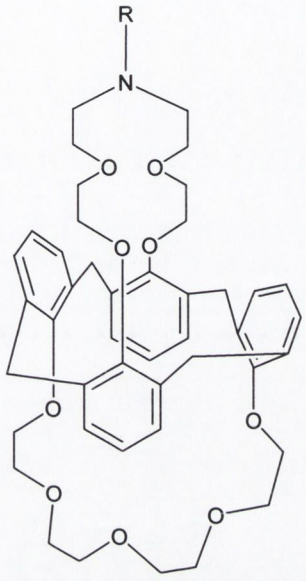

20

R =

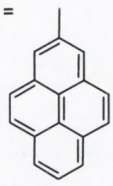

Yoon *et al.* developed novel fluorescent sensors **19** and **20** using Calix[4]azacrown as receptor and pyrene as a fluorophore.[44] The advantage of the Calix[4]azacrown is these receptors utilise two binding sites, one a crown ether the other an azacrown ether. Large chelation enhanced fluorescence (CHEF) effects were observed for **19** upon titration with Cu(II), K^+, Pb(II) and Rb^+ in ethanol. Small CHEF effects were observed with Ag(I) and Co(II). In case of **20**, similar CHEF effects were observed only with Ag(I), Co(II), Cu(II) and Pb(II) while K^+ and Rb^+ caused no fluorescence changes. These differences can be explained by considering the structure of the PET sensor **20**. The presence of two binding sites in the receptor offer the possibility of selective binding of metal ions to one of the sites. With **20,** ions such Cu(II) and Pb(II) show large CHEF effects due to the participation of azacrown ligand in recogntion. The K^+ cannot be bound by **20** as it is too large for the cavity of the azacrown. However, K^+ showed better binding affinity with the crown ether moiety of **20,** thus no CHEF effects were observed. The simultaneous complexation with both metal ions was not favourable due to a combination of steric hindrance and electrostatic repulsion. According to the authors, the process of '*molecular*

taekwondo': 'coming-in' and 'kicking-out' process was observed for sensor **20**. When Ag(I) was bound by sensor **20**, CHEF effects were observed. However, on addition of K^+ to the solution containing **20** and Ag(I), fluorescence quenching was observed. This phenomenon was attributed to the complexation of K^+ by the crown ether, which resulted in decomplexation of Ag(I), hence the process of '*molecular taekwondo'* was thought to be occurring (Scheme 1.1).

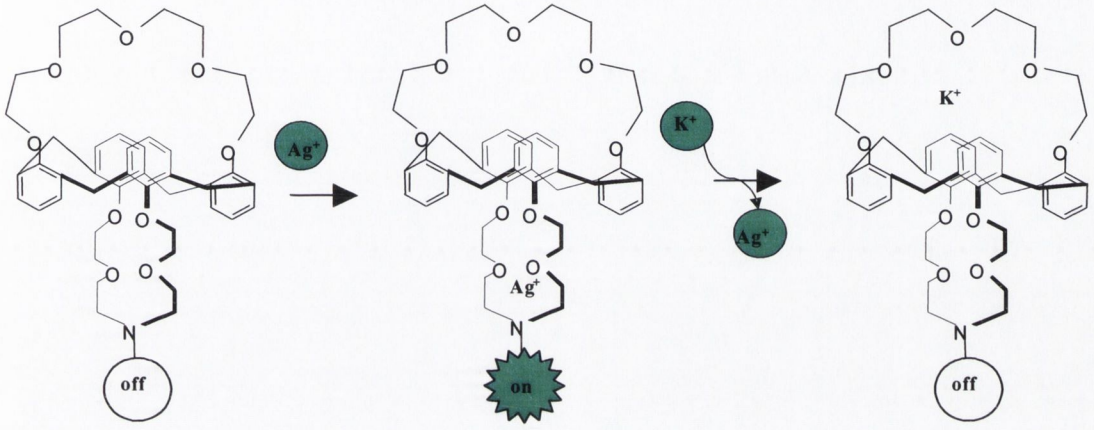

Scheme 1.1 ***'Molecular Taekowndo' process in sensor 20. Ag(I) ions switches fluorescence 'on' by suppressing PET; addition of K^+ dislodges Ag(I) ions and hence PET is operative leading to fluorescence 'off' stage.***

He *et al.* have developed naphthalimide based sensor **21** for Na^+ detection in serum and whole blood samples.[45] Compound **21** is immobilised on a hydrophilic polymer layer and has been packed into a disposable cartridge for commercial use. Naphthalimides are used as fluorophore, as they can undergo excitation and emission in the visible region of the spectrum. The ionophore used in molecule **21** was chosen to be *N*-(*o*-methoxyphenyl) aza-15-crown-5, due to its ability to bind Na^+ in the desired measuring range with minimum interference from pH. Due to the presence of a tertiary nitrogen atom the fluorescence of **21** is quenched by PET process. Binding of the cation to the azacrown ether inhibits fluorescence quenching as PET becomes thermodynamically unfavourable, thus leading to an increase in fluorescence. From the pH titration profile, a pKa value of 5.5 was determined for the *N,N*-dialkyl anisidine receptor, therefore demonstrating the ability of the sensor to work under physiological pH. From fluorescence titration studies with Na^+, a dissociation constant (K_d) of 80 mM was determined. This value was close to the desired 100-180 mM range.

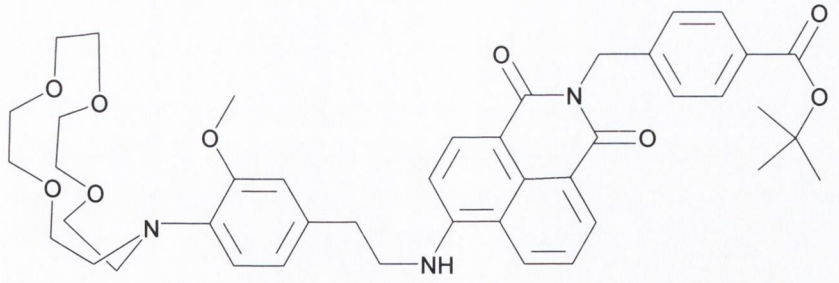

21

Using the same fluorophore, He and co-workers have synthesized sensor **22** for K^+ detection in water by using a cryptand-based receptor.[46] The receptor consists of a cryptand around *o*-alkoxyaniline PET donors. The ethylene spacer moiety separates the fluorophore and receptor, thus modulating the fluorescence response of the fluorophore. The metal ion titration studies were performed in TRIS-HEPES buffer at pH 7.4. The green fluorescence intensity increased substantially with increasing concentration of potassium ions. With cation binding to the triaza cryptand the PET process was inhibited restoring the fluorescence. No other changes were observed in the fluorescence and emission properties of the fluorophore. Higher selectivity for K^+ was observed while Na^+ caused only a minor increase in intensity. No changes were observed with Group 2, and transition metal ions. This sensor is now available commercially and is used for the measurement of potassium in whole blood and serum samples.

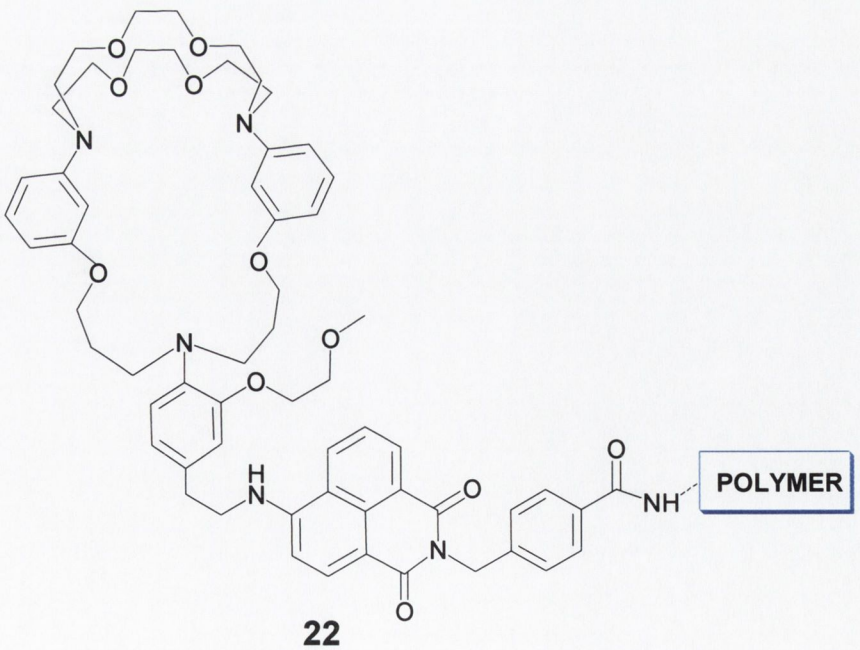

22

1.2.1.3 PET chemosensors for group 2 metal ions

Chelating receptors containing carboxylic moieties are known to bind efficiently to divalent hard metal ions such as $Ca^{2+}$and Mg^{2+}. Many well-known calcium sensors such as **23** and **24** have been synthesised by Tsien and co-workers for application in cellular biology for Ca^{2+} recognition.[47]

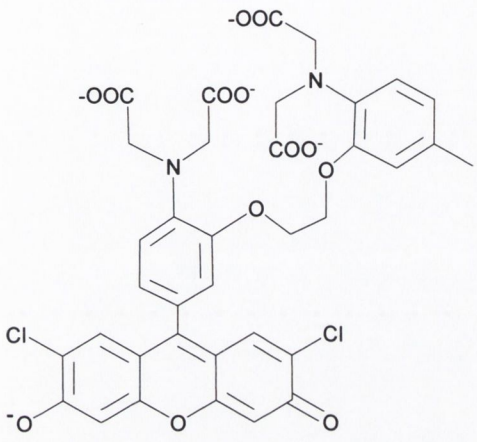

23

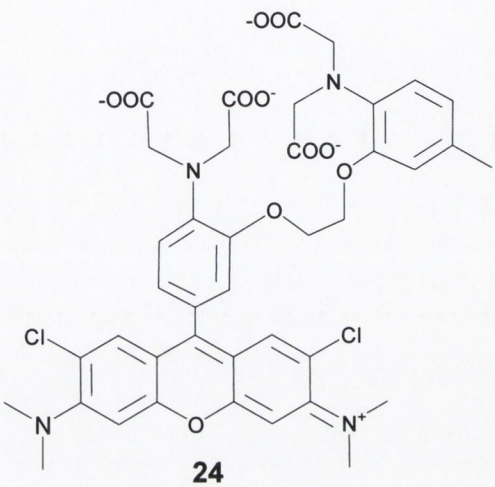

24

Most of these calcium indicators are suitable for intracellular Ca^{2+} (50 nM-50 μM), however bind too tightly for measurement of Ca^{2+} in blood or serum where the concentration is around 5 mM. The fluorophore was linked directly to the bis(2-aminophenoxy)ethane-*N,N,N',N'*-tetraacetic acid (BAPTA) chelating receptor in **23** and **24.** These sensors use the PET principle for Ca^{2+} detection. In the absence of Ca^{2+}, the BAPTA portion of the indicator is electron-rich and therefore able to donate electrons to the fluorophore, quenching its fluorescence. The recognition of the cation decouples the iminodiacetate moieties from the bis-alkoxy phenyl backbone, resulting in a large increase in the receptor's oxidation potential. As in **23** and **24**, the fluorophore and BAPTA receptor are linked by only one bond, which results in effective quenching. The consequence of this is the highest quantum yield (Φ_F= 0.34) and fluorescence enhancement observed for Ca^{2+} binding. The other advantage of these systems is that nitrogen of the iminodiacetate is part of the aromatic ring, which shifts the pKa of the fluorophore to ~ 4 - 5, well below the physiological pH range.

de Silva *et al.* have synthesised bifluorophoric chelating sensors, **25** and **26**.[48] These sensors show large Ca^{2+} induced fluorescent enhancement and lower Ca^{2+} binding constants when compared to monofluorophoric counterparts. This is due to statistic enhancement effects (as electron transfer is possible from two receptor moieties) on PET

rate (in Ca^{2+} free sensor) and remote steric effects respectively. The presence of the two identical fluorophores allows the excitation to reside on either fluorophore. This creates two potential sites for accepting electron transfer, and hence PET effectively quenches the fluorescence. Upon Ca^{2+} binding the electron transfer is suppressed, and hence a large fluorescence enhancement (FE) is observed. This is reflected in the increase in quantum yield. For example, the Φ_F increases from 0.0003 (for free sensors **25**, **26**) to 0.0060 and 0.045 respectively for **25** and **26** when involved in Ca^{2+} binding (measurements were performed in MOPS buffer at pH 7.3). Binding constants (logβ) of 6.8 and 5.2 were determined for **25** and **26** respectively. The lower binding constant observed for Ca^{2+}in the case of **26** was probably caused by steric effects as well as dipole-dipole repulsion, which destabilises the Ca^{2+}-bound sensor.

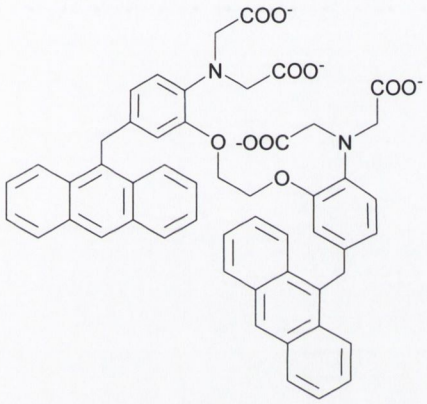

25

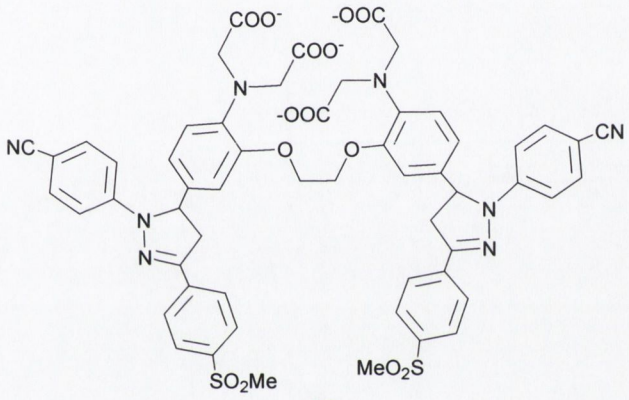

26

Katerinopoulos *et al.* have developed iminocoumarin fluorophore based Ca^{2+} indicators **27** and **28** incorporating BAPTA related receptors.[49] The fluorophore used are 3-(benzothiazoyl) iminocoumarin and 3-(benzimidazoyl) iminocoumarin. These molecules are substituted at the imino nitrogen with an *n*-dodecyl lipophilic chain for their use as near membrane indicators. In the absence of Ca^{2+}, the fluorescence is quenched due to the charge transfer from the receptor to the fluorophore. The absorption spectra of **27** and **28** exhibited absorption maximum of 469 nm and 471 nm, which upon Ca^{2+} addition shifted to 401 nm and 421 nm respectively. The emission maximum for **27** and **28** were observed at 515 nm and 537 nm respectively. Upon addition of Ca^{2+}, the emission maximum of **27** was shifted to 498 nm while that of **28** remained constant at 537 nm. The fluorescence emission was greatly enhanced due to the interaction between receptor and Ca^{2+}. K_d of 5.50 μM and 4.40 μM were determined for **27** and **28** respectively. Therefore these probes offer

advantage for Ca^{2+} recognition in the inner-membrane vicinity, where transient concentration of Ca^{2+} reach levels corresponding to their K_d value.

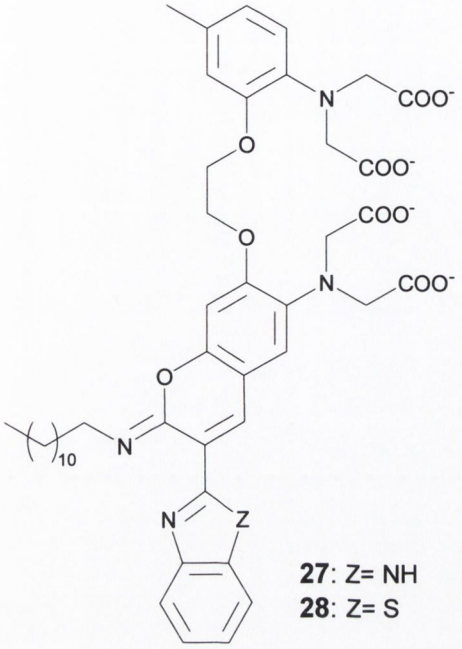

27: Z= NH
28: Z= S

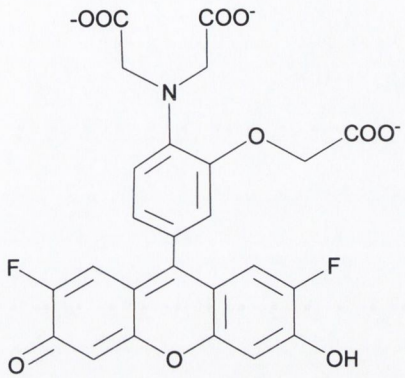

29

Molecular Probes (Eugene, Oregon) have developed visible light-excitable Mg^{2+} indicator mag-fluo-4, **29** for intracellular Mg^{2+} recognition.[50] In the presence of Mg^{2+}, **29** exhibits strong fluorescence enhancement with no absorption or emission shifts. A K_d of 4.7 mM was determined for **29**-Mg^{2+}complex.

1.2.1.4 PET chemosensors for transition metal ions

Fabbrizzi and co-workers have reported several PET sensors containing an anthracene fluorophore linked to polyamine receptor, *e.g.*, **30** and **31,** which were particularly useful for the detection of soft metal ions such as Cu(II) .[51,52]

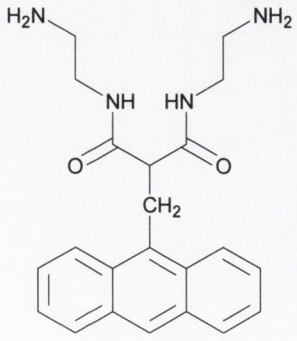

30

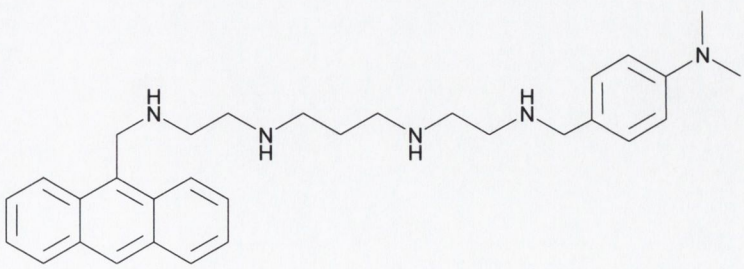

31

Fluorophore **30** displays the normal anthracene emission in $CH_3CN:H_2O$ (4:1,*v/v*). The fluorescence intensity did not change in the pH range 2-12. The addition of 1 equivalent of Cu(II) to an basic solution of **30** resulted in a decrease in the fluorescence intensity. Additionally, there was a change in the absorption spectra, a new band at 520 nm appeared and the solution became pink in colour. This band is assigned to the d-d transition of the square planar complex of **30**-Cu(II) as shown in Scheme 1.2.

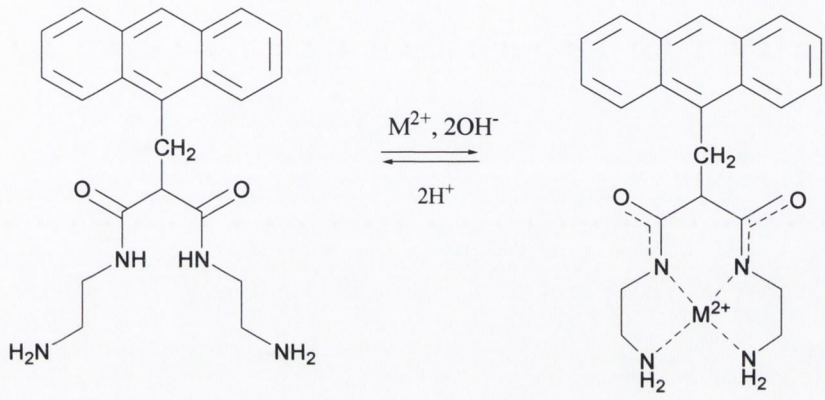

Scheme1.2 Metal binding equilibrium for sensor 30. Under alkaline conditions the square planar complex with transition metal ions are stable and the Cu(II) binding results in fluorescence quenching.

The fluorescence quenching of the anthracene fluorophore was either due to energy transfer or electron transfer from the paramagnetic Cu(II) to the anthracene excited state. The oxidation of Cu(II) to Cu(III) is favoured by the coordination of the deprotonated amide groups (Scheme 2). Similar results were observed for Ni(II) however the newly developed absorption band was centred around 450 nm, which corresponded to a yellow, low-spin complex formation. When an acetonitrile:water (4:1, v/v) solution of **31** was treated with Cu(II), in the pH range of 2.5-3.5 some fluorescence quenching was observed. At this pH range, the formation of a Cu(II) tetraamine complex is thought to take place and proximate Cu(II) deactivates the excited state of anthracene either through electron transfer or energy transfer in a manner similar to **30**. A similar observation was made for Ni(II) in the pH range of 4-6. Zn(II) addition also leads to a decrease in the fluorescence emission of **31** despite the fact that Zn(II) is known to be a "non-quencher" metal ion. The explanation offered for this phenomenon was that Zn(II) binding induces conformational changes in the molecules, which bring the dimethylaniline (DMA) and anthracene fragments close enough to allow electron transfer.

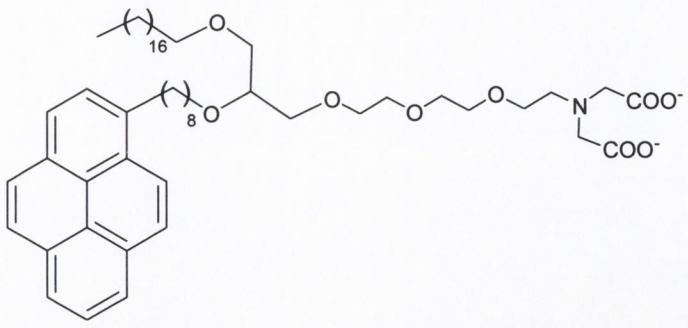

32

Arnold and co-workers described the lipid functionalised sensor **32** containing a fluorescent pyrene residue and a chelating iminodiacetate group for Cu(II) detection.[53] Interestingly, when **32** was added to a diastearoylphosphatidylcholine vesicle at pH 7.5, aggregation within the parent membrane was observed. Upon excitation at 346 nm, the vesicle exhibited two distinct bands; a weak emission band at 377 nm, attributed to small number of isolated monomers of sensor **32,** and a broad, intense band at 470 nm due to the excimer formation between the pyrene monomers. The addition of Cu(II) resulted in an increase in the monomer emission and a decrease in the excimer emission. Cu(II) complexation by the iminodiacetate moiety was thought to induce reorganisation of the lipids by dispersion of **32** in the matrix, resulting in an increase of the '*monomer-to-excimer'* ratio. The addition of copper causes the cell membrane of the vesicle to rearrange. This resulted in the random distribution of these sensors within the cell membrane, leading to a decrease in the excimer emission with an increase in the monomer emission. This process is illustrated in Figure 1.5. The Cu(II)-induced changes in the fluorescence spectrum were fast and reversible, and could be used for the quantification of Cu(II) down to a concentration of 5 nM. This sensor was at least 10 times more sensitive for Cu(II) than for Co(II), Ni(II), Mn(II) or Ca(II). The sensitivity and selectivity for Cu(II) is attributed to the high thermodynamic stability of the Cu(II)-iminodiacetate complex.

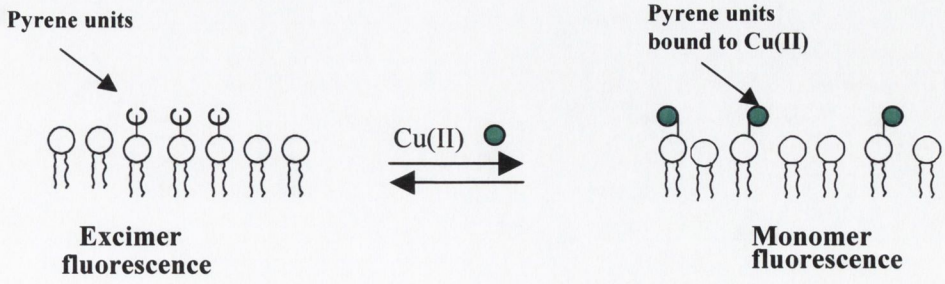

Figure 1.5 ***Rearrangement of membrane bound form of sensor 32 upon Cu(II) recognition.***

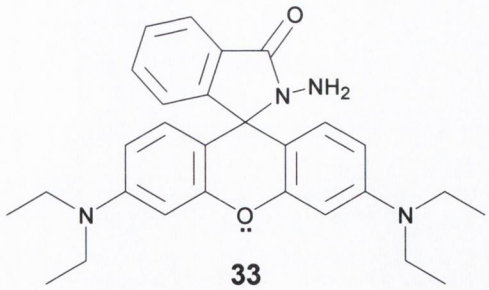

33

Czarnik *et al.* developed an interesting sensor **33** based on rhodamine B hydrazide. The molecule a '*chemodosimeter*' (fluorescence response measured by chemical change) rather than a sensor, as the fluorescent signalling is not reversible.[54] In the absence of Cu(II) ions **33** was non-fluorescent as the nitrogen electron pair are involved in fluorescent quenching. Addition of Cu(II) ions at pH 7.5 resulted in a N, O chelation by the hydrazide moiety. Subsequent redox hydrolysis released rhodamine B, which is highly fluorescent, as the PET process was no longer operates (Scheme 1.3). Czarnik's '*dosimeter*' molecule was the first example of a hydrolysis redox based sensor for Cu(II) detection.

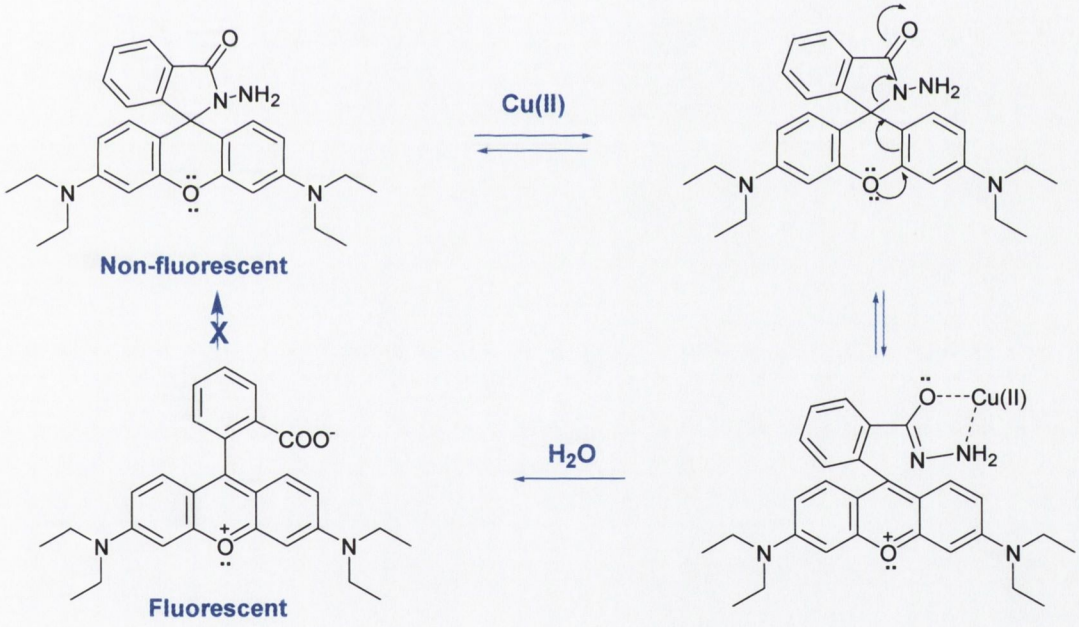

Scheme 1.3 Illustration of Cu(II) sensing mechanism of Czarnik's dosimeter molecule 33.

Kumar *et al.* designed 9,10-anthraquinone and anthracene based chemosensors **34** and **35** for selective detection of Cu(II).[55,56] The receptor moiety in **34** employs mixed ligand sites of S, N and O, which mimics copper binding sites prevalent in azurins and Cu-blue

proteins. On addition of Cu(II) to **34** in a CH_3CN:H_2O (4:1,*v/v*) solution , an increase in the absorption intensity in the 520-800 nm region was observed. No changes were observed for Ni(II), Cd(II), Zn(II), Hg(II) and Pb(II) ions indicating high selectivity for Cu(II). Notably **35** exhibited a fluorescence enhancement in the presence of Cu(II) ions, in contrast to the usual quenching. In the absence of any metal ions, the linker atom of the fluorophore (tertiary nitrogen) quenches the fluorescence of the anthracene fluorophore *via* PET process. However, when Cu(II) occupies the receptor moiety, this nitrogen along with the thioether and the other amines became involved in complexation, thus suppressing the PET process. This overweighs the reverse effect of electron transfer quenching by the paramagnetic Cu(II), thus a net fluorescence enhancement is observed. Metal ion titration studies were also carried out in HEPES buffer at pH 7.0 in CH_3CN:H_2O (4:1, *v/v*) solutions, however, no fluorescence enhancement was observed for Ni(II), Cd(II), Zn(II), Ag(I), Hg(II) salts under these conditions.

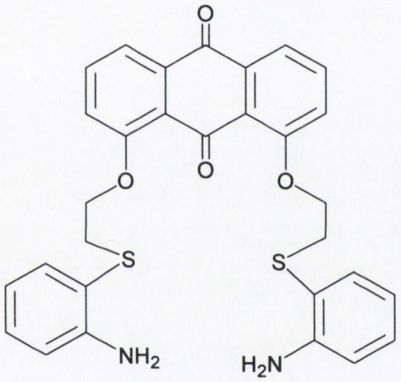

34

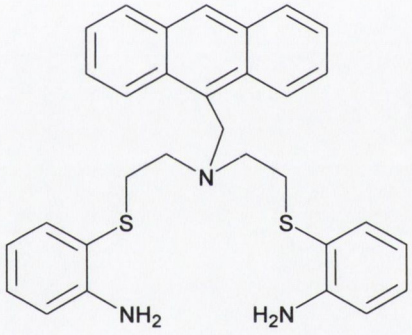

35

The Pallaviani group have cleverly used the idea of the PET process for designing a novel *'on-off-on'* system for the recognition of Cu(II).[57] The system employed in their studies consists of three separate components, which are capable of displaying *'on-off-on'* fluorescence emission with pH variation. The components are a tetraaza ligand (**36**), the Cu(II) and coumarin 343 (**37**), which contains an acidic non-coordinating fragment that transforms into its coordinating conjugate base upon deprotonation (Scheme 1.4). At low pH, both ligand and coumarin fluorophore are protonated and hence the system is in fluorescence *'on'* state [Scheme 1.4(a)]. At intermediate pH values, the Cu(II) binds both to ligand as well as coumarin, completing its coordination sphere and the fluorescence is in *'off'* state, due to the PET process [Scheme 1.4(b)]. At higher pH, the hydroxide ion

displaces the metal from the fluorescent molecule, and thus the fluorescence of coumarin is restored and the system returns to the *'on'* state [Scheme 1.4(c)].

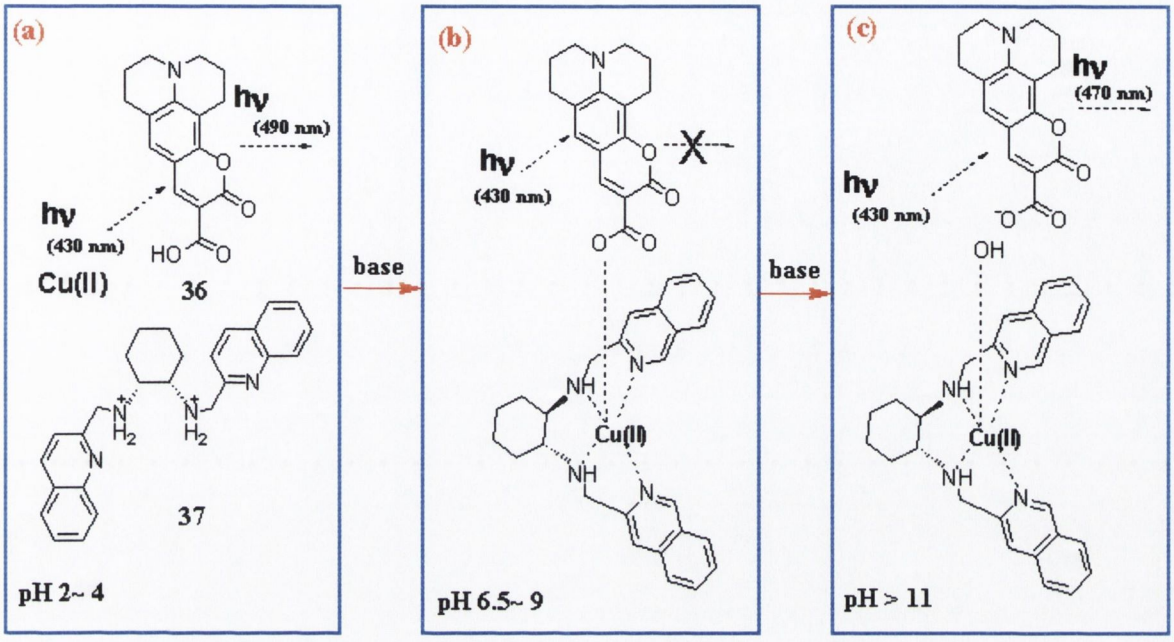

Scheme1.4 Fluorescence changes at different pH for multi-component system

Yoon *et al.* have prepared the 1,8-bis(pyrazolylmethyl) anthracene and the 9,10-bis(pyrazolymethyl) anthracene sensors **38** and **39** respectively, for selective detection of Ag(I).[58] Fluorescence quenching effects were observed when **38** was titrated with Ag(I) and Cu(II) in $CHCl_3$:EtOH mixture (7:3, *v/v*), while **39** displayed a selective fluorescence quenching only with Ag(I). The maximum quenching for Ag(I) was observed for **39**. The association constant of 1.25×10^5 and 1.34×10^5 M^{-1} were calculated for the Cu(II) and Ag(I) complexes of **38**, however **39** displayed selective quenching effects on complexation of Ag(I) with an association constant of 2.4×10^3 M^{-1}.

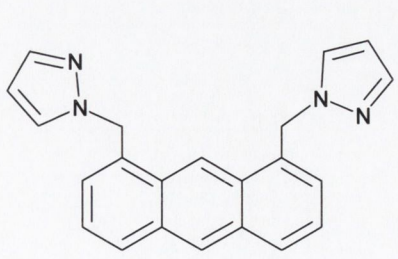

38

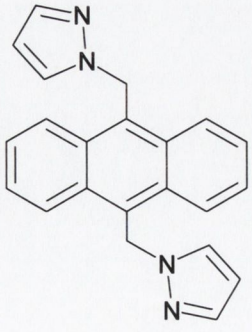

39

In the case of **39**, there was an additional π-Ag(I) interaction, which was absent for **38**, (Scheme 1.5). This interaction was also seen in the absorption spectra of **39,** in which there was a decrease in absorption intensity upon Ag(I) addition, whereas for **39** the absorption spectra was unchanged upon Ag(I) recognition.

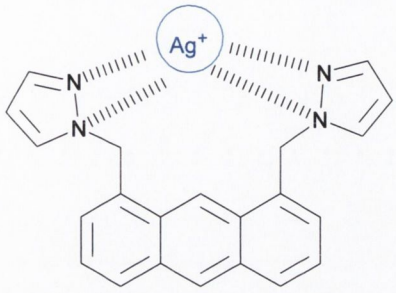

38

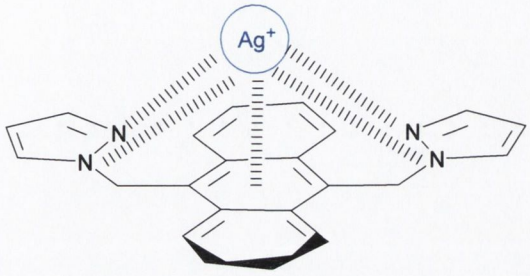

39

Scheme 1.5 Interaction between Ag(I) and anthracene fluorophore in sensor 39. Note that such interaction is absent in 38.

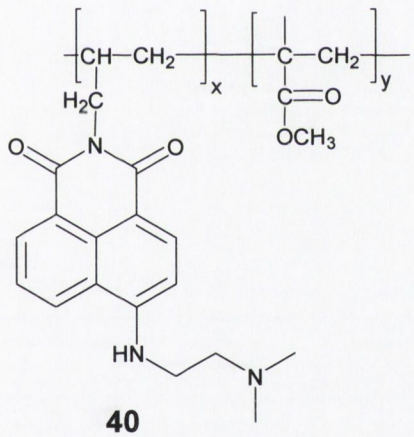

40

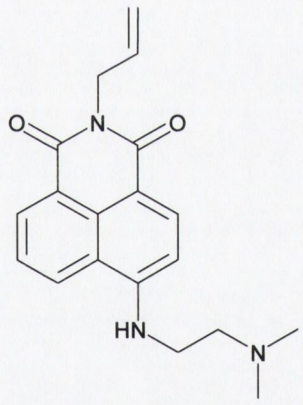

41

Grabchev *et al.* synthesized homogenous polymeric, as well as monomeric, naphthalimide based sensors **40** and **41** for the recognition of transition metal ions.[59] As the PET process is operating in these sensors, in the absence of metal ions, the dye has a low quantum yield of Φ_F = 0.04. Addition of metal ions leads to an increase in fluorescence intensity as the electrons of receptor nitrogen become involved in metal binding. In addition weak hypsochromic shifts ($\Delta\lambda$ = 3-5 nm) were observed in fluorescence maxima, indicating interaction between the fluorophore and the metal ion. Fe(III), Ni(II), Zn(II), Fe(II) and Pb(II) metal chlorides were titrated with **40** in

dimethyformaide (DMF), but only Fe(II) induced higher fluorescence enhancement (Φ_F= 0.83). Similar results were obtained for **41**. However, for the polymeric sensor **40,** the fluorescence increase towards Fe(II) ions was much higher than the monomer, indicating that the cumulative effect of large numbers of monomer units results in an amplification of the fluorescence response.

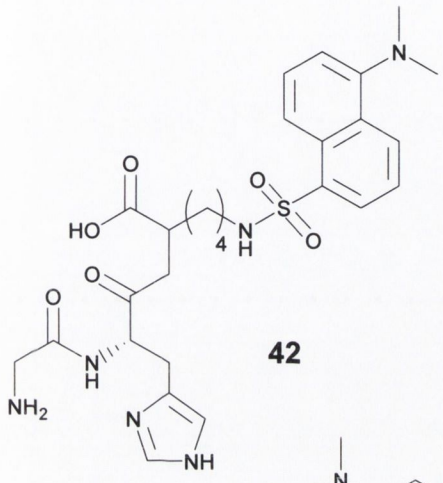

42

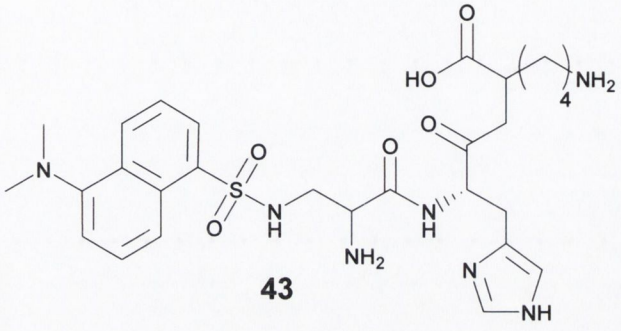

43

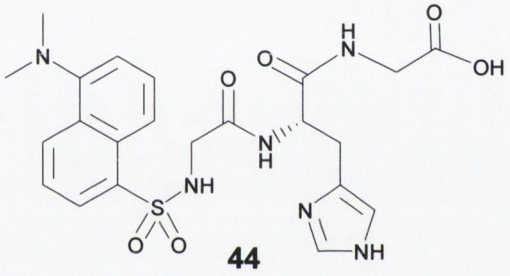

44

Recently Andreopoulos *et al.* have demonstrated how the phenomenon of molecular recognition can be controlled by the judicious design of supramolecular systems.[60] They have synthesized series of Dansyl-Gly-His peptide motif based fluorescent chemosensor (**42-44**) for the detection of Cu(II). The functionality of the chemosensors was greatly influenced by the spatial alignment of the fluorophore in the molecule. In sensor **42**, the dansyl group is attached to the side chain of lysine residue, and is 4-carbons away from the Cu(II) binding site. In sensor **43**, the dansyl group is also on a side branch but the close placement due to the single CH_2 linkage allows it to directly participate in binding with Cu(II). In **44**, the dansyl group is directly attached to a binding participating nitrogen atom. This difference in distance to the binding site had a profound effect on the complexation characteristics of these sensors. For **44**, 1:1 complexation equilibrium was observed with Cu(II), for **42** and **43**, both 1:1 and 2:1 (ligand:metal) complexes were also involved. The side branched labelled ligand **42,** showed more selectivity for Cu(II) than for Fe(II), Fe(III),

Zn(II), Co(II) and Ni(II). In the case of **43,** which is also a side branched labelled ligand, the dansyl groups present an auxiliary binding site. This mechanism offers enhanced interaction between the peptide and metal ions, so the selectivity was compromised. Thus sensor **43** showed strong binding with all the transition metal ions. The highest selectivity for Cu(II) was observed for the **44,** as the dansyl group is attached to the *N*-terminal end of the peptide, therefore it is also involved in binding to Cu(II). Thus both selectivity and molecular sensitivity are improved. The binding model of the peptide sensor **44** is shown in Scheme 1.6.

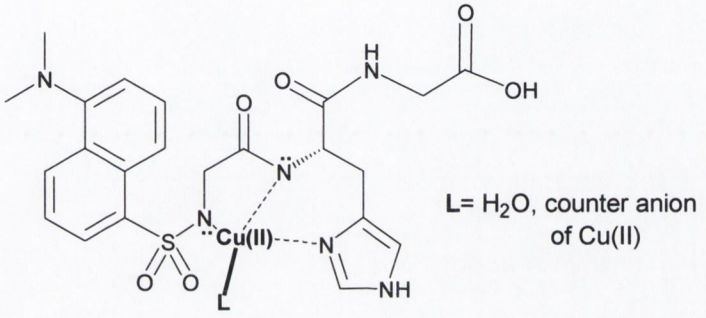

Scheme 1.6 Complexation of sensor 44 with Cu(II). Note the nitrogen of fluorophore involved in binding

1.2.1.5 PET chemosensors for anions

The field of anion sensing has grown rapidly over the last few years.[13,30] A few important examples will be discussed to illustrate how the PET process has been applied elegantly to this rapidly developing field. Czarnik *et al.* developed anthrylpolyamine conjugate **45** and **46** probes for phosphate and citrate recognition.[61]

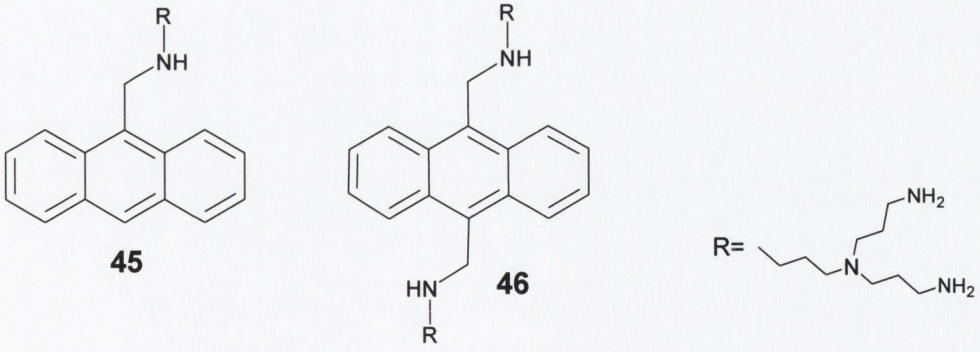

Compound **45** exists, as a trication at pH 6, where the nitrogen atom proximal to the anthracene ring is not protonated, therefore enabling the molecule to acts as an anion sensor. In this form, PET quenching from the amino moiety to the anthracene occurs and the

emission intensity is low (Scheme 1.7A). This trication can bind complementary structures such as phosphate. The three oxygen atoms on the anion interact with the three positive charges on the ammonium ions leaving the remaining OH group in close proximity to the free amine, and therefore in a favourable position to undergo proton transfer to the unprotonated amino group (Scheme 1.7B). This proton transfer suppresses the PET process (Scheme 1.7C). Thus, anion binding is accompanied by an increase in the fluorescence emission intensity. Binding of **45** to adenosine triphosphate, citrate and sulphate also lead to fluorescence enhancements, although to a smaller degree than those observed for phosphate. Similar chelation enhanced fluorescence was observed in case of citrate binding to **46.**

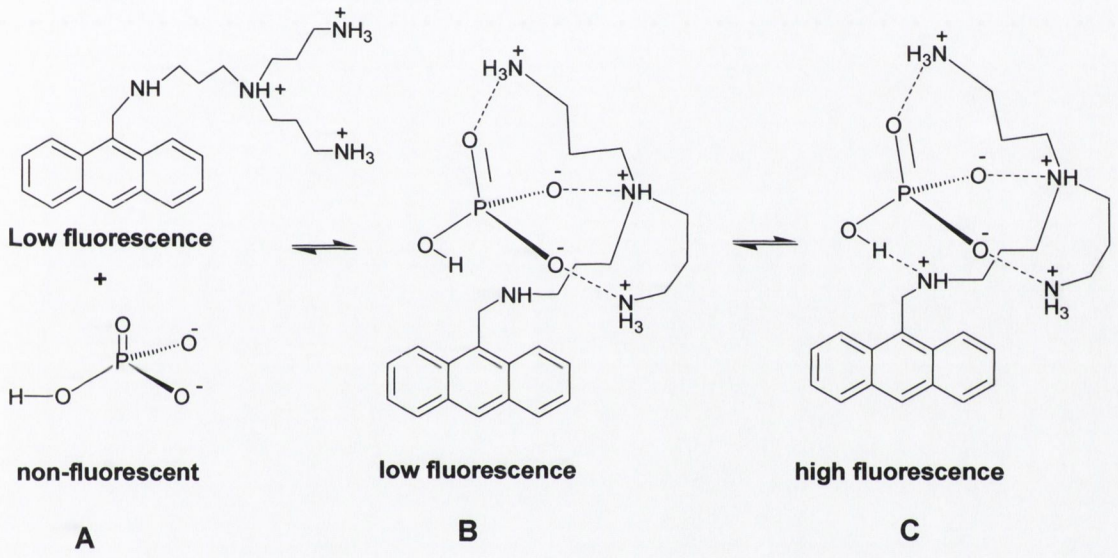

Scheme 1.7 Modulation of electron transfer process upon hydrogenphosphate binding in sensor 45.

Gunnlaugsson *et al.* synthesised novel charged neutral anthracene based fluorescent sensors **47-49** containing an aromatic or aliphatic thiourea moiety as an anion receptor which exhibit ideal PET behaviour.[62] The fluorescence of the fluorophore in DMSO was selectively quenched upon binding with AcO^-, $H_2PO_4^-$ and F^-. When fluorescence titrations were carried out in CH_3CN, CH_3CO_2Et or THF, the emission was also quenched upon addition of AcO^-, but to a smaller degree. In a competitive hydrogen bonding solvents such as ethanol, no binding was observed for AcO^-. 1:1 binding with log β of 3.35, 2.55 and 2.05 was determined for F^-, AcO^- and $H_2PO_4^-$ respectively. As **47** contains an electron-withdrawing CF_3 group, stronger anion binding was observed due to the higher acidity of the thiourea-receptor protons in these systems

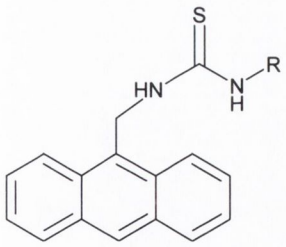

47: R= $C_6H_5CF_3$
48: R= C_6H_5
49: R= CH_3

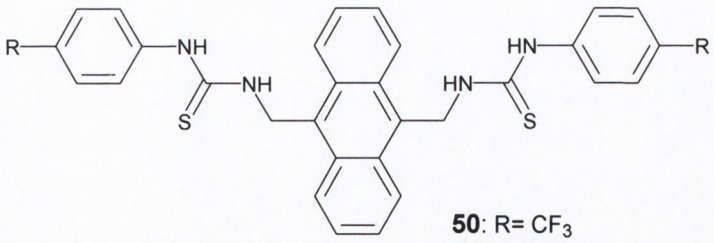

50: R= CF_3
51: R = H

Substitution of the 10-position of anthracene resulted in the development of the bis anthracene systems **50** and **51.**[63] Both thiourea moieties were available for anion recognition. The fluorescence quenching for both **50** and **51** was observed with AcO^- with 2:1(anion:ligand) ratio. Both sensors showed good affinity for biologically important ions such as glutarate, malonate and pyrophosphate with 1:1 complexation (Scheme 1.8).

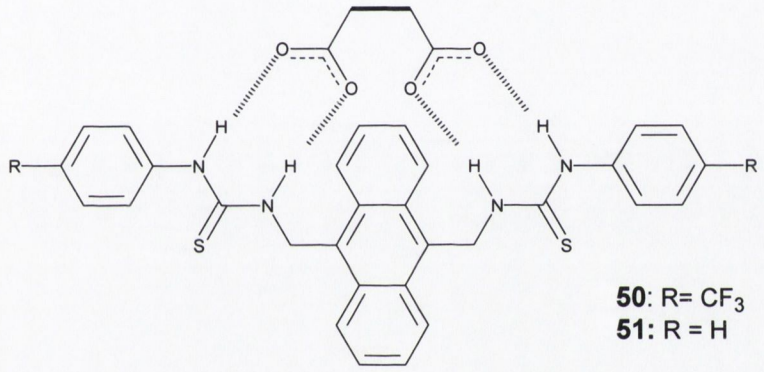

50: R= CF_3
51: R = H

Scheme 1.8 Complexation of 50 and 51 with carboxylate receptor.

1.2.2 Fluorescent chemosensors based on internal charge transfer (ICT)

Fluorophore containing electron-donating groups coupled to electron-withdrawing groups can undergo intramolecular charge transfer upon excitation by light of suitable wavelength.[21] The ICT takes place from donor to acceptor, which results in a change in the dipole moment of the fluorophore.[64] Interaction of cation with either the donor or acceptor causes changes in the photophysical properties of the fluorophore as the complexed ion affects the efficiency of ICT.[65] Upon the interaction of the donor unit of fluorophore with a cation, loss of conjugation occurs, due to the increase in the reduction potential of the fluorophore. Consequently, the absorption spectrum is shifted towards lower wavelengths (blue-shift) with a corresponding decrease in the extinction coefficient.[65] On the other hand, interaction of acceptor moiety with a cation decreases the reduction potential of the fluorophore and thus extends conjugation. The absorption spectrum is thus red-shifted

resulting in an increase extinction coefficient. The fluorescence spectra are in principle shifted in the same direction as those of the absorption spectra but this is not always the case, and is dependent upon the nature of fluorophore and guest in the excited state.[65]

These changes can also be explained in terms of charge dipole interaction.[40(a)] When the cation interacts with the donor group, the excited state is more strongly destabilised than the ground state and a blue shift in absorption and emission spectra is observed. Conversely, when the cation interacts with the acceptor group, it leads to stabilisation of the excited state more than ground state, causing red shifts in the absorption and emission spectra. These changes are depicted schematically in Figure 1.6. The photophysical changes in the fluorophore during absorption and emission also depend on the charge, size and complexation affinity of the cations.[65]

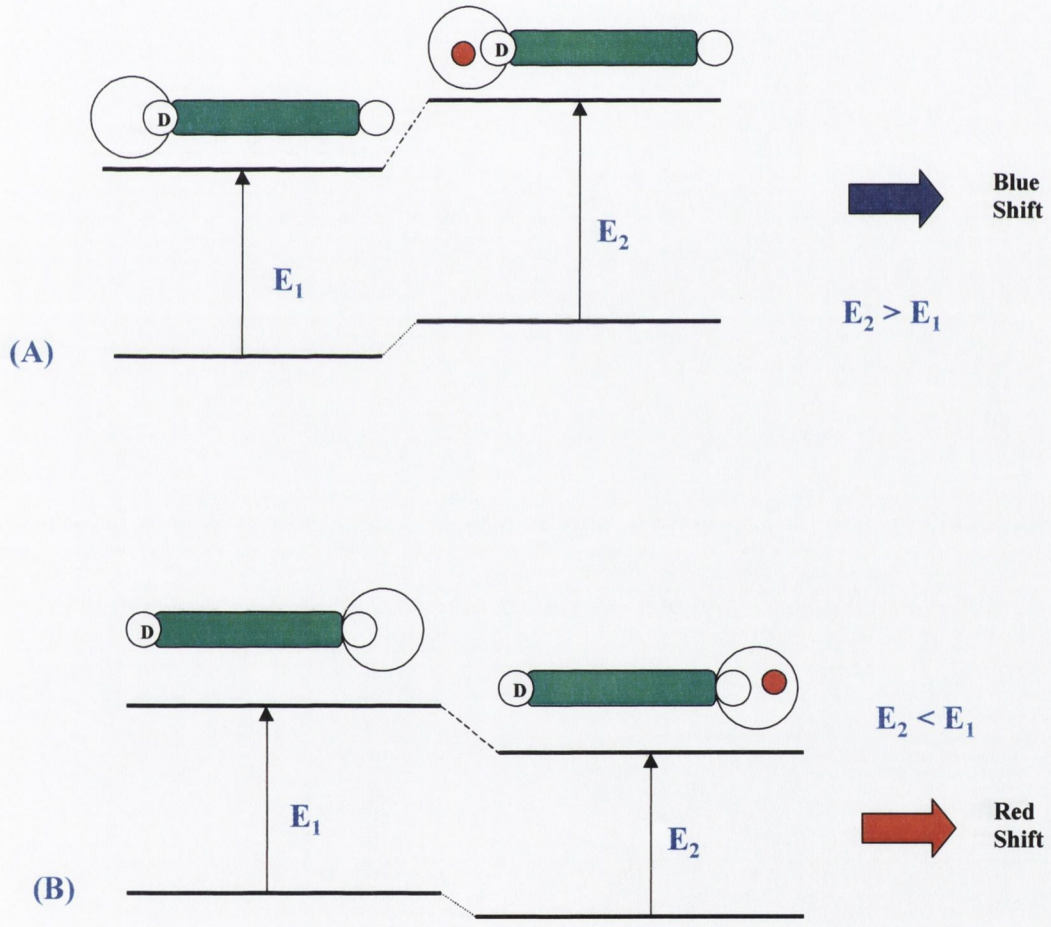

Figure 1.6 ***Energy level diagram depicting the analyte control of photoinduced charge transfer in conjugated donor-acceptor systems. (A) interaction of cationic guest with donor and (B) with acceptor.***[69]

1.2.2.1 Literature survey of ICT chemosensors

Some of the earlier examples of ICT sensors utilized azamacrocycle as the ionophore, for example sensor **52**.[66] In sensor **52**, the absorption spectrum is drastically perturbed upon addition of Ca^{2+} and Mg^{2+}, however no shifts were observed in the emission spectra. Unexpectedly the excited-state lifetime was almost unaffected by complexation, whereas the quantum yield was reduced. These observations were explained by considering the dissociation of the cation in the excited state. The disruption of the interaction between a cation and crown ether nitrogen atom is extremely fast and occurs in less than 20 picoseconds. Such disruption arises from the appearance of a partial positive charge on the nitrogen atom of the crown ether as a result of the photoinduced ICT from the electron-donating moiety towards the electron-withdrawing group. Consequently, the stability of the complex in the excited state is lower than in the ground state leading to dissociation of the cation. This was further proved by picosecond pump-probe spectroscopy in which an intense light pulse causes some complexed cation to leave the crown and diffuse away.

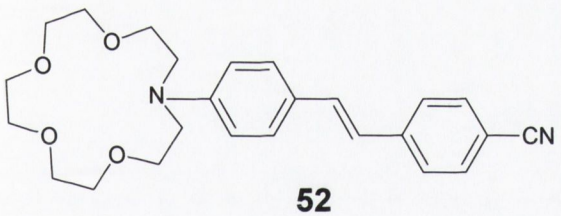

52

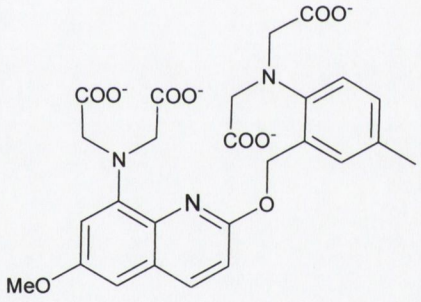

53

Quin-2, **53**, was the first fluorescent tetracarboxylate indicator used for biological detection of intracellular Ca^{2+}.[67] The ring nitrogen atom in quinoline takes on the role of one of the ether oxygen atom of BAPTA. The double function of quinoline keeps the molecule compact, but lowers the Ca^{2+}/Mg^{2+} selectivity by almost an order of magnitude. Ca^{2+} binding causes large spectral shifts and a 6-fold increase in excitation amplitude at 337 nm. The K_D for Ca^{2+} was determined to be 115 nM at 37 ^{0}C. Drawbacks such as low quantum yield when bound to Ca^{2+}, small extinction coefficient and photobleaching, limited its use for microscopic Ca^{2+} imaging.

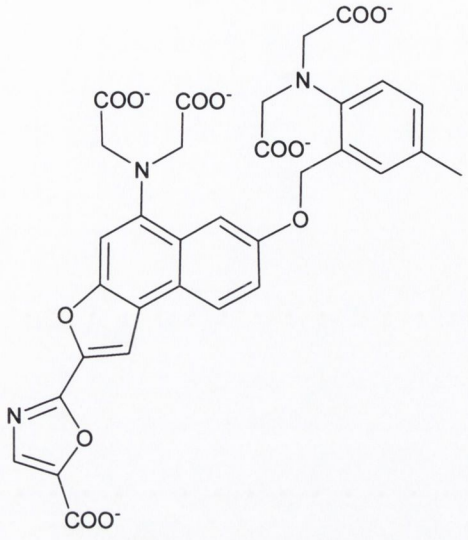

54

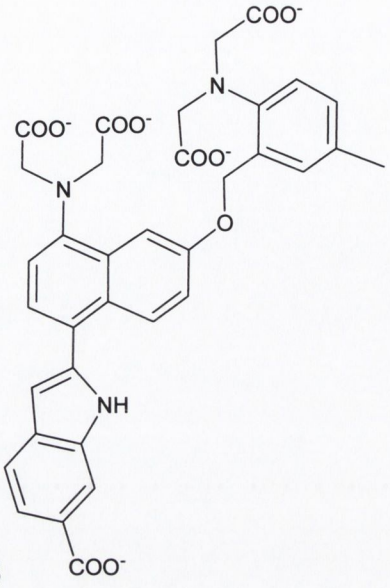

55

Fura-2, **54** developed by Tsein *et al.* was the first indicator to be used for single-cell imaging studies for Ca^{2+}.[67] Fura-2, **54** has several advantages, e.g. high emission wavelength, large Stokes' shift, photochemical stability and easy introduction into cells as its ester derivative. Cation-free sensor **54** has an absorption maximum at 362 nm and on Ca^{2+} binding, shifts to 335 nm with an increase in amplitude. The K_d for Ca^{2+} was determined to be 135 nM in HEPES buffer at pH 7.4. The emission maximum of the free dye was at 518 nm, and was shifted to 510 nm upon titration with Ca^{2+}. As explained earlier, in the case of **52**, this was probably due to the dissociation of Ca^{2+} from the amino group in the excited state. Evidence for this excited-state relaxation is when fura-2 solutions are made highly viscous (for example by the addition of 70% sucrose and reducing the temperature to -10^0C), Ca^{2+} binding in these conditions leads to a shift of 55 nm in the emission wavelength.

In comparison, Indole-1, **55** shows significant blue emission wavelength shifts from 482 nm to 398 nm upon Ca^{2+} binding.[68] The reason for the emission shift is the electron-rich nature of indole fluorophore, which is less prone to accept electron density form the BAPTA amino nitrogen in the excited state when compared to the oxazole. This leaves the electrons of the BAPTA available for strong binding to Ca^{2+}, thus preventing dissociation of Ca^{2+} in the excited state. The Ca^{2+} binding in turn shifts the emission to shorter wavelengths.

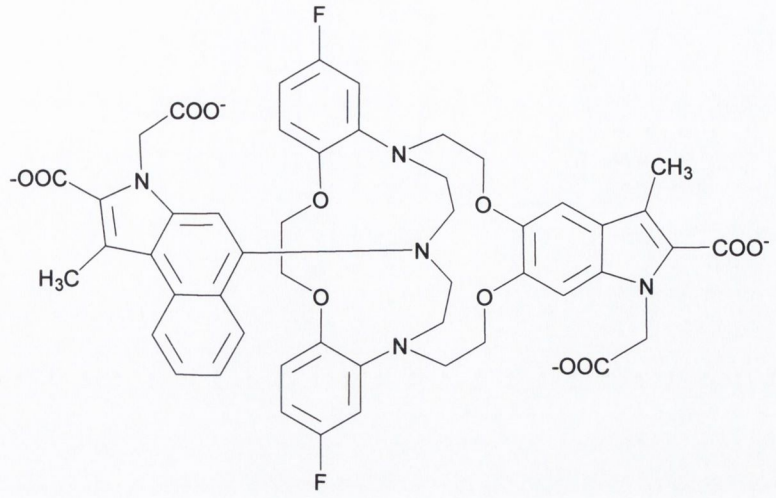

56

The indole based fluorescent chemosensor **56,** consists of a specially designed ionophore for the specific determination of intracellular Na^+ ion concentration, as the cavity size of **56** matches the size/charge ratio of Na^+.[69] Upon Na^+ binding the emission maximum was shifted from 460 to 395 nm with a 25 fold increase in emission intensity. The blue-shift of the emission spectrum on Na^+ binding is thought to be due to the reduction of the electron-donating character of the nitrogen atom of the cryptand to which the fluorophore is bound.

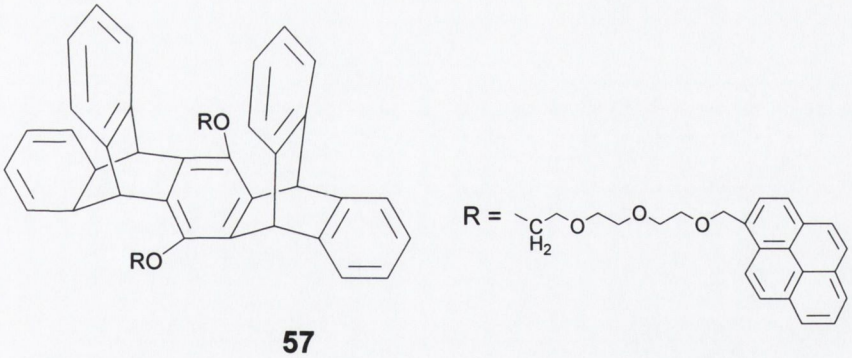

57

Wang *et al.* have reported a pyrene-based sensor **57** for Ca^{2+} and Cu(II) recognition.[70] Upon addition of Ca^{2+} in dichloromethane, there was a decrease in excimer formation and a simultaneous increase in the monomer emission. With transition metals, only Cd(II) and Cu(II) show changes in the fluorescence emission of **57**. Cd(II) ions behave in a similar manner to Ca^{2+}. In contrast, when Cu(II) was used there was an enhancement in the excimer formation along with a substantial 35 nm red shift in the emission spectrum. This

result was interesting, as Cu(II) usually quenches the excited state. The difference in the fluorescence spectra of Ca^{2+} and Cd(II) compared to that of Cu(II) suggests that **57** adopts different conformations depending on the metal ion present. Pyrene is known to form two different types of excimers; a sandwich type, which emits at longer wavelengths (475nm) and a partially overlaping type, which emits at a shorter wavelength (440 nm). A dynamic equilibrium exists between these two forms and they can interconvert, both in the ground and in the excited state. The equilibrium is more favourable for the sandwich excimer type in dynamic binding systems, while under static binding the overlapping state predominates. Upon titration with Cu(II), the system reverts from the dynamic to the static due to conformational changes upon binding, hence no interconversion was observed. Cu(II) locks the system into the static state, thus stabilizing the partially overlapping excited dimer state of pyrene.

Laurent *et al.* reported a novel donor-spacer-acceptor podand system **58**, as an efficient dual channel sensor for Li^+, Mg^{2+} and Ca^{2+}.[71] When **58** is treated with Li^+, Mg^{2+} and Ca^{2+} there was both a decrease in both the absorption intensity as well as a hypsochromic shift of the absorption bands. Large effects were observed for Mg^{2+} and Ca^{2+}, whereas Li^+ induced moderate modifications. The fluorescence emission of the podand **58** was strongly affected by these ions while Na^+ and K^+ have only negligible effect. The free complex emits at 399 nm however, on addition of excess of Li^+ this emission band was blue-shifted (388 nm) on excitation at 330 nm. No other emission bands were observed on titration with Li^+. In contrast, addition of excess Mg^{2+} and Ca^{2+} resulted in blue-shifted emission bands, at much higher wavelength than was observed for Li^+. The band was shifted to 371 nm upon excitation at 330 nm for both Mg^{2+} and Ca^{2+}. Furthermore, for both Ca^{2+} and Mg^{2+}, a second band centred at 431 nm, was observed upon excitation at 360 nm. These observations were explained in terms of changes in the reduction potential of the *N*-oxide moiety of **58**. When Mg^{2+} and Ca^{2+} were present, the *N*-Oxide shows better coordination to these ions. This makes the reduction of the isoquinoline *N*-oxide possible by inducing the charge transfer (CT) from the alkoxybenzene donor moiety, leading to the emitting CT state. However, the *N*-oxide function could not be significantly involved in Li^+ coordination, due to its small size, so isoquinoline *N*-oxide remains a poor acceptor and no charge transfer emission was observed.

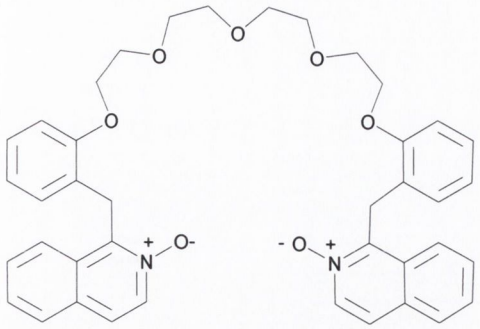

58

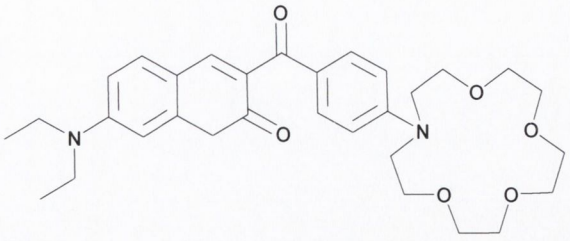

59

Recently Chen *et al.* designed highly selective coumarin based sensor **59** for Pb(II).[72] They used this ketoaminocoumarin as a signal transducer as it possesses excellent photochemical stability and can be excited in the visible region. 15-monoazacrown-5-ether was used as the receptor unit. The absorption and fluorescence spectra of **59** in CH_3CN were red-shifted upon addition of Pb(II). Group 1, group 2 and other divalent transition metal ions resulted in minor increase in the fluorescence emission intensity. The fluorescence enhancement observed was explained in terms of photoinduced charge transfer (PCT) and conformational restrictions induced upon Pb(II) complexation. The large Hill coefficient and Job plot analysis revealed the formation of 2:2 complex (metal:ligand) (Scheme 1.9). This structure supported the small red-shift observed in the absorption spectrum as one of the coordination sites was situated close to the negative end and other to the positive end of the dipole.

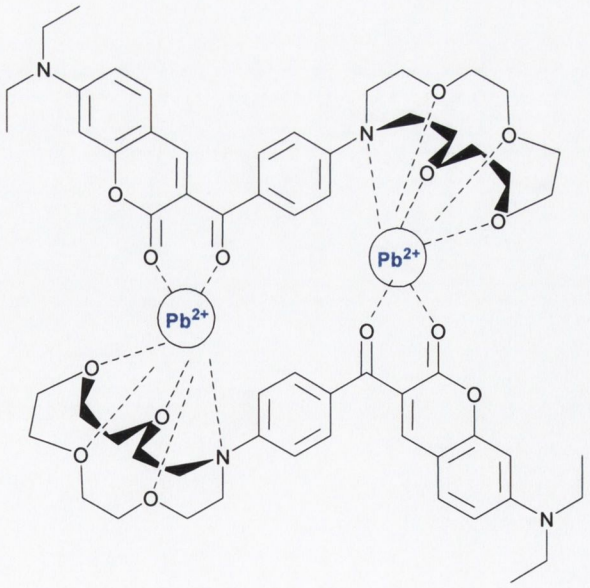

Scheme1. 9 Formation of 2:2 complex with Pb(II) for 59.

1.2.3 Lanthanide based fluorescent chemosensors

The use of delayed lanthanide luminescence has proved to be an immensely successful technique for sensing, overcoming the difficulty posed by autofluorescence and light-scattering observed in many biological systems.[73] Research into the unique luminescent properties of rare earth elements, coupled with a suitable ligand and a chromophore, is strongly motivated by their technological importance in optoelectronic devices, sensors, and other materials.[74,75,76] The optical transition in the lanthanide involves 4f orbitals, which are well shielded from their chemical environment by $5s^2$ and $5p^6$ electrons, the consequence of which is the external perturbation of the various energy states is very low ~ 100 cm^{-1}.[81] The f-f transitions are parity forbidden, thus absorption coefficients are low(0.5-3 dm^3 mol^{-1} cm^{-1}). All these factors results in a long-lived and line like emission bands for lanthanide luminescence.[77,78] These factors make direct excitation of lanthanides unfavourable and only practicable with lasers.[79] These drawbacks have been overcome by many different ways, the most important being:

- ligand centred absorption followed by energy transfer to the lanthanide ions
- ligand to metal charge transfer followed by lanthanide f-f emission
- matrix excitation followed by energy transfer to the lanthanide ions.

The main focus of this section is on examples involving energy transfer from ligand to the lanthanide excited state. The ligands used mainly contain organic chromophores (antenna), which can absorb light of suitable wavelength and possess high extinction coefficients and can pass this excitation energy to the excited state of the lanthanide ions by the following mechanism (Figure 1.7).[80] The ligand may also serve other functions, for example to hold the lanthanide ion close to the receptor and also to prevent radiationless decay of the rare earth metal ions.[80] A multitude of ligands bearing aromatic sensitising chromophores such as bipyridine, terpyridine, triphenylene, naphthyl and more recently benzoazacrown ethers have been used.[80] A few examples have been chosen to illustrate how the above mentioned concepts can be used for the detection of various cations.

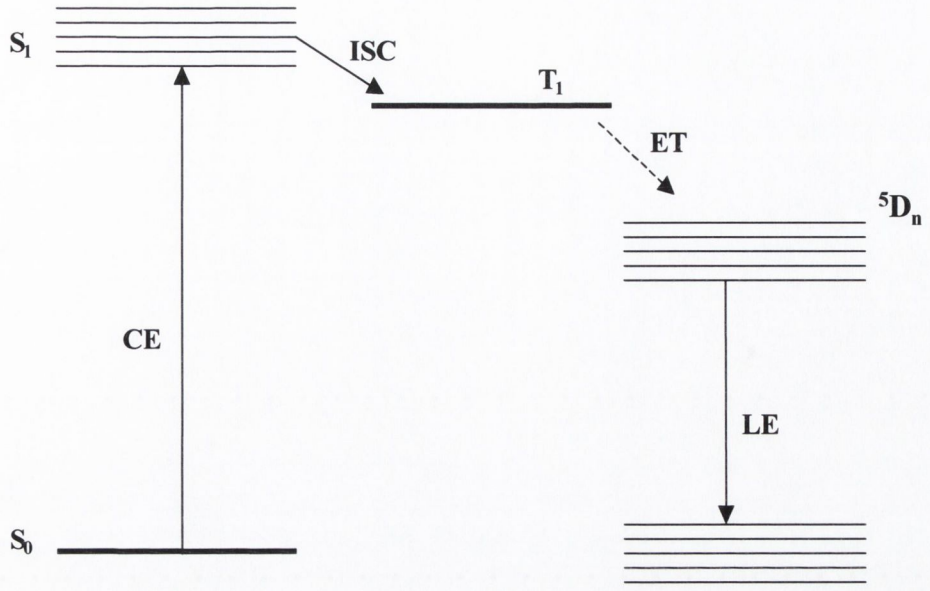

Figure 1.7 ***Modified Jablonski diagram showing the principle of delayed lanthanide luminescence due to electron transfer process from chromophore to lanthanide d energy level. CE = chromophore excitation, ISC = intersystem crossing, ET = energy transfer, LE = lanthanide emission.***

1.2.3.1 Literature survey on lanthanide based chemosensors

de Silva *et al.* reported a novel PET based lanthanide probe **60** for pH meaurement.[81] The ligand used was a common terpyridyl moiety, which has been previously used for protein and DNA detection.[82] The ligand was attached to two aliphatic tertiary amine receptors each separated by a methylene spacers. Both Tb(II) and Eu(III) complexes of **60** were studied. In case of **60**.Eu(III) the delayed emission was pH dependent in the pH range 8.2-3.3 The FE increase was by a factor of 16 upon protonation of the amino moieties, which prevented PET quenching of the terpyridyl moiety. No other spectral changes were observed. In these sensors the amino groups were protonated under acidic conditions and electron transfer was suppressed in the excited state resulting in lanthanide fluorescence enhancement.

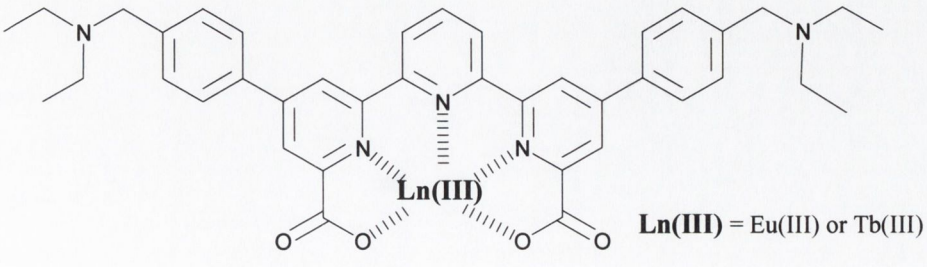

Ln(III) = Eu(III) or Tb(III)

60

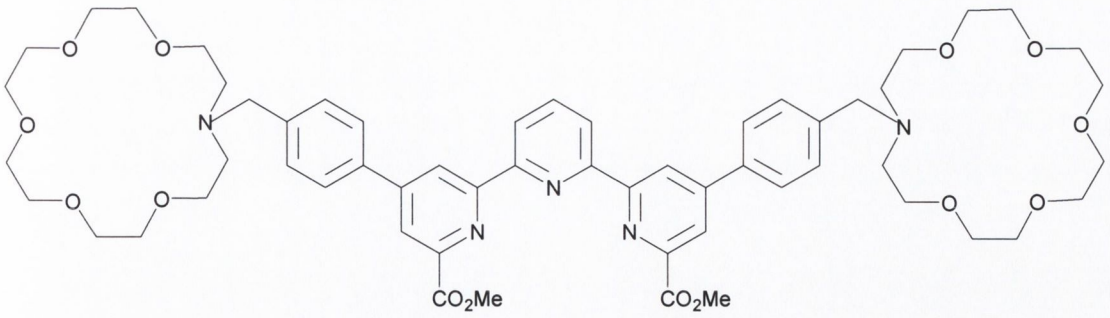

61

de Silva *et al.* also reported the metal-triggered metal centred emission from lanthanide ions in **61**.[83] It also contains a terpyridyl , which can strongly bind lanthanides Eu^{3+}, Tb^{3+} and a 18-crown-6 ether to potentially bind K^+, and to a lesser extent to Na^+. Excitation energy transfer from this type of ligand to Eu(III) is known to occur *via* the triplet state and resulted in luminescence from Eu(III). However, in the free receptor, only weak luminescence was observed, due to PET quenching from the nitrogen atom of the crown ether to the singlet excited state of **61**.Eu(III). K^+ binding introduced a large fluorescent quantum yield enhancement (Φ_F= 0.47 in methanol) due to suppression of the PET process. The addition of Na^+ did not lead to such large enhancement, presumably due to the small size of Na^+ compared to K^+. In case of the **61**.Tb(III) complex weak luminescent enhancement was observed, although the addition of acid did show a moderate increase in quantum yield (Φ_F= 0.016). This weak emission was explained due to rapid back energy transfer to the T_1 state as the energy difference between the excited state of the ligand and Tb(III) $^5D_4$ state is only about 4.1 kcal mol^{-1} compared to about 13.2 kcal mol^{-1} for **61**.Eu(III).

Gunnlaugsson *et al.* reported the development of luminescent chemosensors, using lanthanide ions such as Eu(III), Tb(III) and Yb(III) as emitting moieties (**62-65**).[84] In these complexes the metal centre can govern the response of the device to external interferences such as those arising from ion or molecular recognition. The neutral monoamide complex **Eu.62** and the cationic tetraamide complex **Eu.64** are examples of such systems. These lanthanide sensors possess long lived excited states emitting at long wavelength (500-700 nm) with large Stokes' shifts and line like emission band under ambient conditions. In these PET sensors, the excitation energy transfer occurs *via* the triplet state of the chromophore to the Eu(III).

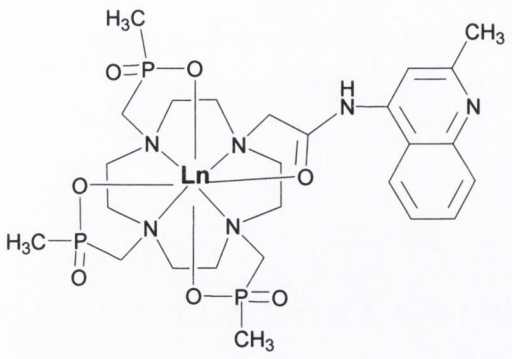

62: [Eu.1]: Ln = Eu(III)

63: [Tb.1]: Ln = Tb(III)

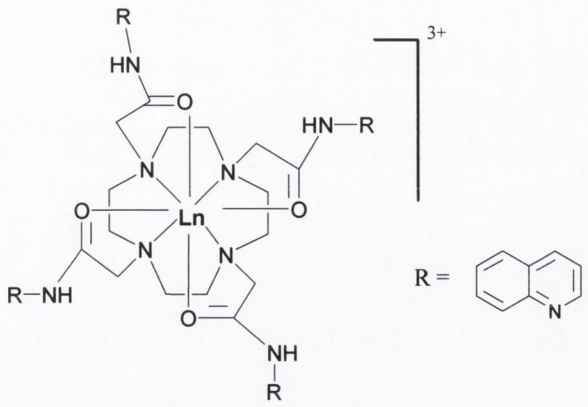

64: [Eu.2]: Ln = Eu(III)

65: [Yb.2]: Ln = Yb(III)

Gunnlaugsson *et al.* have also reported the synthesis of heptadentate triamide Tb(III) cyclen complex **66,** for the recognition of salicylic acid in water.[85] The addition of 0.4 mM solution of salicylic acid to 17 μM solution of **66** gave rise to a large enhancement in the Tb(III) emission indicating the formation of a ternary complex structure. It was reasoned that the oxygen atoms of the aromatic carboxylate bind to the Tb(III) forming a four-membered chelate ring with subsequent displacement of a labile metal-bound water molecule which switches the luminescence *'on'*.

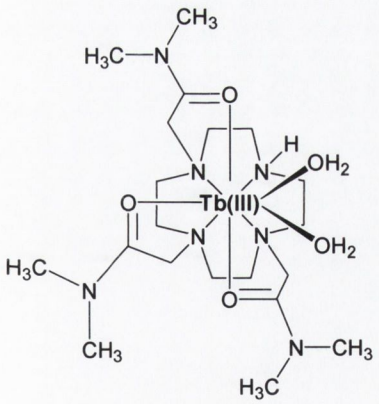

66

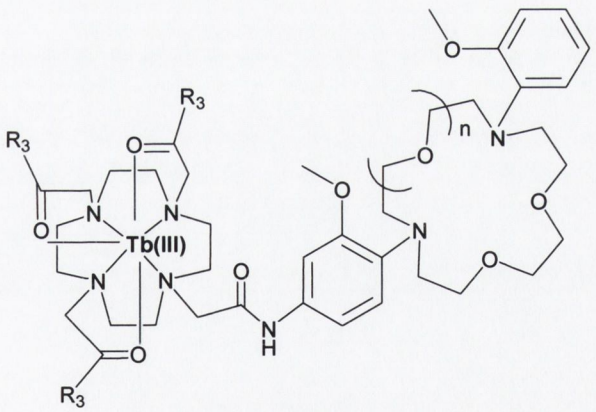

67: n=1, $R_3 = NMe_2$
68: n=2, $R_3 = NMe_2$
69: n=1, $R_3 = OH$
70: n=2, $R_3 = OH$

Recently Gunnlaugsson *et al.* have reported the design and synthesis of lanthanide luminescent sensors for the recognition of Na^+ and K^+ (**67-70**).[86] Tb(III) emission was switched on upon recognition of the alkali metal ion by the diazacrown ether moiety. The studies were performed in TRIS buffer solutions at pH 7.4. A pH titration resulted in hypsochromic shifts in the absorption bands and pKa values of 11.0 and 5.5 were determined from these changes. These are assigned to the amide deprotonation and aniline protonation of the receptor respectively. Upon titration with alkali metal ions the delayed lanthanide luminescence was switched on with a greater magnitude of fluorescence enhancement. For **67** and **68** the emission was effectively switched by Na^+, whereas for **69** and **70** K^+ was the major contributor to the increased emission. This selectivity was due to the size of diazacrown ether receptors. Negligible changes were observed for Li^+ and group 2 metal ions. This was explained by the structural change in the receptor moiety upon alkali metal ion binding, which lead to the loss of conjugation and an increase in the oxidation potential of the receptor. This in turn increased the electron transfer rate to the Tb(III) $^5D_4$ state, which gave rise to the luminescent enhancement.

1.3 Miscellaneous fluorescent chemosensors

Finney *et al.* have designed polyaryl fluorescent chemosensors **71** and **72**, in which the metal ions (Li^+, Ca^{2+}) induces conformational restriction in the fluorophore, resulting an increase in emission intensity.[87] Upon metal ion binding, non-radiative processes such as intersystem crossing (ISC) and internal conversion (IC) are modulated favouring radiative decay.

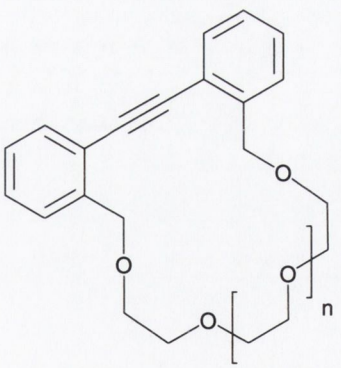

71: n = 1
72: n = 2

Ajayaghosh *et al.* have reported the first example of 'rigid-flexible-rigid' bichromophor **73**, for Ca^{2+} recognition.[88] The squalene dye acts as the rigid signalling moiety and oxyethylene chain as the flexible recognition moiety in **73**. In acetonitrile solutions, **73** exhibited an absorption and emission band at 630 nm and 652 nm respectively. However,

on Ca^{2+}additon, the intensity of the absorption maxima at 630 nm decreased with the concomitant growth of a hypsochromically-shifted band at 552 nm. Additionally, fluorescence emission was quenched on Ca^{2+} addition, for example the quantum yield of the sensor decreased from 0.03 (free) to 0.008 (Ca^{2+} bound). This observation was explained due to the formation of face-to-face stalked foldamer on Ca^{2+} recognition (Scheme 1.10). Only minor changes were observed with Mg^{2+}, Ba^{2+} or Sr^{2+}.

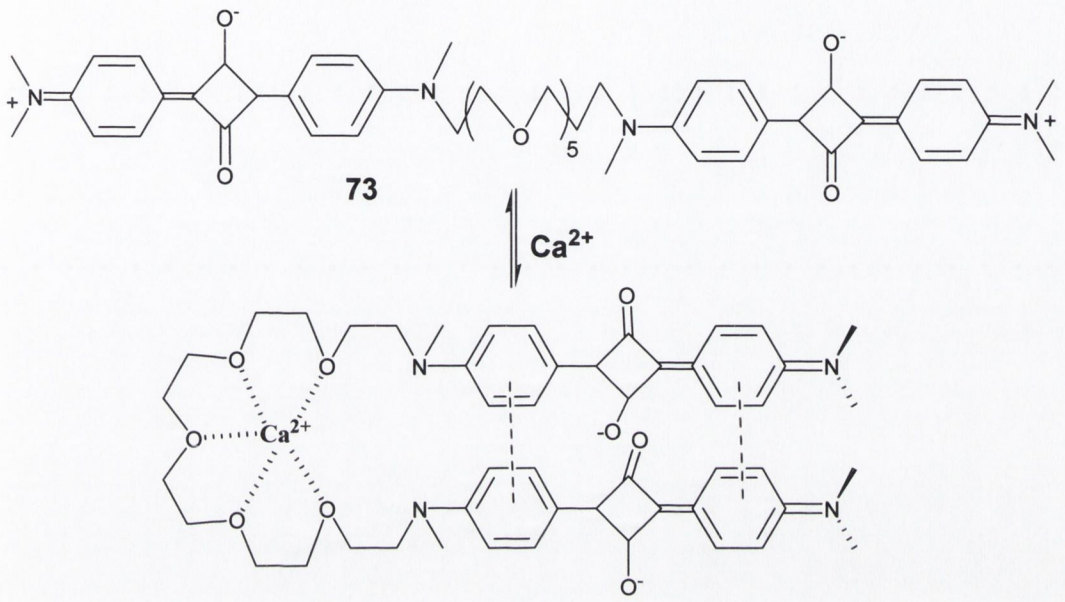

Scheme1.10 Ca^{2+} recognition mechanism in 73.

An elegant example in which rigidity is utilized for anion sensing has been developed by Beer *et al.*[89] The macrocyclic receptor in **74** and **75** exhibited preferential selectivity for Cl^- than $H_2PO_4^-$. It was reasoned that the large size and tetrahedral shape of $H_2PO_4^-$ makes it incompatible with the macrocycle's cavity. A blue-shift of metal to ligand charge transfer emission band (MLCT), with increased FE was observed on addition of Cl^-. A binding constant of 4×10^4 $M^{-1}$for **74**-Cl^- complex (1:1) was observed in DMSO.

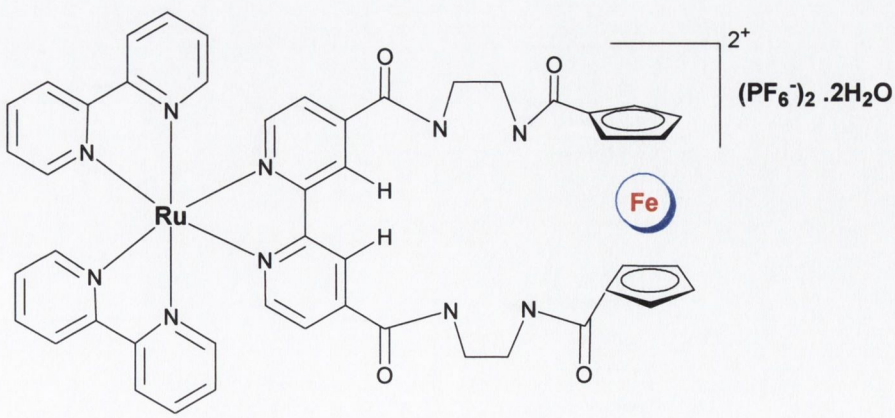

74

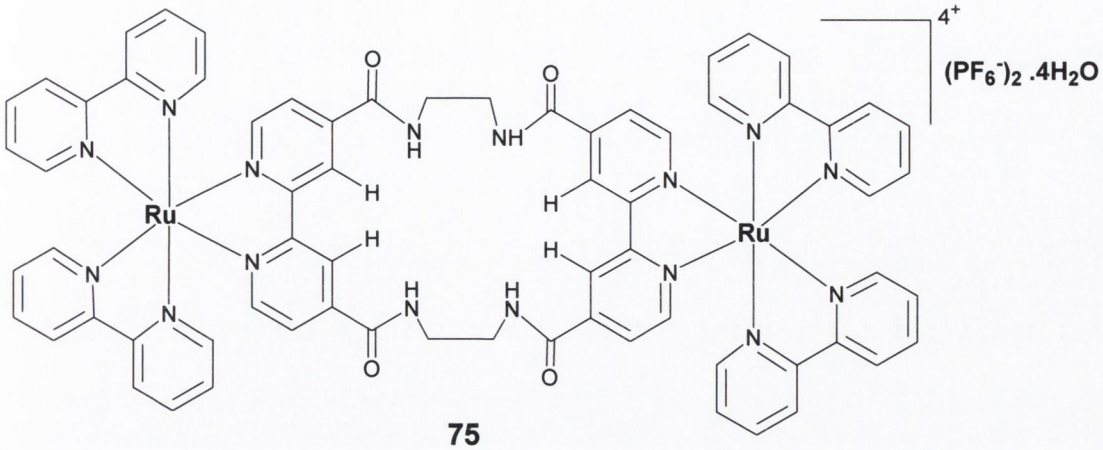

75

The above sections have clearly outlined in the first page of this chapter, how the supramolecular principle can be controlled for the selective sensing of desired analyte. The major part of this thesis deals with the application of supramolecular principle outlined above for biological problems such as microdamage detection in bones. The fundamental aspects required for understanding bone microdamage are discussed in more detail below.

1.4 Anatomy and physiology of bone

The skeletal system is one of the most important organ systems in the human body both biochemically and metabolically. It is composed of individual bones and the connective tissue that joins them.[90,91] Bone is the main constituent of the skeletal system. Although bone itself is a connective tissue consisting of cells and matrix , it differs considerably from other connective tissues in terms of both rigidity and hardness. Bone is a rigid but dynamic organ which undergoes continuous repair, moulding and shaping.[91] The main functions of bone include:

- metabolic - homeostasis of blood calcium levels and supporting haematopoiesis (blood formation).
- mechanical - support to soft tissue, serves as levers for muscle action and houses brain and spinal cord.
- self-repairing – bone is able to adapt its mass, shape, and change properties in response to mechanical stimuli or other voluntary physical activity.[91]

1.4.1 Structural characteristics of bone

A typical adult long bone consists of a long cylindrical shaft called the diaphysis and two round wider ends called ephiphyses. Each epiphysis is connected to the diaphysis by a conical region called the metaphysis. The epiphysis and metaphysis are mainly composed of cancellous, or spongy bone, forming an open network of struts and plates called trabeculae.[92] The diaphysis is composed mainly of cortical or compact bone that is a dense, solid mass with only microscopic channels. (Figure 1.8, insert).

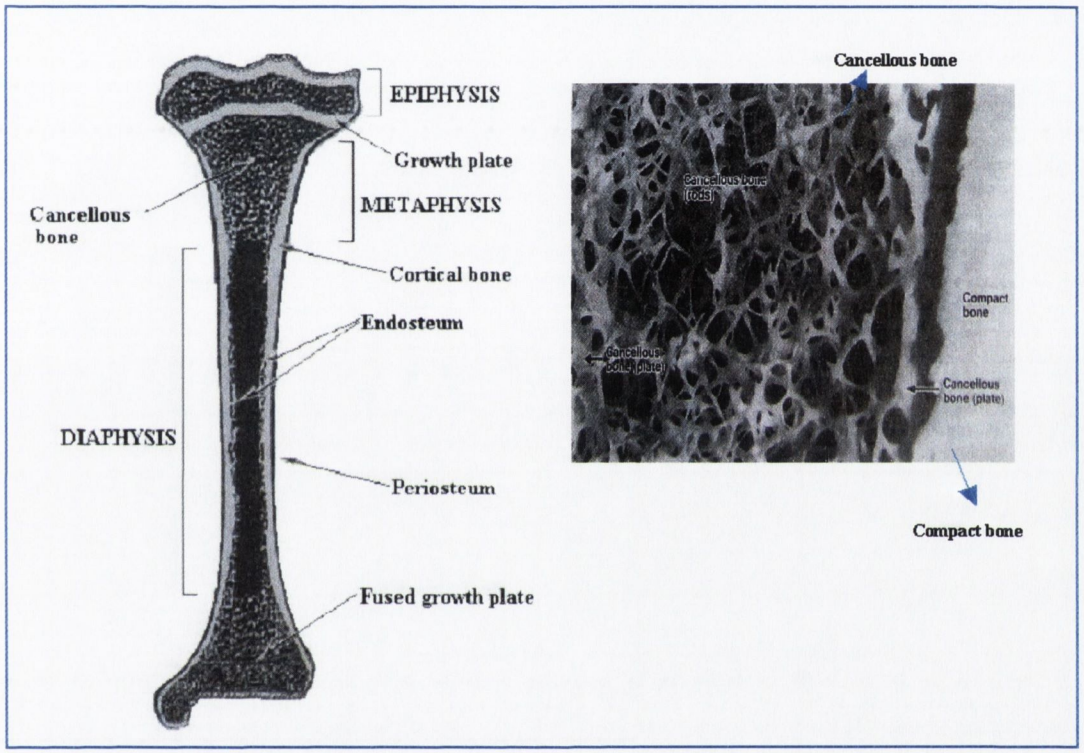

Figure 1.8 ***Schematic internal structure of a typical long bone such as tibia. Insert shows the Photograph of a thick ground section of part of proximal tibia showing the cortical bone and Cancellous.***[92]

Compact bone also forms a thin shell around spongy bone. In growing bones, the epiphysis is separated from the metaphysis by a plate of hyaline cartilage known as the growth plate-metaphyseal complex, or the epiphyseal plate. Almost 80% of adult bones consist of cortical bone, which is responsible for the supportive and protective functions of the skeleton. The remaining 20% of the bone is cancellous or spongy. This distribution varies dramatically in each specific bone. Most bones are covered on the outside by the

periosteum. Periosteum consists of an outer sheet of fibrous connective tissue and an inner cellular layer. The marrow cavity of the diaphysis and cavities of cortical and cancellous bones are lined with a thin cellular layer called the endosteum. This layer is highly active metabolically during bone growth, repair and remodelling.[93]

1.4.2 Bone- composition and cells

Bone is a specialised form of dense connective tissue composed of cells and matrix made up of inorganic mineral and organic matrix. Bone consists of 65 % minerals, 20 % organic matrix, 10 % cells and the remainder is water.[94,95] The main constituent of bone mineral is impure hydroxyapaptite ($Ca_{10}(PO_4)_6(OH)_2$) containing other constituents such as carbonate, citrate, magnesium, fluoride and strontium incorporated into the crystal lattice or absorbed onto the crystal surface.[96] The mineral phase is located within the organic matrix in the form of small crystals of needles, plates and rods. The mineral phase has vacant sites, which can incorporate tetracycline, polyphosphate, and bisphosphonate with a high affinity.[96,97] The organic matrix of bone is composed of 90 % collagen and 10 % of various noncollagenous proteins such as osteocalcin, osteonectin, osteopontin and bone sialoprotein. Bone mainly consists of Type I collagen with traces of Types III, and X collagen.[98] The combination of collagen and hydroxyapaptite offers bone gel-like characteristics. The amounts of these non-collagenous proteins in the plasma or serum level is unique to bone and are used clinically to assess bone turnover.[99] The mineral phase and organic matrix form composite imparts high mechanical strength. The dynamic nature of bone is due to the cells. The four major cell elements of bone are:

- *osteoprogenitor or bone-lining cells* - bone-lining cells may be involved in homeostatic, morphogenetic, and restructuring process that constitute regulation of bone mineral mass and architecture as well as the haematopoietic process. These cells may develop into osteoblasts.[91-96,100-102]
- *osteoblasts* - these are the main bone forming cells. These cells are involved in the synthesis and secretion of unmineralized bone matrix (osteoid), participate in the calcification of bone, and regulate the flux of calcium and phosphate in bone
- *osteocytes* – 10 % of osteoblasts become embedded in the matrix of osteocytes. osteocytes regulate the response of bone to the mechanical environment by responding to the amount and distribution of strain within bone tissue that influence

adaptive modelling and remodelling behaviour through cell-cell interactions. They also help in microdamage detection.

- osteoclasts – these are polykaryotic cells responsible for mineral dissolution and collagen degradation.

Additionally, bone also consists of precursors of these specialised cells, cells of the marrow compartment, and an immune regulatory system that supplies the precursor cells and regulates bone growth and maintenance.[94,95,100]

1.4.3 Woven and lamellar bones

In the developing embryo and infants the matrix of collagen fibres and osteocytes are irregularly distributed resulting in woven bone.[94] This provisional bone is eventually resorbed and replaced by lamellar bone which is built of unit layers called lamellae in which the collagen fibres are regularly arranged. Under polarized light, these lamellae appear as alternate light and dark layers due to their different orientation of collagen fibres in adjacent lamellae[95] (see Figures 1.9 and 1.10). The lamellae of adult cortical bone appear in three major patterns:

- *concentric:* - lamellae are arranged as circular rings surrounding a longitudinal central canal that together forms an osteon or Haversian system. The longitudinal central canal contains the vascular supply and nerves and is called a Haversian canal. Short radial canals, called Volkmann's canals, in turn connect the Haversian canals to each other.
- *circumferential:* - several layers of lamellae surrounding part or all of the diaphysis.
- *interstitial:* - angular fragments of concentric or circumferential lamellae crammed between gaps of Haversian systems.[91-95,96]

In cancellous bone, two types of lamellae are found: trabecular packets or Hemiosteons, and interstitial lamellae. Throughout the woven and lamellar bone small cavities called lacunae are found, which are joined by tubular canals called canaliculi. Osteocytes and their long cytoplasmic processes occupy the lacunae and canaliculi, respectively.

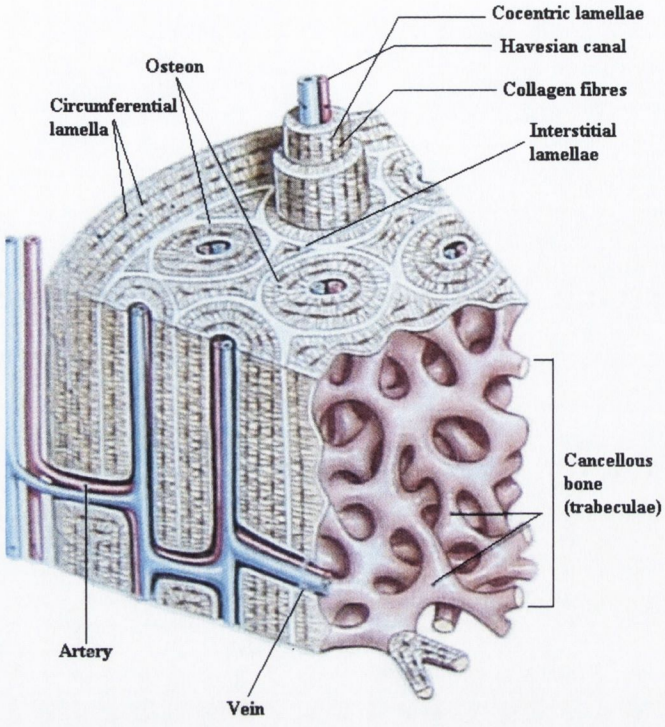

Figure 1.9 *Schematic diagram of a portion of long bone shaft.*[94]

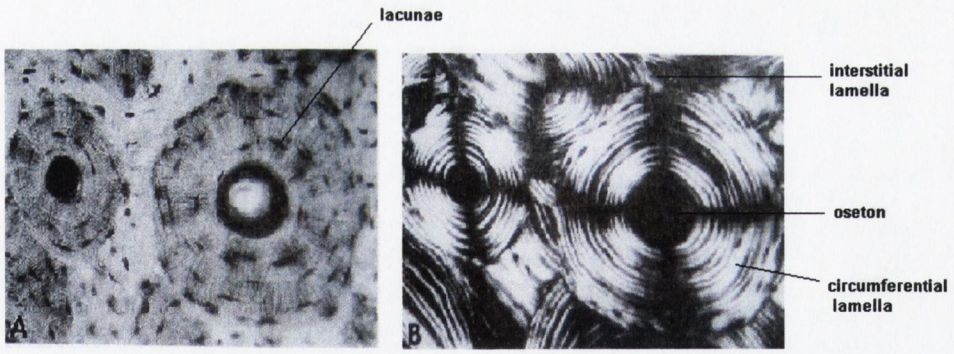

Figure 1.10 *(A) Cross-section through compact bone. (B) same section in polarized light. Concentric as well as interstitial lamellae are clearly visible as well as lacunae and Haversian canal.*[95]

1.4.4 Growth and development of skeletal system

Bone development and growth involve the process of osteoid formation and mineralization. Bone formation occurs through two different ossification processes, intramembraneous and endochondral ossification.[91-95]

Intramembraneous ossification begins with an increase in the number of mesenchymal cells and fibres.[91-95] The cells differentiate into osteoblasts that secrete osteoid, which mineralises. Some of the osteoblasts become trapped in the matrix surrounding them and differentiate into osteocytes. The factors controlling the shape and manner of growth are specific for each bone and are also genetically controlled. Loose spicules or trabeculae, are formed by osteoblasts, which interlink to form primary cancellous bone (spongiosa). Compact bone is formed when primary osteons fills in the spaces between the primary spongiosa. Secondary osteons then gradually replace this bone. Most bones of the vault of the skull, bones of the sense organs and facial skeleton, as well as parts of the clavicle and mandible are formed by this mechanism.

During the endochondral ossification process of skeletal development, the cartilage enlarges through apposition and interstitial growth and a cartilage analagen is formed. Cartilage cells (chondrocytes) proliferate and deposit matrix until a cartilage model of future bone is formed. As cartilage cells mature and grow, their size increases greatly and the matrix is reduced to a series of struts and subsequently calcifies. Enlarged chondrocytes then die and disintegrate. Blood vessels start to grow around the cartilage and cells from the perichondrium differentiate into osteoblasts and migrate to the shaft. The osteoblasts cause the formation of primary spongosia, which then spreads along the shaft towards both ends. As blood vessels penetrate the cartilage, mesenchymal cells are differentiated into osteoclast which start eroding the trabeculae creating the marrow cavity. Osteoblasts migrate to the epiphysis and both epiphyseal cartilage and osteoblasts continue to grow increasing the length of the bones. The epiphysis is eventually replaced with a lamellar trabecular packet or hemiosteon called the secondary spongosia. With age the epiphyseal cartilage gets narrower and narrower until it ultimately disappears. With age the spongosia bone is replaced with cortical bone in most places. On the other hand the diameter of the bone also increases due to the appositional growth.[91-96]

Growth and modelling go hand in hand.[103] Modelling involves resorption drifts and formation drifts which remove or add bone over wide regions of the bone surface.[103] Thus modelling controls the growth, shape, size, strength and anatomy of bones and joints. Modelling not only involves the development of normal architecture, but also the modulation of this architecture and mass when the mechanical conditions are changed.[104]
The replacement of immature (primary) and old bone occurs by resorption, followed by formation of a new lamellar bone by a process termed remodelling.[105,106] Remodelling is believed to be carried out by a structural unit called a Bone Remodelling Unit (BRU) or

Basic Multicellular Unit (BMU) (Figure 1.11).[107,108] The life cycle of the BMU in both trabecular and cortical bone includes six consecutive stages of resting, activation, resorption, reversal (coupling), formation, mineralisation and back to resting.[107,108] Bone remodelling maintains skeletal integrity in humans and higher vertebrates. Imbalances of remodelling can result in gross perturbation in skeletal structure and function, and to morbidity and mortality.

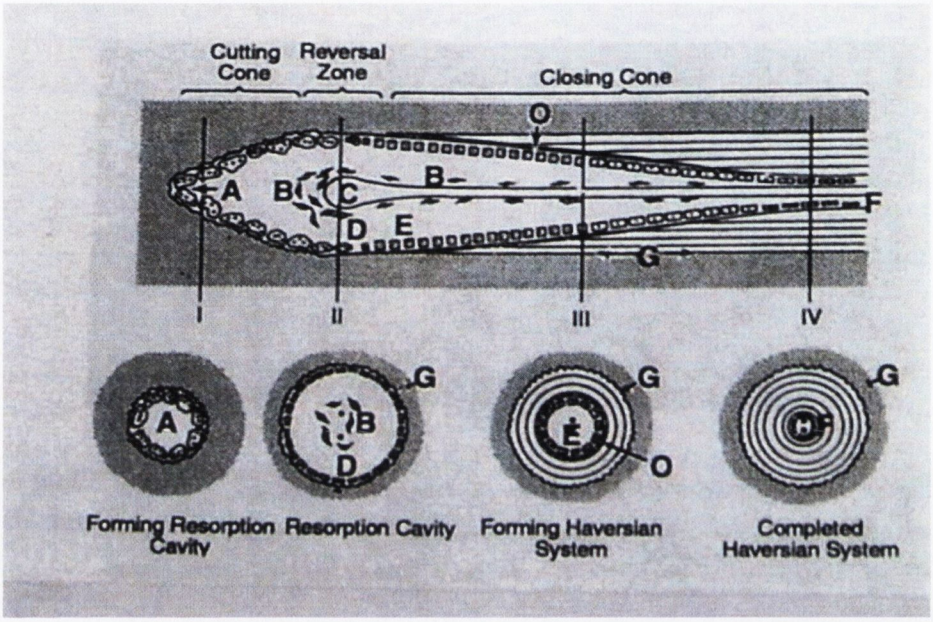

Figure 1.11 ***Longitudinal section (above) and cross-section through Bone remodelling unit (cortical bone). A= multinucleate osteoclasts, B= precursor cells, C= capillary loop, D= osteoblast progenitors, E= osteoblast, F= flattened cells lining Haversian canal, G= cement line, H= Haversian system, O= osteoid. I, II, III and IV are transverse sections of BMU at different stages of development. (I) resorption cavities lined with osteoclast. (II) completed resorption cavity lined by mononuclear cells (III) developing Haversian system (IV) completed Haversian system or osteon.***[108]

The widely accepted hypothesis for bone remodelling was the assumption that signals generated by osteocytes to mechanical loading stimulate bone lining cells to activate remodelling.[108,109] However, this fails to explain the common observation by many researchers that remodelling increases both during low and high mechanical loads. In order to put an end to these discrepancies, Martin hypothesised a unified theory to explain the phenomenon of bone remodelling.[109(b)] According to Martin " *lining cells are inclined to activate remodelling unless restrained by an inhibitory signal and that the mechanically provoked osteocyte signal serves this inhibitory function*". Thus remodelling is elevated when signal production declines due to reduced loading or when excessive loading or mineralization disturbs signal generation or transference. Martin's theory has combined all the earlier known facts[110] to explain remodelling in bones.

1.4.5 Microdamage in bones

Bone is continuously renewing and repairing itself from the ravages of time and injury. As bone is under constant stress due to the repetitive loading during normal day-to-day activity, this results in the generation of microcracks or microdamage.[112] Frost reported the observation of *in vivo* microdamage in the cortical bone of human ribs.[113] It was suggested that microdamage in bone acts as a stimulus for bone remodelling. This remodelling is mediated by the well-balanced actions of osteoclasts, which initiate old bone resorption, and osteoblasts, which form new bone. Many investigators further supported this hypothesis.[114,115,116] It is clear that in healthy bone, a critical balance is maintained between microdamage creation and the repair mechanism, which removes these cracks. An imbalance in these processes lead to accumulation of microdamage. The accumulation of microdamage occurs as a result of two processes:

- the high rate of damage generation which overtake the repair or remodelling mechanism, ultimately leading to excess damage
- a normal rate of damage generation which accumulates due to a defective repair or remodelling mechanism leading to deficient repair.

The clinical manifestations of excess damage and deficient repair result in stress fractures and fragility fractures respectively.

1.4.5.1 Stress fractures

Stress fractures[117] are the clinical manifestations of the accumulations of stress-induced microcracks.[118,119,120] They are mainly observed in athletes and military recruits, who are subjected to repetitive cyclic loads.[121,122]

1.4.5.2 Fragility fractures

Fragility fractures are those fractures that occur in response to minor traumas, which are part of everyday life. This debilitating condition is continuing to grow at an alarming rate, affecting approximately a hundred million people worldwide.[124] Shaffler *et al.* have reported increased microdamage in femoral compact bone with age.[125] This accumulated microdamage resulted in decreased strength and stiffness; the consequences of this are profound susceptibility to fracture.[125] Of these, hip fractures in the elderly are the most serious, resulting in 20% mortality within six months.[126] Demographic trends suggest that

hip fracture incidences worldwide will increases from 1-7 million in 1990 to 6.3 million by 2050.[127] At present, only symptomatic treatment is available in the form of inhibitors of bone resorption. However, drugs inducing bone formation are limited in number.[128] This one-sided approach is limiting the efficacy of restoring a normal balance and bone mass. A defective intrinsic repair mechanism is responsible for increased bond fragility associated with aging and osteoporosis.[123]

1.4.5.3 Osteoporosis

Osteoporosis is a skeletal disease characterised by a decrease in bone strength (a decrease in bone mass and a deterioration in bone microarchitecture), which leads to an increased fragility of the skeleton and consequently to a greater risk of fracture.[108,123,124,129] The main cause of osteoporosis is the continuous loss of bone during life, which is exacerbated in women after the menopause and in men with the andropause. During osteoporosis, the osteoclasts resorb the bone resulting in disruption in the hydroxyapaptite lattice (Figure 1.12).[129] This destroys the bonding within the hydroxyapaptite matrix leaving coordinatively unsaturated Ca^{2+} sites. It is reasoned that by using fluorescent chemosensors, which bind selectivity to free Ca^{2+} sites, it would be possible to detect the microcracks.

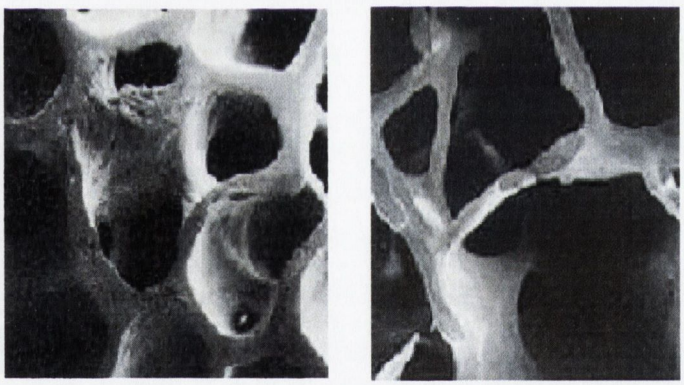

Figure 1.12 ***Photomicrograph showing differences between normal cancellous bone (a) and osteoporotic bone (b). Note large holes in (b) created due to the uncontrolled resorption by osteoclasts.***[129]

1.5 X-ray contrast agents

X-rays are generated when high-energy electrons emitted from a cathode impinge atoms of an anode target at high voltage.[130] As these electrons hit the anode target, they are rapidly decelerated due to multiple collisions with the target nuclei. The kinetic energy lost by the electrons is emitted directly in the form of X-ray photons. Production of X-ray

normally involves two principle mechanisms: bremsstrahlung and characteristic radiation.[130] As the electrons generated from cathode have different initial energy and the loss of energy occurs only in stages, the emitted photons have a continuum of energy. This process is called bremsstrahlung or "braking radiation" and results in the generation of continuous X-rays.[130,131] On the other hand some electrons having certain critical energy are able to pass the energy barrier and collide with electrons of the innermost shell (K) of the atoms of the anode targets, and can knock these electrons from their energy levels. The electrons from the higher energy levels (L, M, N) jump to fill the vacant energy level, and during the process emit photons of a particular wavelength depending upon the atom and the energy gap between various energy levels. Thus these radiations are characteristics of target atoms and are known as characteristic X-ray (M to K transition generates $K_{\alpha 1}$, $K_{\alpha 2}$: L to K generates $K_{\beta 1}$, $K_{\beta 2}$)

The voltage applied between cathode and anode in X-ray tube is expressed as its peak kilovoltage (kVp), while the energy of the resultant X-ray photons generated is expressed in kiloelectronvolts (keV).[131] In medical imaging, tungsten is usually selected as the X-ray tube material (anode). Its high atomic number makes it more efficient for the production of X-rays than atoms with low atomic number.[132] A plot of X-ray intensity *versus* photon energy from a tungsten X-ray tube (Figure 1.13). According to the photoelectric principle, increasing the voltage of an X-ray tube will lead to the production of photons with higher energy and curve shown in Figure will shift to right. However, the increase in the current does not increase the energy but instead will only increases intensity of the radiation.

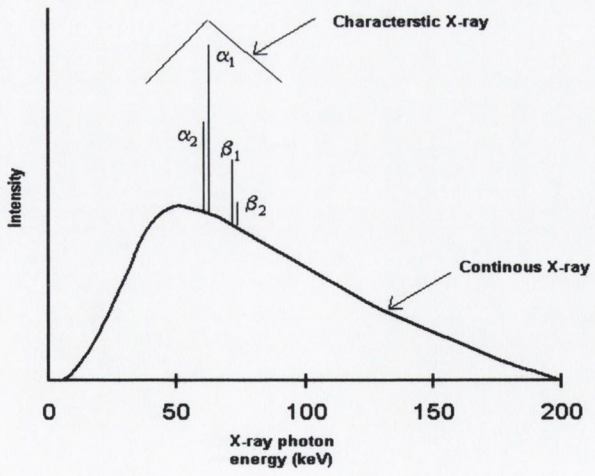

Figure 1.13 ***Typical X-ray emission spectrum.***

The reduction in X-ray beam intensity due to absorption and deflection of photons defines the degree of X-ray attenuation and can be mathematically expressed (Equation 1.2)

$$\mathbf{I} = \mathbf{I}_0 \mathbf{e}^{-\mu x} \qquad (1.2)$$

where I = transmitted X-ray intensity

I_o = incident X- ray intensity

x = thickness of matter (absorber)

μ = mass attenuation and is expressed in cm^2/g.[136]

X-ray attenuation comes from three interactions between X-ray photons and traversed matter in the energy range meaningful for diagnostic imaging: coherent scattering (ω), the photoelectron effect (ι), the Compton scattering (δ). The mass attenuation coefficient (μ) is the sum of these three interactions.[132,] Coherent scattering produces scattered radiation and contributes to noise on X-ray films, but it is so small that it can be excluded from further consideration. The contribution of photoelectron effect to X-ray to attenuation is high with low-energy X-ray radiation and with absorbers of high atomic number. It produces almost no scattering radiation and results in a high-quality image. However, since most of its energy is being absorbed, it exposes the patient to a high dose of radiation. Compton scattering arises from the interaction of an X-ray photon with an outer-shell electron. When an X-ray photon with high energy collides with an outer-shell electron, it will eject the electron from its orbit. The photon itself will be deflected as scattered radiation to a new direction with a lower energy. The scattering probability depends on the total number of electrons in an absorber and is independent of the atomic number. The scattered radiation contributes to the noise in the X-ray and therefore decreases contrast. The quantity of Compton scattering gradually diminishes as the X-ray photon energy increases, so that high-energy photons are more likely to pass through the body than low-energy photons. As a result, the radiation exposure to patients is lower with high energy X-ray than that with low-energy X-rays.[117]

It is clear from the above discussion that contrast and radiation exposure to patients is inversely correlated. A compromise is needed between the optimal image quality and patient radiation dose. The inherent contrast between bone and other tissues is large enough for clinical use in the low to middle X-ray energy range. It is clear that in order to observe the contrast within bone or between fat and muscle (within soft tissues), X-ray on

itself are not useful. To enhance such a contrast, contrast agents have been employed. All contrast agents contain a heavy element.[133] Elements with high atomic number can be effectively used as contrast agent *e.g.* bromine, iodine, barium, bismuth, and lead. However, the issue of safety, tolerability by the body needs to be fulfilled.[134] Initial trials involved strontium bromide, sodium iodide, bismuth salts as contrast enhancing agent. It was soon discovered that iodine compounds are the most suitable as contrast agent as they can be easily introduced into any organic framework leading to the production of a safer, well-tolerated, water-soluble, non-ionic contrast agent. Moreover, with the advance in synthetic chemistry it is possible to synthesize contrast agent containing increased number of iodine atoms and thus enhancing the contrast further. Modern day contrast agents can incorporate as high as nine-iodine atoms per molecule.[134] The upper limit of safety now appears to have been approached with ionic contrast agent.[134] However, the synthetic pursuit of ideal contrast agents is still ongoing. With synthetic organic methodology growing rapidly, it is closer than ever to synthesise ideal contrast agent with complete biological inertness.

1.6 Conclusions

This chapter highlights important advances made in the field of fluorescent chemosensors for various metal ions and anions. The logical integration of fluorophore and receptor offers selective recognition. The theoretical principles of both PET as well as ICT based sensors have been briefly outlined. The literature survey of selected examples demonstrates the advancement in the field of molecular recognition based on supramolecular principles. Examples discussed have been critically evaluated in terms of their photophysical properties, selectivity, sensitivity and binding ability. The understanding of biological processes at the molecular level is greatly dependent on fluoroprobes. The detection and investigation of microdamage in bone has profound clinical relevance. Iodinated contrast agents illustrate another aspect of supramolecules that generate signalling by contrast enhancement.

1.7 Proposed work

1.7.1 Selective Zn(II) detection

1. To design, and synthesise stable (photochemically and thermally), water soluble highly selective chemosensors for Zn(II) detection.

2. Evaluation of these sensors in terms of their photophysical response and binding abilities.
3. To assess the suitability of these sensors for Zn(II) recognition in pancreatic tissue.

1.7.2 Selective Cd(II) detection

1. To synthesise and photophysically evaluate novel anthracene based sensors for Cd(II) signalling in aqueous solution .
2. To explore selective detection of Cd(II) in the presence of Zn(II).

1.7.3 Microdamage detection in bone

1. To explore the application possibility of PET based fluorescent chemosensors for histological detection of microdamage in bone.
2. Investigation of the structural aspect of microdamage by using various techniques such as Raman Spectroscopy and Scanning Electron Microscopy SEM) coupled with Energy Dispersive X-ray Analysis (EDXA).

1.7.4 Iodinated contrast agents

1. The design and synthesis of supramolecular X-ray contrast agents containing chelatable groups for the specific detection of microcracks in bones.
2. To explore the suitability of these contrast agents for non-invasive microdamage detection by using micro-CT (μ-CT).

CHAPTER - 2

Highly Selective Naphthalimide Based Fluoroscent Sensors for Biological Detection of Zinc

2.1 Biological importance of zinc

Zinc is the second most abundant heavy metal after iron and a vital component of most living cells.[135] It is an essential nutrient and strongly influences cell division and differentiation and hence is very important to the growth and development of all forms of life.[136] In microorganisms, plants and animals more than 300 enzymes require Zn(II) for their proper functioning.[137,138] Zn(II) is now regarded as one of the most important co-factors in the regulation of apoptosis.[139] It also plays a key role in the synthesis of insulin and the pathological state of diabetes.[140] It has been reported that hyperglycaemia from either type I or type II diabetes causes physiologically important losses of Zn(II) from the body.[141] Zn(II) plays an important role in cellular anti-oxidative defence and is an integral component of numerous functional proteins wherein it exerts specific properties over a wide range of physiological systems.[142-144] It is involved in the processes of transcription and translation.[138,145] It has been observed by Fuji that cell nuclei contain Zn(II) and that it binds to RNA and DNA.[146] It is also known that Zn(II) serves as a mediator for cell-cell signalling in the Central Nervous System (CNS).[147,148] The brain, the main organ of the CNS contains a high concentration of Zn(II), which is mainly localised near the presynaptic terminals, and is released during neural activity. Upon proper stimulus, free Zn(II) concentrations as high as 150 μM are attainable in these terminals.[148,149] The physiological effects of this phenomenon are poorly understood but it has been demonstrated that such high Zn(II) concentrations can alter the behaviour of multiple channels and receptors, in particular decreasing the *N*-methyl-*D*-asparatate (NMDA) receptor response.[149,150] In addition to affecting the neuron activity, it has also been observed that cortical neurons undergo cell death if exposed to intense Zn(II) levels.[151] This has been attributed to the influx of Zn(II), which enters these neurons through multiple routes, likely in large part overlapping with routes of Ca(II) entry.[152] Recent research links the above findings to many degenerative conditions, the most important being Alzheimer's disease (AD), cerebral ischemia, and epilepsy.[153-161] Zn(II) also plays an important role in glucose metabolism the details of which are discussed in Section 2.9

2.1.1 Why is zinc important in biological systems?

Zn(II) plays a vital role in both physiological and metabolic pathways in the body. In fact, zinc is the only metal to have representatives in all six of the International Union of

Biochemistry (IUB) classes of enzymes.[162] Zn(II) ligands in enzymes can have four different binding sites:

- catalytic
- structural
- cocatalytic
- protein interface.

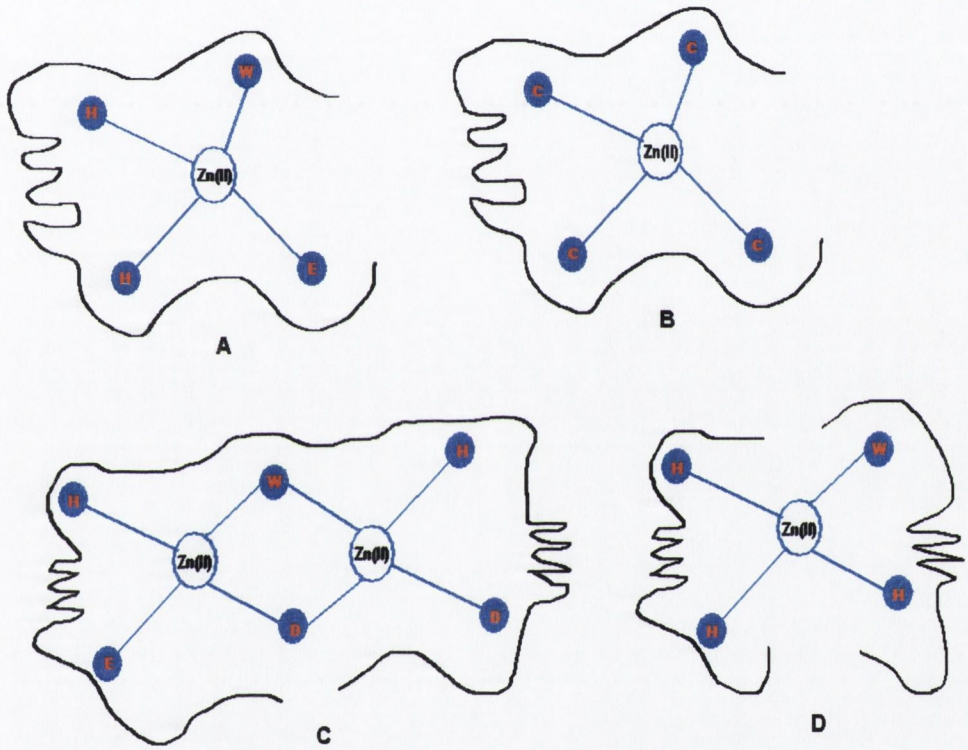

Figure 2.1 ***Illustration of zinc binding sites in enzymes: (A) catalytic (B) structural (C) cocatalytic (D) protein interface: Letters C, D, E, and H stands for amino acids cysteine, aspartic acid, glutamic acids and histidine respectively and W refers to water.*** [138,162-165]

Many important enzymes such as alcohol dehydrogenases have *catalytic* sites (Figure 2.1). The coordination number for such sites is generally 4 or 5, with water as one of the ligands.[138] In the case of a structural site with a coordination number of 4, there is usually no bound water molecule. A cocatalytic site generally contains two zinc atoms. Enzymes such as metallothionein, contain both a catalytic zinc site and a separate cocatalytic site. In

recent years, a fourth type of Zn(II) binding site has emerged - protein interface.[166] In this binding mode the amino acid ligands of the two protein molecules are involved in zinc coordination (examples include γ-carbonic anhydrase and superantigen).[167,168] The reasons for such a rich coordination chemistry of Zn(II) in biological system are:

- amphoteric nature of zinc, existing both as the aquo and hydroxo metal complex at physiological pH.
- stereochemical adaptability of Zn(II) to assume multiple coordination geometries (coordination number ranging from two to eight), an unusual feature that contributes to its biochemical versatility.
- coordinate complexes of four, five and six are most frequent with geometries ranging from regular or distorted tetrahedral to trigonal bipyramidal, square pyramidal and octahedral.
- under physiological conditions, Zn(II) does not undergo reduction or oxidation, rendering it stable in biological media.

All these factors make Zn(II) a versatile interactant for different donor groups of varying ligand types, resulting in a broad range of stability constants, mobilities, reactivities and functions.[138] Several Zn(II) ion transporters have been identified and the transport of zinc by metallothionein is well known.[168] However, the details of zinc uptake, transport, distribution, incorporation into proteins, and the mechanisms of these processes are largely unexplained. There is a need to understand the role of zinc in biological systems in terms of its function, properties and biochemistry. Indeed such studies have been hindered by the limited availability of selective Zn(II) signalling probes. In this context, highly sensitive and zinc specific fluorescent sensors would permit a much more detailed understanding of the biological activity of Zn(II). Here, the most important and recent examples of Zn(II) recognition will be discussed. Special attention will be paid to the probes excited with visible light because of their obvious advantages, such as reduced autofluorescence and light scattering (Chapter 1).

2.2 Literature survey on Zn(II) selective fluorescent chemosensors

Nagano *et al.* designed fluoroprobes **76** and **77** containing cyclen as Zn(II) receptor site attached to a fluorescein fluorophore.[169] The alkylation of the nitrogen atoms lowers the

pK_a value of the macrocyclic amine, thereby reducing the chances of protonation at neutral pH. Fluorescence enhancement (FE) of 14- and 26-fold was observed upon Zn(II) titration in HEPES buffer at pH 7.5 for **76** and **77** respectively. Due to the poor complexation ability of alkali and alkaline earth metals to the cyclen, no significant increase in the fluorescence emission was observed with K^+, Ca^{2+} and Mg^{2+} titrations. Cu(II) complexes of **76** and **77** were non-fluorescent due to the ability of Cu(II) to quench the excited state of the fluorophore.

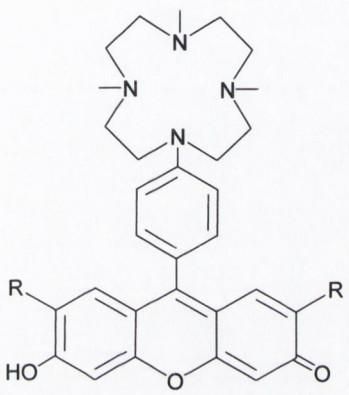

76: R = H
77: R = Cl

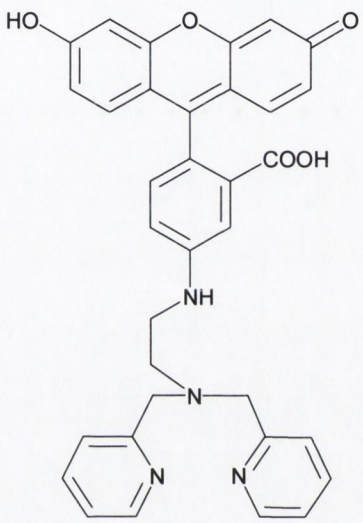

78

Nagano *et al.* also designed fluorescent sensor **78** utilising *N,N,N',N'*-tetrakis(2-pyridylmethyl)ethylenediamine (TPEN) as the ligand and fluorescein as fluorophore.[170] In the absence of metal ions the fluorescence was quenched due to PET. Upon titration with Zn(II) ions in HEPES buffer at pH 7.5, a 17-fold FE was observed without any changes in the excitation and emission wavelengths. In addition, a K_d of 0.78 nM was calculated for Zn(II) complexation. Molecular Probes Inc. (Eugene, Oregon) introduced the use of the di-2-picolylamine (DPA) moiety as a selective recognition site for Zn(II) in Newport green, **79**.[50,171] Under physiological conditions, a 3.3-fold FE was observed upon Zn(II) titration and a K_d of 1 μM was determined for Zn(II) complexation.

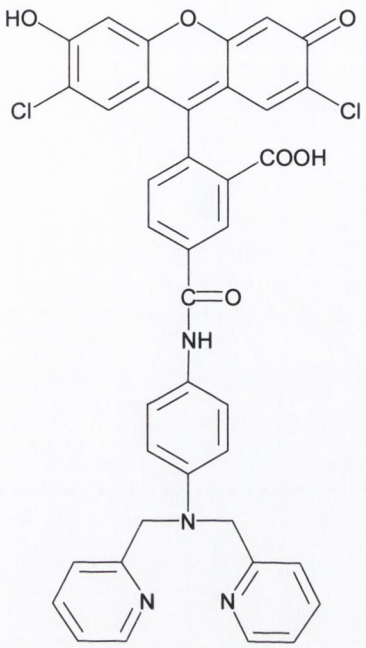

79

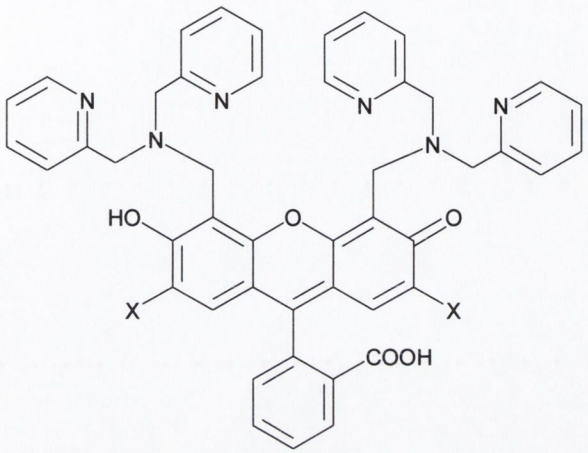

80: X= H
81: X= Cl

Lippard *et al.* developed two new fluorescein based Zn(II) fluoroprobe, **80** and **81** by integrating fluorescein with bis (2-pyridylmethyl) amine, an intracellular Zn(II) chelator.[172] In the absence of metal ions quantum yields of 0.38 and 0.25 were determined for **80** and **81** respectively. This increased to 0.87 and 0.92 for **80** and **81** respectively, upon addition of 25 μM of Zn(II) ions in PIPES buffer at pH 7.4. K_d values of 0.5 nM and 0.7 nM for **80** and **81** respectively have been reported for Zn(II) complexation at pH 7.0. Small hypsochromic shifts were observed in the absorption spectrum upon Zn(II) coordination which was attributed to the interaction between the phenolic moiety of the fluorophore with Zn(II). No fluorescence response was obtained with group 1 or group 2 metal ions, whereas transition metals such as Cu(I), Cu(II), Ni(II), Co(II) and Mn(II) induced some degree of fluorescence quenching. The high quantum yields obtained for the unbound state of **80** and **81** leads to poor signal recognition as the background fluorescence from the unbound fluoroprobe was too high at physiological pH. These factors, coupled with low yielding synthesis of various intermediates, limit the practical application of these sensors *in vivo*.

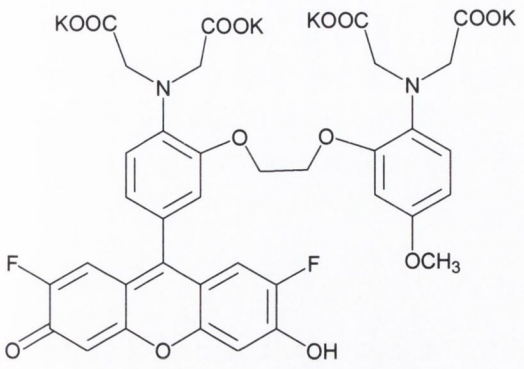

82

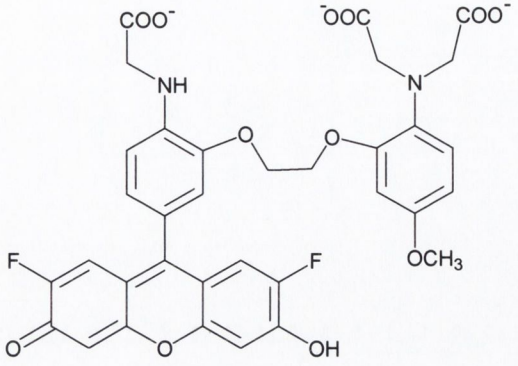

83

Kennedy *et al.*[173] developed **83** by modifying the well-known calcium fluorosensor fluo-3 (**82**)[47] with removal of one of the chelating *N*-acetic acid moieties from the BAPTA receptor to improve Zn(II) selectivity. The free sensor has a very low quantum yield (0.005) due to electron transfer from the receptor, which quenches the excited state of the fluorophore. The quantum yield increased significantly (0.43) in the presence of a saturating amount (5 μM) of Zn(II). A K_d of 15 nM was calculated from Zn(II) binding equilibrium data in HEPES buffer at pH 7.4. This was promising for use in the physiological environment. However, **83** was pH sensitive due to the protonation of the fluorophore at low pH (~ 4.8-6). Titration studies with metal ions such as Ca^{2+}, Fe(II), Cd(II) and Hg(II) also showed some selectivity. The molecule has been used for Zn(II) signalling in pancreatic beta cells.[44]

Walkup *et al.* and Godwin *et al.* simultaneously designed the peptide based sensors **84** and **85** respectively.[174,175] A K_d of 1.4×10^{-10} M of Zn(II)-**84** complex was obtained upon Zn(II) titration at pH 7 in HEPES buffer.[174] A K_d value of 1.0×10^{-12} M was estimated for the **85**-Zn(II) complex at pH 7.1.[175] In the absence of Zn(II), the peptide moieties in **85** are unfolded eliminating the intramolecular energy transfer. The presence of Zn(II) induces peptide folding resulting in intramolecular energy transfer due to the close proximity of the two fluorophores. Despite their high affinity and selectivity for Zn(II), the necessity for a reductive environment for complex formation is disadvantageous. It was also observed that protease enzymes in the cells easily digest these molecules, limiting their *in vivo* use.

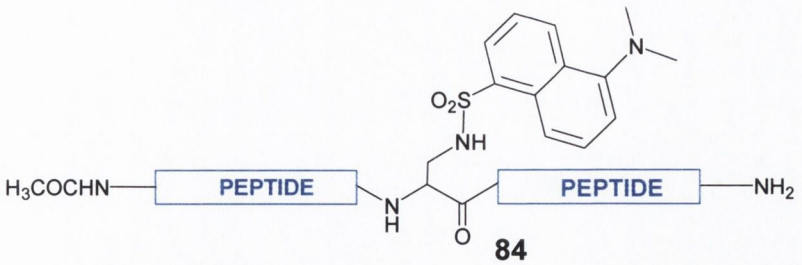

84

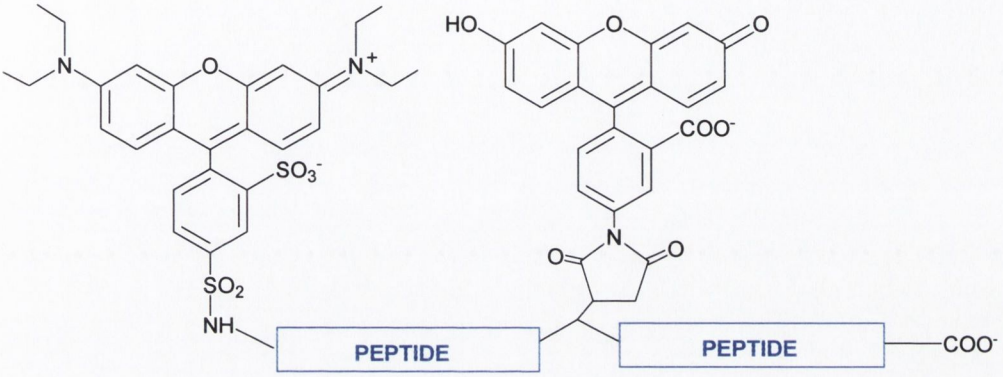

85

Maruyama *et al.* reported benzofuran based sensors **86** and **87** for the ratiometric analysis of Zn(II).[176] Upon excitation by light, the fluorophore undergoes ICT between the electron donating amino groups conjugated to the electron-withdrawing terminal. Upon interaction with a cation, a partial positive charge is photogenerated adjacent to the cation, inducing a blue-shift in the absorption and excitation spectra. The sensor was cell permeable and sensitive for Zn(II), but the signalling of Cd(II) was also appreciable. Moreover, the excitation wavelength was close to the UV region, which is not suitable for biological applications. K_d values of 0.79 nM and 2.8 nM were reported for **86** and **87** respectively in HEPES buffer at pH 7.4.

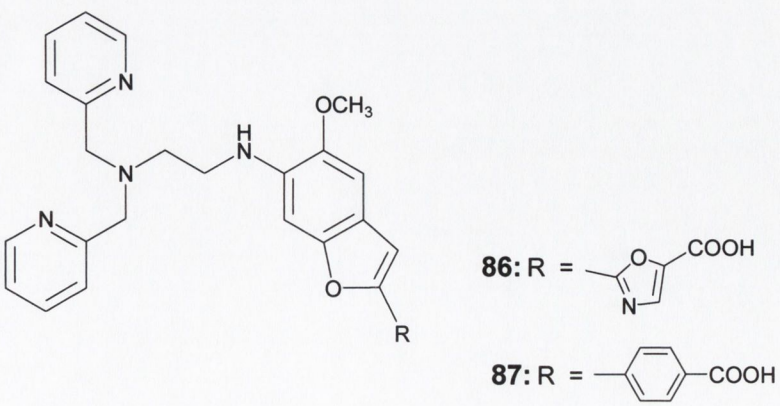

Recently, Lippard *et al.* have designed the neurosensor **88** as a Zn(II) stain for brain tissues.[177] It differs form other fluorescein based sensors **80** and **81** as the aniline nitrogen atom in **88** is involved in binding with Zn(II), thus rendering the sensor suitable for physiological conditions. Upon fluorescence titration with Zn(II) in PIPES buffer at pH 7 a 5-fold FE was observed. A K_d = 0.65 nM was determined for the **88**-Zn(II) complex.

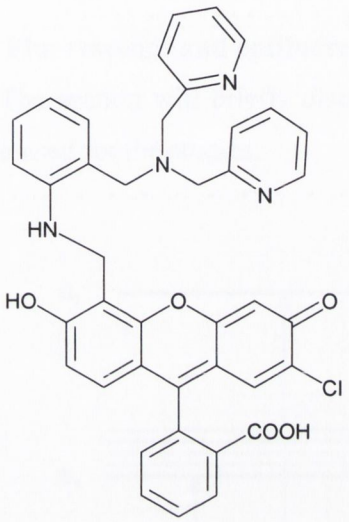

88

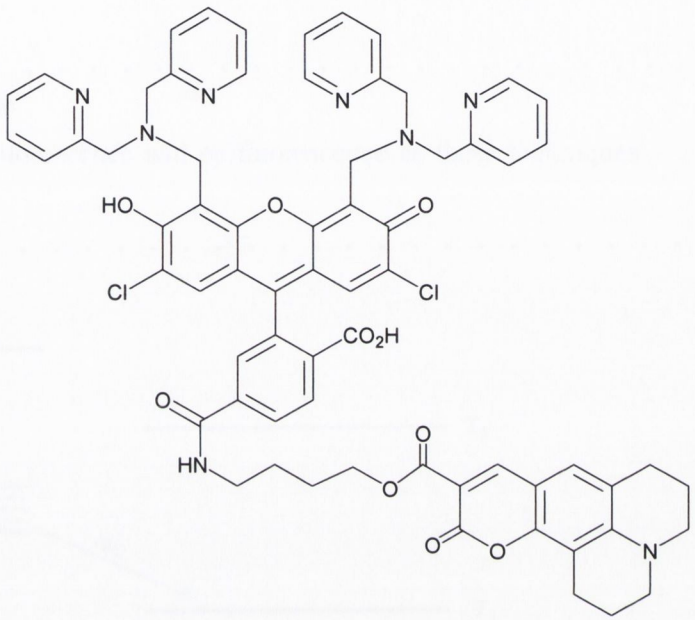

89

A novel two fluorophore based approach was introduced by Lippard *et al.* for the ratiometric sensing of Zn(II).[178] Fluoroprobe **89** comprises of two fluorophores (coumarin and fluorescein), both excited by visible light. The signalling is based upon the esterase-mediated cleavage of the sensor where one (fluorescein derivative) is sensitive to Zn(II) and the other (coumarin 343) is insensitive. Fluorescence emission intensity of the fluorescein derivative increased relative to coumarin 343 upon Zn(II) addition.

The development of fluorescent sensors has greatly improved our understanding of the physiological and biochemical role of Zn(II) particularly in glucose metabolism, neuron signalling and apoptosis. The Zn(II) sensing field is still in its infancy and much progress is required to match the evolution of calcium sensors started by Tsein *et al.* in 1980's.[67] The study carried out in this chapter is an advance in that direction.

2.3 Motivation for the present work

The main aims of the present study were two fold:

- to synthesise improved Zn(II) fluoroprobes both in terms of synthetic methodology and physical properties for efficient Zn(II) signalling
- to use these sensors for Zn(II) staining in biological samples using epifluorescence microscopy.

2.4 Fluorescence and epifluorescence

The section will briefly discuss fluorescence and epifluorescence as these techniques were used for the studies.

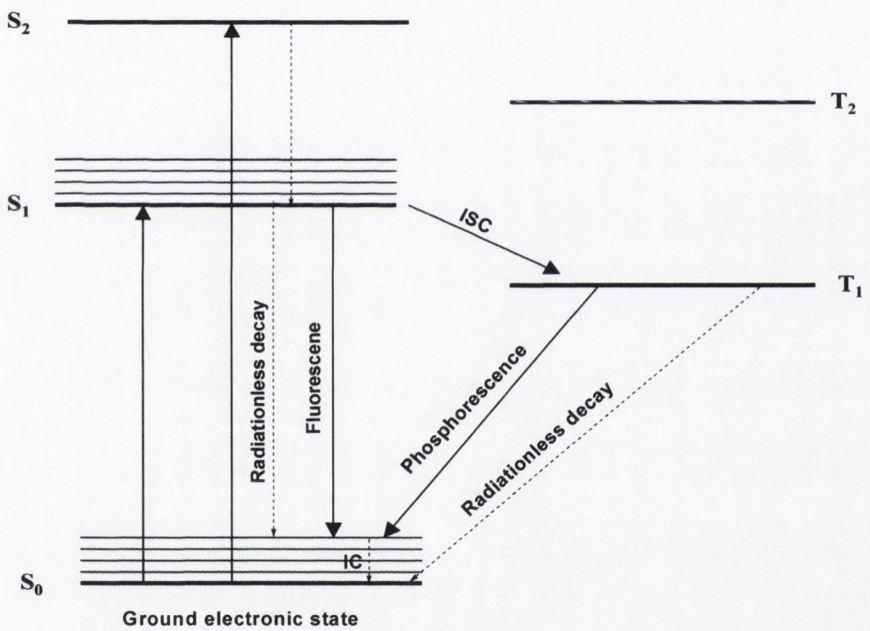

Figure 2.2 ***Jablonski diagram showing the process of fluorescence and other de-excitation pathways. ISC = inter-system crossing, IC = internal conversion. S_1, S_2 = first and second excited singlet electronic state, T_1, T_2 = first and second excited triplet electronic states.***[180]

Compounds exhibiting fluorescence are called fluorophores. Fluorophores are characterised by a series of closely spaced energy states (S_0, S_1, S_2) as shown in Figure 2.2. They can be excited from lower to higher energy states by absorption of quantum of light

of suitable frequency. The process of absorption is very fast (10^{-5}s) so there is no concomitant displacement of the nuclei according to the Franck-Condon principle.[179,180] Absorption of a photons can bring a molecule to one of the excited vibrational levels of S_1, S_2 and so on. The molecule can undergo many possible de-excitation processes, as illustrated in Figure 2.2 (Jablonski diagram). The emission of photons accompanying the $S_1 \rightarrow S_0$ relaxation is called fluorescence. Since there is energy loss in the excited state due to vibrational relaxation, the fluorescence spectrum is located at longer wavelengths than the absorption. The difference between the wavelengths of the excitation and emission maxima is called Stokes' shift.[179-181] According to Stokes' rule, the wavelength of a fluorescence emission is almost always longer than the wavelength of absorption. It is this shift in wavelength that makes the observation of the emitted light in an epifluorescence microscope possible, as an excitation filter selectively transmits light at the excitation maximum to strike the fluorophore and then, *en route* to the eyepiece, a barrier filter blocks this wavelength while transmitting as much as possible of the fluorescence emission.[182]

2.5 Design and synthesis of novel Zn(II)-fluoroprobes

The various fluoroprobes previously reported showed some need for further improvements to utilise them for the signalling of zinc in a biological environment. The main areas that need to be addressed are:

- pH independent nature in the physiological range
- highly selective signalling towards Zn(II)
- visible excitation wavelength
- ease of synthesis
- solubility and cell permeability.

Initially a series of fluorophores such as anthracene, fluorescein and sulphonamide were reviewed but these fluorophores suffer from one or more drawbacks such as ultraviolet excitation, pH sensitivity, low water solubility and small Stokes' shift. For the purpose of this work, 4-amino-1,8-naphthalimide derivative (**90**) was finally selected as the suitable fluorophore due to its many attractive features (Figure 2.3).

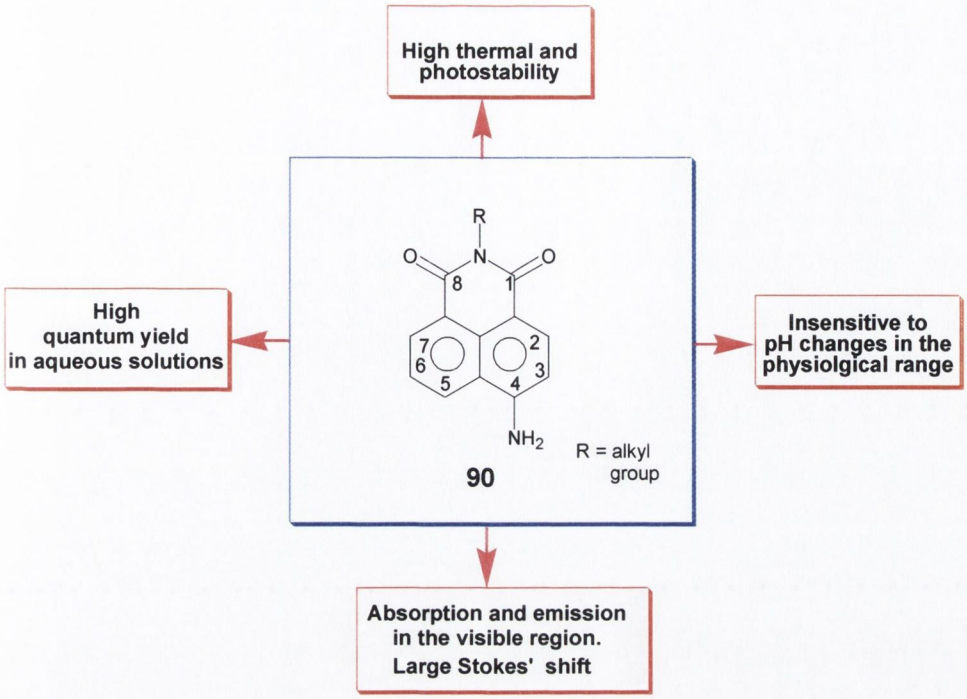

Figure 2.3 *Advantages of 4-amino-1,8-naphthalimide fluorophore* in chemosensing.

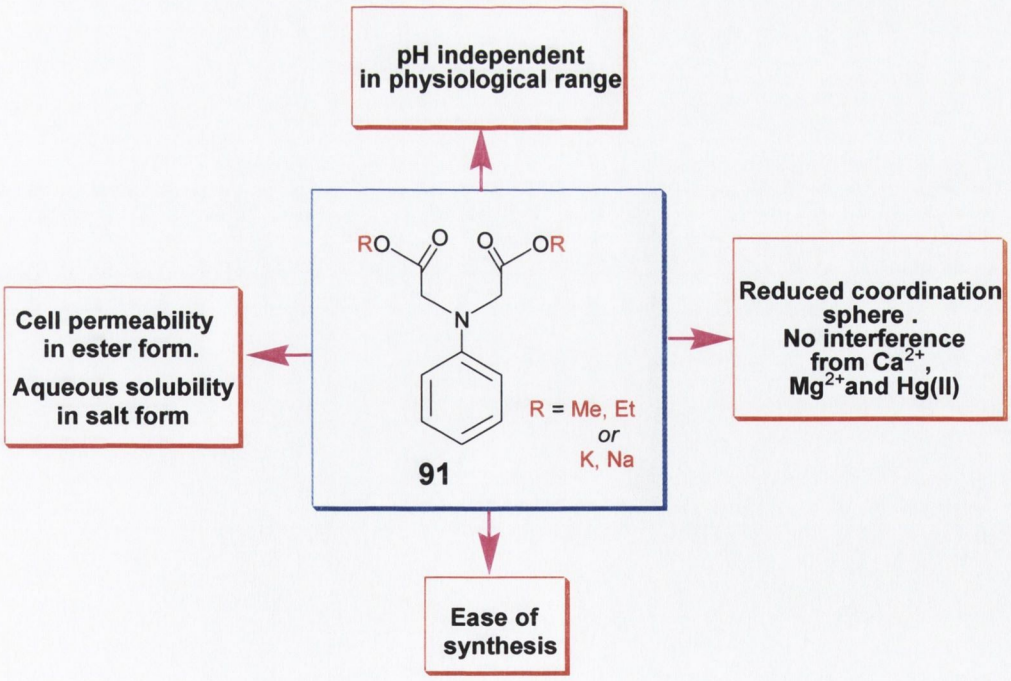

Figure 2.4 *Illustration of salient features of receptor.*

Out of multitude of receptor moieties screened, phenylimino derivative **91** was found to be a suitable candidate for integration into a chemosensor as a receptor due to its several advantages as illustrated in Figure 2.4.

By integrating fluorophore, receptor and spacer components, two new PET fluorescent chemosensors, **92** (methylene spacer) and **93** (ethylene spacer) were designed to explore the selectivity and sensitivity to Zn(II) under physiological conditions.

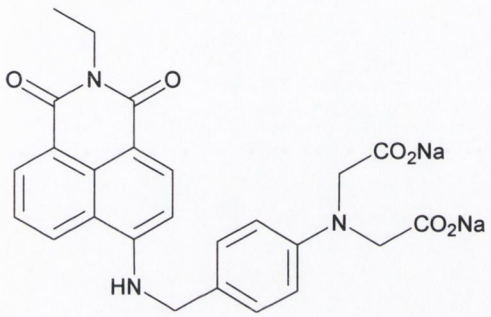

92

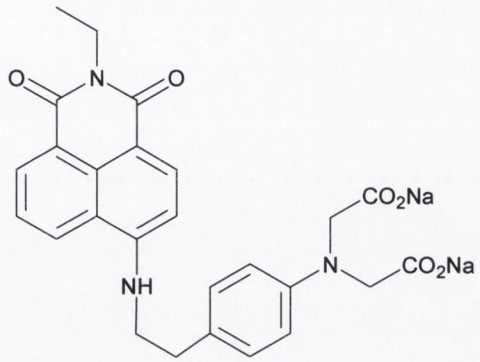

93

Both **92** and **93** are based on the same principle of *'fluorophore-spacer-receptor'* format developed by de Silva *et al.* and is discussed in detail in Chapter 1.[19] As stated, the only difference between the two structures is spacer length. The rationale behind the synthesis of **93** was the ethylene spacer could impart more thermal- and photo-stability, thus preventing the photobleaching of the sensor as reported by He *et al.* for naphthalimide based Na^+ and K^+ sensors.[45,46]

It can be argued that the ethylene spacer will reduce the PET quenching rate as it decreases exponentially with distance ($1/r^6$).[183] However, experimental studies carried out by Dabestani *et al.* have shown maximum PET rate can be operative up to three unit carbon spacers.[184] As stated above He *et al.* have synthesized both Na^+ and K^+ sensors utilising the same fluorophore and same spacer length and reported no major decreases in the PET rate.[45,46] Gunnlaugsson *et al.* have also reported similar observations for the naphthalimide based proton sensors.[185] The reasons for selecting the ethyl group on the imide nitrogen of the naphthalimide fluorophore was based mainly upon ease of synthesis and the high yields obtained using ethylamine. Photophysical studies carried out by

Alexiou *et al.* have shown that the nature of the alkyl group has negligible effect on the photochemistry of the naphthalimide fluorophore.[186]

2.5.1 Synthesis and characterisation of 92

The retrosynthetic analysis shows that **92** can be synthesized readily by the alkaline hydrolysis of ester **94** as shown in Scheme 2.1.

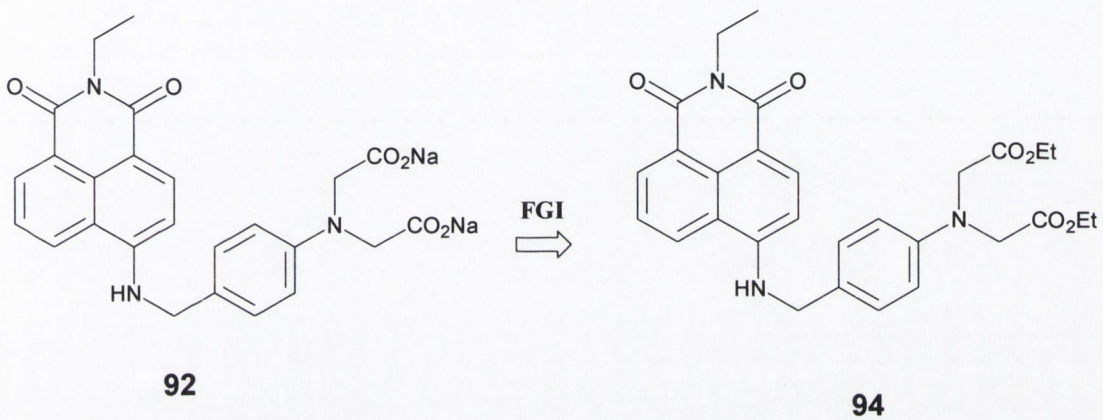

92 **94**

Scheme 2.1 ***Retrosynthetic analyses of 92 from the intermediate ester 94. FGI = Functional group interconversion.***

Three different retrosynthetic strategies can be envisioned for the intermediate ester **94** as illustrated in Scheme 2.2. Strategy 1, requires a nucleophilic attack of **95**, which is the fluorophore moiety of **92,** on the *para* substituted aniline derivative **96**. Strategy 2 employs the benzyl amine derivative **98** as a nucleophile. The desired S_N^2 attack of this intermediate on the 4-bromo-1,8-naphthalimide derivate **97** will result in the formation of an intermediate ester, **94**. Synthetic strategy 3 involves the linear synthesis of **94**. In this protocol, the intermediate **99** is first synthesised from 4-bromo-1,8-naphthalimide and 4-aminobenzylamine. This is followed by *N*-alkylation of the **99** using ethyl bromoacetate as an alkylating agent to obtain intermediate the ester **94**.

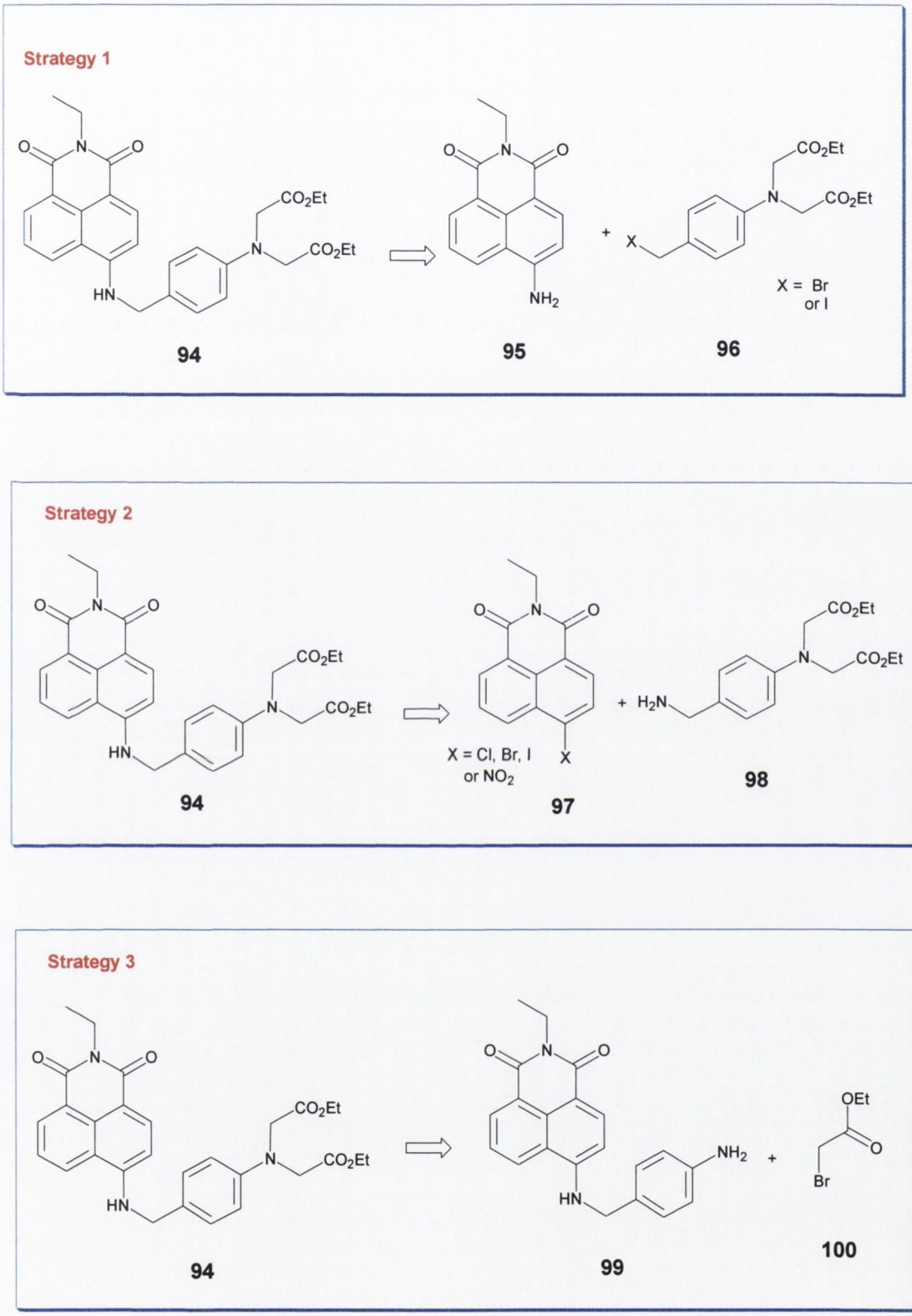

Scheme 2.2 ***Three alternative synthetic strategies for 94.***

A literature[29] survey resulted in the elimination of synthetic strategy 1 for further consideration as the ICT character of **95,** as illustrated in Scheme 2.3, reduces the nucleophilicity of the amino group considerably, due to the partial positive charge on nitrogen atom.

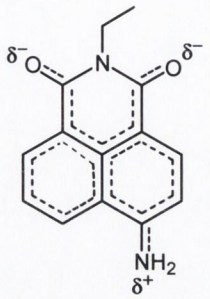

95

Scheme 2.3 ***Electron delocalisation in 95 due to push-pull mechanism.***

Strategy 2 looked more promising and hence was attempted first. The synthesis of **97,** involved refluxing 6-bromo-1,8-naphthalic anhydride in toluene with anhydrous ethylamine using triethylamine as the base. A number of difficulties were encountered using the procedure, such as:

- handling and storage of anhydrous ethylamine, which is a gas at room temperature
- isolation of **97** involved column chromatography which resulted in low yields

These difficulties were however, avoided by using 1,4-dioxane as a solvent. Under these conditions the synthesis of **97** was easily accomplished by refluxing 6-bromo-1,8-naphthalic anhydride (**101**) in 70% aqueous ethylamine (*w/v*) (Scheme 2.4).[187] Upon completion, the mixture was poured into water to obtain an off-white precipitate of **97** in 85% yield. The spectral assignment was in good agreement with the reported values.[187]

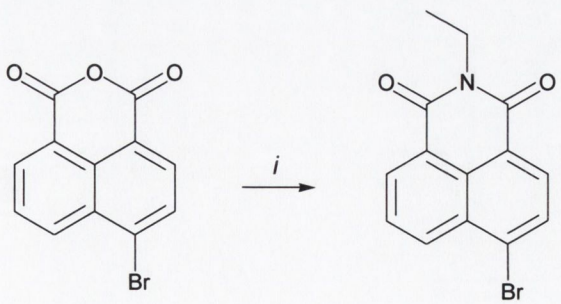

101 **97**

Scheme 2.4 ***Synthesis of 97: (i) ethylamine (70%), 1,4-dioxane, reflux, 2 hours.***

The next step was the synthesis of **98**, which unfortunately proved difficult and many unsuccessful procedures were attempted. The initial method used for the synthesis is outlined in the Scheme 2.5.

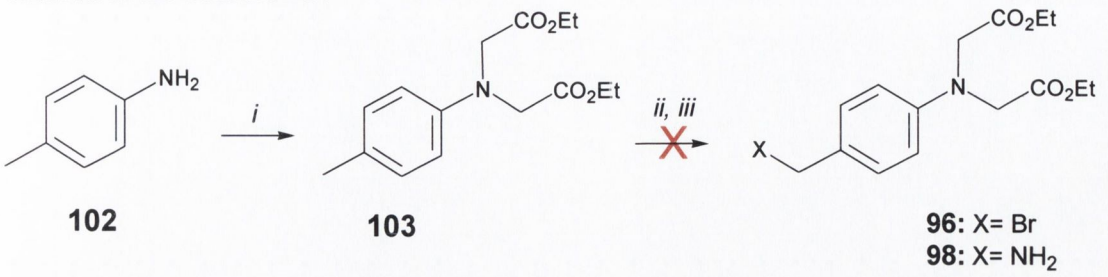

Scheme 2.5 ***Attempted synthesis of 96 and 98: (i) ethyl bromoacetate, K_2HPO_4, KI, CH_3CN, reflux, 24 hours; (ii) NBS, benzoyl peroxide, CCl_4, reflux; (iii) Gabriel conditions could be used but not attempted as synthesis of 96 was not realised.***

The alkylation of *p*-toludine (**102**) with ethyl bromoacetate using K_2HPO_4 in refluxing CH_3CN proceeded smoothly giving **103** in 90% yield. Bromination of **103** with *N*-bromosuccinimide (NBS) using benzoyl peroxide as the initiator CCl_4 did not lead to the formation of the desired product **96**. ^{1}H-NMR, ^{13}C-NMR and Electrospray mass spectroscopy (ESMS) showed that no benzylic bromination had taken place, instead pointed to nuclear bromination. The ^{1}H-NMR spectrum of the starting material (**102**) and the product (**104**) are shown in Figure 2.5 and Figure 2.6 respectively.

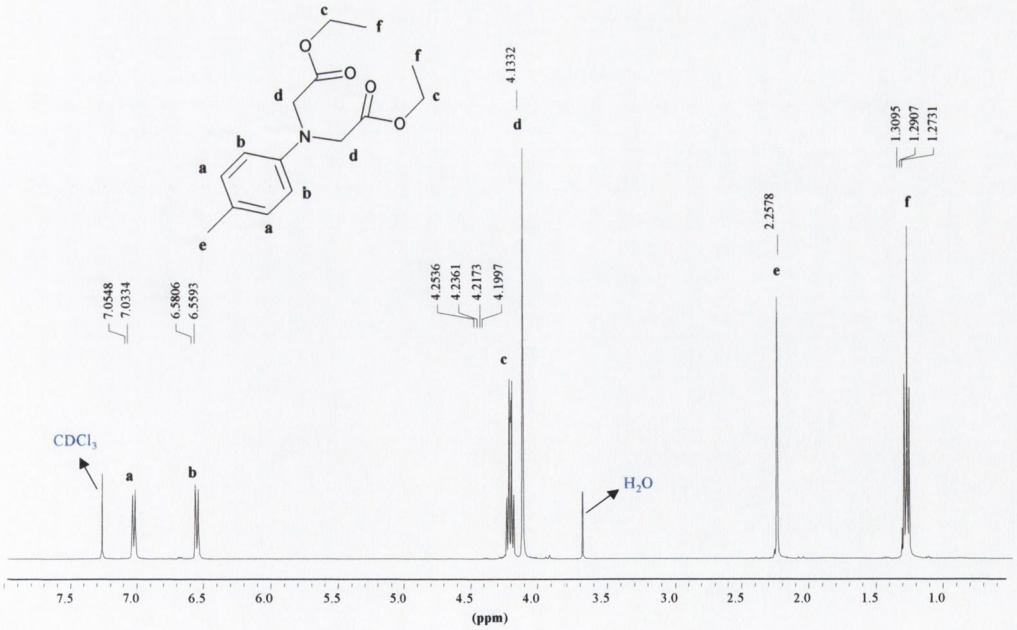

Figure 2.5 ***^{1}H-NMR (400MHz, $CDCl_3$) of starting material, 103.***

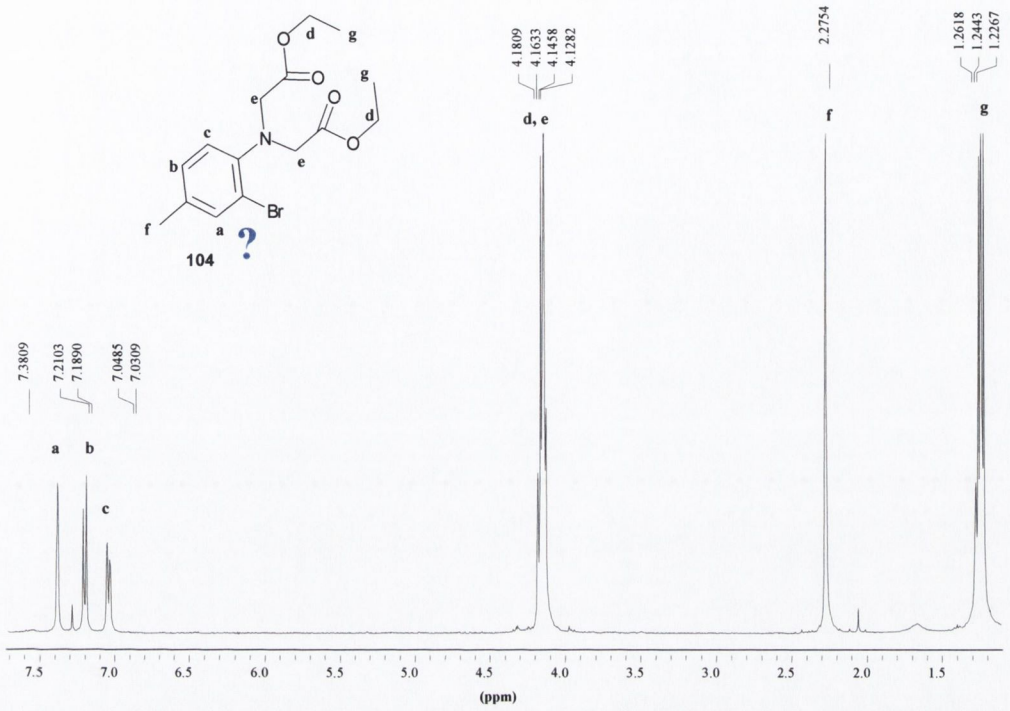

Figure 2.6 ***^{1}H-NMR (400MHz, $CDCl_3$) unexpected bromination product, 104.***

The starting material **103** showed a resonance corresponding to the methyl peak at δ 2.26, and two clear doublets represent the aromatic protons at δ 6.67 and δ 7.04. As can be seen from Figure 2.5, the methyl resonance is clearly visible in the brominated product **104** at δ 2.28. Furthermore, the aromatic proton resonances have lost the symmetry that was clearly present in the starting material. Three resonance signals, one singlet at δ 7.38 and two doublets at δ 7.03 and δ 7.20, can be assigned to the aromatic protons in the brominated product, **104**. The integration of these resonances corresponds to three protons, which is evidence for ring substitution. No peak corresponding to a benzylic group in the brominated compound was observed. The carbon spectrum also shows many signals in the aromatic region of the brominated product **104**, which can be explained only if nuclear bromination is visualised rather than benzylic bromination. The most likely reason for nuclear bromination in **103,** is the electron-rich nature of the aromatic ring. ESMS of **103** showed a peak at 280 mass units (M+H, 100%) while for **104** a peak at 358 mass units ($M+H^+$, 100%) was observed. Elemental analysis for both products was in good agreement with the calculated values. Combination of all these factors clearly indicates a preference

for nuclear bromination rather than side-chain bromination is occurring. This reaction was again attempted with/without the use of benzoyl peroxide, at various temperatures and in different solvents as summarised in Table 2.1. Unfortunately, the desired product **96,** was never obtained. Consequently this synthetic pathway was abandoned.

Table 2.1 ***Conditions employed for benzylic bromination of 96.***

Reagent and reaction conditions	Product obtained
NBS, CCl_4, benzoyl peroxide, reflux	Nuclear bromination
NBS, CCl_4, benzoyl peroxide, 25^{0}C	Starting material, nuclear bromination
NBS, CCl_4, benzoyl peroxide, -5^{0}C	Starting material, nuclear bromination
NBS, CCl_4, 25^{0}C	Starting material, nuclear bromination
NBS, CCl_4, -5^{0}C	Starting material
NBS, chlorobenzene, benzoyl peroxide, reflux	Nuclear bromination
NBS, chlorobenzene, benzoyl peroxide, 25^{0}C	Nuclear bromination
NBS, chlorobenzene, benzoyl peroxide, -5^{0}C	Starting material, nuclear bromination
NBS, chlorobenzene, reflux	Starting material, nuclear bromination
NBS, chlorobenzene, 25^{0}C	Starting material, nuclear bromination

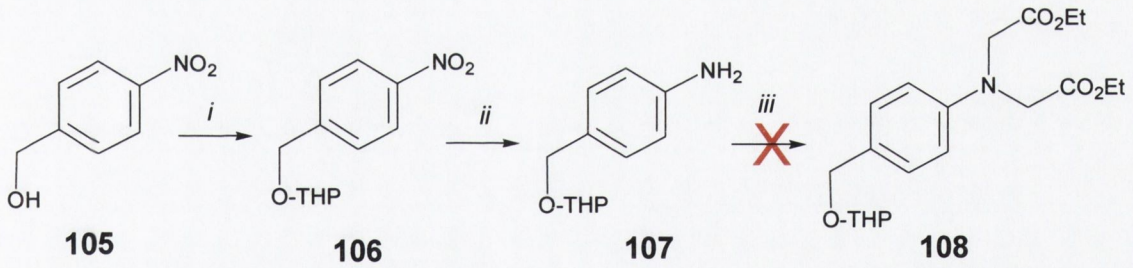

Scheme 2.6 ***Attempted Synthesis of 108: (i) 3,4-dihydro-2H-pyran, p-toluenesulfonic acid monohydrate, DCM, 2hours; (ii) H2, Pd/C (10%), 1 atmosphere, 1 hour; (iii)*** K_2HPO_4***, KI,*** CH_3CN***, 24 hours.***

A new synthetic route was developed as illustrated in the Scheme 2.6. Here, the hydroxyl group of the commercially available 4-nitrobenzyl alcohol was first protected as the tetrahydropyrene (THP) ester to give *O*-tetrahydropyranyl-4-nitrobenzyl alcohol **106.**[188] The nitro group was then reduced using Pd/C (10%) at one atmosphere to give the amino derivative **107**. The introduction of a stereogenic centre in **107** (due to the THP group)

resulted in a complicated ^{1}H-NMR spectrum. However, it was possible to assign all the observed peaks. Two multiplets at δ 3.53-3.58 and δ 3.92-3.97 can be attributed to the CH_2 group adjacent to the sterogenic centre. The aromatic protons appeared as two distinct doublets at δ 6.68 and δ 7.18. A peak at 208 mass units ($M+H^+$, 100%) was observed in the ESMS. The next step involved the alkylation of **107** with ethyl bromoacetate in acetonitrile. This proved to be difficult as it lead to the formation of a mixture of products. Both ^{1}H- and ^{13}C-NMR ($CDCl_3$), and ESMS suggested that the desired product was not formed. A multitude of alternative reaction conditions were employed but failed to achieve the desired product (Table 2.2).

Table 2.2 ***Some of the conditions used for N-alkylation of 107.***

Regents	Solvent and conditons	Results
K_2HPO_4, KI	CH_3CN, reflux,	^{1}H-NMR spectra complicated, deprotection of THP group was observed.
K_2CO_3, KI	CH_3CH, reflux	Same as above.
K_2HPO_4, KI	DMF, 25^{0}C and 90^{0}C	Mixture of products as shown by ^{1}H-NMR, not possible to separate
K_2CO_3, KI	DMF, 25^{0}C and 90^{0}C	^{1}H-NMR and ESMS showed mixture of starting material, mono and bis-alkylated product.

A new synthetic route for **98** was developed as shown in Scheme 2.7. This involved *N*-alkylation of aniline to **110,** followed by formylation of **110** at the *para* position in 1,2-dichlorobenzene using phosphoryl oxychloride ($POCl_3$) and DMF as formylating reagents. This afforded the aldehyde **111** in 60% yield, after purification by silica flash column chromatography using ethyl acetate:hexane (1:1, *v/v*) as eluant. ^{1}H-NMR, ^{13}C-NMR, IR and ESMS analysis confirmed the structure of **111**. The ^{1}H-NMR ($CDCl_3$) showed a singlet at δ 9.78 attributed to the aldehyde proton. Two doublets at δ 7.45 and δ 6.67 were observed for phenyl protons. Reduction of **111** using $NaBH_4$ at room temperature yielded a mixture of unidentified products. However, modification of the reaction conditions resulted in the formation of **112** in 80% yield. The aldehyde **111** was dissolved in methanol at –5 ^{0}C followed by slow addition of $NaBH_4$ until the complete disappearance of the starting material, as observed by TLC (using ethylacetate:hexane (2:3, *v/v*) as eluant)

had occurred. Spectral analysis confirmed the structure of **112**. The ^{1}H NMR showed aromatic doublets at δ 7.25 and δ 6.63, and a singlet at δ 4.58, which was assigned to the benzyl group. Chlorination of **112** in refluxing 1,4-dioxane using thionyl chloride ($SOCl_2$) resulted in high yields (85%) of **113**. The amination of **113** using the Gabriel method was, however, not successful. Direct conversion of the alcohol to the amine using triphenyl phosphine (PPh_3) and sodium azide (NaN_3), also did not resulted in the target compound **98.**

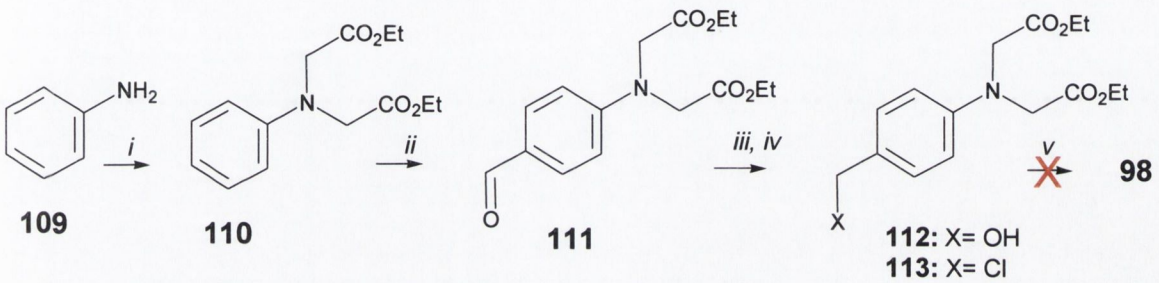

Scheme 2.7 ***Attempted synthesis of 98: (i) ethyl bromoacetate, K_2HPO_4, KI, CH_3CN, 24 hours. (ii) $POCl_3$, DMF, o-dichlorobenzene, 120 ^{0}C, overnight (ii) $NaBH_4$, CH_3OH, -5^{0}C, 20 minutes; (iv) 112, $SOCl_2$, 1,4-dioxane, reflux, 5 hours (v) PPh_3, NaN_3, diethyl ether, 25^{0}C (not successful).***

At this stage it was decided to investigate synthetic strategy 3, which involved the synthesis of a primary aromatic amine derivative **99,** as the initial step. Retrosynthetically, **99** could by achieved readily by the reaction of 4-amino benzylamine with either 4-bromo or 4-nitro-1,8-naphthalimide (Scheme 2.8).

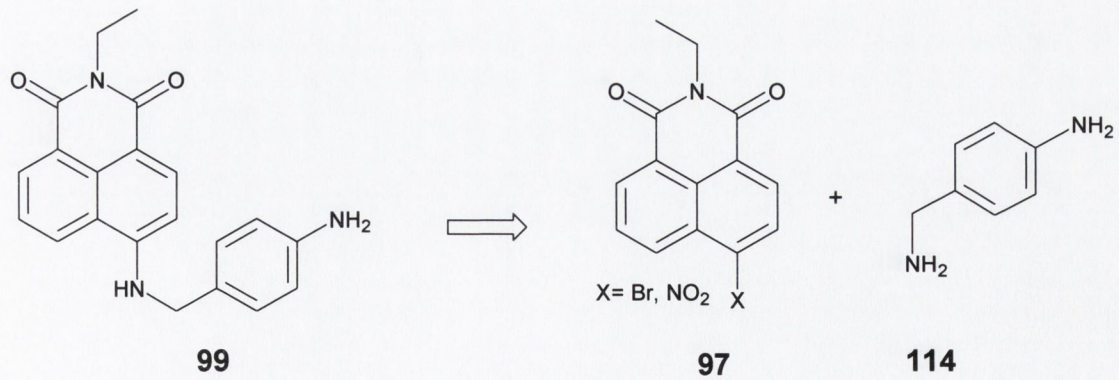

Scheme 2.8 ***Schematic illustration of retrosynthesis of 99.***

Alexiou *et al.*[186] and Garbacheve *et al.*[59,188] have synthesised various 4-*N* alkyl derivatives of **97** by reaction of 4-bromo or 4-nitro-*N*-ethyl-1,8-naphthalimide either in refluxing ethanol or DMF at 90^{0}C. Unfortunately, these methods failed to achieve the target compound **99**. The uses of different reaction conditions were not successful in obtaining the desired compound **99** (Table 2.3).

Table 2. 3 ***Various conditions used for synthesis of 99.***

Conditions used	Results
1,4-dioxane, refluxing temp.	Starting material, substitution at imide nitrogen
DMF solvent, 25^{0}C and100^{0}C	Starting material
DMA solvent, 25^{0}C and120^{0}C	Starting material
DMA, base, 25^{0}C and120^{0}C	Starting material, substitution at imide nitrogen
1,2-ethoxyethane, 130^{0}C	Starting material
1,2-ethoxyethane, $CuSO_4$, 130^{0}C	Starting material

At this stage, an alternative approach to this synthetic problem was developed. Heating of **97** to near melting temperature (130 ^{0}C) followed by subsequent addition of neat 4-amino benzylamine resulted in formation of the desired product **99**. The reaction was complete in 10 minutes. However, it was allowed to proceed for 30 minutes. Pouring of the reaction mixture into water, to precipitate the product, followed by recrystallization from ethanol afforded **99** in 85% yield (Scheme 2.9).

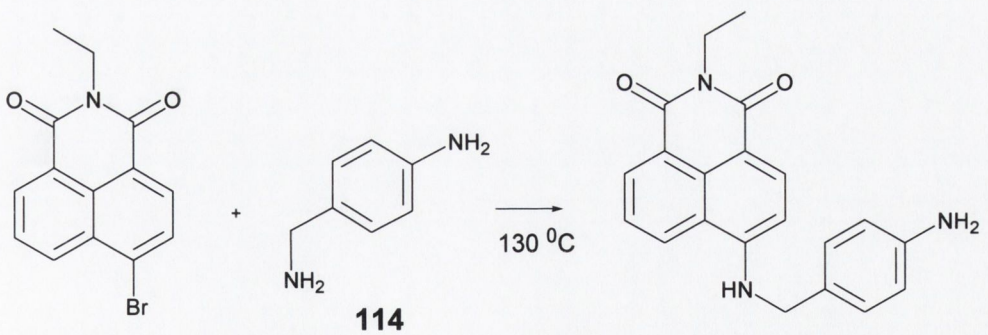

97 **114** **99**

Scheme 2.9 ***Synthesis of 99.***

The structure of **99** was confirmed by ^{1}H-NMR, ^{13}C-NMR, IR and ESMS and elemental analysis. The aromatic protons of the phenyl moiety appear as doublets at δ 6.54 and δ 7.07 (**h** and **g** in ^{1}H-NMR of **99** as shown in Figure 2.7). The naphthalimide protons appear as five different resonance frequencies as a doublet, a triplet and three doublets (at δ 6.70, δ 7.69, δ 8.18, δ 8.43 and δ 8.73) represented as **g, e, d, b** and **a** respectively in Figure 2.7. The imino proton (–NH) appeared as broad singlet at δ 8.27. A singlet at δ 4.95 was attributed to the primary aromatic amine protons, whereas a resonance at δ 4.46 was assigned to the methyl spacer. The ^{13}C-NMR spectrum of **99** showed peaks at δ 163.53 and δ 162.67, indicating the non-equivalence of the imide carbonyl groups.

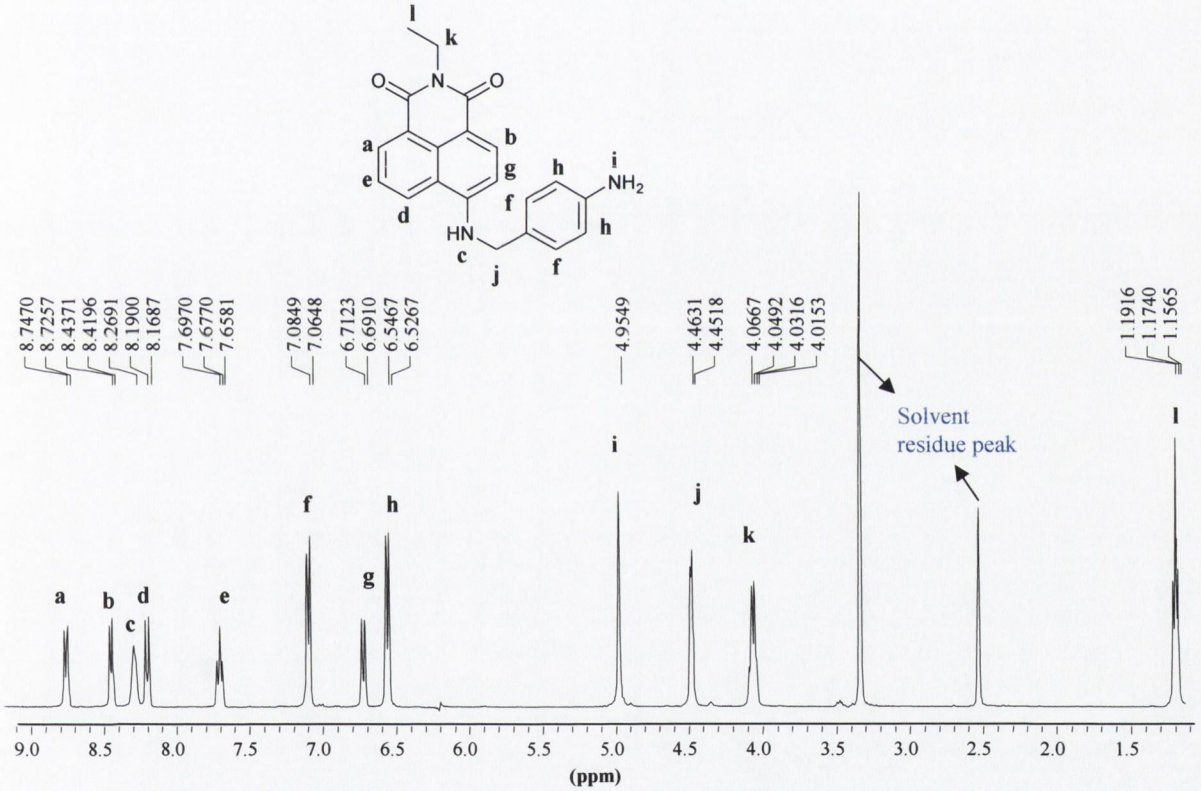

Figure 2.7 ***^{1}H-NMR (DMSO-d_6, 400MHz) of primary aromatic amine 99.***

Different methods were attempted for the alkylation of **99** using ethyl bromoacetate (Table 2.4). However, the procedure involving K_2CO_3 base in DMF (Scheme 2.10) resulted in the target product **94** in high purity and yield (90%) after recrystallization from 2-propanol.

Table 2.4 ***Different synthetic methodology for N-alkylation of 99.***

Base	Solvent and reaction conditions	Results
K_2HPO_4	CH_3CN, reflux	Mixture of products, difficult to separate.
K_2CO_3	CH_3CN, reflux	Mixture of products difficult to separate
K_2HPO_4	DMF, reflux	Highly green fluorescent unidentified compound obtained
K_2CO_3	DMF, 90^0C	Target product **94** obtained in 90% yield

Fortunately, alkaline hydrolysis of **94** with 3M NaOH in CH_3OH:H_2O (10:1, *v/v*) proceeded smoothly to give the desired sensor **92** in a quantitative yield (Scheme 2.10).

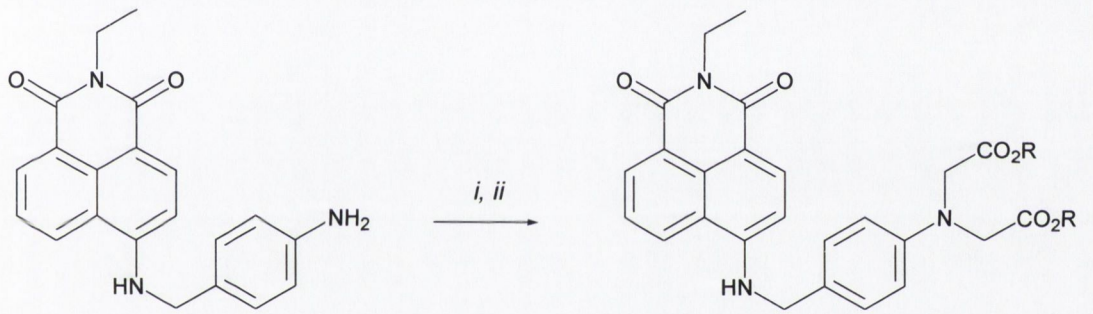

99

94: R = Et
92: R = Na

Scheme 2.10 ***Synthesis of 94 and 92: (i) ethyl bromoacetate K_2CO_3, KI, DMF, 90^0C; (ii) NaOH, CH_3OH-H_2O, reflux, 2 hours.***

Structures of both the ester **94** and corresponding sodium derivative **92** were confirmed by standard spectroscopic methods. The ^{1}H-NMR of **94** was similar to the amine **99** with additional peaks for the *N*-ester groups (Figure 2.8). The aromatic protons of the phenyl ring appeared as doublets at δ 6.49 and δ 7.21. The naphthalimide protons appear as five different resonance frequencies, a doublet, a triplet and three doublets (at δ 6.69, δ 7.69, δ 8.18, δ 8.45 and δ 8.78) represented as **g, e, d, b** and **a** respectively in Figure 2.8. The –NH proton appeared at δ 8.37 as a singlet. A resonance signal at δ 4.51 was attributed to the methylene spacer protons. The proton resonances of the ethyl groups of the ester overlapped with those of the ethyl group of the imide nitrogen. Carbonyl peaks in the ^{13}C-

NMR were observed at δ 170.22, δ 163.55 and δ 162.69. IR spectrum analysis showed absorption bands at 1684-1747 cm^{-1} assigned to the C=O stretching. ESMS showed a peak at 517 mass units ($M+H^+$, 40%).

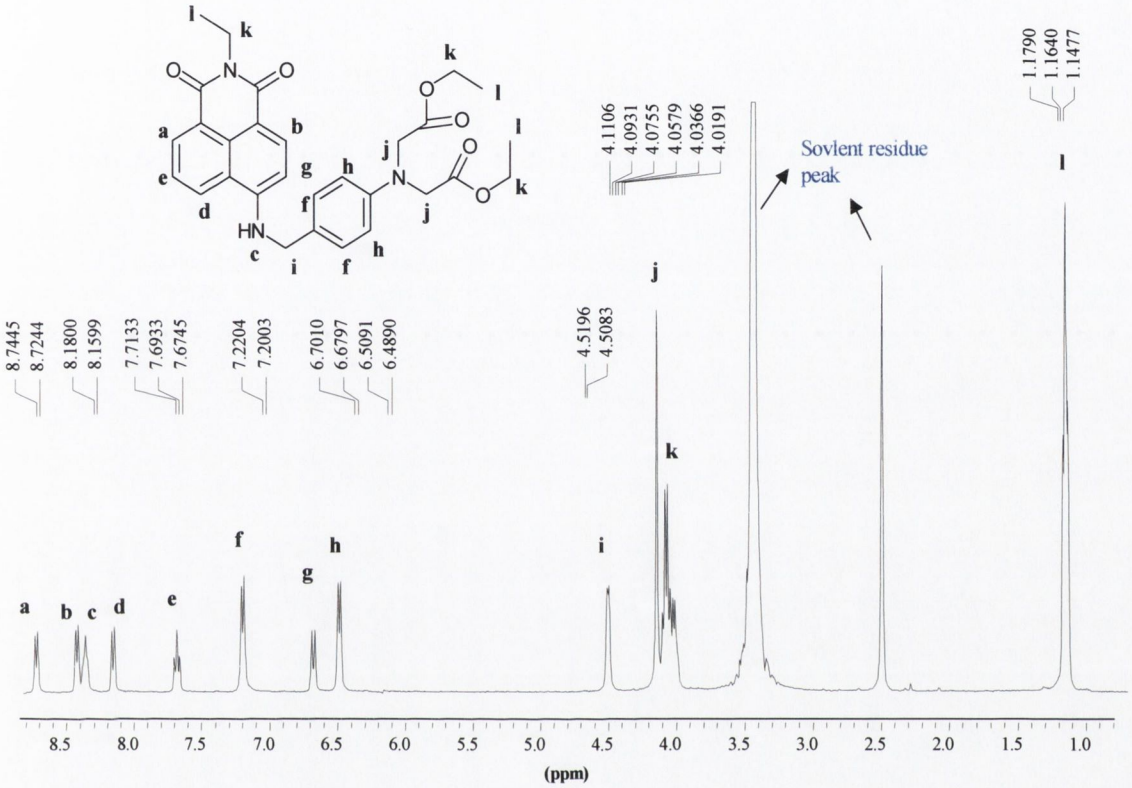

Figure 2.8 ***^{1}H-NMR (DMSO-d_6, 400MHz) of ester 94.***

The ^{1}H-NMR spectrum of **92** showed some differences in the aromatic region. The phenyl protons were observed as doublets at δ 6.46 and δ 7.21. The naphthalimide protons were observed as a doublet, a triplet and three doublets (at δ 6.18, δ 7.09, δ 7.53, δ 7.63 and δ 7.76) represented as **g**, **e**, **c**, **a** and **b** respectively in Figure 2.9. The lower chemical shift value of the doublet at δ 6.24 might be due to the electron-donating effect of the carboxylate groups. The singlet at δ 4.22 was attributed to the methylene spacer. Both methylene protons of the $-CH_2CO_2Na$ group were observed as a single resonance at δ 4.28. The CH_2 protons of the ethyl appeared as a quartet at δ 3.77, while the methyl protons were represented as a triplet at δ 1.10. The ^{13}C-NMR also showed the expected peaks with carbonyl group appearing at δ 179.06, δ 164.31 and δ 163.28. The IR spectrum showed

peaks at around 1615-1680 cm^{-1} due to the carbonyl stretching absorption. A peak at 505 mass units ($M+H^+$, 50%) was observed in the ESMS spectrum.

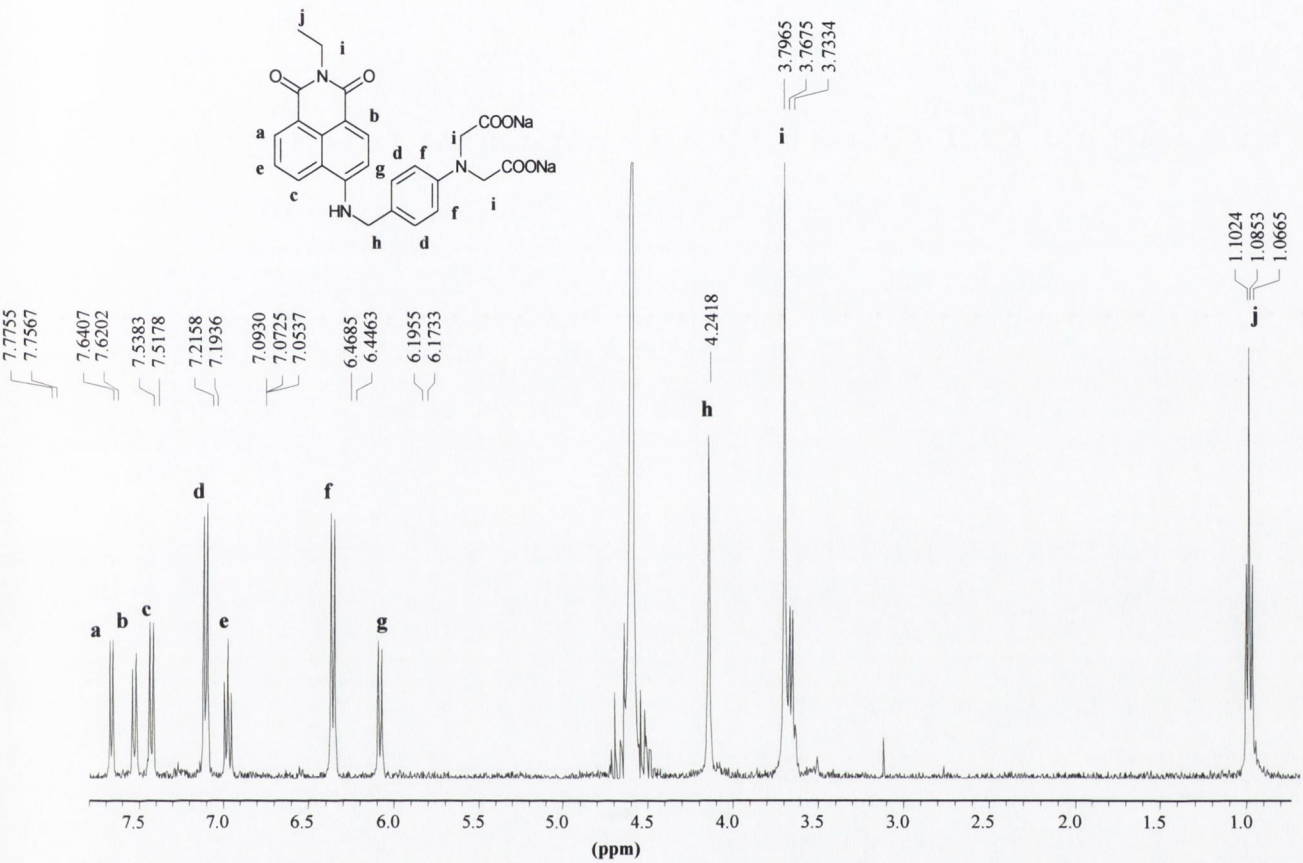

Figure 2.9 ***^{1}H-NMR (DMSO-d_6, 400MHz) of ester 92.***

2.5.2 Synthesis and characterisation of 93

The synthesis of **93** was easily accomplished using the same protocol established for the synthesis of **92** and is outlined in Scheme 2.11. The condensation of commercially available 4-aminophenyl *N*-ethylamine with **97** at 130 ^{0}C followed by precipitation and recrystallization from 2-propanol resulted in an 80 % yield of desired primary aromatic amine **116**. As described before for **99**, the *N*-alkylation was carried out in DMF using K_2CO_3 as base and resulted in a 90 % yield of the intermediate ester **117**. The alkaline hydrolysis of **117** followed by recrystallization from ethanol resulted in the almost quantitative yield of the sensor **93**. The structure of **116**, **117** and **93** were confirmed by all the available spectroscopic techniques and elemental analysis.

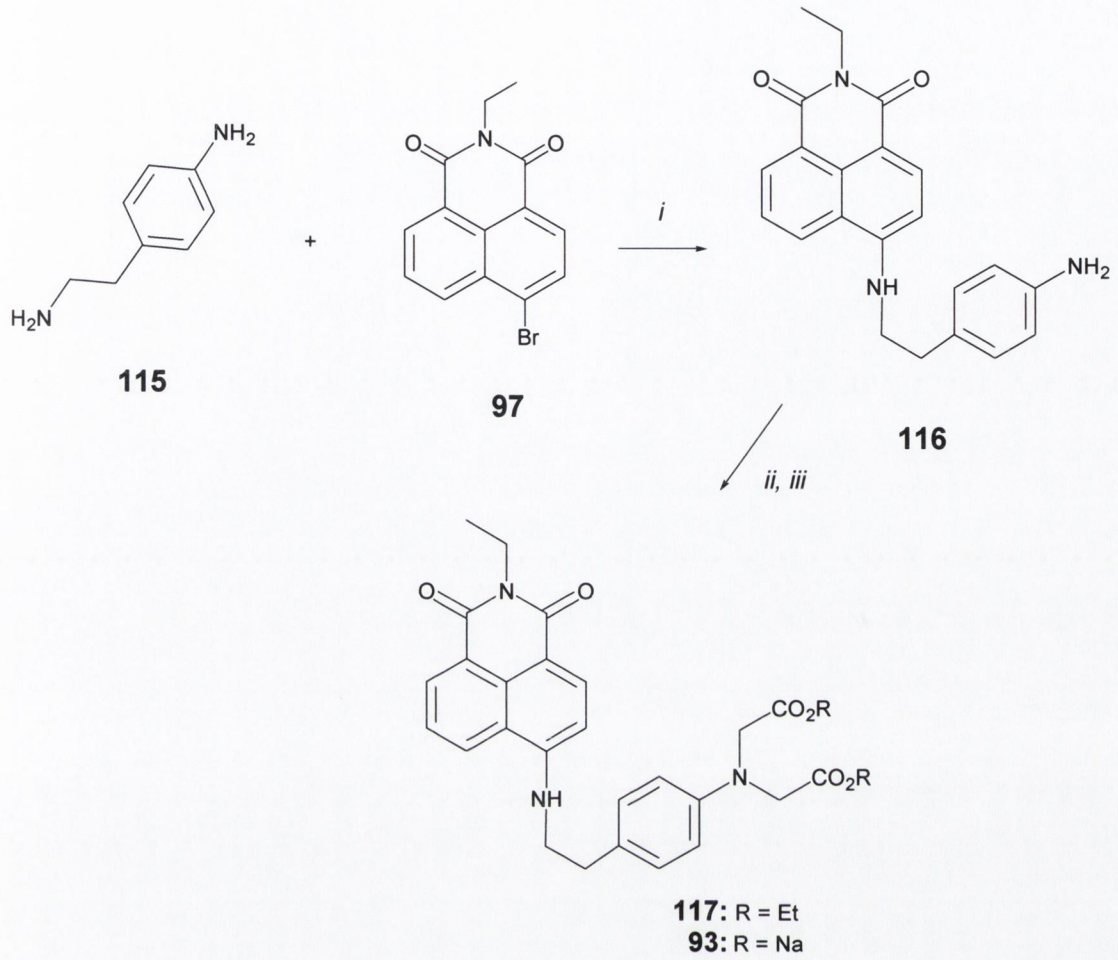

Scheme 2.11 ***Synthesis of 117 and 93: (i) 130^{0}C, 30 minutes: (ii) ethyl bromoacetate, K_2CO_3, KI, DMF, 90 ^{0}C; (iii) NaOH,CH_3OH-H_2O, reflux, 2 hours.***

^{1}H-NMR (DMSO-d_6) of **116** showed two doublets at δ 6.51 and δ 6.97 respectively attributed to the phenyl protons (Figure 2.10). The naphthalimide protons were all non-equivalent appearing as a doublet, triplet and three doublets at δ 6.83, δ 7.68, δ 8.28, δ 8.44 and δ 8.66 respectively. The ethylene spacer protons were observed as multiplets at δ 3.48-3.54 and δ 2.81-2.85. Protons of the ethyl group linked to the imide nitrogen appeared as a quartet and triplet at δ 4.05 and δ 1.18 respectively. Bands observed in the region of 1638-1680 cm^{-1} in the IR spectrum were assigned to the C=O stretching. ESMS showed a peak at 360 mass units $(M+H)^+$.

In the ^{1}H-NMR (DMSO-d_6) of **117** two aromatic doublets were observed at δ 6.49 and δ 7.13 for the phenyl group protons. The aromatic protons of the naphthalimide ring appeared as four doublets and a triplet. The proton signals for the ethylene spacer were

observed as multiplets at δ 3.50-3.52 and 2.87-2.90. The ^{13}C-NMR spectrum showed the peaks for the carbonyl groups at δ 170.61, δ 163.54 and δ 162.71. The IR peaks in the region 1700-1753 cm^{-1} were assigned to the carbonyl stretching frequency. ESMS spectrum showed a peak at 532 mass units $(M+H)^+$.

The ^{1}H-NMR of **93** showed a similar splitting pattern as was observed for **92**. Doublets observed at δ 6.44 and δ 7.08 were assigned to the phenyl protons. The naphthalimide protons appear as a doublet, a triplet and three doublets (at δ 6.17, δ 6.97, δ 7.09, δ 7.48 and δ 7.70) represented as **g, e, b, c** and **a** respectively in Figure 2.10. Protons of the ethyl group were observed as a quartet and a triplet at δ 3.71 and δ 1.06 respectively. The CH_2 protons of *N*-acetate moiety were represented by a singlet at δ 3.79. Similarly the four protons of the spacer moiety showed up as multiplets at δ 2.76-2.79 and δ 3.30-3.33. An IR absorption band observed at 1680 cm^{-1} was assigned to the C=O stretching frequency. ESMS showed a peak at 520 mass units $(M+H)^+$.

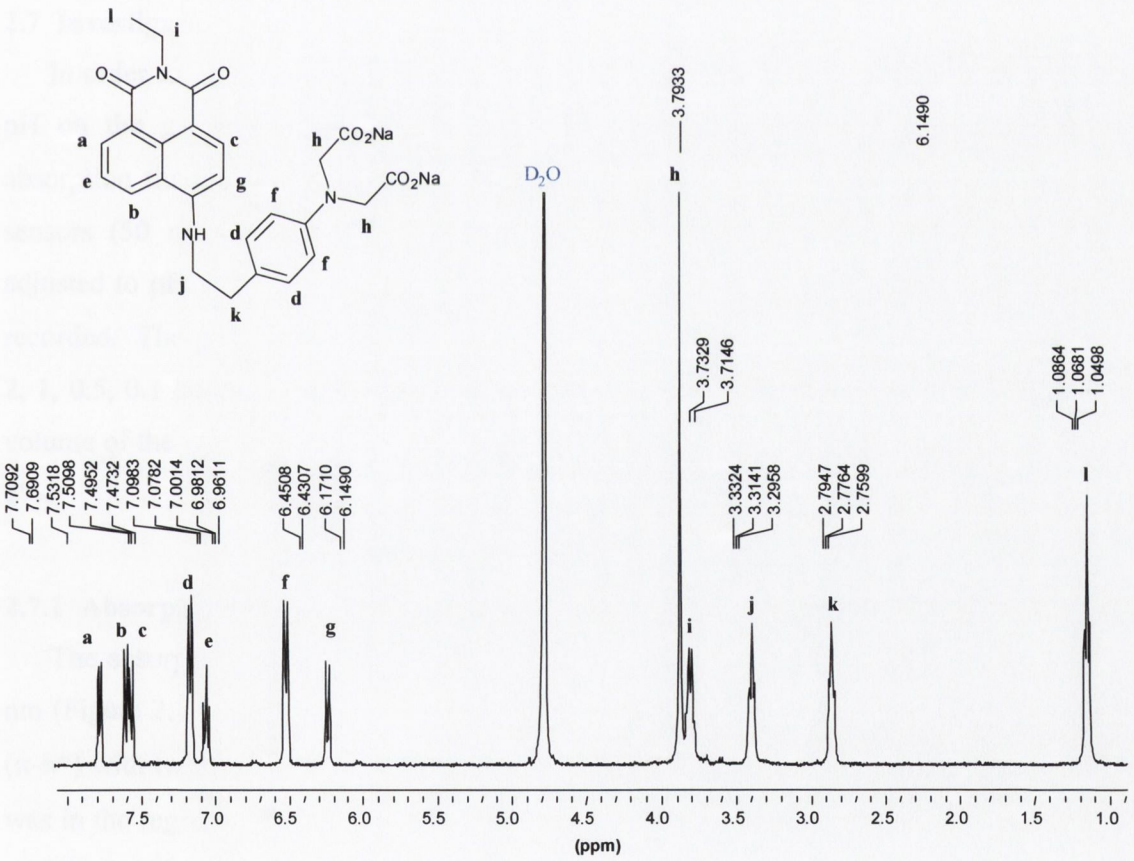

Figure 2.*10* ^{1}*H-NMR (DMSO-d_6, 400MHz) of sensor 93.*

2.6 Experimental methods for photophysical evaluation

All the solutions were prepared in deionised water. $ZnCl_2$, $CdCl_2$, and $HgCl_2$ (99 %) were used for preparing stock solution (1 M) of Zn(II), Cd(II) and Hg(II). Zn(II), Cd(II) and Hg(II) solutions of varying concentration were prepared by the dilution of an appropriate amounts of 1 M stock solution with deionised water. Absorption spectra were recorded on a Shimadzu diode array spectrophotometer under the control of a Pentium IV-based PC utilising the manufacturer supplied software package. Fluorescence spectra were recorded on a Varian spectrofluorimeter interfaced to the PC *via* an IEEE-488 (GPIB) card using Cary Eclipse software. Excitation was provided by a 150 W Xe lamp operating at a current of 5 A. Spectra were acquired in a 1x1 cm quartz cuvette (3 mL) using a slit width of 5 nm and a scan rate of 400 nm/minute. Both absorption and fluorescence spectra were acquired at room temperature. Data was analysed with either Microsoft Excel or Sigma Plot. pH values of the solutions were recorded with a calibrated glass electrode.

2.7 Investigation of the ground and excited state properties

In order to use **92** and **93** as chemosensors in the physiological pH range, the effect of pH on the ground and excited state properties was investigated. Fluorescence and absorption titrations were performed in the pH range 12–1.3. A 1 μM solution of both sensors (50 mL) containing 135 mM KCl (to maintain constant ionic strength) was adjusted to pH 12 by an appropriate amount of 2M KOH, and the UV-Vis spectrum was recorded. The pH was lowered in steps of $\Delta pH = 0.25$ with the appropriate amounts of 5, 2, 1, 0.5, 0.1 M HCl solutions, recording the absorption spectra at each pH interval. The volume of the solution was controlled such that the overall change in volume was less than 2%.

2.7.1 Absorption and fluorescence pH response of 92

The absorption spectrum analysis for **92** showed two main spectral regions above 200 nm (Figure 2.11, insert). The higher energy band was observed in the region 258-293 nm (π-π^*) with two absorption maxima of 259 nm and 284 nm. The lower energy broad band was in the region 350-520 nm (π-π^*) with absorption maxima at 450 nm, which gradually shifted to 430 nm with increasing acidity. The absorption intensity of the band at 259 nm was higher in acidic solutions. No regular pattern was observed between the absorption

intensity and the pH at this absorption maximum. The extinction coefficient at 450 nm was determined to be = 18.92×10^3 $M^{-1}cm^{-1}$.

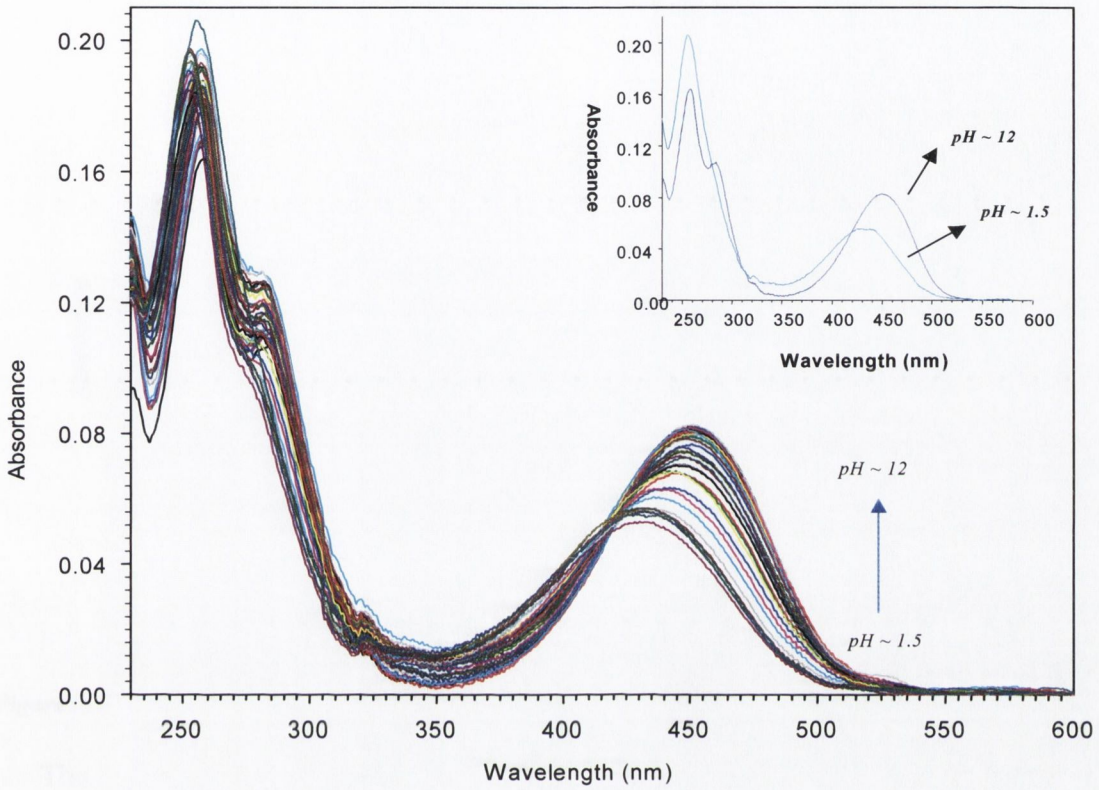

Figure 2. 11 ***Absorption spectra of 92 under basic and acidic conditions. Insert shows isosbestic point observed at 422 nm.***

The changes in absorption spectra during UV-Vis titration studies are shown in Figure 2.11. At low pH the spectra are hypsochromically shifted ($\Delta\lambda$ = 20 nm) with an isosbestic point at 422 nm. de Silva *et al.* also observed such hypsochromic shifts in related compounds utilising the same fluorophore.[29] The hypsochromic shift observed can be explained by considering the 'push-pull' mechanism operating in these molecules, which results in the ICT excited state (Scheme 2.3). The partial positive charge on the nitrogen atom attached to the naphthalimide ring creates a repulsive interaction with the protonated *N*-acetate moiety thus shifting the absorption spectra to lower wavelengths. The plot of absorbance at 450 nm against pH is shown in Figure 2.12. As can be seen there are negligible changes in the pH region 12-6.5. Minor changes are observed in the pH region 5-4, most likely due to the protonation of the water molecule bound to **92**. Maximum

absorption changes were observed in the pH region 4-2. The absorption reached saturation value at pH ~ 2. From these changes a pK_a value of 3.21 ± 0.1 was calculated, demonstrating a pH independent behaviour for **92** at physiological conditions.

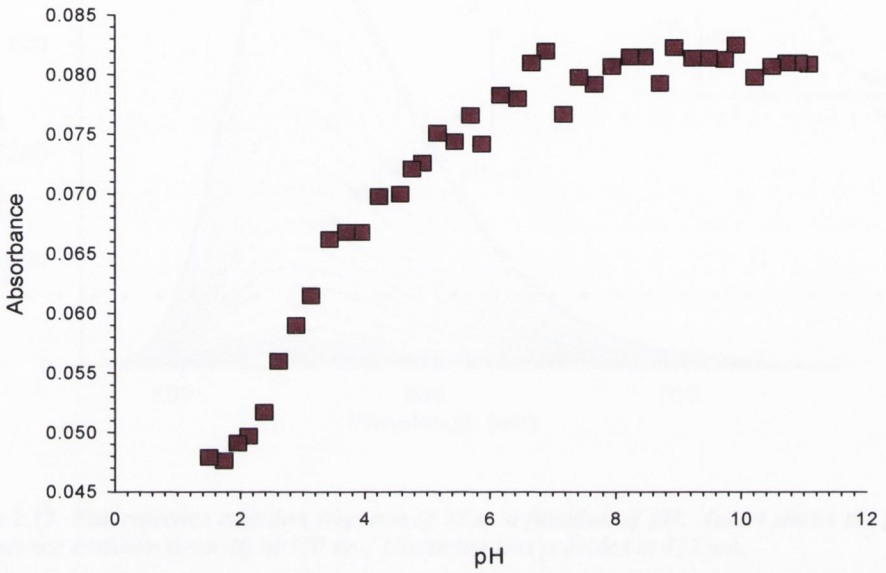

Figure 2.12 ***Absorption versus pH titration profile for 92. The changes are plotted at 450 nm.***

The fluorescence response was measured using excitation wavelengths of 422 nm (isosbestic point) and 450 nm and no shifts in the emission wavelengths were observed. The fluorescence pH titration was performed in the same manner as was for the absorption titration. The fluorescence emission spectrum in the pH range 12-1.3 is shown in Figure 2.13. In the basic solution at pH-12, the emission was switched '*off*' due to the electron transfer from the receptor to the fluorophore thus quenching the ICT excited state. In acidic solution, due to the protonation of the nitrogen moiety, the fluorescence was switched '*on*' with a fluorescence increase of more than 100 fold. A broad emission band extending from 500-650 nm with emission maximum at 550 nm was observed. As can be seen clearly from the Figure 2.13, there are no shifts in the emission wavelength. Thus, **92** can be considered as an ideal *'on-off'* PET chemosensor. A plot of the emission intensity changes corresponding to the emission maximum at 550 nm *versus* pH resulted in a sigmoidal curve (insert, Figure 2.13). The curve shows slight changes in the pH range 6-4.6, that might be due to the protonation-deprotonation of the water molecule bound to **92**, which is well documented.[189] Major changes were observed in the pH range 4.6-2.4.

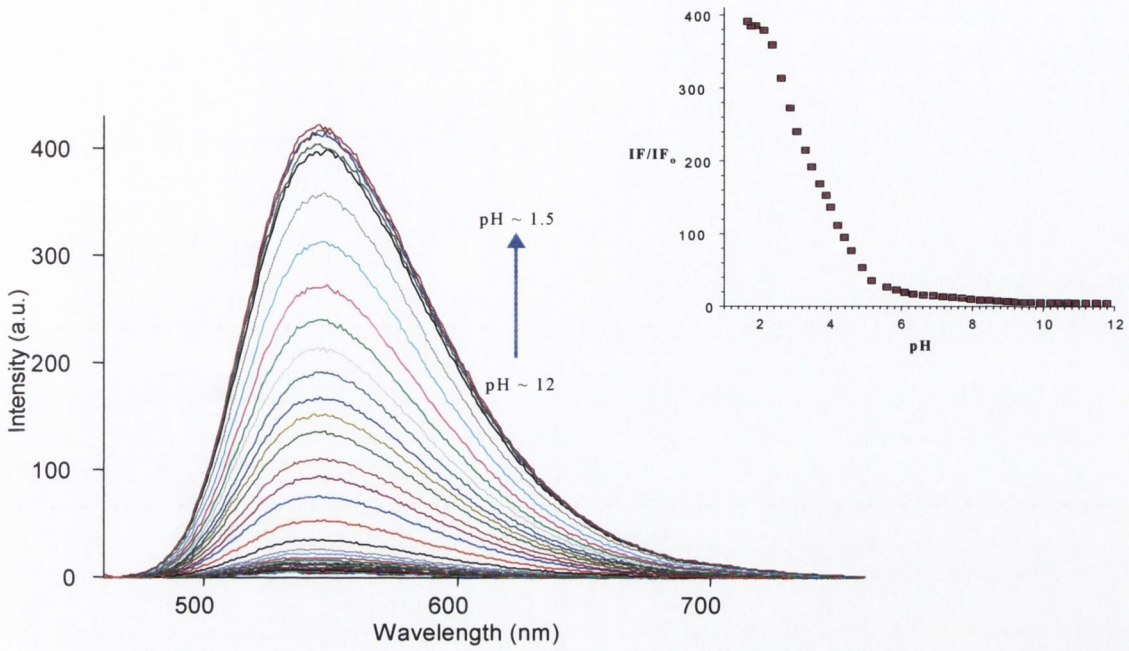

Figure 2.13 ***Fluorescence emission response of 92 as a function of pH. Insert shows the plot of relative fluorescence emission intensity at 550 nm. Excitation was provided at 422 nm.***

Fitting the data obtained from the fluorescence measurement into equation 2.1[20], resulted in a pK_a value of 3.20 ± 0.1 for **92** which is in close agreement with the value obtained from the absorption measurement.

$$\mathbf{pH = pK_a + Log[(IF_{max} - IF_{min})/(IF - IF_{min})]} \qquad \mathbf{(2.1)}$$

IF_{max} = maximum fluorescence intensity

IF_{min} = minimum fluorescence intensity

IF = fluorescence intensity at particular pH.

2.7.2 Absorption and fluorescence pH response of 93

The absorption response of **93** against pH is depicted in Figure 2.14. The main absorption band was observed at 453 nm ($\varepsilon = 20.1 \times 10^3$ $M^{-1}cm^{-1}$), with a lower intensity band at 306 nm. There was a slight decrease in the absorption intensity of both bands with decrease in pH, but surprisingly no hypsochromic shift was observed unlike that for **92**. This is because the receptor is separated from the fluorophore by an ethylene spacer, thus

the repulsive interactions are expected to be smaller. It was not possible to determine a pK_a value from the changes in the absorption intensity, as the slope of the curve was almost zero (Figure 2.14, insert).

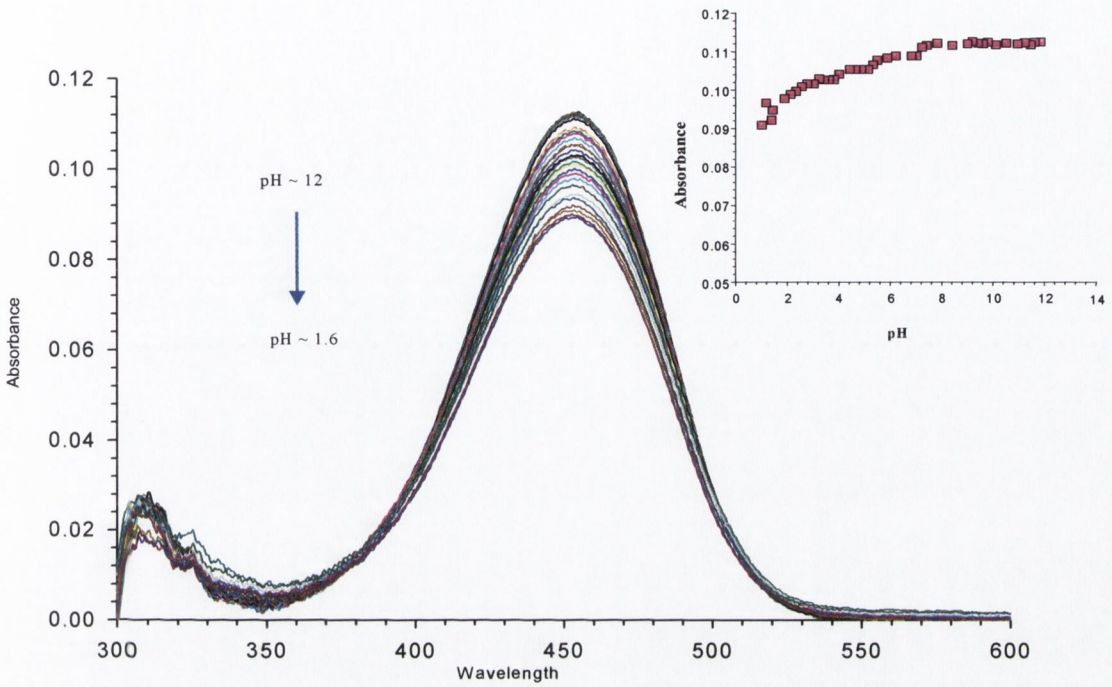

Figure 2. 14 ***Absorption spectra of 93 against pH. Insert shows the plot of absorption intensity at 453 nm versus pH.***

The fluorescence response of **93** as a function of pH was similar to that observed for **92**. The fluorescence emission was completely quenched in basic solution and was switched on with a dramatic fluorescent enhancement upon acidification. A broad emission band with emission maximum of 554 nm was observed upon pH titration on excitation at 453 nm with no shifts in the emission wavelength. The emission showed *'on-off'* characteristics (Figure 2.15). Plotting the emission intensity changes *versus* pH also results in the sigmoidal curve (insert, Figure 2.15). There appears to be two sigmoidal regions in the curve, one in pH range 4-3 and another in the range 3-1. However, the changes in the pH range 4-3 are negligible and may be due to the protonation-deprotonation of water molecules bound to **93** as described for **92**. The major fluorescence emission changes are in the region 3-1. Thus a simple equilibrium is still valid for **93**.

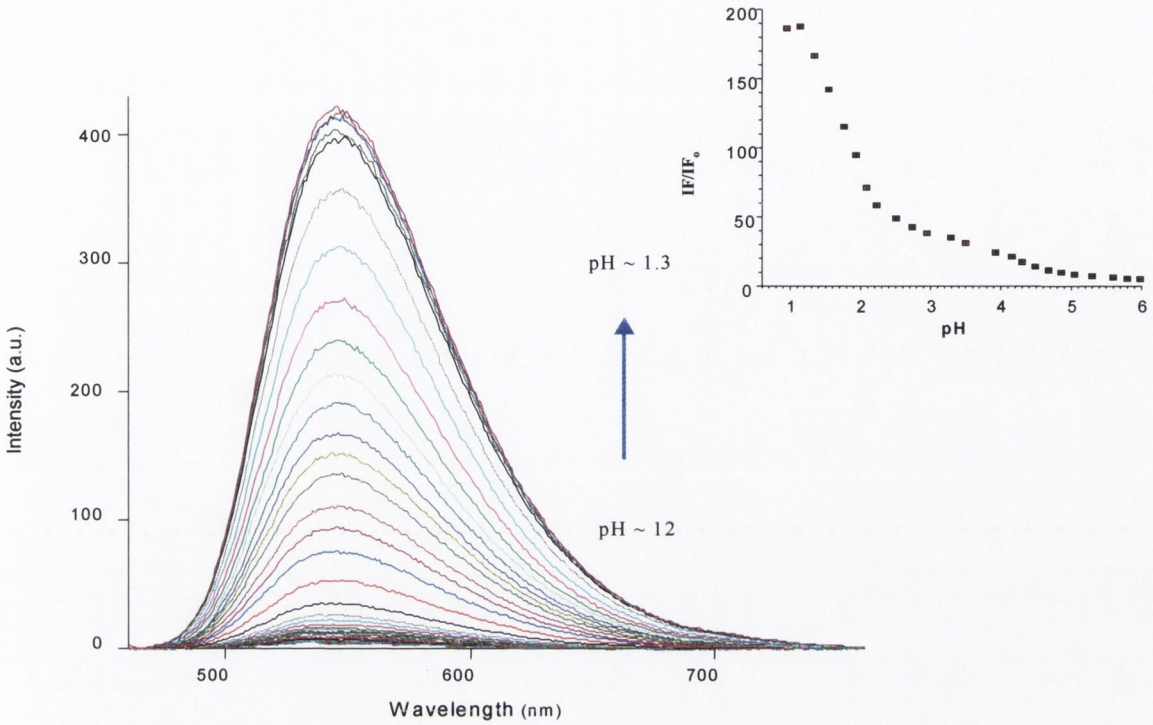

Figure 2.15 ***Fluorescence emission response of 93 as a function of pH. Excitation was at 453 nm. Insert shows the relative emission intensity plot at 554 nm versus pH.***

The pH changes fit to an apparent pK_a value of 2.10 ± 0.1, which is considerably less than that observed for **92**. This might be due to the electronic or conformational effects of the ethylene spacer. The spectral parameters and protonation constants obtained from the absorption and fluorescence studies for **92** and **93** are summarised in Table 2.5

Table 2.5 ***Protonation constant of 92 and 93. pKa and pKa* = protonation constant from absorption and fluorescence changes.***

Parameter	92	93
λ_{abs}	450 nm (basic conditions)	453 nm (basic conditions)
	430 nm (acidic conditions)	453 nm (acidic conditions)
λ_{em}	550 nm	554 nm
pKa	3.23 ± 0.1	2.10 ± 0.1
pKa*	3.20 ± 0.1	Not possible to determine

2.8 Photophysical evaluation of 92 and 93 with different metal ions

Both **92** and **93** were evaluated for fluorescence and absorption response with group 1, group 2 and transition metal ions (Zn(II), Cd(II), Hg(II), Cu(II), Co(II), Ni(II) and Fe(III)). No changes were observed with group 1 or group 2 metals even at the concentrations of 10^{-2} M. Among the transition metal ions, Cu(II), Fe(II) and Fe(III) did not result in any changes in fluorescence intensity. Minor changes were observed at higher concentrations ($\sim 10^{-2}$ M) of Co(II), Ni(II), Hg(II) and Cd(II). However, Zn(II) induced the dramatic changes in fluorescence emission intensity, indicating the sensitivity of **92** and **93** for Zn(II). Additionally, no changes were observed in the absorption spectra upon titration with all these metal ions. The fluorescence response with Zn(II) ions will be discussed in detail first followed by the response towards other metal ions.

2.8.1 Absorption and fluorescence response of 92 and 93 to Zn(II)

The absorption and fluorescence spectra were recorded mimicking the physiological conditions (20 mM HEPES, 135 mM KCl, pH 7.4). A 1 μM buffered solution (50 mL) of both sensors was prepared, and initial absorption and emission measurements were made. Zn(II) aliquots were added to give final metal ion concentrations of 1.2 nM,1.4 nM, 1.6 nM, 2.4 nM, 3.20 nM, 4 μM, 8 μM, 12 μM, 20 μM, 60 μM, 80 μM, 100 μM, 180 μM, 280 μM, .4 mM, 0.6 mM, 0.8 mM, 0.10 mM, 1.2 mM, 1.5 mM and the absorption and emission spectra were recorded at each addition. The data was exported into Microsoft Excel and analysed using Solver. Sigma Plot, a non-linear least square-fitting software was also used for regression analysis.

The absorption spectra of the compound **92** exhibited a low energy band with absorption maximum at 442 nm and higher energy bands at 250 nm and 293 nm (Figure 2.16). Upon addition of the increasing Zn(II) concentrations no significant changes were observed in the absorption spectrum. This clearly shows the weak interaction between the receptor and Zn(II) during binding and the insulating role of the methylene spacer which maintains the structural and electronic integrity of both the fluorophore and receptor. In contrast to H^+ addition, no shift in the position of the 442 nm band was observed for **92** upon titration with Zn(II). Grabchev *et al.* have observed hypsochromic shifts in the absorption spectra of the compounds **40** and **41** as discussed in Chapter 1, which was explained by the interaction between metal ion and fluorophore.[59]

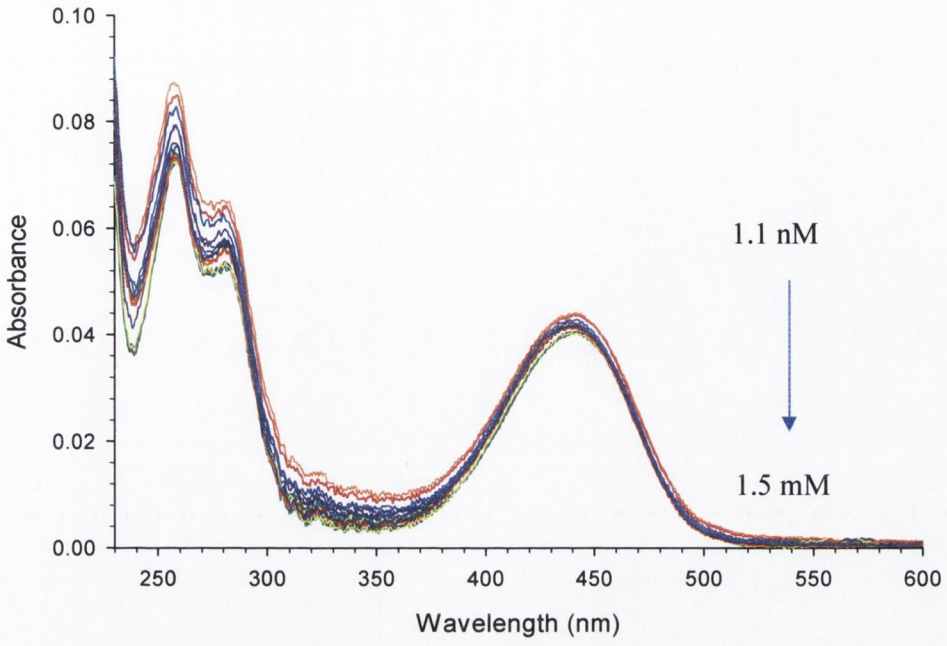

Figure 2.16 ***Absorption spectra response of 92 towards increasing concentration of Zn(II) Spectra were recorded in HEPES buffer at pH 7.4.***

The corresponding fluorescence spectra observed during the Zn(II) titration are shown in Figure 2.17. The spectrum of free sensor almost overlaps with the X-axis indicating the quenching of the ICT excited state by electron transfer from receptor as discussed earlier. Upon the addition of Zn(II), the fluorescence is gradually switched *'on'*. A fluorescence increase of 120- fold was observed, with no shifts in emission wavelength, supporting the earlier observation that Zn(II) is not interacting with the fluorophore. Plotting the fluorescence emission intensity *versus* pZn [= -logZn(II)] resulted in a sigmoidal curve (insert, Figure 2.17). There were some minor changes in the fluorescence at the pZn range of 6-7. This might be due to the exchange of the Zn(II) bound water molecule in **92**. The major changes in the fluorescence emission intensity occurred in the region of pZn(II) 5-3. The pZn changes over two units in this range. Thus it can be assumed that Zn(II) binding follows the simple equilibrium process with stoichiometry of 1:1 (Ligand:Metal). This was further supported by Hill plot data when **92** was titrated with free Zn(II), where a Hill coefficient of 1.05 was determined (Section 2.9.1). A binding constant (log β) of 3.9 ± 0.1 was determined from the emission intensity changes, using least square regression analysis.

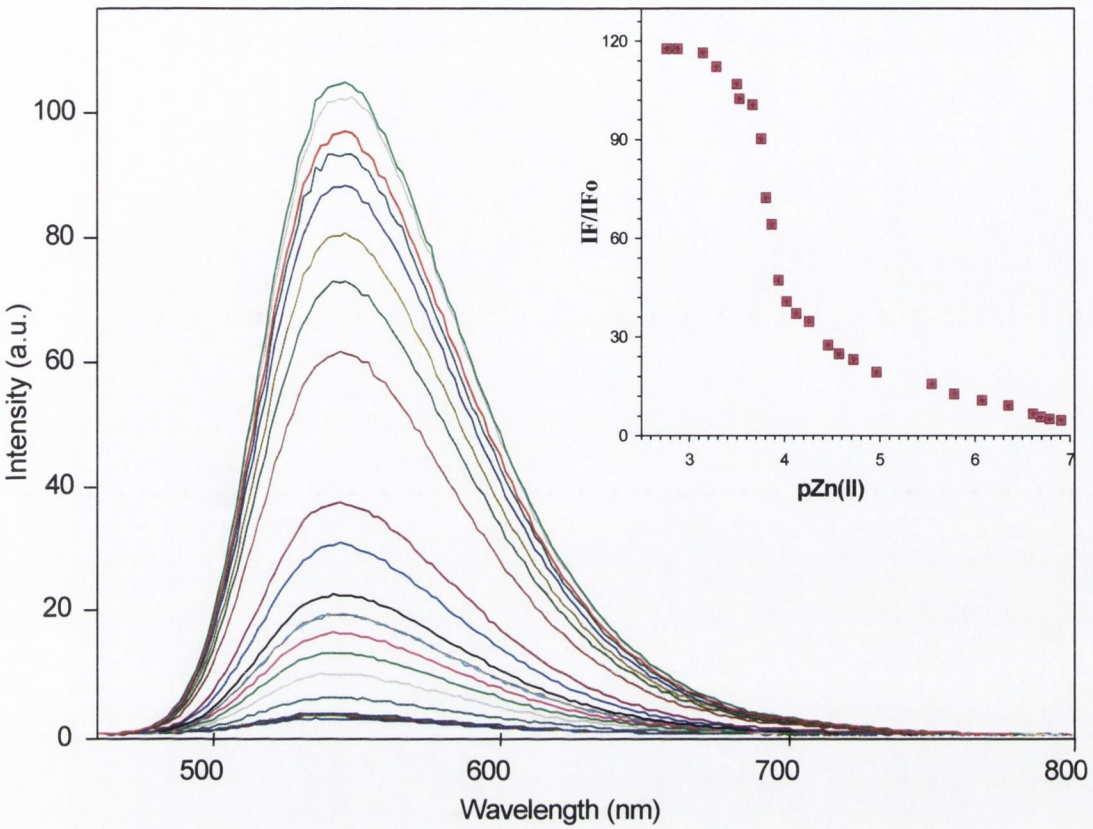

Figure 2.17 ***Fluorescence emission response of 92 as a function of pZn. Excitation was at 422 nm. Insert shows the relative emission intensity plot at 550 nm versus pZn.***

The free sensor **92** has a quantum yield of ~ 0.004 which increased to 0.21 in presence of 5 μM Zn(II). A FE (Φ_{bound}/Φ_{free}) of 56- fold was observed upon Zn(II) binding. The extinction coefficient (ε) of the sensor was calculated to be 18.919×10^3 $M^{-1}cm^{-1}$. Thus the brightness (ε x Φ) of the Zn(II) bound sensor is (1.01×10^6 Int $M^{-1}cm^{-1}$).

The absorption titrations for **93** with increasing amounts of Zn(II) were performed in a similar manner as described for **92**. The absorption spectra exhibits higher energy bands in the region 250-300 nm and a prominent lower energy band at 453 nm (Figure 2.18). Upon addition of the Zn(II) negligible changes were observed in the absorption intensity. In addition, no shifts in the absorption wavelengths indicates that Zn(II) was not interacting with the naphthalimide fluorophore for **93** (Figure 2.18).

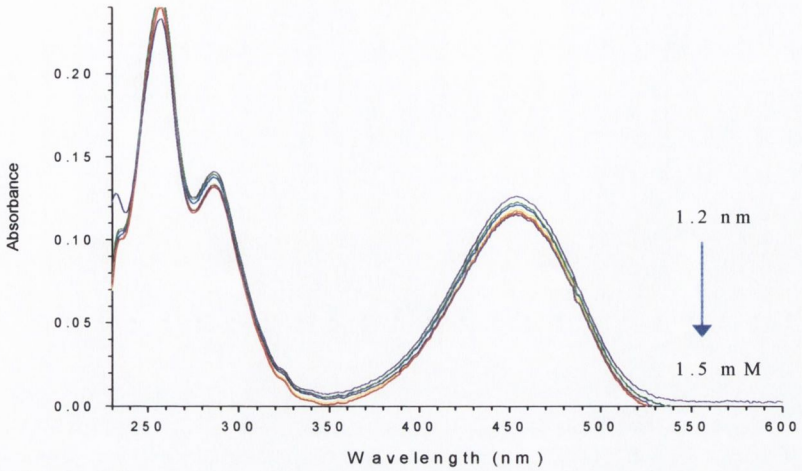

Figure 2.18 ***Absorption response of 93 with increasing Zn(II).***

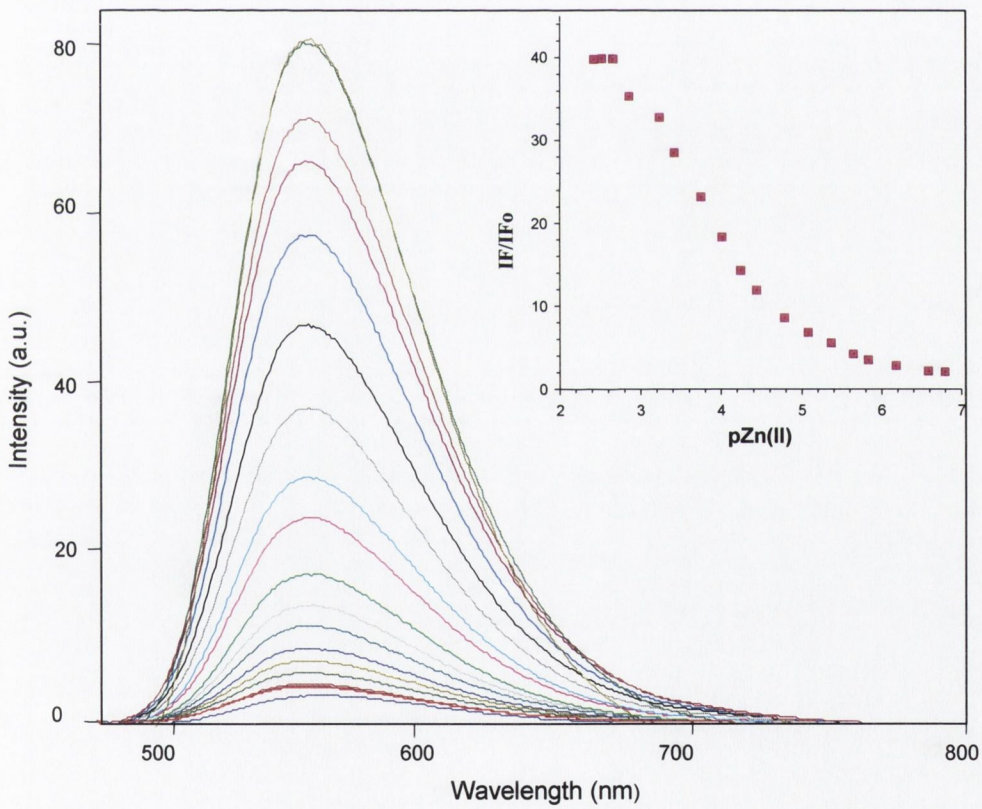

Figure 2.19 ***Fluorescence emission response of 93 as a function of pZn. Excitation was at 453 nm. Insert depicts the plot of relative emission intensity plot at 553 nm versus pZn.***

The fluorescence response of **93** to Zn(II) was similar to that observed for **92**. A broad emission band with emission maximum at 554 nm was observed upon excitation at 453 nm. A fluorescence increase of only 40-fold was observed upon titration with Zn(II), which is slightly less that that seen for **92**. This is most probably due the increased length of the spacer unit. As in the case of **92**, no shifts were observed in the emission wavelength. The plot of relative emission intensity changes *versus* pZn was a sigmoidal curve (insert, Figure 2.19). From these changes a log β of 4.0 ± 0.1 was calculated. The changes in the emission intensity suggest a simple equilibrium and most probably 1:1 binding. The free sensor **93** has a quantum yield of ~ 0.007 which increased to 0.14 in the presence of a saturating amount of Zn(II) (5μM). A fluorescence quantum yield enhancement (Φ_{bound}/Φ_{free}) of 20-fold was observed upon Zn(II) binding. The extinction coefficient (ε) of the sensor was calculated to be 20.1×10^3 $M^{-1}cm^{-1}$. The brightness (ε x Φ) of the Zn(II) bound sensor is (4.02×10^5 Int $M^{-1}cm^{-1}$). The binding constant and quantum yield determined for Zn(II) titrations of **92** and **93** are summarised in the Table 2.6.

Table 2.6 ***Binding constant and quantum yield of 92 and 93 for Zn(II) titrations***

Parameter	92	93
log β	3.9 ± 0.1	4.00 ± 0.1
Φ(bound)	0.21	0.14

2.8.2 Titration response with other metal ions

2.8.2.1 Titration response of 92 and 93 with group 2 metal ions

The fluorescence and absorption response of **92** and **93** to Ca^{2+} and Mg^{2+} were investigated. The addition of Ca^{2+} and Mg^{2+} did not lead to any changes in either absorption or fluorescence spectra of the two sensors, even at higher concentrations of these metal ions (10^{-2} M). Using higher concentrations (10 μM) of **92** and **93** also did not lead to any changes in the fluorescence emission. The fluorescence emission response of **92** to the Ca^{2+} is depicted in Figure 2.20 (A) while the fluorescence emission intensity spectra of **93** upon addition of Ca^{2+} is illustrated in Figure 2.20(B). As can be seen from the emission intensity plot, there are no changes in emission intensity even at higher

concentrations of Ca^{2+} indicating that the metal ion is not coordinating to the receptor. Similar results were obtained for Mg^{2+}.

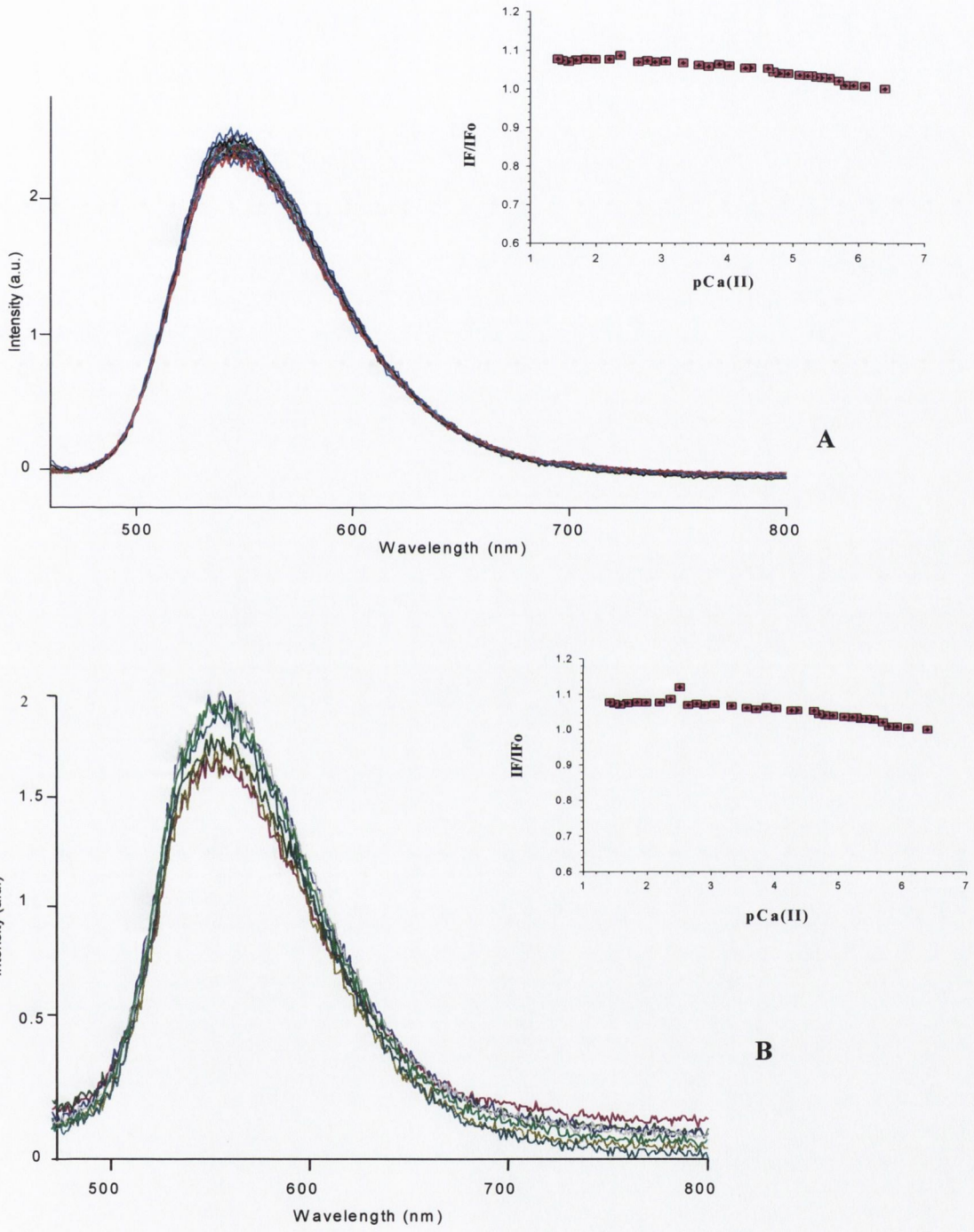

Figure.2.20 ***Fluorescence emission response of 92(A) and 93(B) upon Ca^{2+} addition. Excitation was at 442 nm for 92 and 453 nm for 93. Insert shows the emission intensity plot at 550 nm for 92 and 554 nm for 93.***

2.8.2.2 Absorption and fluorescence response of 92 and 93 towards Cd(II) and Hg(II)

The addition of Cd(II) and Hg(II) did not lead to any changes in the absorption spectra of **92** or **93**. Also, no shifts were seen in the absorption maxima indicating that these ions are not interacting with the fluorophore (Figure 2.21).

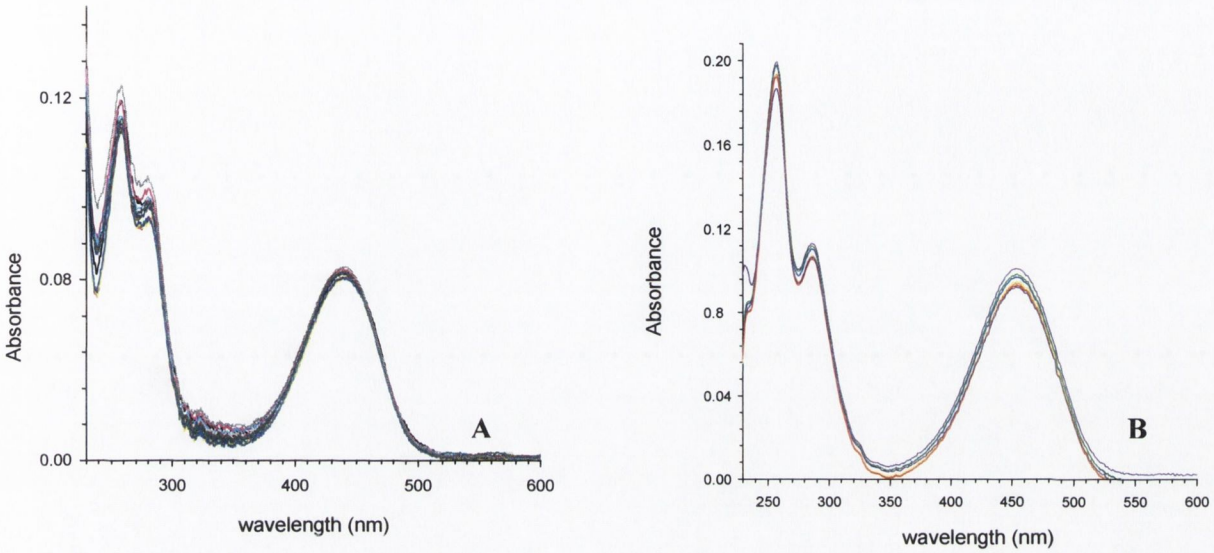

Figure 2.21 ***Absorption response of 92 (A) and 93 (B) as a function pCd.***

The fluoresence titration of **92** with Cd(II) lead to a 10-fold increase in fluorescence (Figure 2.22). Plotting relative fluorescence intensity changes *versus* pCd resulted in a sigmoidal curve. The changes in fluorescence suggest 1:1 binding. From these changes a log β of 2.0 ± 0.1 for the **92**-Cd(II) complex was determined. This is much lower than that observed with Zn(II). For **93** even higher concentrations of Cd(II) were required for an increase in the fluorescence intensity to be observed. The fluorescence emission response of **93** to Cd(II) titration is shown in Figure 2.23. There are virtually no changes even at a higher Cd(II) concentration of 10^{-2} M. A slight increment in the emission intensity was observed for Cd(II) at a concentration range of 10^{-2} M – 2.24 × 10^{-2} M. Plotting these changes resulted in a sigmoidal curve (insert, Figure 2.23). The changes can be approximated to a simple 1:1 binding equilibrium and from the data analysis a log β of 1.8 ± 0.1 was determined. It can be concluded that both these sensors show minor changes with Cd(II). As the concentration of Cd(II) in the body is low (except in cases of Cd(II) poisoning), it will not interfere in the measurement of the Zn(II) ions in important organ such as the pancreas and brain.

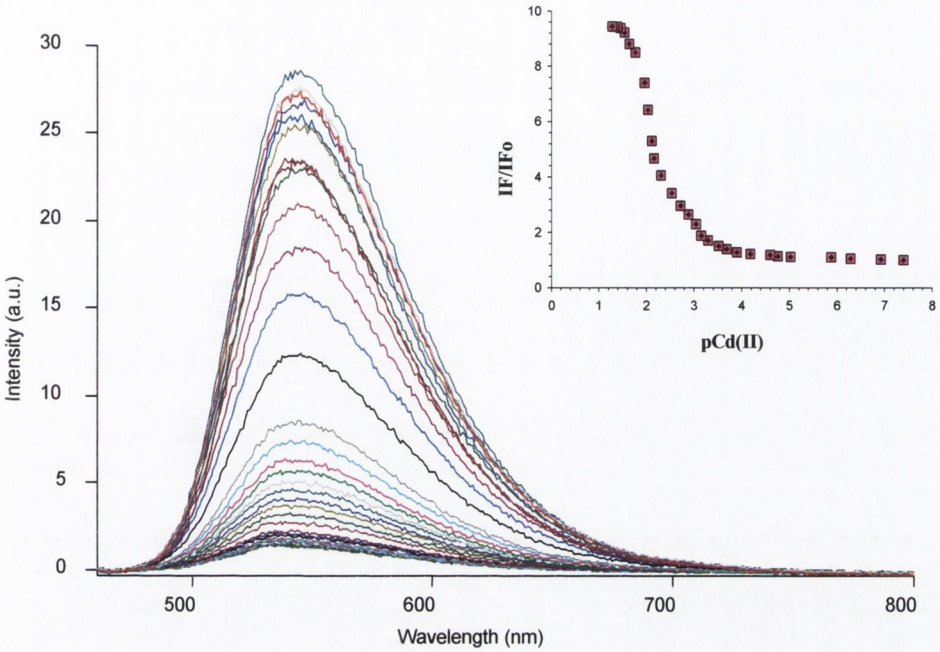

Figure 2.22. ***Fluorescence emission response of 92 to Cd(II). Insert shows the relative emission intensity plot at 550 nm versus pCd(II).***

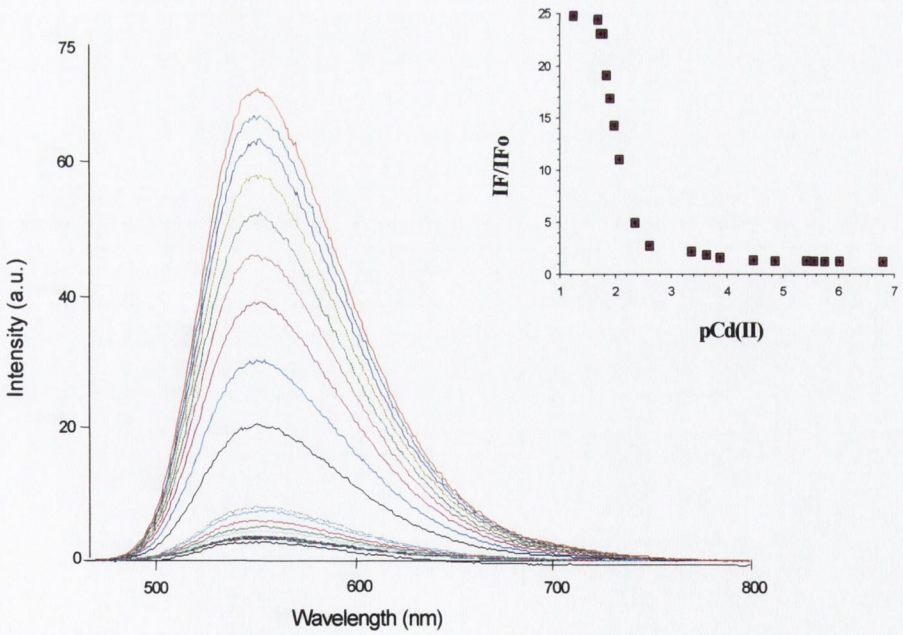

Figure 2.23 ***Fluorescence emission response of 93 to Cd(II). Insert shows the relative emission intensity plot at 554 nm versus pCd(II).***

The absorption and fluorescence responses of **92** towards Hg(II) were also investigated. The response behaviour towards Hg(II) was negligible and mirrored the Cd(II) response. There was no change in the absorption spectra upon titration with Hg(II). The fluorescence emission intensity does increase with Hg(II) addition at higher concentrations (10^{-2} M). The fluorescence response of **92** upon Hg(II) titration is shown in Figure 2.24. As can be seen there are insignificant shifts in the emission wavelength indicating that Hg(II) does not perturb the excited ICT state of the fluorophore. A fluorescence increase of 4- fold was observed on titrations of **92** with Hg(II).

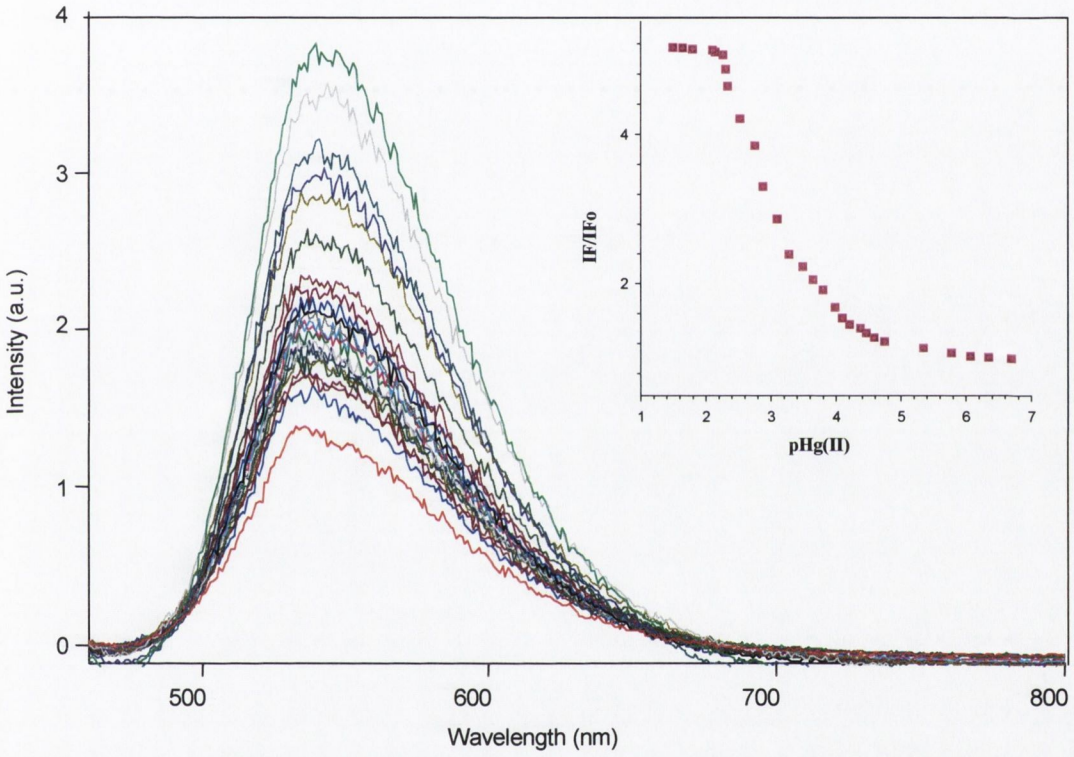

Figure 2.24 ***Fluorescence emission response of 92 to Hg(II). Insert shows the relative emission intensity plot at 554 nm versus pHg(II).***

A plot of relative fluorescence emission intensity *versus* pM for various metal ions is shown in Figure 2.25 for sensor **92.** As can be seen clearly the fluorescence response of **92** towards Zn(II) was very high thereby indicating the selectivity and sensitivity of this sensor towards Zn(II).

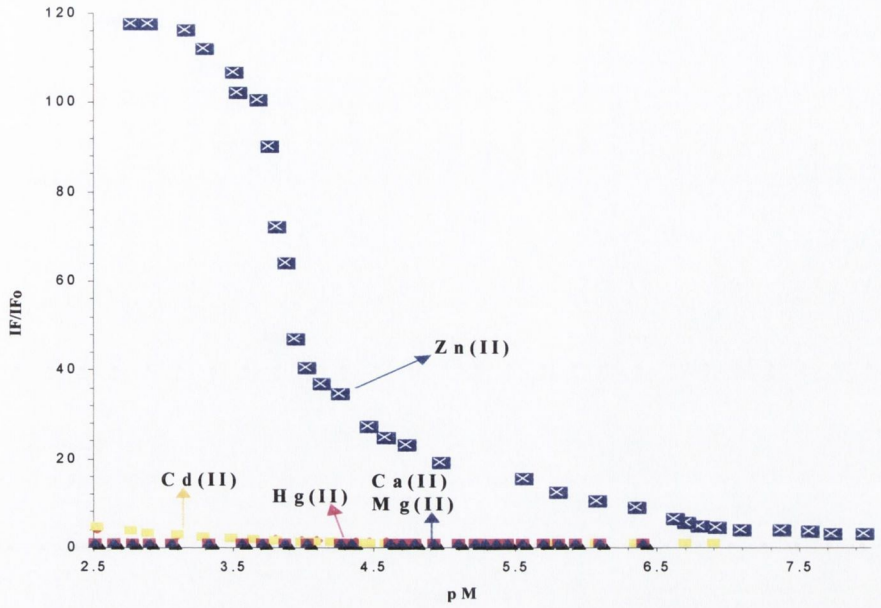

Figure 2.25 ***Normalised fluorescence emission intensity plot of 92 versus the concentration of Zn(II), Cd(II), Hg(II), Ca^{2+} and Mg^{2+}. pM= -Log [M], M= Zn(II), Cd(II), Hg(II), Ca^{2+}, Mg^{2+}. IF = fluorescence intensity at particular metal ion concentration IF_o = fluorescence intensity at zero metal ion concentration. All the titrations were performed in HEPES buffer. Excitation was at 422 nm.***

The results obtained in the fluorescence titrations of **92** and **93** with various metal ions can be summarised as follows:

- no changes were observed for both group 1 and group 2 metal ions. It can be argued that Ca^{2+} and Mg^{2+} requires a larger coordinating sphere for complexation and hence prefer BAPTA rather than the phenyliminodiacetate chelators.

- only small changes were seen in the fluorescence spectra at high concentration upon titration with Cd(II) and Hg(II) compared to that observed for Zn(II). As both Zn(II) and Cd(II) have completed d-energy levels, no ligand field stabilisation effects are observed. Thus, the geometry of the complex is simply governed by size, electrostatic forces and supramolecular interactions. However, the larger size of Cd(II) makes it more likely to prefer octahedral coordination, which explains the weak complex formation with **92** and **93**. As Zn(II) prefers 4 or 5 coordination (Figure 2.1), it shows a stronger binding affinity with the ligands **92** and **93**.

2.8.2.3 Competitive analysis of fluorescence response with different metal ions

The fluorescence titrations of **92** with Zn(II) were performed in the presence of other metal to investigate the selectivity towards Zn(II). A 1 μM solution of **92** was prepared in HEPES buffer consisting of 20 mM HEPES, 135 mM KCl at pH 7.4. Aliquots of concentrated stock solutions of each metal ion were added to provide a solution consisting of 5 μM total metal ion and fluorescence spectra recorded (Figure 2.26). The results obtained can be summarised as follows:

- the fluorescence response of **92** to Zn(II) in the presence of Ca^{2+} and Mg^{2+} was similar to that observed in their absence. This clearly indicates that **92** has no affinity for the group 2 metals
- Cd(II), Hg(II), Co(II) and Ni(II) addition lead to an increased fluorescence emission but when the Zn(II) was added the emission increased further. This behaviour is expected as Zn(II) shows better binding ability.

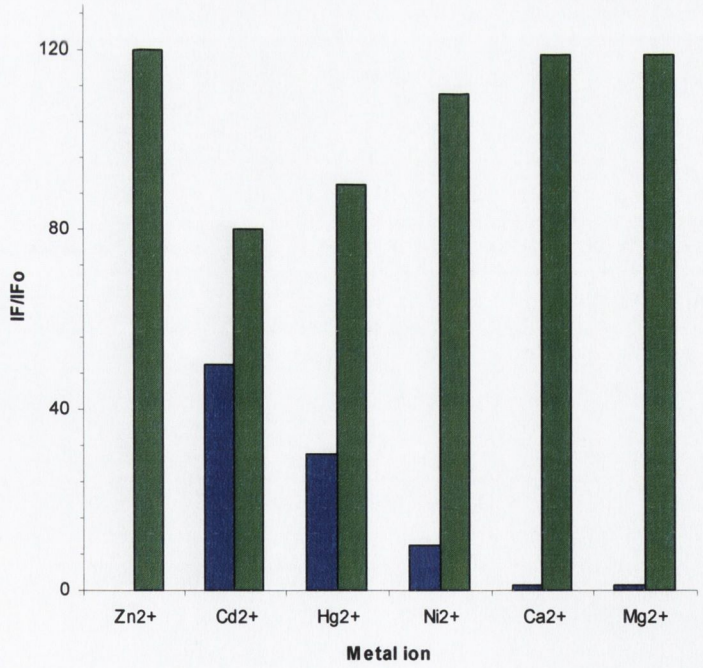

Figure 2.26. ***Fluorescence response of 92 to various metal ions. Bars represent the relative fluorescence intensity. Excitation was provided at 422 nm and changes plotted at an emission wavelength of 550 nm. Blue bar represent the emission without Zn(II) for a particular metal ion. Green bars (except the first one) represent the emission upon addition of Zn(II) to respective metal ion.***

2.9 Preliminary biological application of 92 for Zn(II) detection in pancreatic tissues

The pancreas is an important organ, responsible for the production of the hormone insulin.[92] 99% of the pancreatic tissue is made up of clusters of gland cells, known as pancreatic acini. These glands are involved in the digestion process through their various enzymatic secretions. The pancreatic islets, or *the islets of Langherhans*, make up the remaining 1% of the pancreatic tissue and consist of four major cell types- alpha, beta, delta and F.[92] Beta cells are involved in both insulin production (for glucose metabolism) as well as storage.[92,190] Inside these beta cells the insulin is initially produced as a single chain peptide, which stabilises itself on folding due to inter-chain disulfide linkages.[190,191] This proinsulin is finally converted into insulin monomers that consist of two peptide chains - alpha and beta - each consisting of 51 amino acids residues.[192] These two chains are linked to each other by disulfide linkages. In the presence of Zn(II) inside the cells, the monomer is converted to its dimeric form.[193] The dimeric form undergoes further assembly and forms a stable hexamer consisting of three dimeric units linked to two Zn(II). It is this form (2-Zn(II)-hexamer),which is stable and predominant inside beta cells. It is clear that Zn(II) plays an important role in both structural and functional aspects of insulin.[192]

Whenever there is an injury or external stimuli of any kind (for example a high glucose concentration), exocytosis occurs from these beta cells and insulin is released into the extracellular spaces.[193] In order to be active for metabolism the insulin must dissociate from Zn(II) to is biologically active insulin monomer.[193] This creates a large pool of chelatable loosely bound Zn(II) in the extracellular spaces surrounding beta cells. It was reasoned that by utilising **92** it would be possible to histologically visualise these extracellular spaces as the sensor binding to free Zn(II) would result in fluorescence intensity increases. This could be detected using epifluorescence microscopy as described in Section 2.3. These studies will provide new insights into the mechanistic aspects of insulin as defects in insulin production and release have been linked to type II diabetes.[141] Thus the rationale behind this investigation were two fold:

- to generate free Zn(II) and observe the fluorescence response of **92** for Zn(II)
- to utilise **92** as histological stain for Zn(II) detection in the pancreas.

2.9.1 Fluorescence response of 92 towards free Zn(II) ions

It is impossible to produce the free zinc in normal buffered solutions so ethylene glycol tetra acetic acid (EGTA) was used. The reaction between EGTA and Zn(II) can be represented by equation 2.2

$$\mathbf{Zn(II) + EGTA \rightarrow [Zn - EGTA]} \qquad \mathbf{(2.2)}$$

The dissociation constant (K_d) in terms of free zinc concentration ($[Zn(II)_f]$) can be shown as:

$$\mathbf{K_d = \frac{[Zn(II)_f][EGTA]}{[Zn - EGTA]}} \qquad \mathbf{(2.3)}$$

As it is possible to prepare Zn(II) and EGTA solutions of known concentrations accurately, ($[Zn(II)_f]$) can be easily obtained from equation 2.3. A buffered solution containing 135 mM KCl, 20 mM HEPES, 1.1 mM EGTA was prepared and the pH adjusted to 7.4. A 1μM solution of **92** was prepared in this buffer and to this was added varying amount of 1mM $ZnCl_2$ solution to give free Zn(II) concentrations of 1, 3, 5, 9, 12, 20, 30, 45, 80, 90, 100, 120, 140, 160, 200, 220, 240 and 280 nM. The fluorescence and absorption spectra were recorded at each addition. As described earlier (Section 2.8.1), there was no change in absorption intensity as well as any shifts in the absorption wavelength. The fluorescence emission response was switched 'on' with fluorescence increase of almost 140- fold (Figure 2.27). A plot of fluorescence response *versus* free Zn(II) concentrations is shown in Figure 2.28. Using equation 2.4, a K_d can be obtained as shown below:

$$\mathbf{[Zn(II)f] = K_d \times (IF - IF_{min}) / (IF_{max} - IF)} \qquad \mathbf{(2.4)}$$

where IF, IF_{max}, and IF_{min} are the fluorescence intensity values obtained with an excitation wavelength of 422 nm at each $[Zn(II)_f]$, at $[Zn(II)_f]$= 0, and at saturating $[Zn(II)_f]$ respectively. A K_d was obtained by plotting the log $[(IF - IF_{min}) / (IF_{max} - IF)]$ versus the log of free Zn(II). This plot gives an x-intercept (Log K_d) of 8.34, therefore K_d = 4 nM. The concentration of free Zn(II) can reach levels as high as 1mM in the pancreas, which clearly demonstrates that **92** could potentially be used for the detection of free or chelatable Zn(II) in pancreatic tissues.

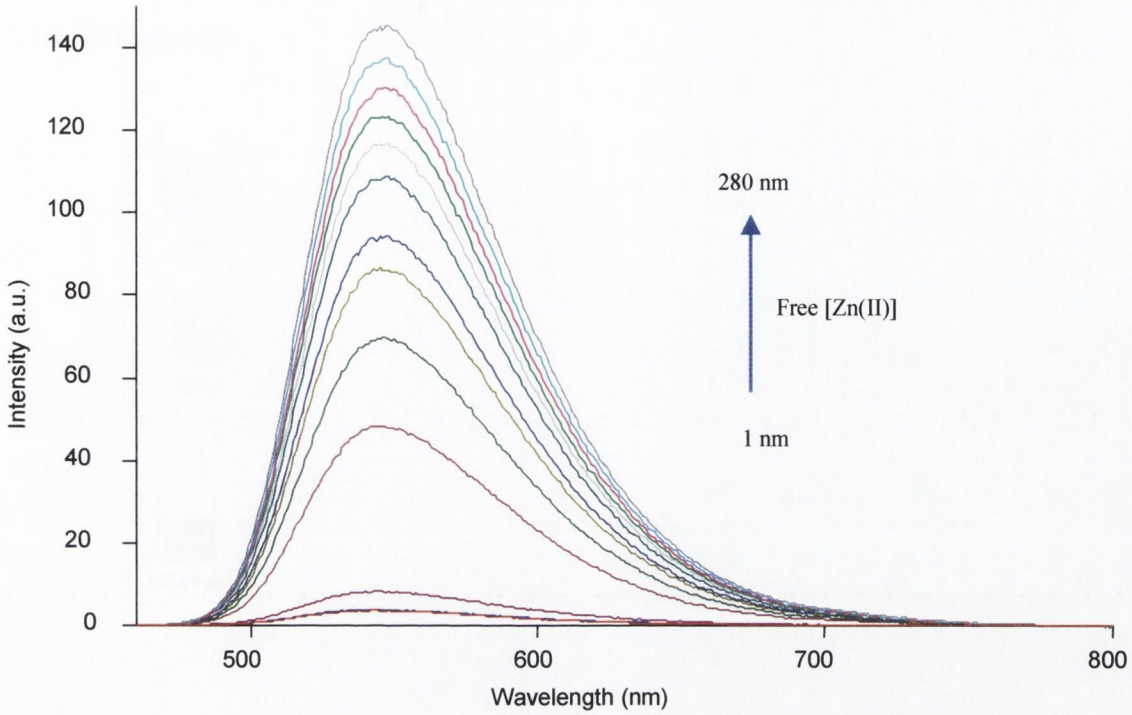

Figure 2.27 ***Fluorescence emission response of 92 to free Zn(II). Excitation was at 442 nm. Free Zn(II) was generated by an equilibrium between buffered EGTA and $ZnCl_2$ as described in the text.***

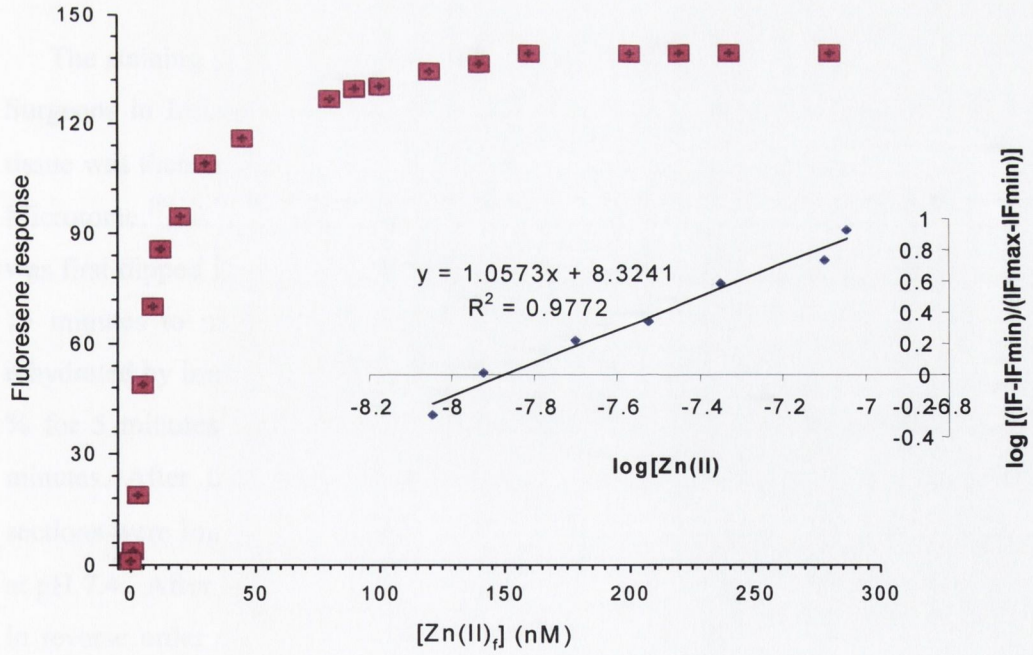

Figure 2.28 ***Changes in the fluorescence emission of 92 (1 μM) at 550 nm as a function of free Zn(II). Insert shows the corresponding Hill plot.***

2.9.2 Protocol for histological staining of pancreas tissues

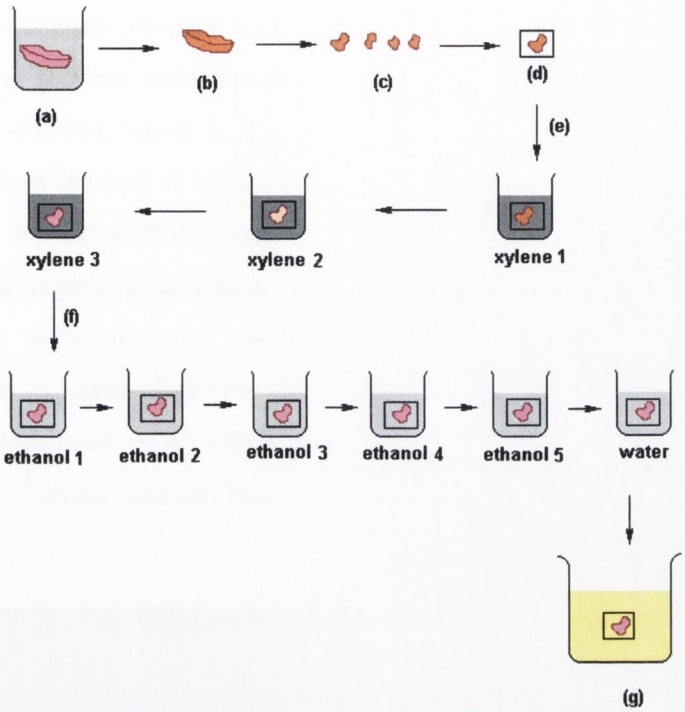

Figure 2.29 ***Schematic illustration of staining protocol followed for the pancreas tissue: a= pancreas tissue in formalin; b= wax embedding; c= section cutting; d= mounting on glass slide; e= cleaning stages using xylene solution; e= hydration stage using ethanol-water mixture; g= final staining with 92.***

The staining studies were carried out in the Department of Anatomy, Royal College of Surgeons in Ireland. Human pancreas tissue was initially fixed in 10% formalin. The tissue was then embedded in paraffin wax. and cut into thin sections of 30-50 μM using a Microtome.[194] A staining protocol was followed from a published procedure.[194] The tissue was first dipped into three different solutions of pure clearing agent (xylene) for 5, 10 and 15 minutes to make the tissue more transparent and clear. The cleared sections were rehydrated by immersing them into graded solutions of alcohol starting from absolute to 50 % for 5 minutes each. Finally, thin sections were dipped into pure water for 5 more minutes. After this protocol was finished, the glass slides containing pancreas tissue sections were immersed for 10 minutes in a bath containing 5 μM buffered solution of **92** at pH 7.4. After this procedure was complete, the earlier protocol was again followed but in reverse order to rehydrate and clear, starting first with pure water and going through various graded solutions of alcohol right up to the xylene solutions. The glass slide was mounted with a cover slip and viewed under a green epifluorescence (546 nm) microscopy. The procedure is schematically shown in Figure 2.29.

2.9.3 Results and discussion

The sensor **92** was able to label portions of the tissue green which might be due to the formation of chelate complex with the Zn(II) ions. The control tissue section (without any stain) and the sections stained with **92** are depicted in Figure 2.30. The control appears as dull green coloured, which is due to autofluorescence from proteins and light scattering. Tissue sections marked in black boxes emit green fluorescence. These portions are most likely to be the extracellular space surrounding the beta cells. It is hypothesised that the tissues sections process acts as a stimulus for the exocytosis of insulin from the beta cells. The insulin accumulates in the extracellular spaces and dissociates to releases zinc. Figlewicz *et al.* have observed the accumulation of zinc granules in these extracellular spaces.[195] Lukowiak *et al.* employed Newport Green **78**, for the histological labelling of labile zinc in human pancreas beta cells.[196]

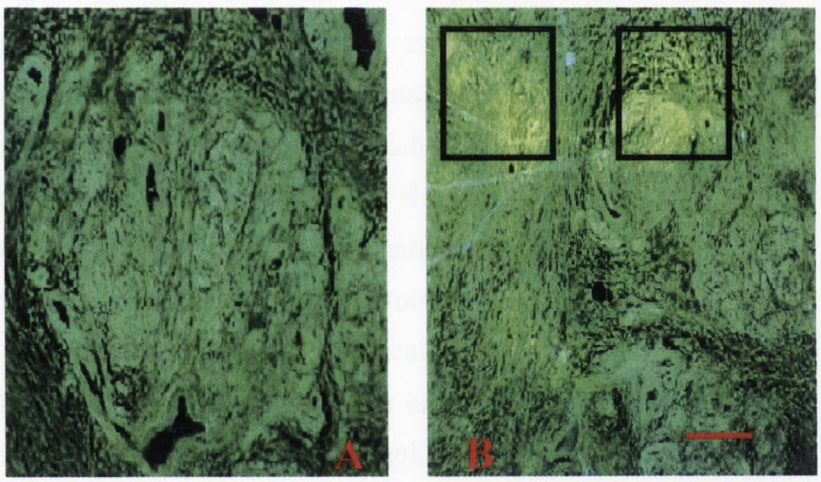

Figure 2.30 ***Pancreas tissue slices stained with 92: (A) control with no stain; (B) section stained with 92. Bar represents= 100 μm. Black boxes indicates the area of staining.***

This staining method gives vital information about the properties of **92** and its practicability for tissue staining *in vitro*. However, more rigorous analysis is needed for an *in vivo* biological application of **92.** Single-cell experiments whereby the beta cells are perturbed by external stimuli (such as glucose) inducing exocytosis accompanied by secretion of insulin, will provide vital insights into the mechanism of binding as well as the fluorescent imaging response of these dyes. Unfortunately, technical difficulties have so far prevented the single-cell confocal imaging experiments.

2.10 Conclusions and future work

Two novel Zn(II) sensors have been designed, synthesised and characterized. The sensors were synthesised in a few high yielding steps. This allows for the efficient preparation of **92** and **93** for biological applications. These sensors demonstrated good selectivity and sensitivity for Zn(II). No interference was observed with physiologically important metal ions such as Ca^{2+} and Mg^{2+}. The main competitor of Zn(II), Cd(II), can bind to **92** and **93** at higher concentrations (10^{-2} M). In the body, the concentration of Cd(II) is very low unless poisoning has occurred. This makes **92** and **93** useful sensors for the practical application of Zn(II) recognition. The key feature of sensors **92** and **93** is the presence of the phenyliminodiacetate receptor, which, due to the presence of the aromatic nitrogen atom avoids the 'false positive' fluorescence response due to protonation. As the background fluorescence from the free fluoroprobes is considerably small, both **92** and **93** are more sensitive than the contemporary sensors. Also, the use of the 4-aminonaphthalimide fluorophore has many attractive features such as a high aqueous quantum yield and large Stokes' shift, as well as not being sensitive to pH in a physiological environment. This is advantageous for the application of these sensors in cell organelles such as lysosomes in which the pH can reach a value of ~ 5.[172] The fluorescence titration of **92** involving the single-ligand EGTA buffer system has clearly demonstrated the application of **92** for nanomolar free Zn(II) detection. Preliminarily studies carried out for chelatable Zn(II) detection in pancreatic beta cells have shown some promising results as **92** was able to specifically label area which are most likely to contain granular chelatable zinc. Sensor **93** with an ethylene spacer unit would be particularly more biocompatible as this spacer length imparts high thermal and photochemical stability.[45,46] Future work in this area will involve the use of these sensors for understanding the role of Zn(II) in apoptosis.

CHAPTER - 3

Anthracene Based Fluorescent Sensors for Selective Detection of Cadmium

3.1 Introduction

Cadmium has a low abundance in nature (0.1-0.5 ppm) and is obtained by the extraction of ores such as sphalerite.[197] Cadmium levels as high as 500 ppm have been reported to accumulate in sedimentary rocks and marine phosphates and phosphorites.[198] In addition, volcanic activities and forest fires are also known to contribute to the natural cadmium levels in the atmosphere.[199] Additionally, phosphate fertilizers also contribute to cadmium concentration in atmosphere.[198,199]

Recent reports show that the concentration of cadmium is steadily increasing in the environment, the main culprit being anthropogenic (manmade) sources.[199-201] Outpouring of cadmium occurs to all three sections of the environment- air, water, and soil. As these are closely interlinked, considerable transfer occurs between them raising concerns about both health and environmental hazards.[202,203,204]

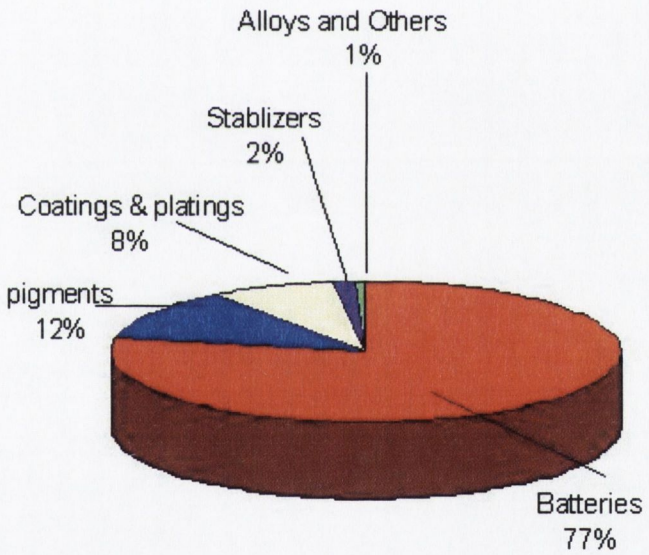

Figure 3.1 ***Schematic illustration of cadmium levels in environment from anthropogenic sources.***[200]

The contribution of various anthropogenic sources such as cadmium pigments, alloys, stabilizers and coatings all contribute to the cadmium discharge to the enviornment but the major contributor is the Ni-Cd batteries (Figure 3.1).[201,202] Cadmium hydroxide is used as one of the two principal electrode materials in the Ni-Cd batteries.[201,205] Ni-Cd batteries have the advantage of being cost-effective, have high cycle lives and possess excellent low and high temperature performance relative to other batteries.[205] Ni-Cd batteries have found

a wide range of applications in both industrial and consumer goods.[201,205] The environmental effects, which arise due to the significant discharge of cadmium from the continuous use of these batteries, have been well documented.[205,206] Quantitatively, the impact is measured in terms of Lithospheric extraction indicator (LEI).[205] LEI is the ratio of metals release from anthropogenic sources to natural sources.[205] Recent investigations indicate high LEI for cadmium (37%) and the level is increasing steadily.[205] Even though lithium based batteries are now becoming more common, the disposal of unused cadmium batteries is a major problem.

3.2 Effects of Cd(II) on health

Exposure to cadmium have profound biological effects such as renal dysfunction, reduced lung capacity and emphysema.[206-208] The tendency of this toxic metal to easily accumulate in organs such as kidney, hippocampus, thyroid and spleen, results in severe physiological effects.[208,209,210] Although only about 0.4% of the total amount of ingested cadmium is retained in the human body, it still poses a great threat as cadmium is estimated to have a biological half-life of 20-30 years.[211] Studies conducted have reported toxic levels of Cd(II) in the kidney and thyroid glands of miners who were continuously exposed to high levels of cadmium possibly from water, food, air, and/or soil.[212] Investigations showed that cadmium could be considered toxic at concentrations less than 10 μM and results in a 50 % mortality rate with 50 μM Cd(II) over a period of approximately 4 hours.[213] When combined with low-levels of Zn(II), Cd(II) is known to induce fetotoxicity (still-births) and various forms of congenital abnormalities.[214] Recent studies carried out by Bhattacharyya *et al.* have indicated that Cd(II) stimulates bone demineralisation by activating the osteoclast bone cells.[215] International Agency of Research on Cancer (IARC) considers that there is enough evidence to classify cadmium as a carcinogenic agent.[205,214] Experimental studies in animals are being carried out to evaluate the risk of lung, prostate, kidney, testicle and bladder cancer.[206,214] All of these factors make the detection and quantification of Cd(II) a vital area of research.

3.3 Cadmium detection and elimination

There are several methodologies in the literature for the determination of cadmium in soil, urine and others biological fluids. Onar and Temizer used a differential-pulse anodic stripping voltametry (DP-ASV) method to determine Cd(II) and Pb(II) in urine.[216] Several

methods have been developed using electrothermal atomic absorption spectrometry (ET-AAS) for Cd(II) determination[217-220]. Carmack and Evenson determined urinary Cd(II) by ET-AAS with carbon tubes impregnated with molybdenum.[217] The determination of Pb(II) and Cd(II) in blood and urine by ET-AAS was accomplished using extraction into methyl isobuthyl-ketone (MIBK) after chelation by ammonium pyrrolidine dithiocarbamate (APDC).[218,219] Bhattacharyya *et al.* have developed assay for Cd(II) in whole blood and urine using deuterium background-correction ET-AAS.[220] Inductively coupled plasma-atomic emission spectrometry with ultrasonic neublization has been used to detect Cd(II).[221] All of these methods are quite attractive as analytical tools however, they do suffer from a number of disadvantages such as:

- use of sophisticated and expensive equipment
- most of the methods outlined require sample pre-treatment
- low sensitivity and selectivity
- high concentration of Cd(II) required for detection
- real-time detection is not possible.

Currently there is a need for developing better methods of Cd(II) detection. In recent years, due to the advantages offered by fluorescence spectroscopy as outlined in Chapter 1 and 2, the use of fluorescent chemosensors is an active area of research. Such devices are based upon a simple design, where an external input such as an ion or a molecule can modulate either or both the ground state and excited state properties of the host.[21,26] Extensive efforts are being made to synthesise chemosensors with suitable fluorophore and receptor moieties to selectively sense Cd(II), Hg(II) and Pb(II) heavy metal ions.[72] A critical discussion of some of these sensors, followed by the motivation for the present work is given in the next section.

3.4 Review of fluorescent chemosensors for Cd(II) detection

As early as 1988, Czarnik *et al.* reported the use of anthracene-based sensors **118-122** for Zn(II) and Cd(II) detection.[222-225] Sensors **118-121** utilise the azamacrocycles as the receptor moiety while open chain acts as the receptor for **122**. Chelation-enhanced fluorescence (CHEF) was reported in the presence of Zn(II) and Cd(II) in CH_3CN.

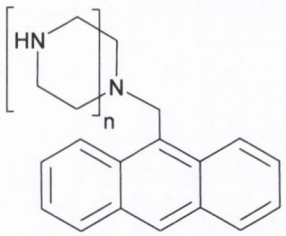

118: n= 1
119: n= 2
120: n= 3
121: n= 4

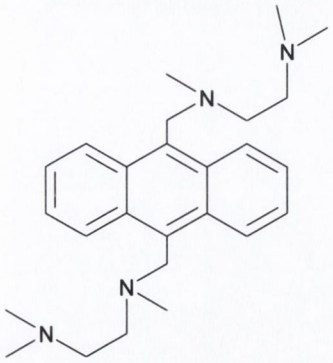

122

Compounds **118-121** showed changes in the fluorescence upon metal ion complexation in aqueous solutions at pH 10. Titration studies were carried out in highly alkaline conditions (pH~ 10) to avoid the interference from H^+ ions. The aliphatic nitrogens are easily protonated and consequently would give rise to changes in the fluorescence emissions that can be regarded as a false fluorescence *'response'*. Among **118-121**, all except 9-anthrylmethyl-1,4,7,10,13-pentaazatridecane (**120**) exhibited normal anthracene emission. However, the **120**-Cd(II) complex displayed an additional broad, red-shifted band centred at 446 nm. The ^{1}H-NMR spectrum of this complex in D_2O revealed the presence of more than one chelate in solutions since the H-10 signal (anthracene fluorophore) was clearly represented by two singlets. Interestingly, the **120**-Cd(II) complex uniquely experiences deuterium exchanges at the 1- and 8- positions of anthracene. All of these observations were attributed to aromatic chelatoselective cadmination at these positions. This can be envisaged by considering the formation of a π-complex between the anthracene π-electron cloud and Cd(II), which subsequently changes to a high-energy σ-complex (Scheme 3.1).

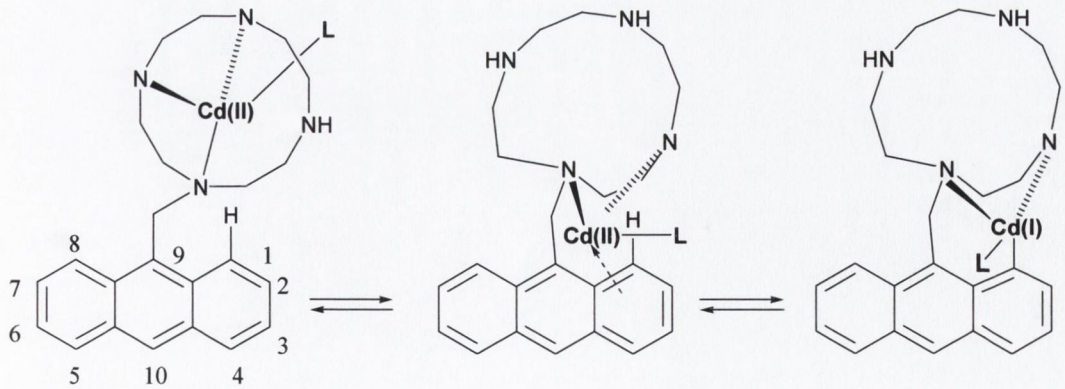

Scheme 3.1 *Schematic representation of π and σ- complex of 120-Cd(II). L= H_2O or counterion of Cd(II) salt.*

No such observation was noticed for the Zn(II)-**122** complex. The fluorescence emission of the free sensor **122** was almost zero, as the electron transfer from the two nitrogen atoms efficiently increased the non-radiative decay of the fluorophore. Protonation and metal complexation inhibited the electron transfer from the nitrogens to the anthracene and the fluorescence was restored. A 120-fold FE was observed upon complete protonation. In addition, **122** was found to have a much higher affinity for Zn(II) than for Cd(II). The receptor moiety in **118-122** possesses aliphatic nitrogen atoms so they have higher pK_a value. As a result sensors **118-122** cannot be used as a practical fluorophore for Zn(II) and Cd(II) under physiological conditions.

Savage *et al.* reported the synthesis and photophysical properties of diaza-18-crown-6 functionalised 5-chloro-8-methoxyquinoline **123** for Cd(II) recognition.[226] A large fluorescent enhancement was observed on Cd(II) and Zn(II) addition. Log β values of 3.98 and 4.3 were determined for Zn(II) and Cd(II) complexation respectively in methanol. Group 1 and 2 metals, such as Ba^{2+} and K^+ formed only weakly fluorescent complexes with **123** at higher concentrations. Transition metal ions such as Ni(II), Cu(II) or Hg(II) form stable non-fluorescent complexes with **123**. The low water solubility and pH sensitivity of **123**, limits its practical applications for Cd(II) detection.

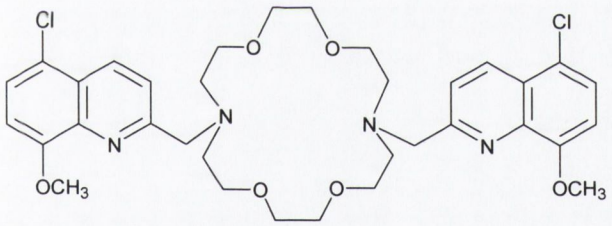

123

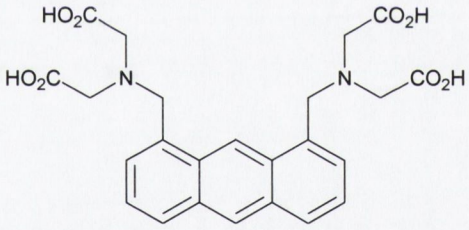

124

Yoon *et al.* developed a reverse PET (*'on-off'* compared to *'off-on'*) chemosensor **124** using an anthracene fluorophore for the detection of various metals ions such as Co(II), Cu(II), Hg(II), Mn(II), Pb(II), Zn(II) and Cd(II).[227] According to the their study, the fluorescence of the sensor is in the '*on*' state in the absence of a metal ion because of the existence of the compound as a *zwitterion*. Upon metal ion binding the pK_a of the benzylic amino group is reduced, resulting in fluorescence quenching of the anthracene. Normal anthracene emission was observed for all the metal ion complexes except for Cd(II) which displayed an additional broad, red-shifted band at 435 nm, similar to that observed for **120**. Electrophilic aromatic cadmination at the 9-position of anthracene was observed upon

Cd(II) titrations. These observations were further supported by the ^{1}H-NMR analysis of the compound in D_2O where the H-10 position of anthracene was observed as a major and minor singlet indicating the formation of more than one chelate. Moreover, the H-9 signal was substantially broad and decreased upon addition of 1.1 equivalent of Cd(II). It was reasoned that the Cd(II)-**124** complex uniquely populates a conformer in which an anthracene-Cd(II) (π-d orbital) interaction promotes the anthracene-Cd(II) complex (π-complex), which is subsequently converted to a higher energy σ-complex.

3.5 Motivation for the synthesis of cadmium selective sensors

Chemosensors reported to date for Cd (II) detection suffer from several drawbacks such as low aqueous solubility, less sensitivity and selectivity.[222-226] Furthermore they are not suitable for physiological pH range. The need for ideal Cd(II) sensors that satisfy these criteria are currently of great importance. With this in mind, the objectives of the present study are:

- the design of Cd(II) selective sensors that can discriminate between competitor ions such as Ca^{2+}, Mg^{2+}, Zn(II) or Hg(II)
- physiological pH independent nature to avoid false 'positive' response due to protonation.

3.6 Novel PET fluorescent chemosensors based on anthracene fluorophore

3.6.1 Design strategy, synthesis and characterisation

The synthesis, characterisation and photophysical evaluation of two new anthracene based PET chemosensors, **125** and **126** for Zn(II) and Cd(II) detection was undertaken.

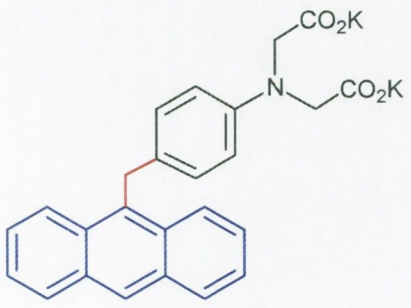

125

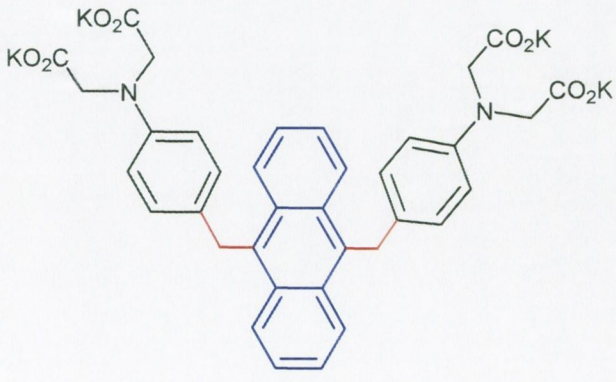

126

Anthracene is well exploited as an efficient fluorophore for constructing fluorescent chemosensors.[228-231] Anthracene displays an intense emission band with a well-defined and characteristic vibrational structure.[231] The structural aspects of anthracene such as planarity, rigidity and a well-delocalised π-system provides an absorption band with a low value for the intersystem crossing rate constant and consequently a higher value for the fluorescent quantum yield.[232] A relatively high chemical stability allows the facile functionalization of its framework, which makes the synthesis of anthracene-based sensors especially convenient.[233]

The choice of receptor is critical to overcome the interference from metal ions such as Ca^{2+}, Mg^{2+}, Cu(II) and Pb(II), which are known competitors for Zn(II) and Cd(II). For this purpose, simple phenyliminodiacetate was used. Its advantages have already been discussed in Chapter 2. The presence of two receptor units in **126** would statistically increase the PET rate from the receptor to the excited singlet state of the anthracene resulting in effective quenching in the absence of any ion. A methylene spacer connects the fluorophore and receptor moieties in both **125** and **126**. Sensors **125** and **126** are based on *'fluorophore-spacer-receptor'* and *'receptor-spacer-fluorophore-spacer-receptor'* models respectively. The *'fluorophore-spacer-receptor'* format is discussed in Chapter 1.[26] The FMO approach as well as PET quenching mechanism of **126** is illustrated in Figure 3.2.

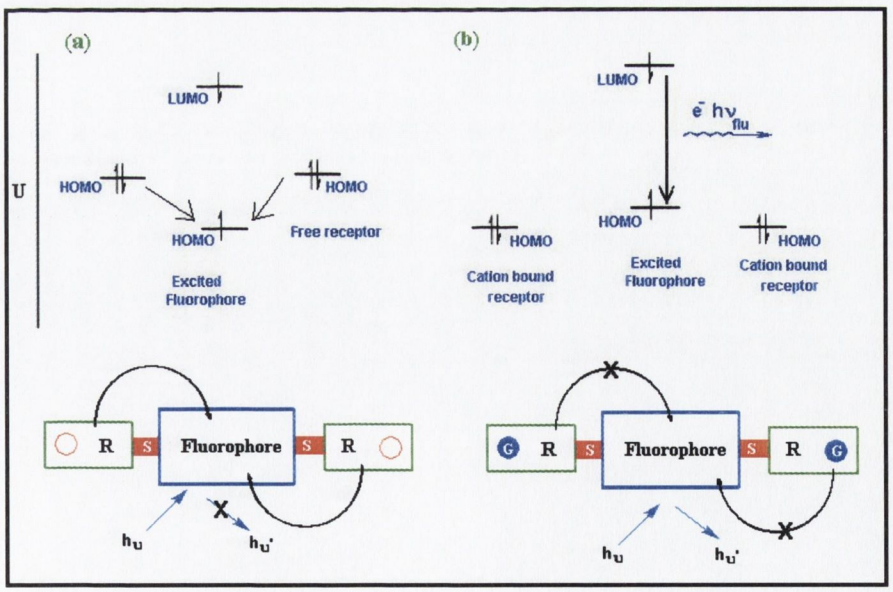

Figure 3.2 ***FMO approach and PET quenching mechanism for 126: (a) guest free receptor; (b) guest bound receptor. R= receptor, S= spacer, G= guest, U= potential energy.***

3.6.1.1 Synthesis and characterisation of sensor 125

The synthesis of **125** as outlined in Scheme 3.2 begins with **110**, which was described in Chapter 2. The Friedel-Craft alkylation of **110** with 9-bromomethyl anthracene **127** using zinc bromide ($ZnBr_2$) as catalyst resulted in a low yield (15%) of the desired product **128**. Use of 9-chloromethyl anthracene[234] as alkylating agent in the presence of $AlCl_3$ catalyst dramatically improved the yield of ester **128** (70%). Purification was accomplished by silica flash-column chromatography using ethyl acetate:hexane (2:3) as eluant.

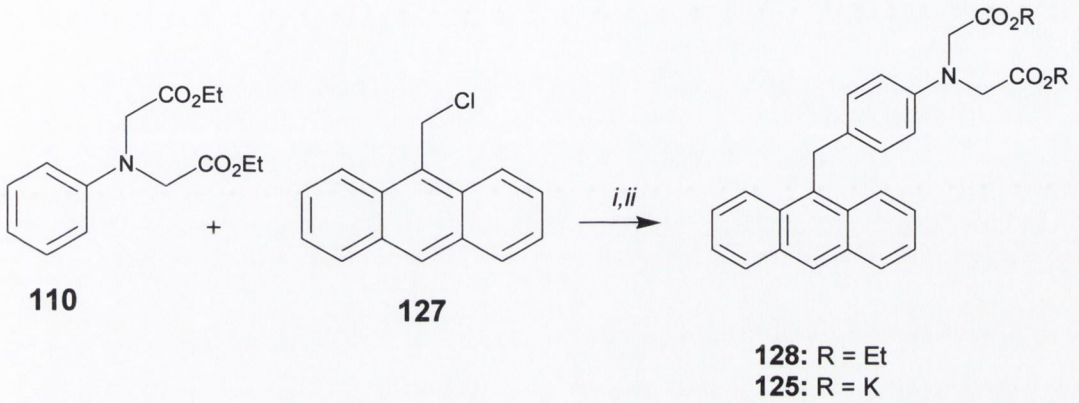

110 **127**

128: R = Et
125: R = K

Scheme 3.2. ***Synthesis of 128 and 125: (i) $AlCl_3$, $CHCl_3$, reflux, 6 hours; (ii) KOH, MeOH-H_2O, reflux, 2 hours.***

Various conditions were attempted to achieve the hydrolysis of **128**. However, the procedure involving the use of 3M KOH in methanol:water 10:1) under reflux solution resulted in almost quantitative yield of the sensor **125** (Table 3.1).

Table 3.1 ***Alkaline hydrolysis for the synthesis of 125.***

Conditions for hydrolysis	Comments
LiOH, MeOH-H_2O, 25^{0}C	Only starting material recoverd
LiOH, MeOH-H_2O, reflux	Partial hydrolysis, separation unsuccessful
NaOH or KOH, MeOH-H_2O, 25^{0}C	Partial hydrolysis, separation unsuccessful
KOH, MeOH-H_2O, reflux	Target compound in quantitative yield

The structures of **128** and **125** were confirmed by the usual spectroscopic methods. A singlet at δ 8.4 and two multiples at δ 8.21-8.24 and δ 8.02-8.05 in the ^{1}H-NMR ($CDCl_3$) of **128** were attributed to the anthracene aromatic protons. Two doublets at δ 6.98 and δ 6.47 were observed for the phenyl protons. The IR spectrum showed a strong absorption

band at 1745 cm^{-1} assigned to carbonyl stretching. ESMS spectrum showed a peak at 455 mass units ($M+H^+$, 100%).

The ^{1}H-NMR of **125** (Figure 3.3) showed two doublets for the phenyl protons at δ 6.20 and δ 6.82. The four resonances of the anthracene protons appeared as a singlet at δ 8.30, a multiplet at δ 7.36-7.38 and two doublets at δ 7.91 and δ 8.12. A peak at 1765cm^{-1} in the IR spectrum was attributed to carbonyl stretching. ESMS spectrum showed a peak at 476 mass units ($M+H^+$, 80%).

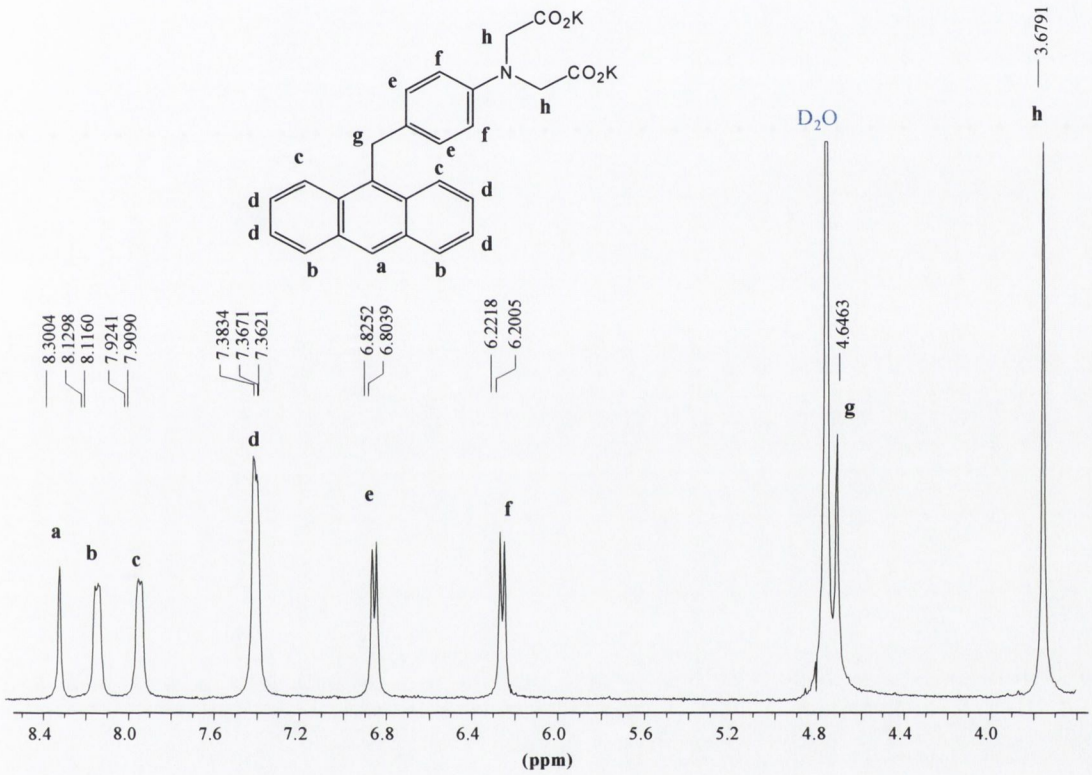

Figure 3.3. ^{1}H-NMR of 125 (D_2O, 400 MHz)

3.6.1.2 Synthesis and characterisation of 126

The synthesis of **126** is illustrated in Scheme 3.3. To facilitate the attachment of two receptor units 9,10-bischloromethyl anthracene (**129**) was synthesised using literature procedure.[235] The Friedel-Craft alkylation of **129** with **110** using $AlCl_3$ as catalyst resulted in a 72% yield of ester **130** after silica flash-column chromatography using ethyl acetate:hexane (1:1) as eluant. The hydrolysis of **130** using KOH in MeOH:H_2O (10:1, *v/v*) resulted in the quantitative yield of **126**.

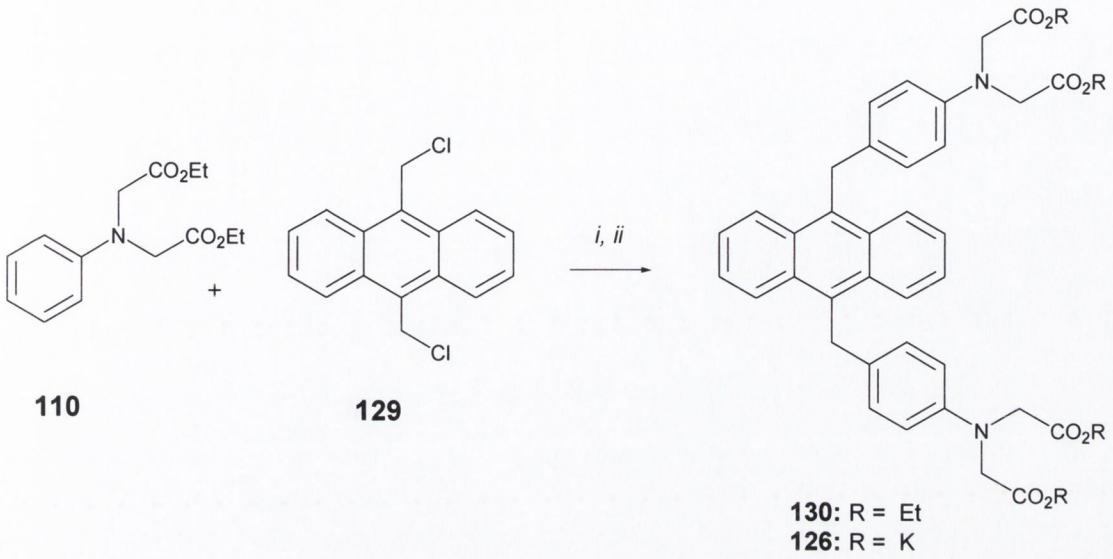

Scheme 3.3. ***Synthesis of 130 and 126 (i) $AlCl_3$, $CHCl_3$, reflux, 12 hours; (ii) KOH, MeOH-H_2O, reflux, 2 hours.***

Compounds **130** and **126** were fully characterised by ^{1}H-NMR, ^{13}C-NMR, ESMS, IR and elemental analysis. The ^{1}H-NMR of the ester and sensor demonstrated the plane of symmetry. In the ^{1}H-NMR of **130**, the phenyl protons appeared as doublets at δ 6.50 and δ 7.01. Anthracene proton resonances were observed as two double-doublets at δ 7.42-7.45 and δ 8.25-8.28. A singlet at δ 4.95 was attributed to methyl spacers. The symmetrical nature of the molecule was further supported by the ^{13}C-NMR in which only 13 carbon resonances were observed. A strong peak in the IR spectrum at 1744 cm^{-1} was assigned to the carbonyl stretching frequency. An ESMS peak was observed at 733 mass units ($M+H^+$, 100%).

In the ^{1}H-NMR spectrum, sensor **126** showed two resonances for anthracene protons observed as double-doublets at δ 8.31-8.29 and δ 7.45-7.42 (Figure 3.4). Phenyl protons were observed as two doublets at δ 6.91 and δ 6.28. The two methyl spacers appeared as singlet at δ 4.86. The symmetrical nature of the molecule was further supported by ^{13}C-NMR in which only 11 carbon resonance were observed. A peak at 1640 cm^{-1} observed in

the IR spectrum was assigned to the carbonyl stretching frequency. ESMS peak was observed at 773 mass units ($M+H^+$, 100%).

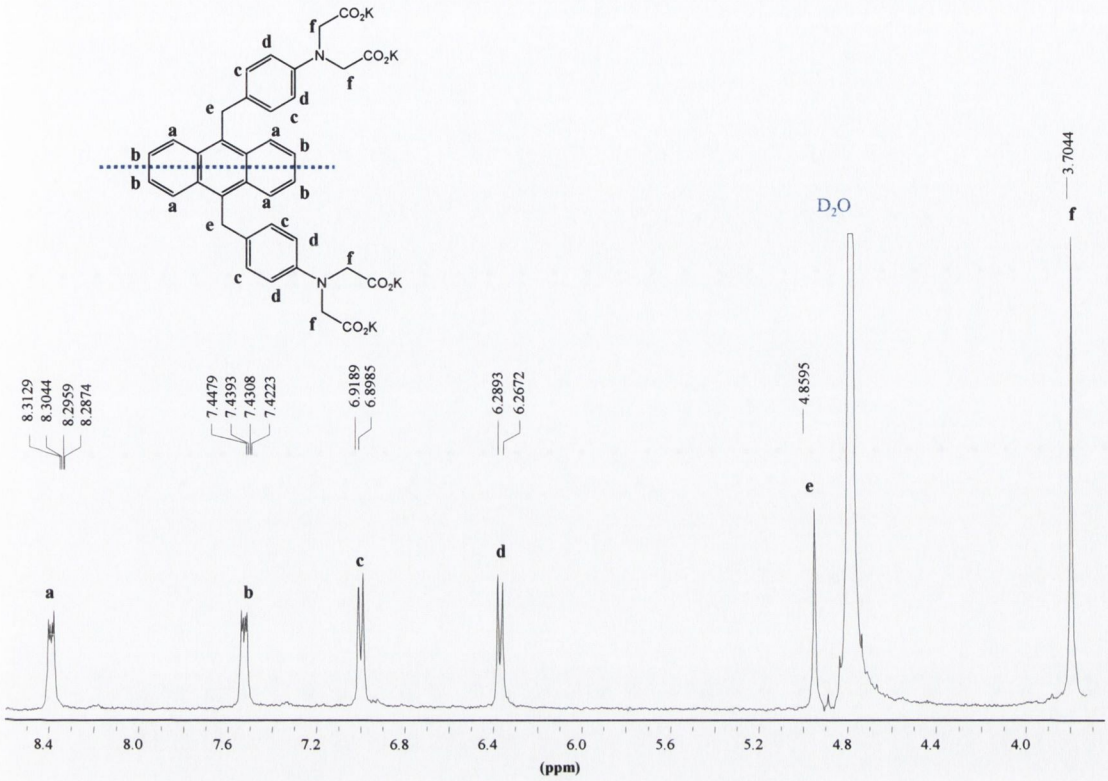

Figure 3.4. ***^1H NMR of 126 (D_2O, 400 MHz).***

3.7 Ground and excited state properties of the 125 and 126

3.7.1 Absorption and fluorescence pH response of 125

The absorption and the fluorescence response of **125** as a function of pH were investigated in deionised distilled water with 0.135 M NaCl, to maintain constant ionic strength. A 1 μM solution of sensor **125** was prepared and the UV-Vis spectrum was recorded. The pH was adjusted to 12 by adding 2 M NaOH. The pH was lowered in steps of ΔpH=0.25 with the appropriate amounts of dilute HCl solution, recording the absorption and emission spectra at each pH interval.

The absorption spectra of **125** exhibited five main absorption bands centred at 313 nm, 335 nm, 351 nm, 369 nm and 389 nm. An extinction coefficient of 18.6 x 10^3 $M^{-1}cm^{-1}$ was measured for the 389 nm band. The absorption spectra of **125** as a function of pH is shown in Figure 3.5. Upon decreasing the pH, no shifts were seen in the positions of these bands. There was however, small decrease in the absorption intensity (<10%). The plot of absorption intensity *verus* pH (at all absorption maxima) is almost a straight line (insert,

Figure 3.5). This clearly shows that no charge transfer or π-π interaction is involved between the receptor and the anthracene moiety in the ground state. de Silva *et al* and Yoon *et al* have also reported similar observations.[47,227]

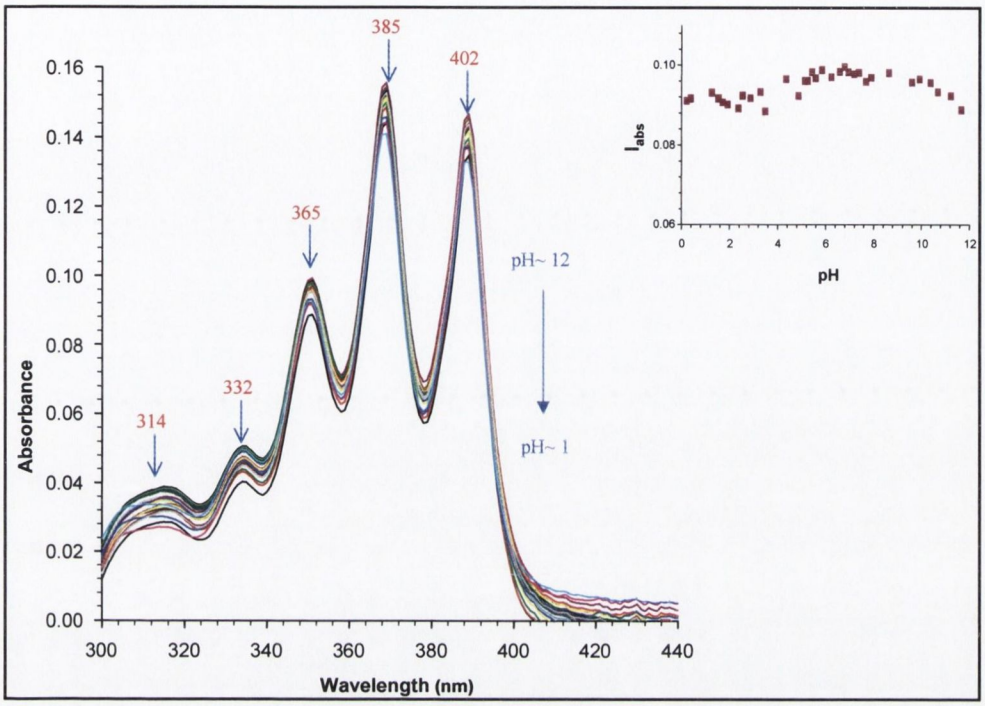

Figure 3.5. Absorption response of 125 as function of pH. Insert shows the plot of absorption intensity at 385 nm against pH.

The fluorescence response of **125** was measured in a similar manner to the absorption. The changes in the fluorescence emission spectra of **125**, as a function of pH are shown in Figure 3.6. In basic solution (pH~ 12), the fluorescence was switched *'off'* as the electron transfer from the highest occupied molecular orbital (HOMO) of the receptor to the fluorophore is thermodynamically favourable. Acid titration resulted in an increase in the fluorescence emission intensity of the anthracene emission of the four characteristic bands centred at 392, 415 and 439 nm and a weak band at 466 nm. A fluorescence increase of approximately 60 fold was observed. The increase in fluorescence is due to the protonation of the tertiary nitrogen atom of the receptor moiety, resulting in a decrease in the reduction potential. This prevents electron transfer from receptor to the excited state of the anthracene, thus restoring the fluorescence. The pH fluorescence response behaviour of **125** is a typical *'on-off'* PET sensor characteristic, as outlined previously. A plot of changes in the fluorescence intensity against pH, resulted in a sigmoidal curve which changes over 2 pH units. This indicates a simple acid-base equilibrium. The relative

fluorescence intensity (IF/IF_o) plot at 392 nm, 415 nm and 439 nm *versus* pH clearly shows that any of these wavelengths can be used to determine the pK_a. These changes were fitted to equation 2.1 (Chapter 2) which yielding pK_a values of 1.75, 1.74 and 2.0 ($\pm$ 0.1) for 392 nm, 415 nm and 439 nm respectively, providing an average pK_a of 1.83 $\pm$ 0.1. This makes **125** particularly attractive for Cd(II) detection in highly acidic soils where the pH can reach ~ 3-4.

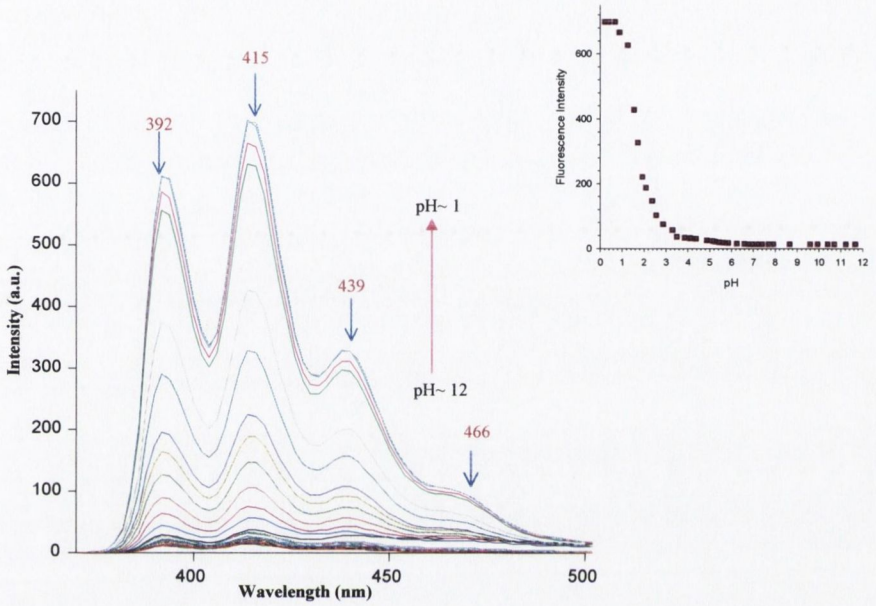

Figure 3.6. Fluorescence emission response of 125 as a function of pH. Insert shows the plot of emission intensity at 415 nm against pH.

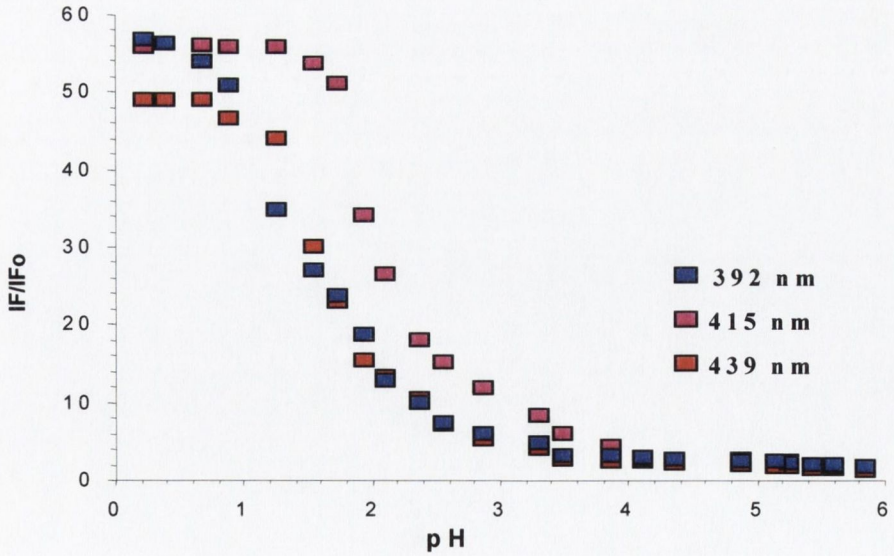

Figure 3.7. Plot of the relative fluorescence intensity versus pH for sensor 125. Changes are plotted for emission maxima of 392 nm, 415 nm and 439 nm. Excitation was provided at 360 nm.

3.7.2 Absorption and fluorescence response of 126

The absorption and fluorescence spectra of **126** as a function of pH were recorded in a similar manner to that described for **125**. The absorption spectra of **126** showed four absorption bands at 343 nm, 362 nm, 381nm and 402 nm. The absorption spectra are almost similar to both 9,10-dimethylanthracene (DMA) and 9,10-diphenylanthracene (DPA). The absorption spectra generated during the pH titration showed only a negligible decrease in the intensity (Figure 3.8). No shifts in the position of the absorption bands were observed. This shows that under these conditions only minor ground state interactions takes place between the receptor and the anthracene moiety, confirming the insulating role of the methylene spacer.

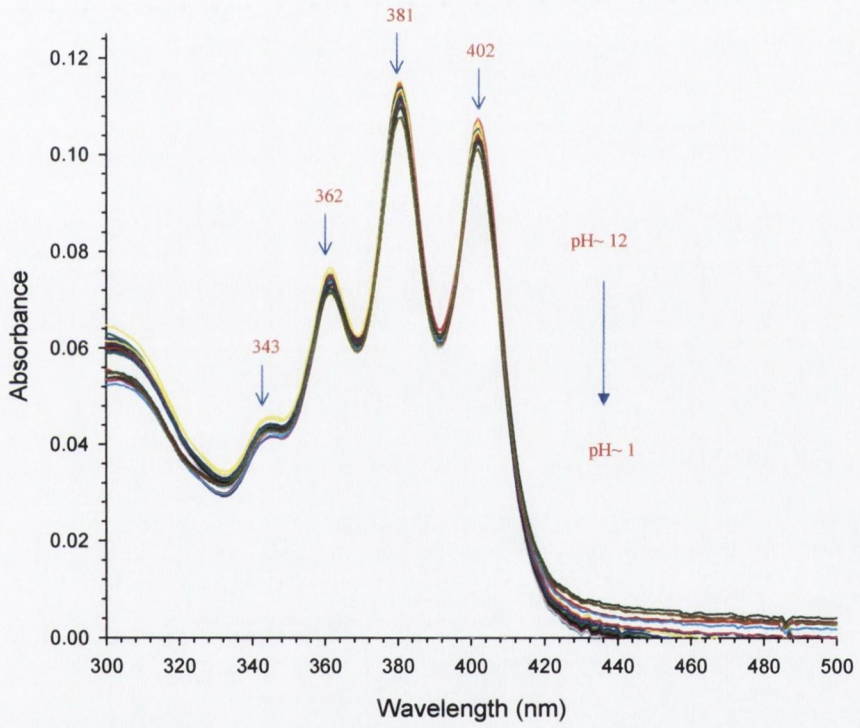

Figure 3.8. Absorption response of 126 as function of pH.

In basic solution, the fluorescence of **126** is quenched (Figure 3.9). In the pH range of 12-3.5 virtually no emission was observed. When the pH was around 3.4, a broad band centred at 470 nm appeared with an increase in emission intensity (insert, Figure 3.9). As the pH was decreased further (3.3-1.0), normal anthracene emission with four main emission bands at 405 nm, 428 nm 454 nm and 480 nm was observed with concomitant increase in the fluorescence intensity and a fluorescence increase of 600 fold was observed.

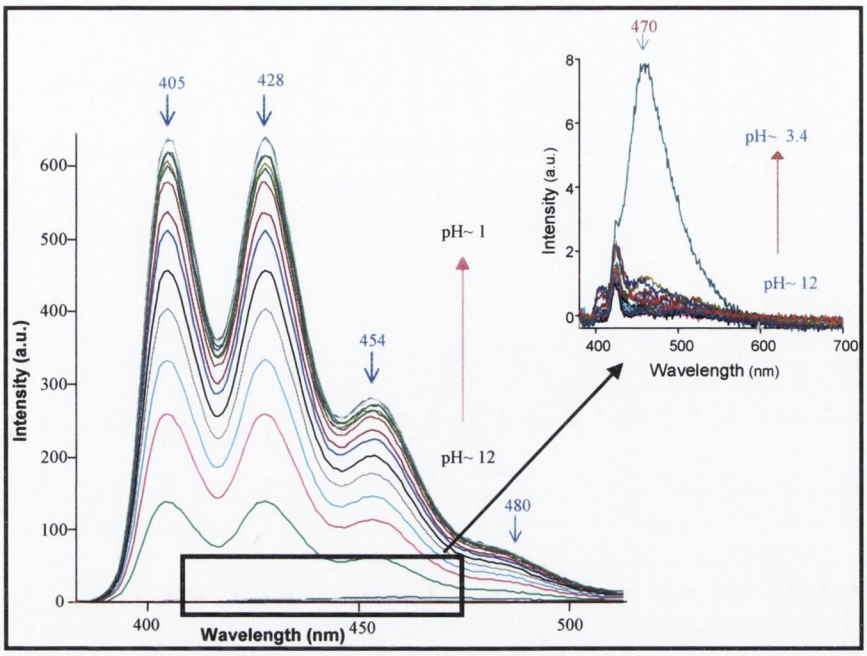

***Figure 3.9** Fluorescence response of 126 as a function of pH. Insert shows the response from pH 12~ 3.4.*

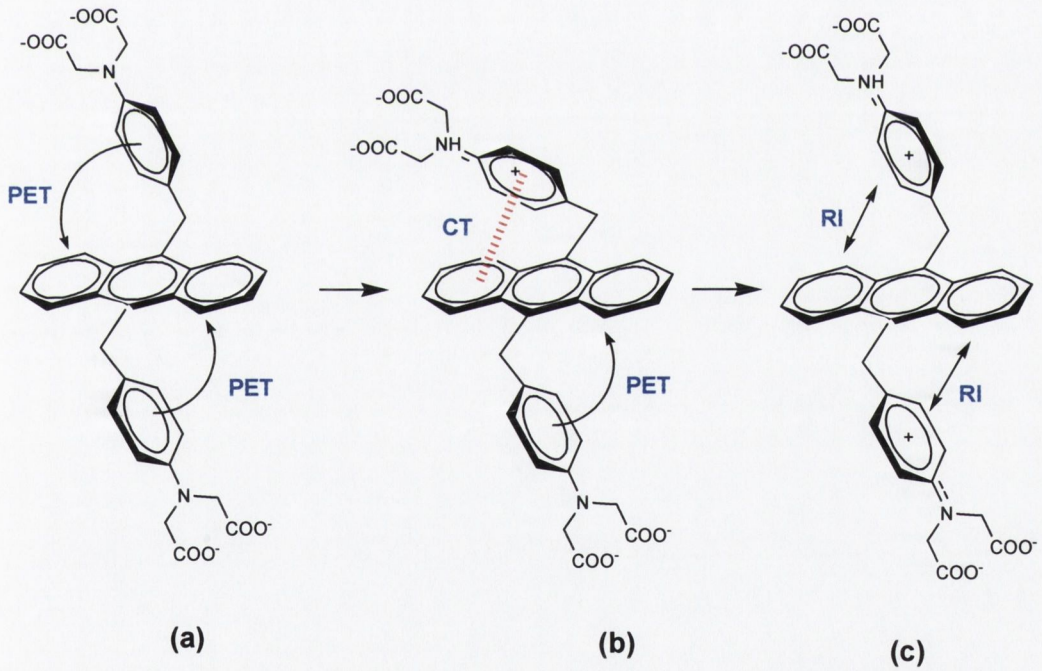

Scheme 3.4 ***Schematic illustration of the pH dependent fluorescence changes of 126: RI= repulsive interaction; CT= charge transfer***

The observed changes can be envisaged as shown in Scheme 3.4. From pH 12-3.5, it is reasoned that the fluorescence of the anthracene is efficiently quenched *via* a PET process from the receptors to the excited singlet state of the anthracene (Scheme 3.4 (a)). As the

pH decreased from 3.5 to 3.4, protonation of the tertiary nitrogen of one receptor takes place, which causes a weak charge transfer (CT) interaction between the protonated receptor and the anthracene fluorophore (Scheme 3.4 (b). This resulted in a charge transfer band at 470 nm. When the pH was decreased further, both receptors were protonated. This results in a repulsive interaction (RI), and to minimise it, the receptors move as far apart as possible in space (Scheme 3.4 (c)). Consequently, typical anthracene emission was observed in the pH range of 3.3-1.

A plot of the fluorescence intensity changes at the emission maxima of 404 nm, 428 nm and 454 nm is shown in Figure 3.10. A sigmoidal curve was obtained for each, and the changes observed can be explained by evoking the simple equilibrium. Although two receptor sites are present, it is most likely that the changes in fluorescence emission correspond to the protonation of one receptor site. Similar observations have been reported by Lippard *et al.* in the case of fluorescein based sensors **80** and **81** (Chapter 2) consisting of two receptor moieties.[172] Data fitting analysis of the emission intensity changes at 404 nm, 428 nm and 454 nm resulted in pK_a values of 2.4, 2.3 and 2.8 respectively, providing an average pK_a value of 2.5 ± 0.1. The sensor **126** can be considered to be pH independent in the physiological range. This is of profound significances for a physiological application, for example the determination of Cd(II) in urine (acidic) caused by Cd(II) poisoning.

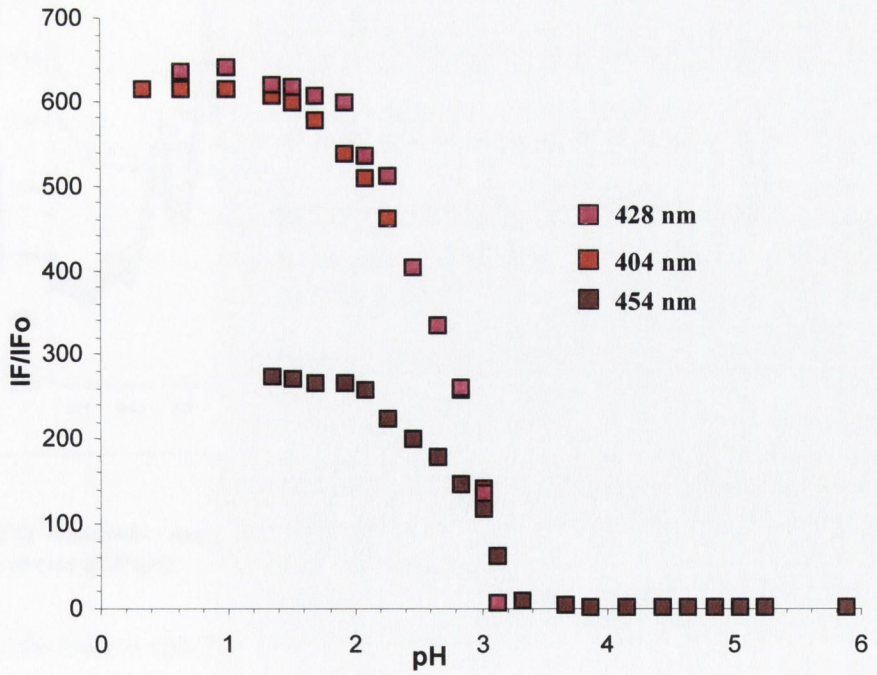

Figure 3.10 *Plot of the relative fluorescence intensity versus pH for sensor 126.*

3.7.3 Fluorescence and absorption response of 125 and 126 with metal ions

Group 2 metal ions and various transition metal ions such as Co(II), Ni(II), Cu(II), Zn(II), and Cd(II) were used to evaluate the metal ion binding ability of compounds **125** and **126**. Even with high concentrations (0.01 M) of Mg^{2+} and Ca^{2+}, no changes were observed in the absorption or fluorescence emission spectra. This indicates that the receptor in these sensors were not coordinating significantly to these ions to prevent quenching by the receptor. In the case of transition metal ions, only Zn(II) and Cd(II) gave rise to significant changes in the fluorescence emission spectra.

A 50 mL solution containing 1 μM **125** and **126** in HEPES buffer was prepared, and initial absorbance and fluorescence measurement were made. Zn(II) and Cd(II) aliquots were added to give final metal ion concentration of 6 μM, 8 μM, 12 μM, 20 μM, 60 μM, 80 μM, 100 μM, 180 μM, 280 μM, 0.4 mM, 0.6 mM, 0.8 mM, 0.10 mM, 1.2 mM, and the absorption and emission spectra were recorded.

3.7.4 Absorption and fluorescence response of 125 to Zn(II)

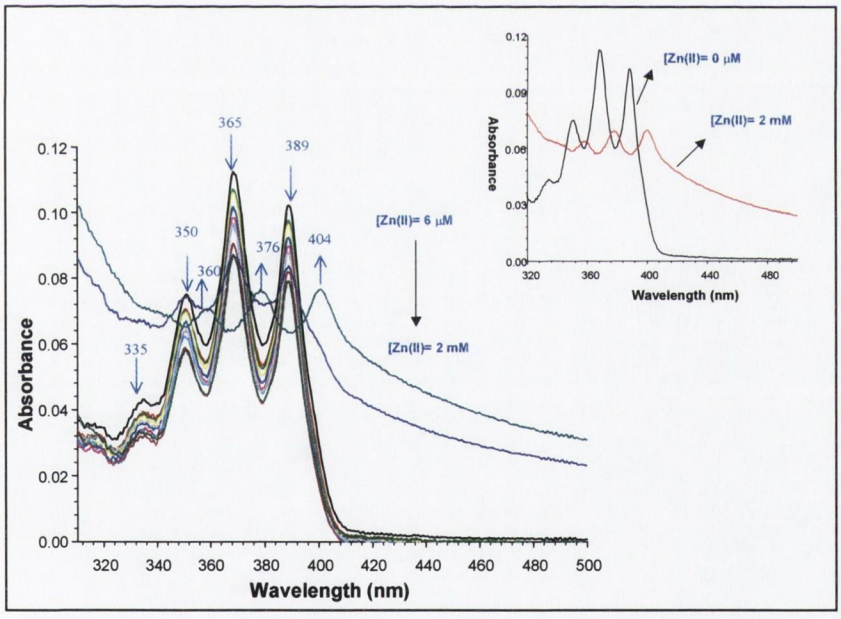

Figure 3.11 ***Absorption response of 125 in presence of Zn(II) ions. Insert shows titration profile without and with excess of Zn(II).***

The absorption spectrum of **125** at pH 7.4 showed four bands at 335 nm, 350 nm, 365 nm and 389 nm. Addition of Zn(II) to the buffered solution of **125** showed a slight

decrease in the intensity. At higher Zn(II) concentrations, dramatic shifts ($\Delta\lambda$= 14 nm) were observed in the absorption bands. This is most likely due to the charge transfer interaction between the anthracene and Zn(II) complexed receptor. Yoon *et al.* and Czarnik *et al.* have observed similar perturbations in absorption spectra utilising the anthracene fluorophore in sensors **120** and **124**.[222-225,227]

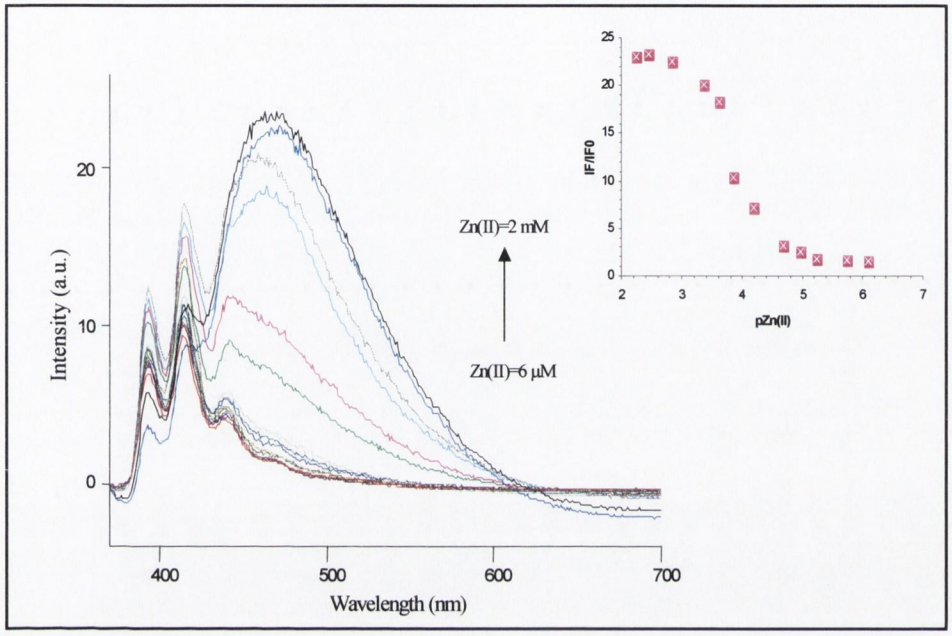

Figure 3.12 ***Fluorescence emission response of 125 to Zn(II). Insert shows the graph of relative emission intensity at 468 nm versus pZn(II). Spectra were acquired in 135 mM KCl, 20 mM HEPES, at pH 7.4. Excitation was provided at 360 nm.***

In the case of the titration of **125** with Zn(II), the normal anthracene emission was slightly increased upon Zn(II) addition. However, on further addition of Zn(II) a new structureless broad band at 468 nm was developed. Further addition of Zn(II) decreased the normal anthracene emission with concomitant increase in the emission intensity of the broad band. These changes can be accounted due to the formation of an intramolecular charge-transfer complex (intramolecular exciplex) between the cation-bound acceptor and anthracene donor.[236] Intermolecular exciplex, excimer and mixed excimer formation can be effectively ruled out as the concentration of the sensor used in the titration studies is very low (1 μM). A plot of relative emission as a function of pZn resulted in a sigmoidal curve exhibiting a change over 2 units. This indicates a simple equilibrium and probably 1:1 binding. From these changes log β of 3.8 (±0.15) was determined for the Zn (II)-**125** complex.

3.7.5 Absorption and fluorescence response of 125 to Cd(II)

The absorption response of **125** to Cd(II) is almost similar to that observed for Zn(II). Three prominent absorption bands were observed at 350 nm, 365 nm and 389 nm. There was a decrease in the absorption intensity upon addition of Cd(II). At higher concentrations of Cd(II), the absorption spectra shifted to longer wavelength with absorption maxima at 360 nm, 376 nm and 406 nm respectively (Figure 3.13). Isosbestic points were observed at 370 nm, 382 nm and 395 nm. As explained earlier, this is probably due to the charge transfer interaction occurring between the anthracene and receptor-Cd(II) complex. Saeva have reported similar observations in 9-methyl anthracene derivatives.[237] Also, Cd(II) additions resulted in a small decrease in the absorption intensities. A binding constant of 4.0 ± 0.1 was determined at 382 nm and 403 nm.

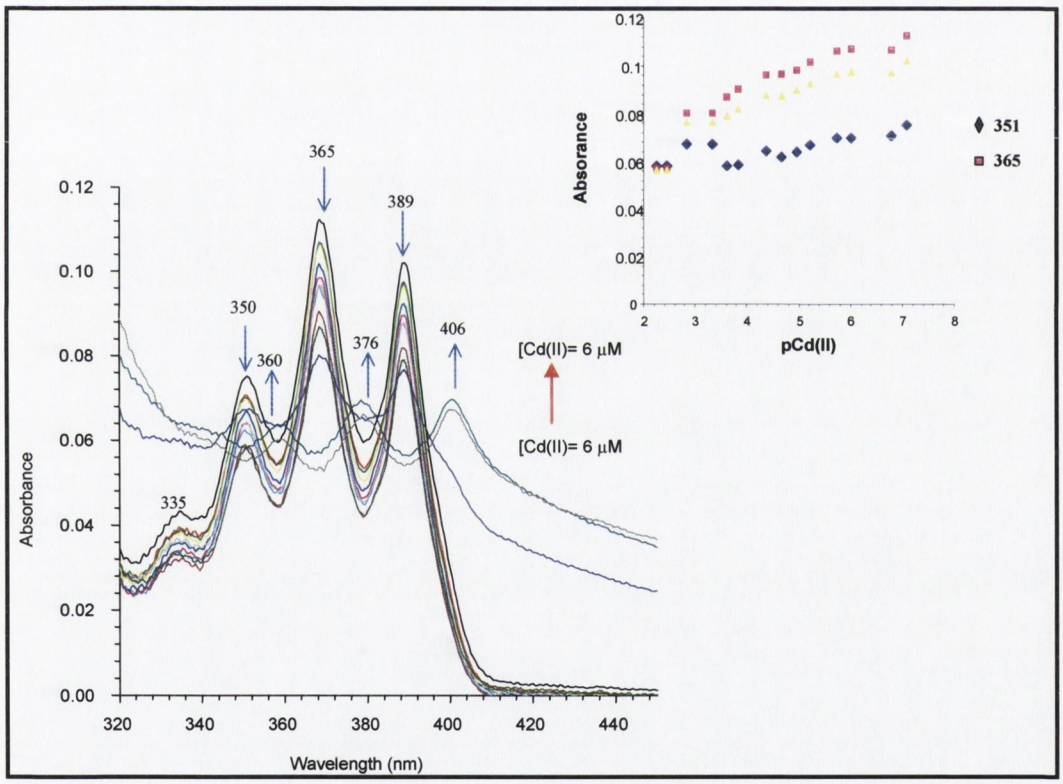

Figure 3.13 ***Absorption response of 125 in presence of Cd(II). Insert shows the plot of absorption intensity versus pCd.***

The fluorescence response of **125** initially showed slightly enhanced in normal anthracene emission. Upon further addition of Cd(II), a new structureless broad band at 505 nm developed. Further additions of Cd(II) decreased the normal anthracene emission

with a concomitant increase in emission intensity of the broad band (Figure 3.14). As with Zn(II), the shift in the emission is due to the formation of a intramolecular exciplex. The larger degree of red shift observed in the case of **125**-Cd(II) complex is most likely due to the stronger charge transfer interaction between Cd(II) and the anthracene π-cloud as indicated by Czarnik *et al.* (Scheme 3.1).[222-225] A plot of fluorescence emission intensity at 505 nm as a function of pCd, resulted in a sigmoidal curve with a pCd change of 2 units which indicates a simple equilibrium (insert in Figure 3.14). A log β of 4.4 (±0.1) was determined for Cd(II)-**125** complex.

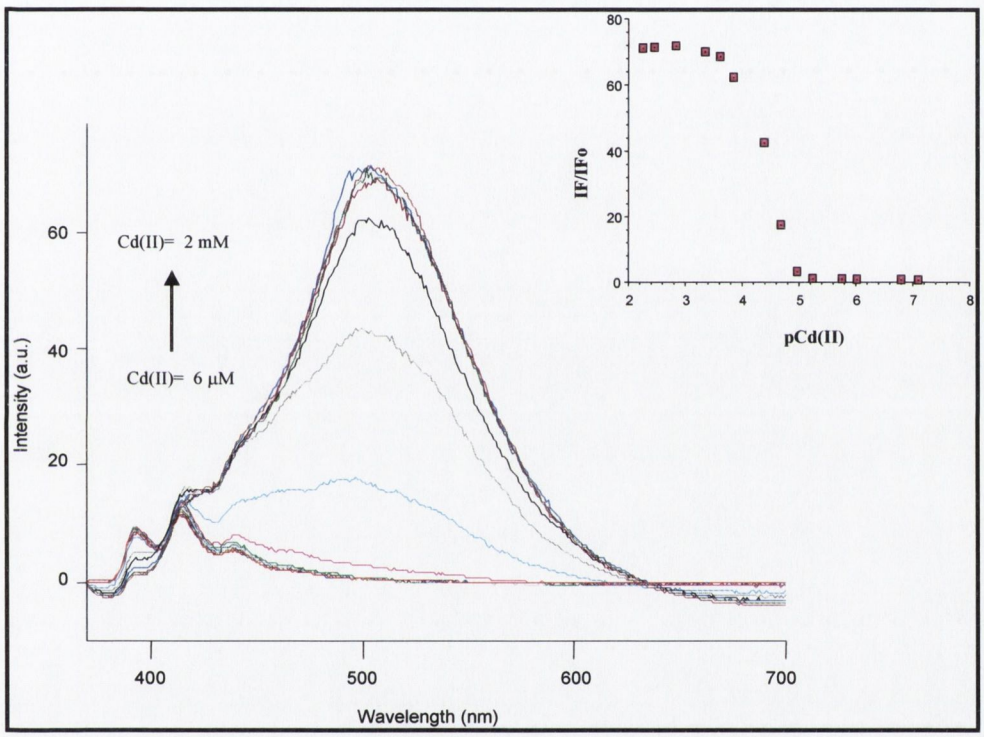

Figure 3.14 Fluorescence emission response of 125 to Cd(II). Insert shows the graph of relative emission intensity at 505 nm versus pCd. Spectra were acquired in 135 mM KCl, 20 mM HEPES, at pH 7.4. Excitation was provided at 360 nm.

3.7.6. Absorption and fluorescence response of 126 to Zn(II)

Upon addition of increasing Zn(II) slight bathochromic shifts were observed for the three prominent bands at 362 nm, 382 nm and 403 nm ($\Delta\lambda = 2$ nm). Isosbestic points were not clearly defined. A small decrease in the absorption intensity was observed as illustrated in Figure 3.15 (insert).

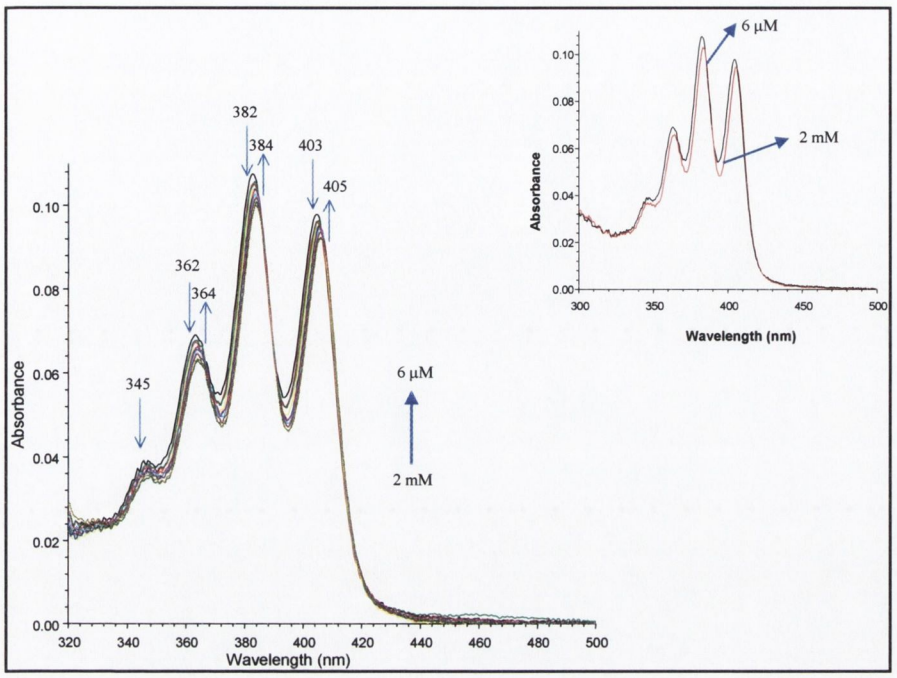

Figure 3.15 ***Absorption response of 126 in presence of Zn(II). Insert shows a plot of absorbance versus pZn.***

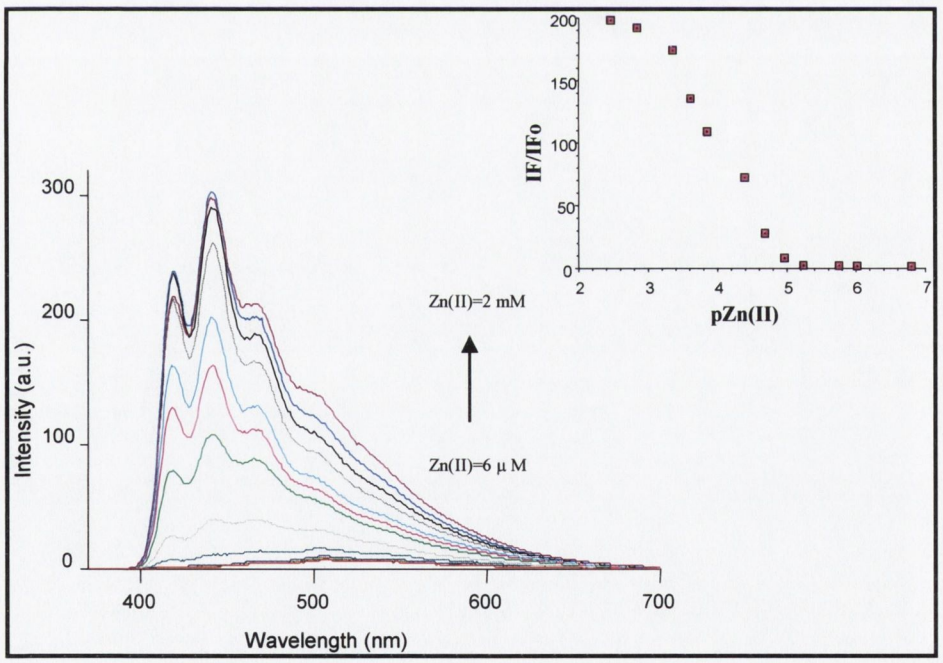

Figure 3.16 ***Fluorescence response of 126 in presence of Zn(II). Insert shows a plot of relative emission intensity at 415 nm versus pZn.***

The fluorescence emission response of **126** was different from **125** for the binding of Zn(II). As before in the absence of Zn(II), the fluorescence of the sensor was in an '*off*' state. During the Zn(II) titration, the spectra recorded showed typical anthracene emission profiles with increase in intensity. This fluorescence modulation is due to inhibition of PET processes. In this case, Zn(II) complexation did not lead to any charge transfer interactions. The plausible reason for this could be that Zn(II) binding forces the receptor to move far apart from the anthracene fluorophore due to steric effects. From the relative fluorescence changes at 415 nm as a function of pH, a sigmoidal curve was obtained which changes over 2 units (Figure 3.16).

3.7.7. Absorption and fluorescence response of 126 to Cd(II)

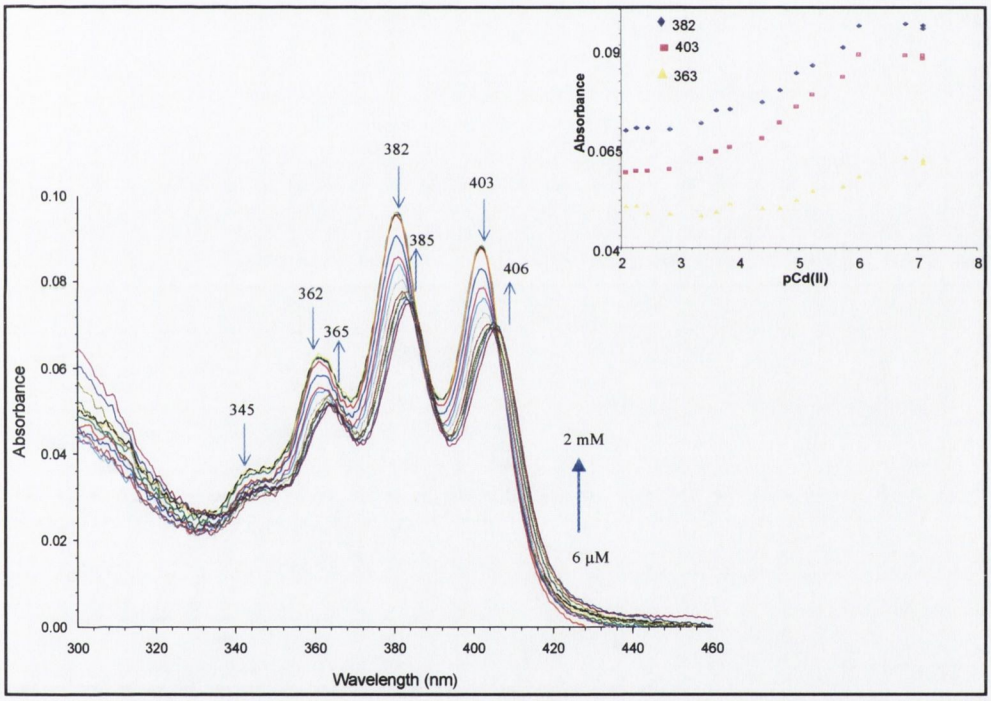

Figure 3.17 ***Absorption response of 126 in presence of Cd(II). Insert shows a plot of absorbance versus pCd.***

Upon Cd(II) titrations, similar to Zn(II), slight shift in the absorption maxima were observed ($\Delta\lambda$ = 2 nm) with concomitant decrease in intensity as illustrated in Figure 3.17. At least five isosbestic points can be observed in the spectra (349 nm, 365 nm, 383 nm, 391

nm and 405 nm). These changes can be due to the charge transfer interaction of the Cd(II) bound-receptor with the polarised anthracene π-system.

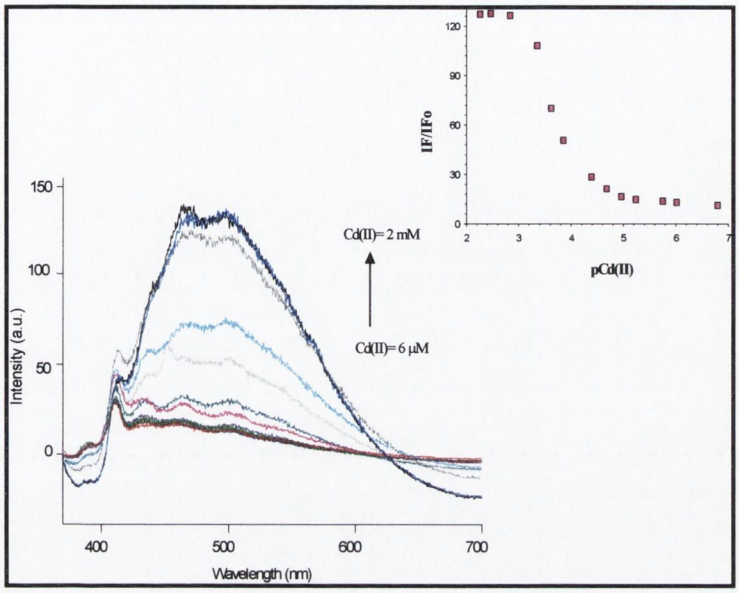

Figure 3.18 ***Fluorescence response of 126 in presence of Cd(II). Insert shows a plot of relative fluorescence intensity at 500 nm versus pCd(II).***

The fluorescence titration of **126** with Cd(II) showed perturbations similar to that of **125**. A broad structureless red shifted band at 500 nm was generated during the Cd(II) titration (Figure 3.18). It is worth noting that the 500 nm band dominates the emission response. As explained before the anthracene-Cd(II) charge interaction is responsible for these observations. A plot of fluorescence changes against pCd(II) resulted in a sigmoidal curve with 2 unit changes indicating a simple equilibrium (insert, Figure 3.18). The various spectroscopic parameters are summarised in Table 3.2.

Table 3.2 Electronic (absorption and emission) spectra and non-binding properties of 125 and 126.

parameter	125	126
pKa	1.83 (± 0.1)	2.5 (± 0.1)
ε (M^{-1} cm^{-1})	17.1×10^3	18.6×10^3
logβ (Zn(II) (fluorescence)	3.8 (± 0.1)	3.8 (± 0.1)
logβ* (Zn(II)	not possible to determine	not possible to determine
logβ (Cd(II)	4.2 (± 0.1)	3.9 (± 0.1)
logβ* (Cd(II) (absorption)	4.0 (± 0.1)	4.1(± 0.1)

3.7.8 Preliminary evaluation of 126 for selective determination of Cd(II) over Zn(II)

The fluorescent signalling of **126** with Zn(II) and Cd(II) were entirely different, Zn(II)-**126** emitted blue light and Cd(II)-**126** green light. Therefore to investigate the degree of selectivity of Cd(II) over Zn(II), it was decided to perform a Cd(II) titration in presence of excess of Zn(II).

A 1 μM solution of **126** was prepared in HEPES buffer at pH 7.4. The absorption and emission were measured and 3 mM Zn(II) was added to this solution. The addition of Zn(II) switched the normal fluorescence emission *'on'*. This Zn(II)-**126** solution was titrated with Cd(II) in the same manner as described in Section 3.7.7 and the spectra generated are shown in Figure 3.19. The addition of Cd(II) induced a shift to longer wavelength with the appearance of a new broad, structureless emission at 500 nm, demonstrating that **126** is capable of selectively signalling the presence of Cd(II) over Zn(II).

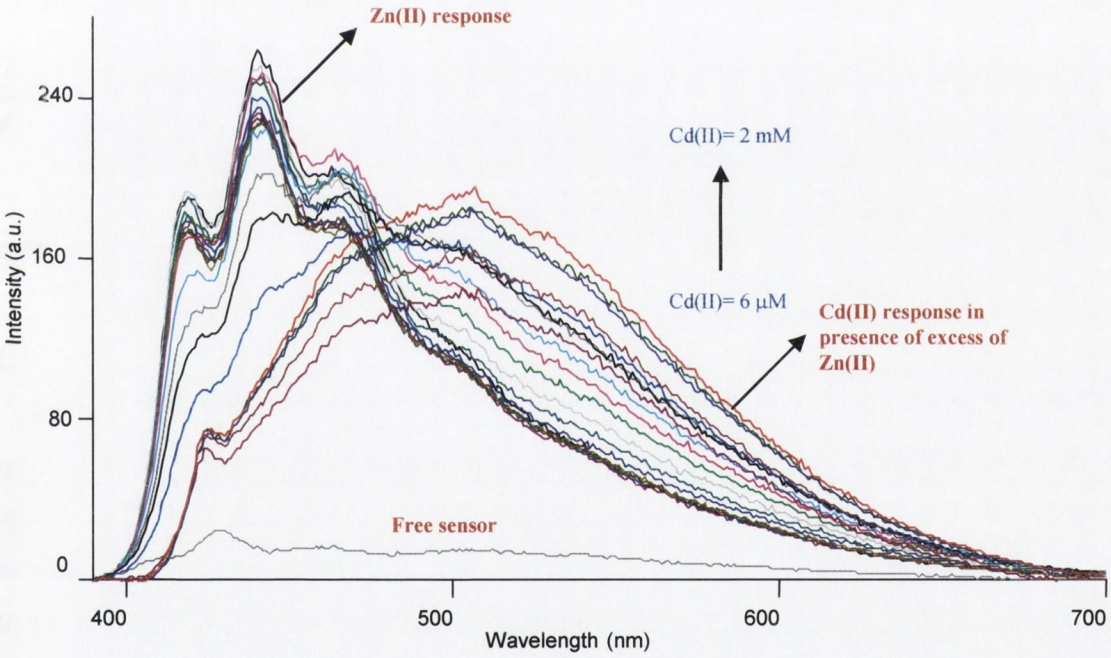

Figure 3.19 ***Fluorescence response of 126 to Cd(II) in presence of Zn(II). The addition of Zn(II) switches the normal anthracene fluorescence while Cd(II) causes structureless red-shift in the emission. The measurements were performed at pH 7.4 (0.020mM HEPES buffer, 0.135mM NaCl, 25 ^{0}C). Excitation was at 370 nm.***

3.7.9 Titration profile with different metal ions

No changes in the absorption and emission spectra of **125** and **126** were observed with group 2 metal ions, even at very high concentrations (10^{-2} M). The emission response of

125 and **126** on addition of Ca^{2+} is depicted in Figure 3.20. As can be seen no increase in the emission intensity even at higher concentration of metal ions.

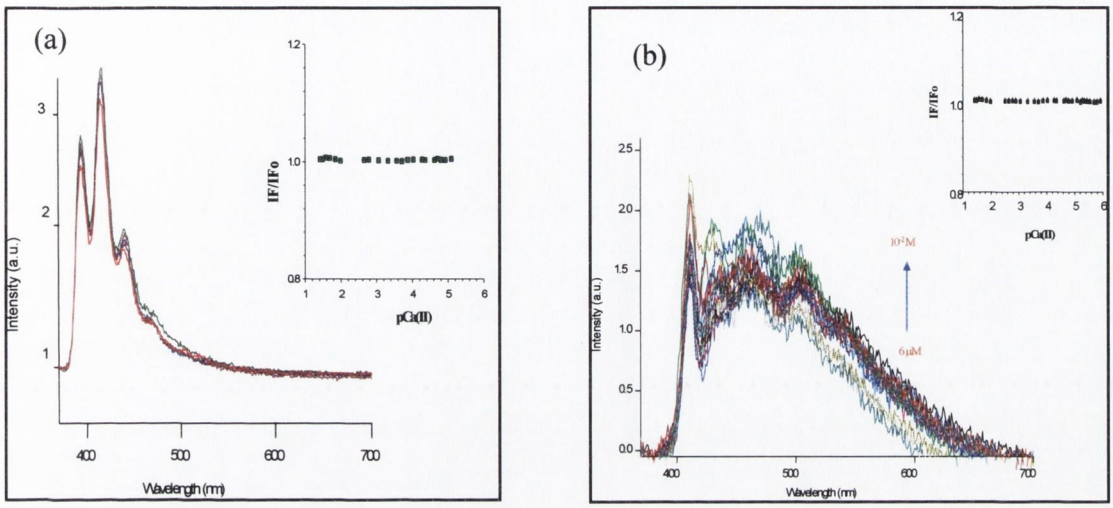

Figure 3.20 ***Fluorescence response of (a) 125 in presence of Ca^{2+} and insert shows a plot of relative fluorescence intensity at 428 nm versus pCa^{2+} at 450 nm (b) 126 in presence of Ca^{2} and insert shows a plot of relative fluorescence intensity at versus pCa^{2+} at 490 nm.***

Among transition metal ions, only negligible changes were observed for Hg(II) and Ni(II) while Cu(II) and Fe(II) did not lead to any changes.

3.8 Conclusions

Two novel anthracene based fluorescent PET sensors **125** and **126** have been synthesised for Zn(II) and Cd(II) signalling. The sensors exhibited high pH stability and aqueous solubility. The evaluation of the photophysical response of these sensors demonstrated their capability to detect Zn(II) and Cd(II) and to discriminate these from group 2 and other transition metal ions. In particular, both sensors have shown distinctive emission colours towards Zn(II) and Cd(II). A discrimination test performed to evaluate the selectivity for Cd(II) in the presence of Zn(II) proved successful. These studies suggested a possible application of these sensors to estimate level of Cd(II) poisoning, in particular sensor **126** which exhibits green emission for Cd(II). In this context further evaluation of **126** is required to determine the degree of toxicity, cell permeability and real time response.

Chapter-4

Microdamage Detection in Bones

4.1. Introduction

Damage in a composite material can be defined as "harm or injury that diminishes the value or usefulness of the "object".[238] This definition is also valid for bone as it is a composite material and is restricted to damage that results in the loss of material continuity. The effect of such damage will result in the degradation of the mechanical properties of bone and will manifest itself as cracks and voids, which are distinct from the naturally occurring voids in bone.[112] The occurrence of microcracks in bones has profound biological effects, as they play a role in the normal turnover process as well as in the adaptive behaviour of bone.[239,240] The repercussions of damage on any particular property depend on how the structure-function relationship is affected by damage.[241] Consequently as bone stiffness, strength, and creep exhibit different structure-function relationships, they are affected differently.[242] It is very important to characterise damage and to obtain a thorough understanding of the factors responsible for the various mechanical, structural and functional properties of bone. Three independent methods are used to characterise microdamage in bone:

- mechanical characterisation based on property degradation
- real-time characterisation by using acoustic emission and Raman spectroscopy
- physical characterisation by using histological and histomorphometric methods.

4.2. Mechanical characterisation

Bone microdamage can be inferred by measuring permanent changes in mechanical behaviour following some form of damage event such as single load-unload cycle, creep loading, relaxation loading, or fatigue loading. The properties used for quantifying the damage include stiffness and strength,[243] hysteresis,[244] creep rate,[245] relaxation,[246] yield strain or stress,[247] microhardness,[248] and residual strength behaviour.[249] Chamay and Tschantz[250] observed 'plastic slip lines' on overloaded ulnae by using scanning electron microscopy (SEM). Carter and Hayes[251] examined the residual strength of machined bovine cortical bone samples subjected to cyclic bending. By comparing the predicted monotonic tensile strength of each sample to its residual strength, the degradation was determined. Martin *et al.* reported the fatigue behaviour of equine cortical bone against a group of nonfatigued control samples for damage detection.[249] Hoshaw *et al.* subjected the canine proximal femur to cyclic compressive loading and used the monotonic failure

strength of the contralateral femur as the nondamaged strength value.[252] Keaveny *et al.* subjected human trabecular bone to a load-unload-reload experimental protocol and defined "residual strength" degradation by comparing the maximum stress attained during the reload cycle to the maximum stress attained during the first load cycle.[253]

4.3. Real-time characterisation

Several investigators have used acoustic emission (AE) to study the onset of yield and post-yield behaviour of bone.[254] During the initiation and propagation of microcracks the stored elastic energy released is converted into elastic wave energy that can be detected as an acoustic event.[255,256] Measuring AE during mechanical loading can be used to quantify the number of events and characterise the energy content of the event. Jonsson and Eriksson[256] detected AE events during loading and unloading of intact canine femurs subjected to a sequence of torsional loads with increasing amplitude. Inoue *et al.* found that low-amplitude AE occurred at yield and high-amplitude AE occurred at the failure regions for bovine bone loaded in the longitudinal direction.[257] Rajachar *et al.* have used AE to characterise focal and diffuse microdamage in bone.[258] Morris *et al.* used Raman spectral shifts to detect fatigue-induced microdamage in bovine bones.[259] They observed the frequency shift in the phosphate band, which was attributed to the formation of more stoichiometric and less carbonated mineral species induced by microdamage.

4.4. Histological detection of microdamage

Histology is by far the most commonly used method for studying the quality and characteristics of damage responsible for mechanical degradation. Transmitted light microscopy can be used either alone or in conjunction with a dye to allow the distinction of microcracks from the surrounding bone matrix. Basic fuchsin was the first dye used to label *in vivo* microdamage by Frost.[112] Basic fuchsin is an ethanol soluble dye but almost insoluble (0.3-2.4%, *w/v*) in water. This insolubility in water ensured that dye did not leach out and stain artifactual cracks induced during sectioning. Basic fuchsin is the traditional name for various mixtures of four triamino-triphenylmethane homologs, with increasing degrees of methylation; namely pararosaniline, rosaniline, megenta II and new fuchsin (Figure 4.1).

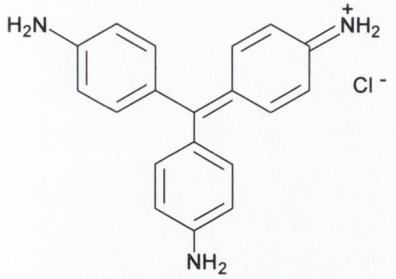

Pararosaniline

131

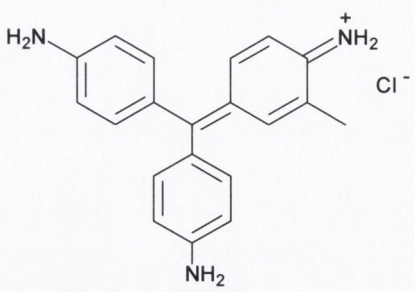

rosaniline

132

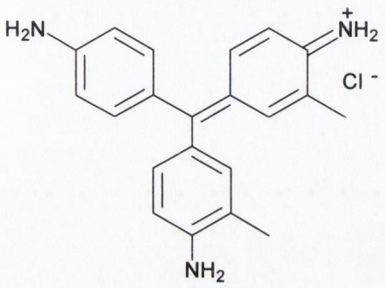

magenta II

133

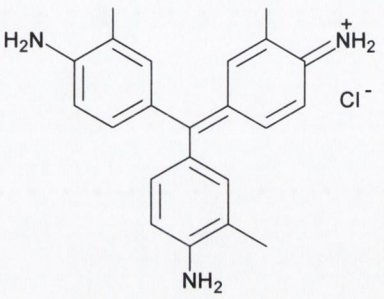

new fuschin

134

Figure 4.1 ***Various constituents of basic fuchsin.***

Forwood and Parker[260] extended the use of the fuchsin for *in vitro* microdamage detection. Burr and Stafford later validated this bulk-staining technique and modified Frost's criteria for identifying microcracks (Table 4.1).[261,262] Bulk staining of bones with basic fuchsin was soon established as the method of choice for differentiating cracks generated during dehydration, sectioning, and polishing from those existing in the tissue prior to processing.[263,264]

Table 4.1 ***Criteria for microcrack detection.***[261,262]

Criteria for identifying microcracks
1. They are intermediate in size, being larger than canaliculi but smaller than vascular channels.
2. They have sharp borders with a halo of basic fuschin staining around them.
3. They are stained through the depth of the section.
4. When the depth of the focus is changed, the edge of the crack can be observed to be more deeply stained than the intervening space.

However there are still many limitations of basic fuschin staining:

- quantification of microdamage is underestimated. As basic fushin stains the bone by a diffusion mechanism, some of the cracks are left unstained
- this technique uses light microscopy, therefore it is not useful for visualisation or quantification of sub-microscopic damage
- bone is an anisotropic biomaterial, it possesses variation in density. There may be some areas of low density, which are overstained, while those of high density may be understained.

Lee *et al* combined epifluorescence microscopy and transmitted light microscopy (TLM) to quantify and improve the prediction accuracy of microcrack detection using basic fuchsin.[264] Their modified criteria and methodology for identifying microcracks are shown in Table 4.2.

Table 4.2 ***Criteria for identifying microcracks using epifluorescence and TLM.***[264]

Modified criteria for identifying microcracks
1. They are intermediate in size, being larger than canaliculi but smaller than vascular channels. detection by fluorescence, green incident light (546 nm), ×125 magnification
2. They have sharp borders with a halo of basic fuschin staining around them. detection by fluorescence, green incident light (546 nm), ×125 magnification
3. They are stained through the depth of the section. detection by fluorescence, UV incident light (365 nm), ×125 magnification.
4. When the depth of the focus is changed, the edges of the crack can be observed to be more deeply stained than the intervening space. detection by light microscopy, ×225 magnification

Although Lee *et al.*[264] modified the Burr criteria, there are still some inherent difficulties in the method itself. During sectioning, large numbers of microcracks are generated. Although it is possible to distinguish pre-existing microcracks from artifactual damage by varying light intensity, depth of focus and magnification, the procedure is both difficult and time-consuming.[264] To distinguish artifactual damage from either *in vivo* or *in*

vitro damage, more than one agent would be required. A sequence of such fluorochromes, which can be applied one after another, would be useful for measuring microcrack propagation. In a revolutionary work Lee *et al.*[265] introduced a novel idea for sequential labelling of microdamage. They used five colorimetric agents - calcein, xylenol orange, alizarin complexone, calcein blue and oxytetracycline (**135-139**) to label microdamage.

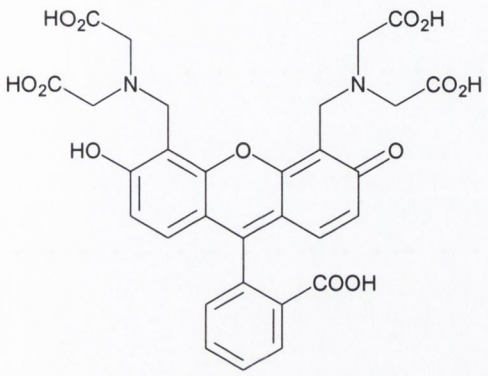

Calcein

135

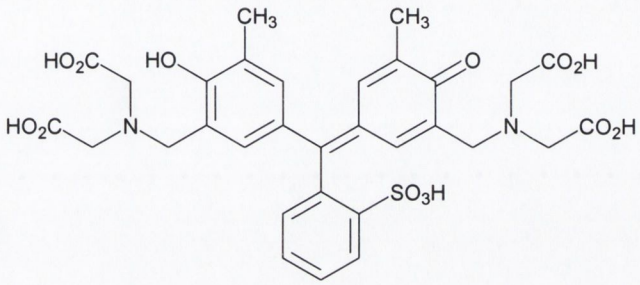

136

Xylenol orange

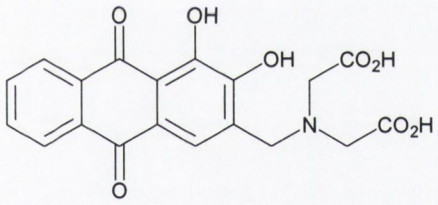

Alizarin complexone

137

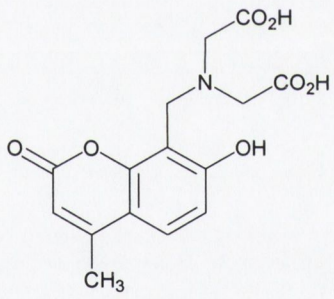

Calcein blue

138

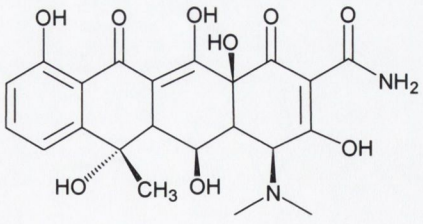

Oxytetracycline

139

The excitation and emission wavelengths and colour of these dyes are summarised in Table 4.3.[266]

Table 4.3 ***Fluorescence parameters of fluorophores.***[266]

fluorophores	Excitation Wavelength (nm)	Emission Wavelength (nm)	Colour
Alizarin complexone	580	625	Red
Xylenol orange	365	615	Orange
Calcein	495	517	Green
Calcein blue	365	450	Blue
Oxytetracycline	390	520	Green

A 1% aqueous solution of each of the chelating agent was used during testing. According to the authors, the chelating fluorochromes were able to form a strong chelate complex with the free calcium ions, which are released during the formation of microcracks thus making the dyes site-specific. Substitution of one dye for another, when the dyes were applied in sequence, made distinguishing individual dyes difficult.[267] Additionally different fluorescence intensities were observed when UV light (365 nm) was used for excitation. O'Brien *et al.*[268] modified the procedure by combining ion-chromatography with a substitution test and were able to determine the sequence and concentrations of the dyes. This eliminated the earlier drawbacks of substitution. The observed sequence of dyes and their optimal concentrations are shown in Table 4.4.

Table 4.4 ***Sequence of dyes and their concentration.***[38]

Dye Sequence	Concentration
Alizarin complexone	0.0005 M
Xylenol orange	0.0005 M
Calcein	0.0005 M
Calcein blue	0.0001 M

4.5. Motivation for the present work

Both Lee *et al.* and O'Brien *et al.* have used the chelating agents for quantifying and monitoring the microcrack growth.[267,268] However the dyes (**135-139**) suffer from a number of disadvantages:

- they have limited solubility in water. For example, the solubility of alizarin complexone and calcein in water is 0.1% and 0.4% respectively (*w/v*)[269]
- these dyes consist of aliphatic nitrogen atoms so they have high pK_a values *e.g.* pK_a of alizarin complexone,calcein blue and calcein is 10.35, 7.80 and 11.70 respectively. The dyes require a basic medium for their application[270,271]
- they show no affinity for Ca^{2+} at neutral pH and weak affinity at pH 10, which increases considerably at pH > 12[272]
- they are already highly fluorescent. At neutral pH, protonation of the nitrogen moiety of the receptor prevents PET (Figure 4.2), so the dyes are highly fluorescent. At higher pH (~ 12), the unprotonated amine in capable of quenching the excited state of the fluorophore. These dyes bind to Ca^{2+} effectively at higher pH, inhibiting PET process.

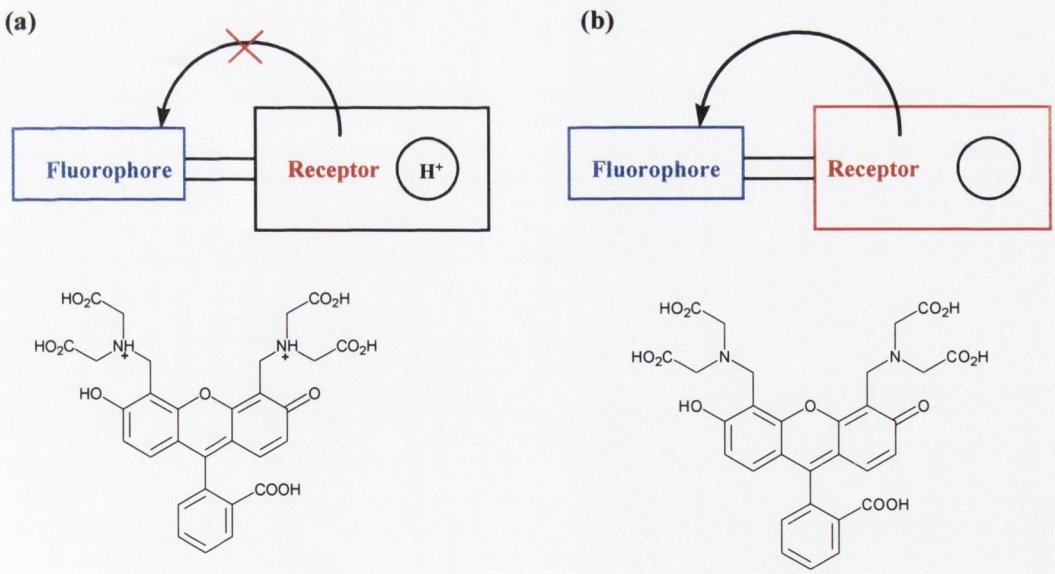

Figure 4.2 ***Schematic representation of PET process operating in calcein (136) (a) At pH~ 7.4 the protonated amine prevents PET. (b) At higher pH, PET is operating and it is at this pH that the dye can bind to*** Ca^{2+}.

With these drawbacks in mind, the aim of this study was two fold:

- it was decided to investigate the fluorescence response of these dyes at pH 7.4 in a buffered solution to Ca^{2+} and to calculate their binding affinities with the Ca^{2+} ions
- it was proposed to refine this technique by using a new set of dyes, which are non-fluorescent in the absence of Ca^{2+} and are highly fluorescent when bound to Ca^{2+}. Also to use the dyes that are pH independent in the physiological range and sufficiently soluble in water.

4.5.1 Fluorescent evaluation of 135, 136 and 138

Dyes were purchased from Aldrich Chemicals and used as received. A 10^{-4} M solution of each dye was made in the 20 mM HEPES containing 135 mM KCl at pH 7.4. Increasing concentration of Ca^{2+} was added and fluorescence spectra were recorded. The fluorescence response of calcein blue (**135**), calcein (**136**) and xylenol orange (**138**) was evaluated at pH 7.4.

Alizarin complexone was highly insoluble in water, so it was eliminated from the study. It is well documented[273] in the literature that, at high pH, these dyes show strong affinity for Ca^{2+} with a large degree of fluorescence enhancement, therefore titrations at higher pH were not performed for the three dyes. Also it is known that absorption spectra do not change with Ca^{2+}, eliminating the need to perform absorption titrations.[273,274] The fluorescence response of these dyes for Ca^{2+} are shown in Figures 4.3, 4.4 and 4.5.

Calcein blue was excited at 365 nm and the emission was observed between 400-550 nm with an emission maximum of 450 nm. Upon addition of Ca^{2+} the negligible emission intensity increase was observed indicating that the dye has no affinity for Ca^{2+} at this particular pH. Similar results were obtained for calcein, when excited at 494 nm. A broad emission band was observed at 517 nm.

The emission profile for calcein is depicted in Figure 4.4. Xylenol orange was excited at 385 nm and the fluorescence emission maximum was observed at 615 nm. The dye initially showed slight increase in the fluorescence intensity with Ca^{2+}. However as the addition of Ca^{2+}continued during titration, a decrease in emission intensity was observed. This might be due the interaction of the metal ions with the fluorophore.

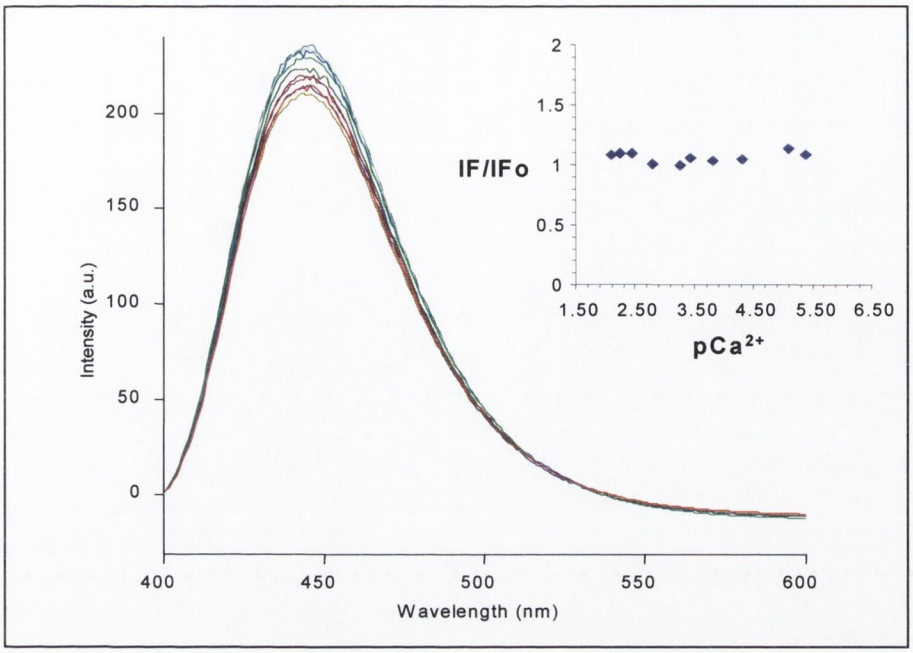

Figure 4.3 ***Fluorescence response of calcein blue (135) with Ca^{2+}. Insert is the plot of relative fluorescence intensity at 450 nm against pCa. Measurements were performed in HEPES buffer at pH 7.4.***

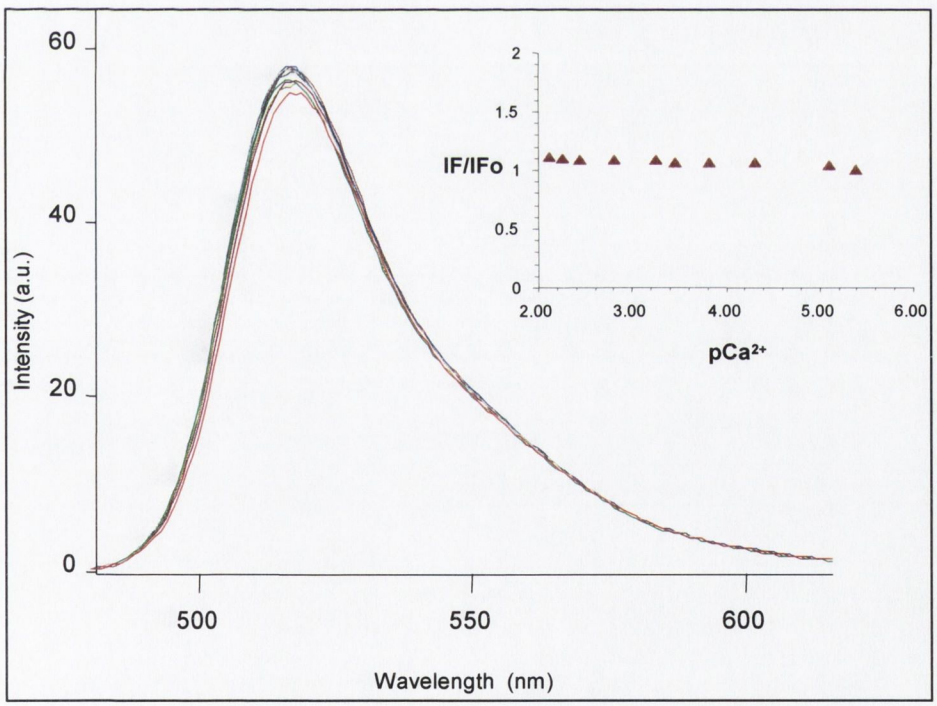

Figure 4.4 ***Fluorescence emission intensity profile for calcein (136) with Ca^{2+}. Insert is the plot of relative fluorescence intensity at 520 nm versus pCa.***

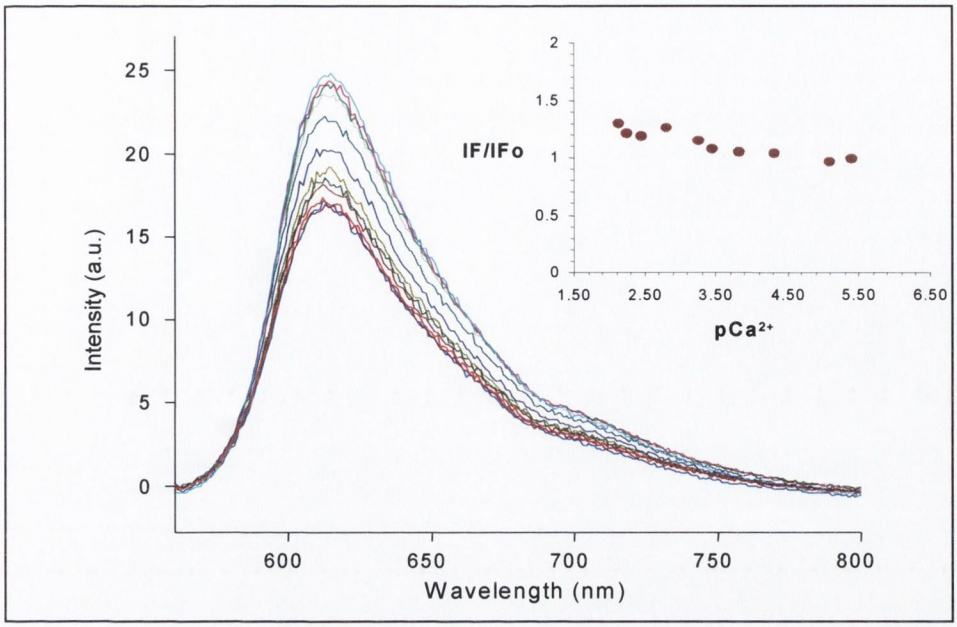

Figure 4.5 ***Fluorescence response of xylenol orange (138) with Ca^{2+}. Insert shows the plot of relative fluorescence intensity at 610 nm against pCa***

The near zero slope of the fluorescence emission response *versus* pCa in all cases clearly demonstrates that there is almost no affinity of these dyes for Ca^{2+} at pH 7.4, eliminating their use as potential Ca^{2+} sensors in microdamage detection at physiological pH. Furthermore, these dyes show strong affinity for other ions such as Cu(II), Fe(III), Fe(II), Pb(II), Zn(II) and other group 2 metals.[269,273,274] All these properties render these dyes unsuitable for *in vivo* use.

At this stage it was decided to use a set of commercially available well known Ca^{2+} indicators whose sensitivity, selectivity and binding affinity are well documented.

4.5.2 Evaluation of PET based Ca^{2+} indicators for detection of microdamage

The dyes chosen for the study were calcium orange (**140**), calcium crimson (**141**) and fluo-3 (**142**). Fluo-3 was developed by Tsien *et al.*[46]and is widely used for imaging intracellular calcium.[275] It is also used in flow cytometry [276] and in cell-based high-throughput screening assays for drug discovery.[189] It has a very low quantum yield of fluorescence in the absence of Ca^{2+}, possibly due to intramolecular electron transfer from the receptor moiety to the fluorophore in a non-emissive twisted internal charge transfer state (TICT).[277] Ca^{2+} binding raises the energy of the TICT state above that of the

fluorophore preventing electron transfer. Fluo-3 shows an almost 100-fold fluorescence enhancement upon Ca^{2+} binding, without any significant absorption or emission shifts.[50] Calcium crimson and calcium orange are long-wavelength indicators introduced by Molecular Probes Inc., Eugene, Oregon.[278] Like fluo-3 these indicators exhibit no shifts in wavelength. Both these indicators are more photostable than fluo-3.[50] Calcium orange has been used to monitor Ca^{2+} in intact photoreceptors modified with genetically altered rhodopsin pigments.[279] It is also used to monitor Ca^{2+} influx and release in hippocampal astrocytes.[280] Calcium crimson has been used to investigate intracellular Ca^{2+}concentration in rat brain tissue.[281]

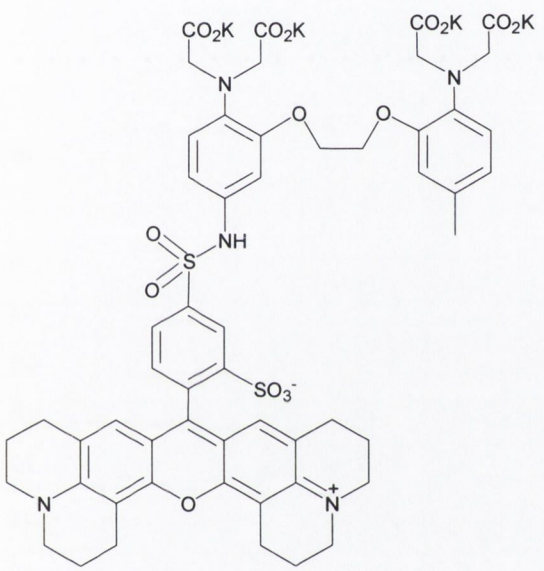

Calcium Crimson

140

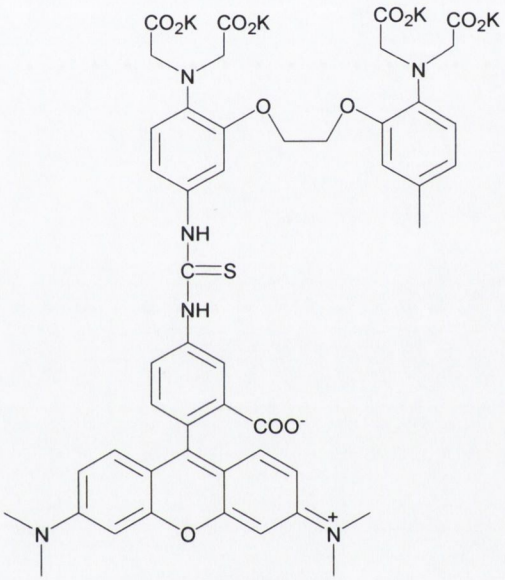

Calcium Orange

141

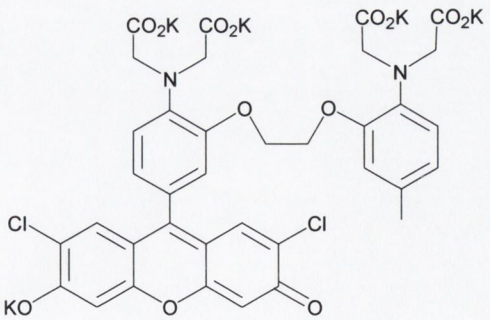

Fluo-3

142

Photophysical parameters and dissociation constants (K_D) of these dyes are summarised in Table 4.5.[50,282]

Table 4.5 ***Spectroscopic and thermodynamical data of 140, 141 and 142.***

Fluoroprobe	Excitation (nm)	Emission (nm)	Extinction coefficient	K_D
Calcium crimson	588	607	113,000	203 nM
Calcium orange	551	574	90,000	423 nM
Fluo-3	506	526	80,000	3900 nM

The receptor in these dyes is a multidentate ligand that has chelating groups organised in three dimensions. This receptor can enclose a metal ion completely. This allows the chelating agent to be highly dependent on the size and charge of the metal ion, and so extremely selective. The use of the BAPTA chelator ensures that the pKa value of the receptor does not overlap with physiological pH range, so the weakly acidic conditions will not provide a false positive response *via* 'protonation'. Also the fluorophore used in these dyes does not contain any ionisable groups in the pH range 7-8. Since the potassium salts of these indicators are used, they possess high water solubility as well as high stability. High wavelength used for excitation will reduce interference from auotofluorescence (from bone proteins such as collagen), and light scattering. The dyes have high extinction-coefficient value, thus they absorb strongly, which permit lower dye concentration to be used in order to prevent photo-toxicity to bones and bone cells when applied *in vivo*.

4.5.3. Epifluorescence studies of 140, 141 and 142

The dyes were purchased from Molecular Probes Ltd., Eugene, Oregon. Fluo-3 (**142**) and calcium orange (**141**) were received as potassium salts and used as received. Calcium crimson (**140**) was obtained as its ethyl ester derivative and was hydrolysed prior to use. The procedure, followed for hydrolysis is the same as that described in Chapter 2 (Section 2.5.1). The ethyl ester was dissolved in 5 mL of methanol and 1 mL of 3 M aqueous KOH was added to it and reaction mixture was refluxed for 2 hours. The solvent was evaporated and the residue extracted in water and precipitated by the addition of ethanol. A 10^{-4} M solution of each dye was prepared in buffer solution (20 mM HEPES, 135 mM KCl, pH =

7.4). Bovine tibia were obtained from a meat wholesaler (KEPAK Ltd., Clonee, Co. Dublin) from animals slaughtered 2-3 days previously. The soft tissue was removed from all bones and they were stored at -20^0C until required. Longitudinal sections of cortical bone from the mid-diaphysis were cut into beams using a band saw and polished using emery paper (grade 400). All machining was carried out in wet conditions and the bones were not allowed to dry at any time. After machining the specimens were stored at -20^0C prior to staining. The bone samples were scratched and then dipped into the dye solution and examined using UV epifluorescence (λ= 365 nm) and green epifluorescence (λ= 546 nm). The microscope used for imaging was Nikon Eclipse E800. Images were captured using a CCD Colour Video Camera and analysed using Image software Lucia.

4.5.3.1 Bone - scratch test, penetration test, and substitution test using 140, 141 and 142

Scratch tests were performed on bone specimens using the dyes **141**, **142** and **143**. The protocol for the scratch test was based on established methods[38] and is shown in Table 4.6.

Table 4.6 ***Methodology for scratch test.***

Protocol for the scratch test
1. 5 mm straight line was scratched on the surface of the bone sample.
2. Samples were dipped in to a 10^{-4} M buffered solution of each chelating agent in an individual vial, which is placed under vacuum (50 mm Hg) for an intervals of 5, 15, 30, and 60 minutes.
3. Specimens were washed in deionised water and examined using epifluorescence microscopy (365 nm).

During substitution tests dyes were applied in sequence, in order of decreasing binding strength (Table 4.5), to the bone samples. The first substitution tests were standardised initially using two agents and then it was extended to all the three agents as outlined in Table 4.7

Table 4.7 ***Methodology for substitution test performed with 140, 141 and 142.***

Protocol for substitution test using dyes
1. 5 mm straight line scratched on the surface of bone samples using a compass
2. Bone samples were immersed in 10^{-4}M buffered solutions of each chelating agent in individual vials and placed under vacuum (50 mm Hg) for 15 minutes.
3. Specimens were washed in de-ionised water and a new line of the same length drawn parallel to the earlier one.
4. Steps 2 and 3 repeated till all the dyes were used.
5. Specimens were washed in deionised water and examined using epifluorescence microscopy (365 nm).

In order to investigate the ability of these dyes to penetrate inside the bone matrix, bone specimens were dipped into solutions of each dye overnight and then cut into transverse sections. The methodology followed is depicted in Table 4.8.

Table 4.8 ***Procedure followed for determining the penetration ability of the dyes 140-142.***

Protocol for penetration test
1. Bone samples were dipped in 10^{-4} M solutions of dye in individual vials and placed under vacuum (50 mm Hg) for 24 hours.
2. Transverse sections were cut using a diamond saw, cleaned and polished with emery paper.
3. Specimens were then washed with deionised water and analysed using epifluorescence microscopy (365 nm and 546 nm).

4.5.3.2. Evaluation of scratch tests with calcium crimson

During scratch tests, the bone specimens were immersed in calcium crimson solution for various intervals of time (5, 15, 30 and 60 minutes). The dye labelled bone specimens were excited at 365 nm using epifluorescence microscopy and the areas of scratch were analysed (Figure 4.6). As can be seen from the pictures there is little difference in the brightness of the calcium crimson labelled scratch with increased time. From the Figure 4.6 (pictures c and d), it is clear that longer immersion times lead to binding of the dye to the surrounding area of the scratch. Qualitative analysis showed that increasing the time did not lead to any improvement in the colour or intensity. Thus 15 minutes was deemed the optimal time for scratch test and was followed for the other dyes.

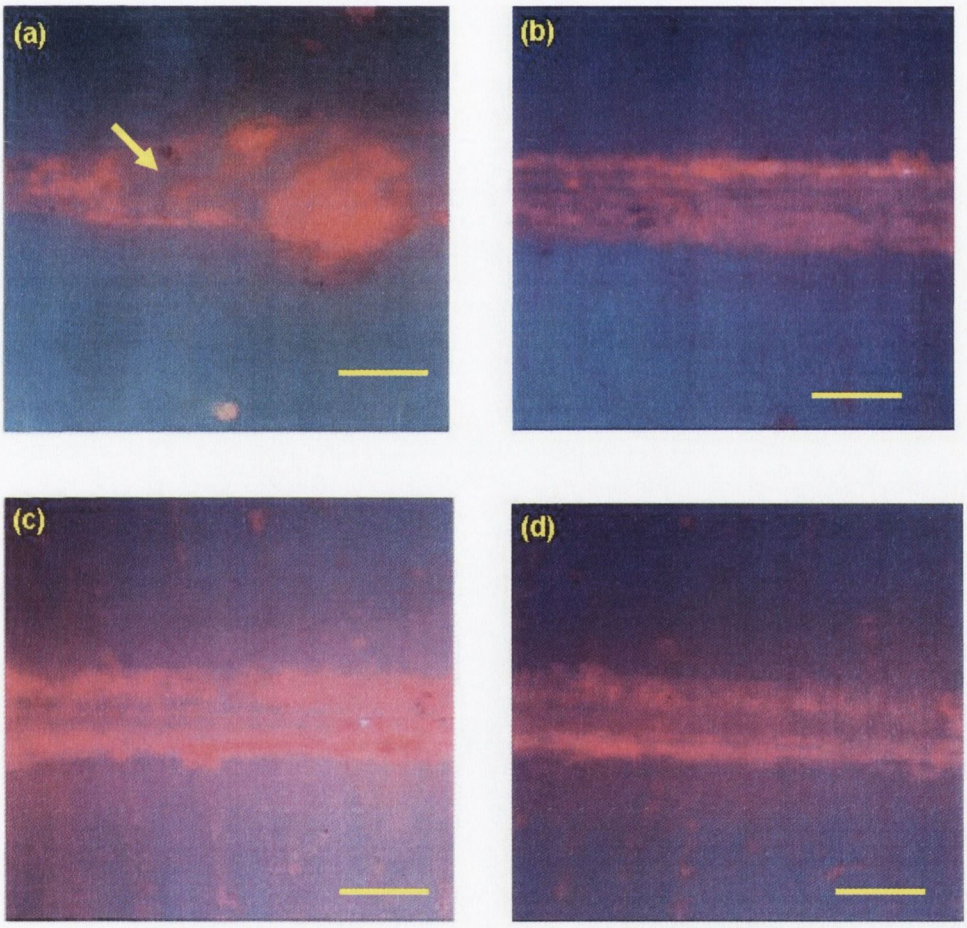

Figure 4.6 ***Scratch (arrow) labelled with calcium crimson (140) at different time intervals. (a) 5 minutes; (b) 15 minutes; (c) 30 minutes; (d) 60 minutes; UV epifluorescence (365 nm). Bar = 100 μm.***

The bright pink colour of the dye provided good contrast from the blue autofluorescence observed from the collagen proteins of bone. It is hypothesised that this scratch area consists of coordinatively unsaturated Ca^{2+} that are available for binding with suitable chelating agent. The well known affinity of **140** towards Ca^{2+} facilitates binding and consequent inhibition of PET process in dye switches the emission '*on*'. The other important advantage is that the dye is highly water soluble and so buffered solutions can be readily prepared.

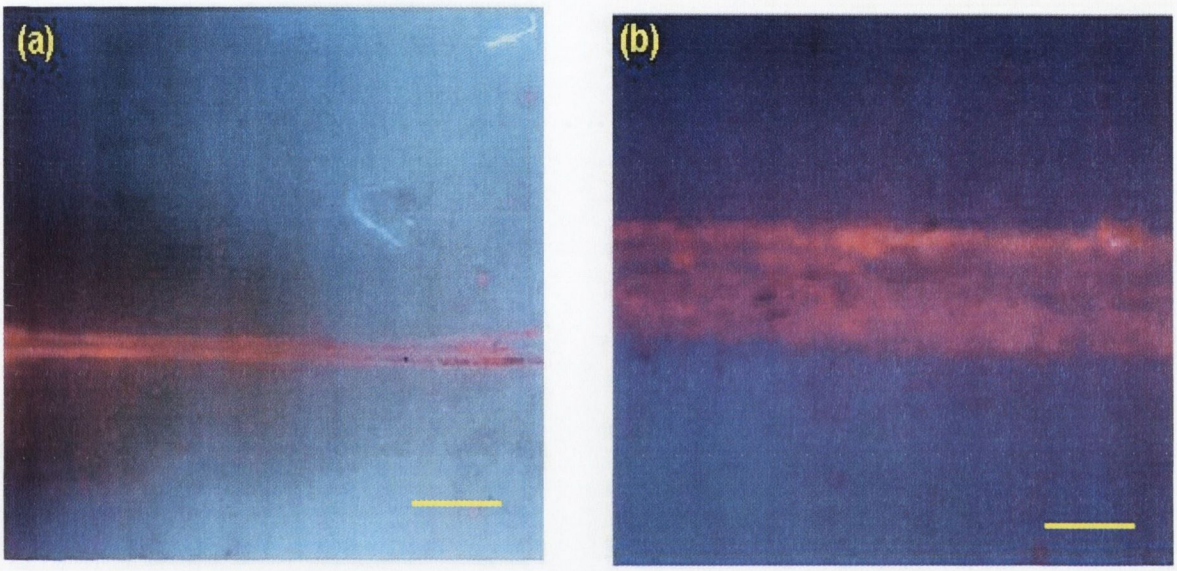

Figure 4.7 ***Bone surface showing scratch labelled with calcium crimson (140) at different magnification: (a) x 2X; bar = 500 μm (b) 10X; bar = 100 μm; UV epifluorescence (365 nm).***

The scratch was completely labelled with the dye (Figure 4.7 a). The image were also analysed under different magnifications as illustrated in Figure 4.7 b. It demonstrates that **140** was able to label the scratch in its entirety without affecting the surrounding area of the bone.

4.5.3.3 Evaluation of scratch tests with calcium orange and fluo-3

Similar results were obtained with both calcium orange (**141**) and fluo-3 (**142**). Both these dyes were excited at 365 nm in the epifluorescence measurements. Dye **141** exhibited orange fluorescence (Figure 4.8) and **142** green fluorescence (Figure 4.9). Both

these dyes were able to label the scratch effectively, making the scratched area distinguishable from the surrounding area of the bone specimens.

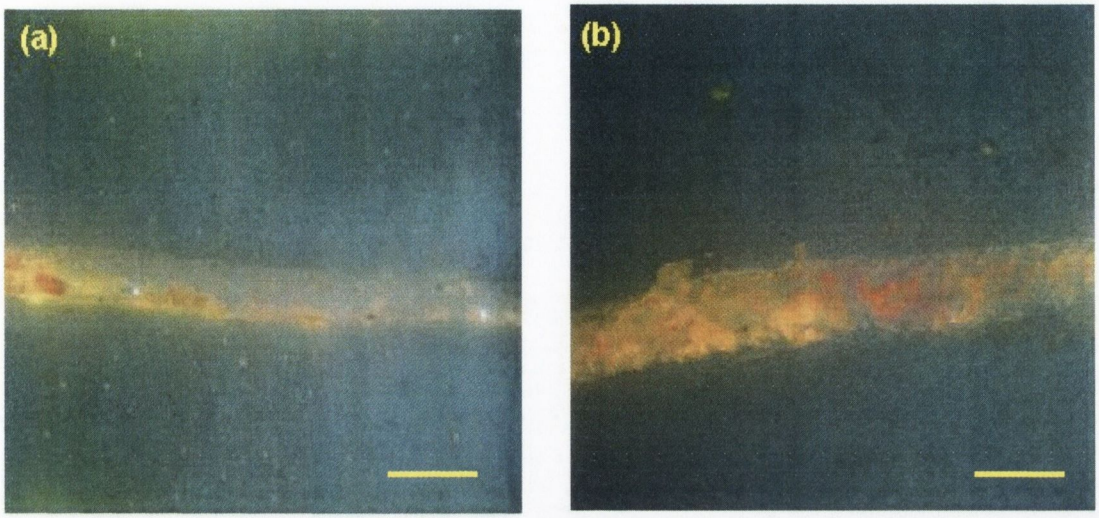

Figure 4.8 ***Bone surface showing scratch labelled with calcium orange at different magnification: (a) x 2X; ; bar = 200 μm (b) x 4X.; bar = μm, UV epifluorescence (365 nm).***

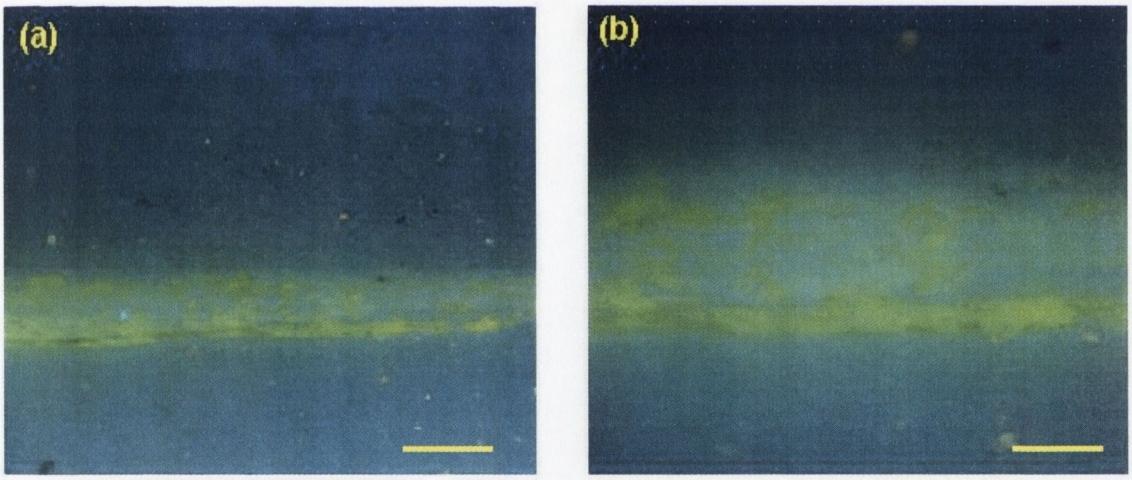

Figure 4.9 ***Bone surface showing scratch labelled with Fluo-3 at different magnification: (A) x 4X; bar = 250μm (B) x 10X; bar = 100 μm. UV epifluorescence (365 nm).***

4.5.3.4. Evaluation of substitution tests with 140, 141 and 142

As shown in Table 4.5, the binding constant of dyes increases in the order of **142< 141<140**. Therefore, in theory, if these dyes are applied in a sequence of decreasing binding constant, no substitution is expected. In order to test this, substitution tests were

performed using a two dye sequence as described in Table 4.7. The results obtained are shown in Figure 4.10.

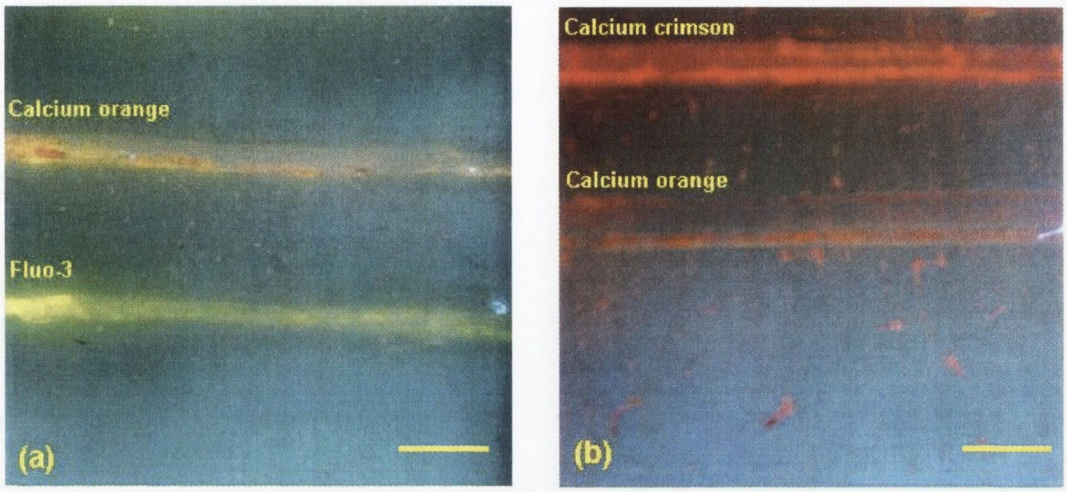

Figure 4.10 ***Substitution test with two dye sequence: (a) calcium orange and fluo-3; bar = 500 μm (b) calcium crimson and calcium orange; UV epifluorescence (365 nm). Bar= 200 μm***

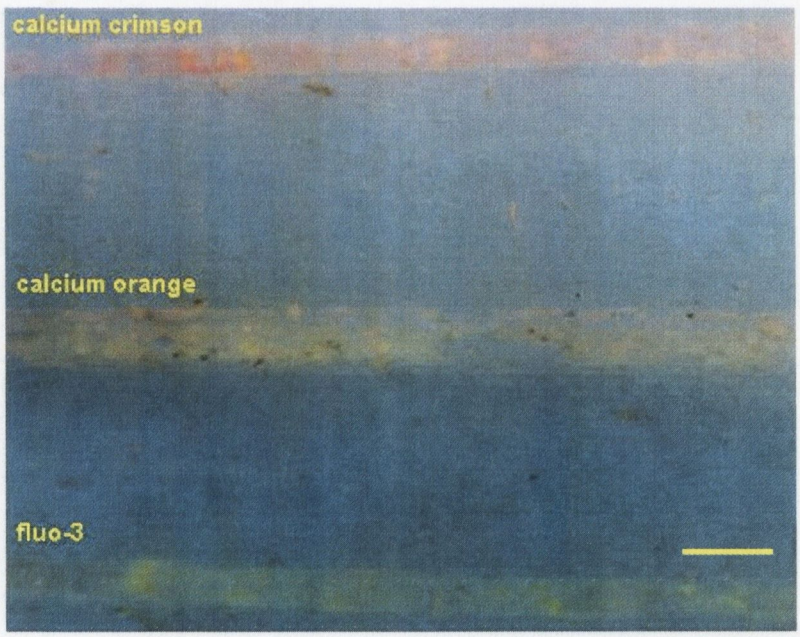

Figure 4.11 ***Three-dye sequence for analysing the substitution pattern: calcium crimson, Calcium orange and fluo-3; UV epifluorescence (365 nm). Bar = 200 μm.***

Extending the test to a three dye sequence resulted in no substitution or mixing, and also the three dyes are clearly distinct both from each other and also from the surrounding bone matrix (Figure 4.11). This noticeable sequencing could be of help in identifying a propagating microcrack in microdamage detection.

4.5.3.5 Evaluation of penetration tests with 140, 141 and 142

Bone is a complex material that consists of canals, Haversian systems, canaliculi and resorption cavities. Dyes that have the ability to penetrate the bone matrix are of considerable significance in understanding this complex morphology. For this purpose a penetration test as described in Table 4.8, is very useful. As a preliminary test, indicator **141** was selected to conduct a penetration test on a transverse section of bone specimen. The UV epifluorescence of **141** is depicted in Figure 4.12.

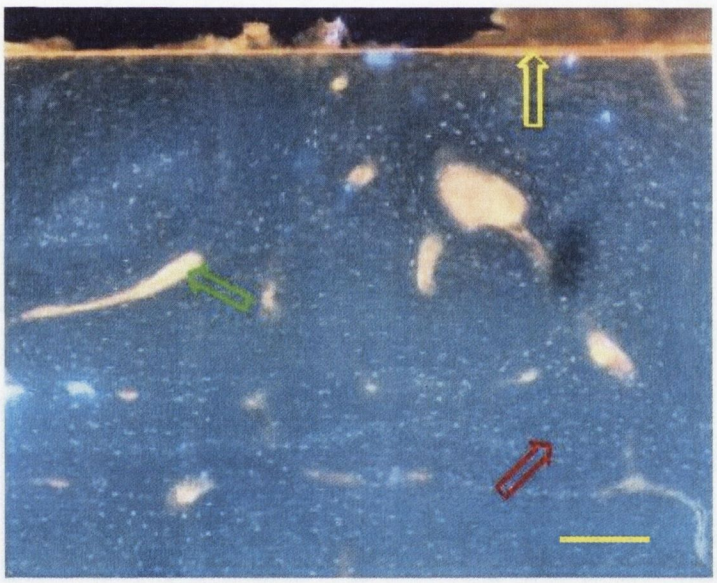

Figure 4.12 ***Transverse section of the bone labelled with calcium orange in UV epifluorescence microscopy (365 nm excitation). yellow arrow = bone surface; red arrow = bone cells; green arrow = bone canal Bar = 100 μm.***

It is clear that **141** is able to label selectively the different components of bone. The area marked with green, yellow and red arrows in Figure 4.12 are a bone canal, bone surface and bone cells respectively. It could be reasoned that these components might contain suitable vacancies such as Ca^{2+} to facilitate the PET inhibiting interaction with the dye. The internal structure of the bone comprising osteons and interstial lamellae are

clearly visible when viewed under green epifluorescence (546 nm) as shown in Figure 4.13 and Figure 4.14.

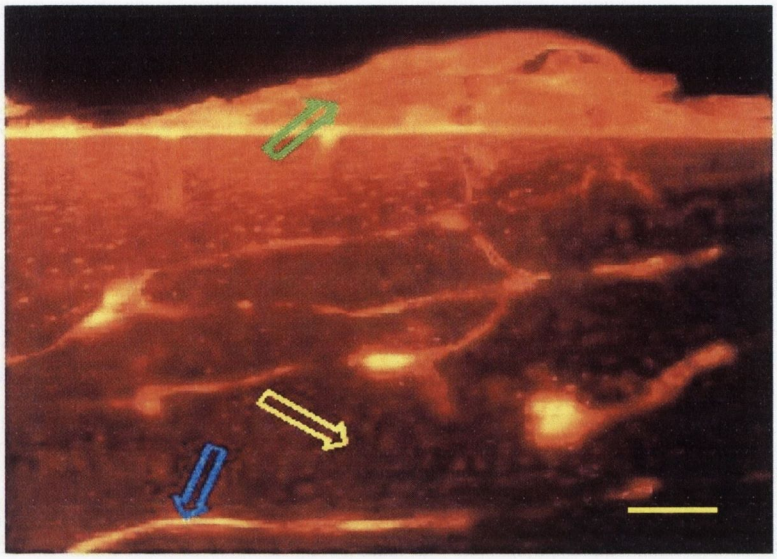

Figure 4.13 ***Transverse section of the bone labelled with calcium orange in green epifluorescence microscopy (546 nm); green arrow = bone surface; yellow arrow = bone cells; blue arrow = bone canal. Bar = 100 μm***

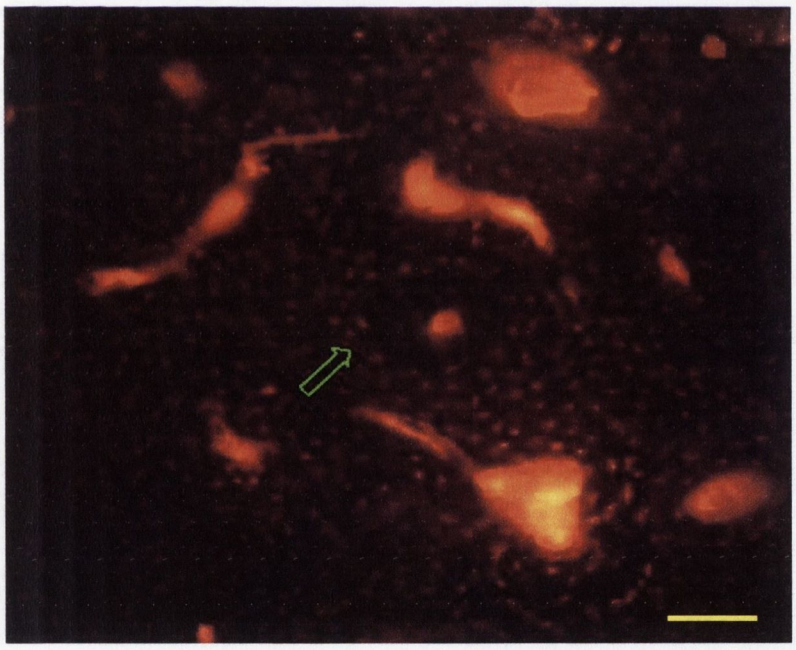

Figure 4.14 ***Transverse section of the bone labelled with calcium orange in green epifluorescence microscopy (546 nm excitation); green arrow shows osteon with its lacunae, Haversian canal and canaliculi. Bar = 100μm***

4.5.4 Bone - scratch tests and penetration tests using 92, 93, 125 and 143

As the hydroxyapatite matrix of bone possess gel like properties and has the ability to incorporate substances containing carboxylate as well as hydroxyl groups, it was decided to investigate the ability of the fluorophores **92**, **93** and **125** to label the scratches generated on the bone surface. The design, synthesis and characterization of **92**, **93** and **125** is discussed in detail in Chapter 2 and 3. The carboxylate groups in these dyes would be able to interact with the chemical components of the damaged bone lattice, providing selective labelling of the scratch.

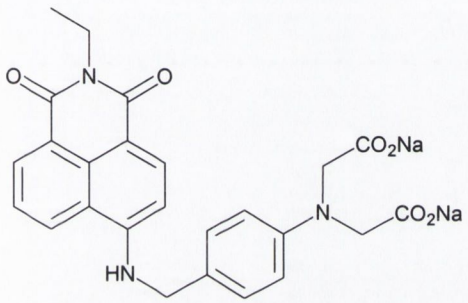

92

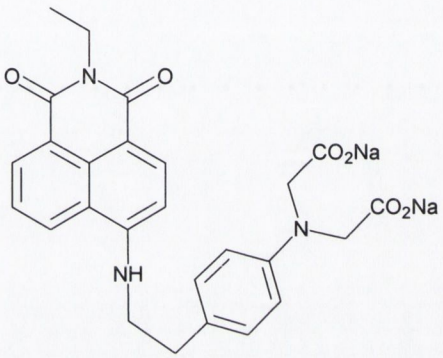

93

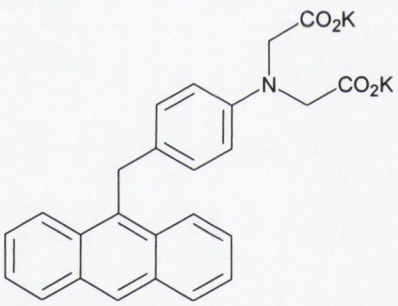

125

4.5.4.1 Evaluation of scratch tests with 92, 93 and 125

The scratch tests were performed in the manner as discussed earlier in Table 4.6. The resulted obtained for the compounds **92** and **93** were encouraging. The dyes showed good affinity for the scratch rather than the surrounding bone matrix (Figure 4.15). However, in the case of **125** it was impossible to distinguish the scratch from the matrix. This is due to the fact that the fluorescence of this dye overlap with the autofluorescence of the bone (Figure 4.16). This dye was then eliminated from the study.

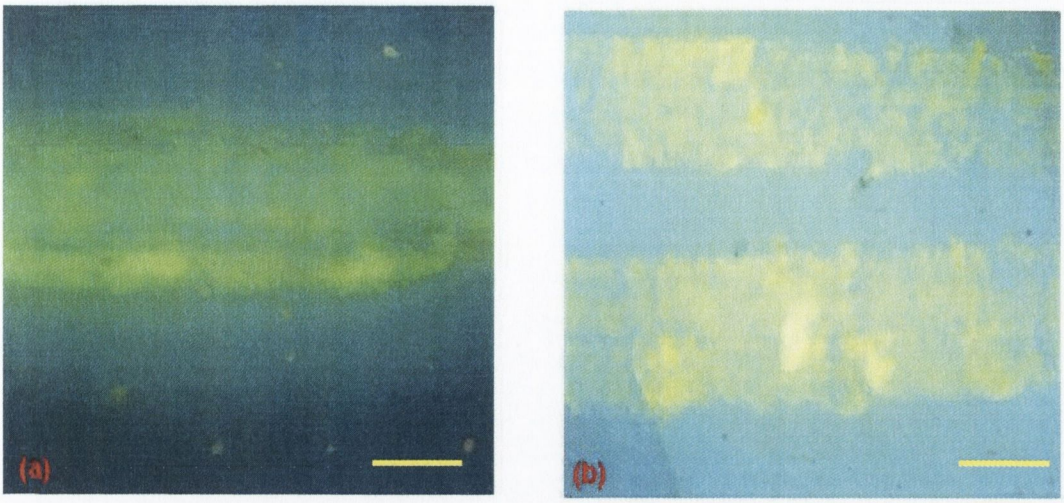

Figure 4.15 ***Bone surface showing scratch labelled (a) with 92 and (b) with 93; at magnification x 10X; UV epifluorescence (365 nm). Bar = 100 μm***

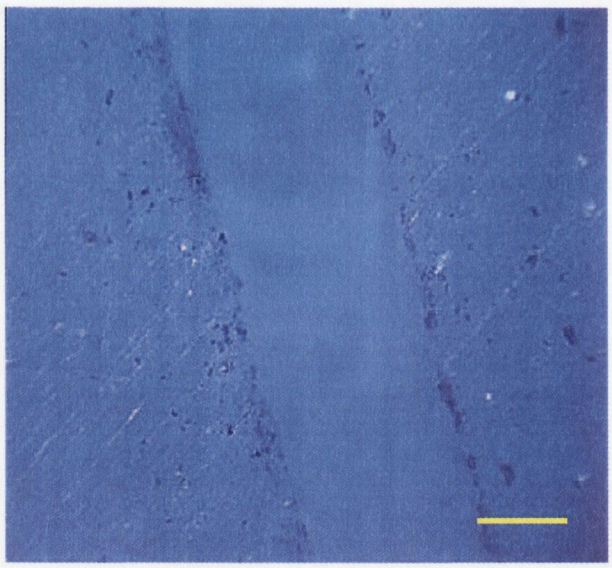

Figure 4.16 ***Bone surface showing scratch labelled 125; at magnification x 10X; UV epifluorescence (365 nm). Bar = 100 μm***

4.5.4.2 Evaluation of penetration test with 92

In the manner as described earlier to investigate the internal structure of the bone, a penetration test (Table 4.8) was performed using **92**. The penetration test results are depicted in Figure 4.17.

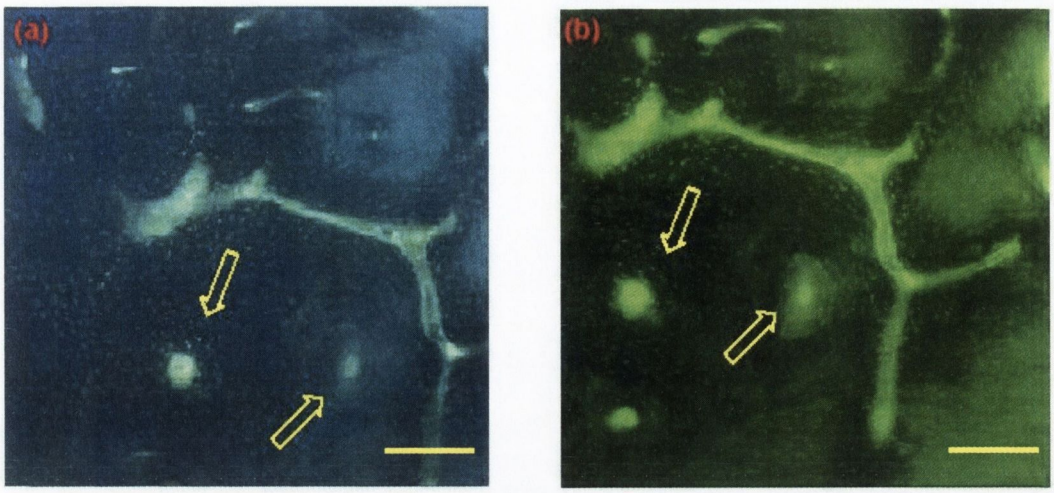

Figure 4.17 ***Transverse section of the bone labelled with 92 viewed in (a) UV epifluorescence (365 nm) and (b) green epifluorescence microscopy (546 nm excitation); yellow arrow shows osteon with its lacunae, Haversian canal and canaliculi. Bar = 100 μm***

These results demonstrates the ability of **92** and **93** to selectively distinct the components of bone matrix although these dyes do not show any binding ability to Ca^{2+} in solution as discussed in Chapter 2. These dyes are PET sensors and in order to show noticeable emission, it is necessary to inhibit the PET process. Therefore it is reasoned that scratch generation creates free vacancies in the bone lattice facilitating some form of binding. In order to further understand this process, rose Bengal (**143**) was used as a control dye, which allows only ionic interaction with the carboxylate group.

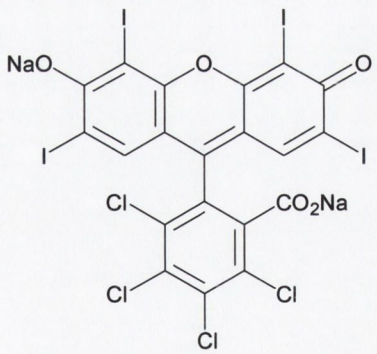

143

Rose Bengal used in the present case is available commercially (rose Bengal B) as its sodium salt. Rose Bengal has many attractive features such as good solubility in water

(36%, *w/v*) and also low pKa values of the carboxylate and hydroxyl groups (3.9 and 4.7 respectively) rendering it pH independent in the physiological range.[283] The scratch test was conducted in the manner described in Table 4.6. The bright pink colour of the dye was clearly visible in the scratched area of the bone demonstrating affinity of this dye for the scratch rather than the surrounding bone matrix. It indicates that a dye capable of forming weak interactions can also specifically label the scratch (Figure 4.18).

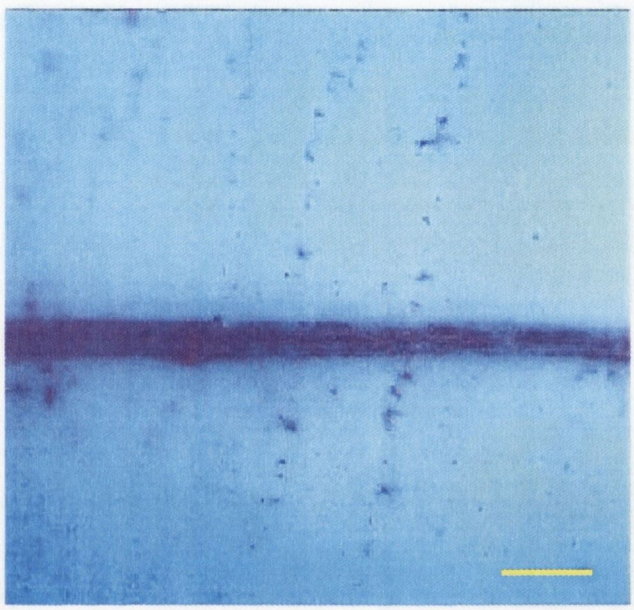

Figure 4.18 ***Bone surface showing scratch labelled 143; at magnification x 2X; UV epifluorescence (365 nm). Bar = 500 μm***

In order to further understand and quantify the selective labelling of the scratch generated on a bone surface two new techniques were explored- Raman confocal microscopy and Energy dispersive X-ray analysis (EDXA) coupled with Scanning Electron Microscopy (SEM). A brief introduction of the principles of the Raman effect and its practical utility followed by its the implications in current work is discussed.

4.6 Introduction to Raman spectroscopy

When a beam of monochromatic light is incident on a sample, most of the light is transmitted, some is absorbed and the rest is scattered (Figure 4.19). Most of the scattered light has the same wavelength as the source. However, careful examination shows that a

tiny fraction of the scattered light is shifted in wavelength and it is this shifted radiation that is known as the Raman shift and the effect is called the Raman effect or Raman scattering after Sir C. V. Raman, the Indian scientist who discovered it in 1928.[284]

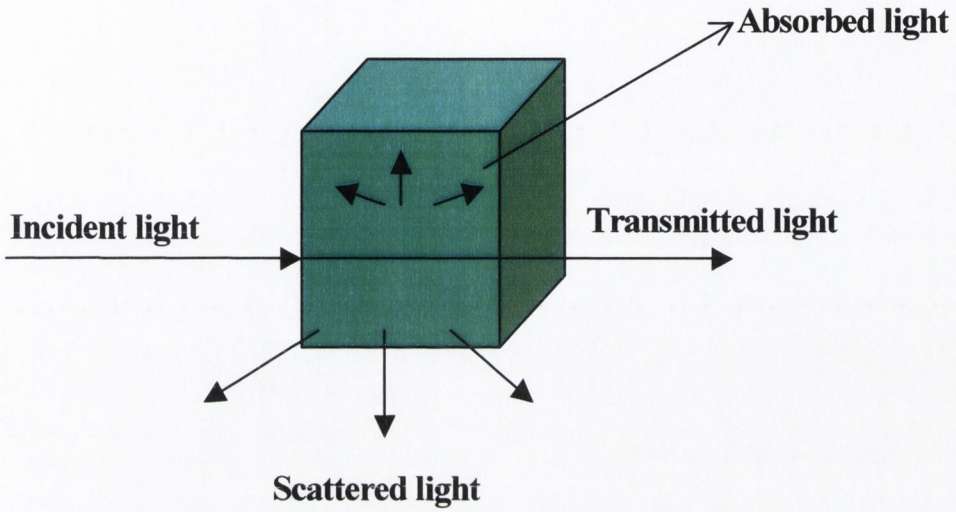

Figure 4.19 ***Scattering phenomenon occurring in a sample.***

4.6.1 Description of the Raman effect in terms of an energy level diagram

The Raman effect can be described using the energy level diagram shown in Figure 4.20. When a photon of frequency ν_0 strikes a molecule it raises the energy of the molecule from the ground state to a 'virtual state' The virtual state is not a true excited state but a distortion of the electron cloud in covalent bonds in the molecule.[285] The molecule immediately loses the energy by scattering and returns to its original electronic state. If the molecule returns to the same vibrational energy level from which it started, the emitted photon has the same energy, and hence the same frequency (ν_0) (Figure 4.20 (b)). This is called Rayleigh scattering.[285] If the molecule returns to a higher vibrational level, the emitted photon has less energy and hence a lower frequency than the incident photon (Figure 4.20(a)). This gives rise to Stokes' Raman scattering.[286,287] On the other hand, if the molecule reverts back to a lower vibrational level, the emitted photon has more energy and hence a higher frequency than the initial photon (Figure2(c)). This event is called anti-Stokes Raman scattering.[285-287]

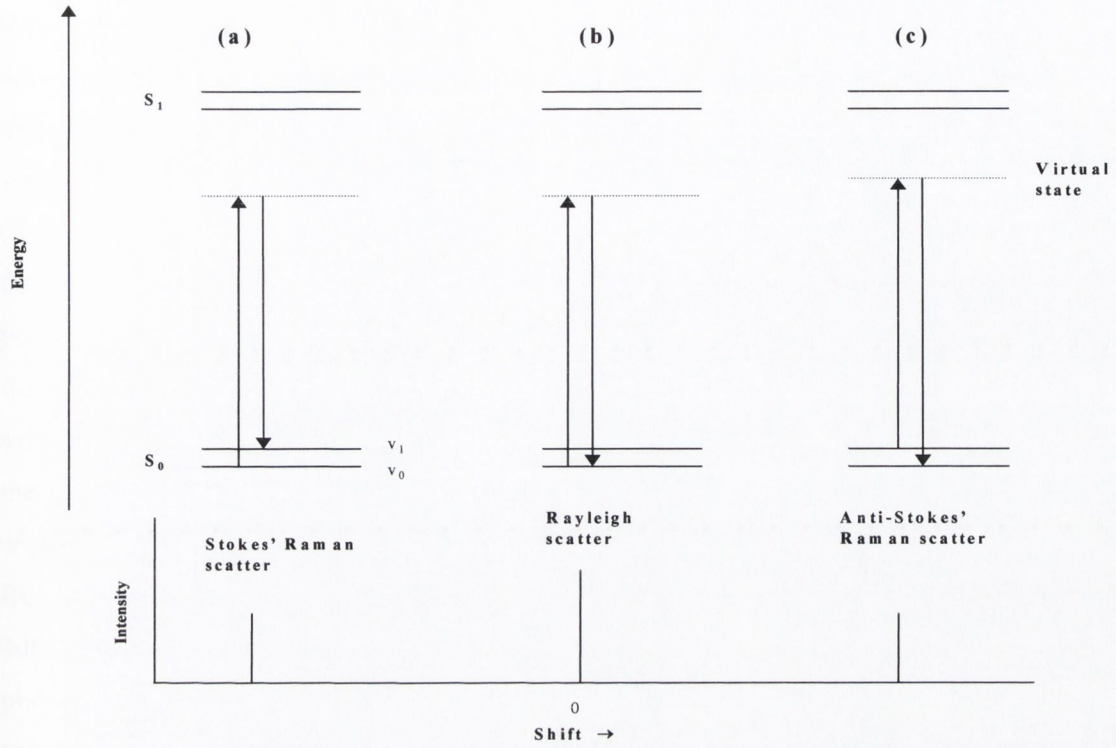

Figure 4.20 ***Energy level diagram showing the origin of (a) Stokes' Raman (b) Rayleigh and (c) anti-Stokes Raman scattering.***[285]

The intensities of Stokes and anti-Stokes Raman scattered light are proportional to the number of molecules in the lower and upper vibrational energy levels respectively. The population of excited state vibrational levels relative to the ground state is given by the Boltzmann distribution[285-287] (Equation 4.1)

$$N_g/N_e = (g_e/g_g)\, e^{-(\Delta E/kT)} \qquad (4.1)$$

Where N_e = population of the molecule in excited vibrational energy level;

N_g = population of the molecule in ground vibrational energy level;

g_e = degeneracy of the higher vibrational level;

g_g = degeneracy of the lower vibrational level;

ΔE = energy difference between the two levels;

k = Boltzmann's constant;

T = temperature, in Kelvin (K).

At thermal equilibrium the number of molecules in the ground state is always larger than in the excited state, therefore the Stokes Raman intensity is always larger than the anti-Stokes Raman intensity. The ratio of the intensities of anti-Stokes lines/Stokes lines falls as the vibrational frequency increases and temperature decreases. Raman data from a sample are usually displayed as a plot of Raman scattering intensity *versus* wavenumber (Raman spectrum). Not all the molecular vibrations are observed in the Raman spectrum. Only those vibrations described by normal coordinates (q) that modulate the molecular polarizability are allowed.[288] If the symmetry of the molecule is such that this condition is fulfilled, then the transition is said to be allowed or Raman active; if it is not fulfilled, it is said to be forbidden or Raman inactive. Raman spectroscopy has come a long way since the Raman effect was discovered. This technique is now gaining wider acceptance in all areas of science namely chemical, pharmaceutical, polymer, materials and biomedical. Recent advances in lasers provide a wide range of excitation wavelengths ranging from 400-800 nm, sophisticated computer software and data acquisition and analysis, and novel photonic devices (CCD detectors, filters, fibre-optic probes) have transformed Raman spectroscopy from that of a delicate laboratory method to a versatile tool.

In the present study, Raman spectroscopy was carried out to quantify microcracks and to explore the role of various dyes in labelling the microcracks. These studies were conducted at Dublin Institute of Technology, Ireland. Raman spectra will provide information about the microstructure of bone at a molecular level under physiological conditions. The other advantage of Raman spectroscopy is that it provides information rich spectral bands, is insensitive to water, sample preparation is very easy and it is non-invasive.[286] It was reasoned that comparison of Raman spectra of the surrounding bone, scratches and labelled scratches, would give new insights into the mechanism by which the dyes label bone.

4.6.2 Bone- Raman imaging studies using calcium crimson, calcium orange and rose Bengal

Bovine tibia was used for the study. The specimens were prepared in the same manner as described in the section 4.5.3. The dyes used for the imaging studies were calcium crimson, calcium orange and rose Bengal. For comparison purposes, specimens without any scratches as well as unlabelled scratched bone specimens were also analysed.

Table 4.9 ***Experimental methodology for imaging studies.***

Protocol used for the Raman imaging studies
1. 5mm scratch was made on the bone surface.
2. The bone samples were dipped into the solution of each dye (10^{-4} M) in individual vials and placed under vacuum (50 mm of Hg) for 24 hours.
3. The samples were washed with deionised water, dried and they analysed. These samples were compared with unscratched and scratched controls.

The Labram system used is a confocal Raman imaging microscope system. The laser sources available were Argon ion (514.5 nm, 50 mW). The 1004 cm^{-1} band of toluene was scanned before the acquisition of the resonance Raman spectra, to ensure correct positioning of the monochromator. The monochromator was stepped using increments of 0.5 cm^{-1}. For calibration purposes, the Raman spectrum of acetonitrile was recorded and peak frequencies and intensities adjusted until it agreed with reported values. A variable objective focuses the line shaped laser beam onto the bone surface and scratch. The scattered light is collected by an objective in a confocal geometry, and is dispersed onto an air cooled CCD array by one of two interchangeable gratings, 1800 lines/mm or 600 lines/mm allowing the range from 150 cm^{-1} to 4000 cm^{-1} to be covered in a single image, or with greater resolution in a combination of images. With the former, a spectral resolution of 1 cm^{-1} per pixel is achievable. The data were analysed using LabView (National instruments Corp.) software. Data were corrected for baseline offset and processed using a filter to remove cosmic events and artefactual spikes.

4.6.3 Evaluation of Raman imaging studies with unscratched and scratched unlabelled bone

First each unscratched and unlabelled bone specimen was scanned to obtain its Raman spectrum as shown in Figure 4.21 (a). This spectrum was further processed by subtraction of baseline and filtration of the data. This dramatically improved the signal-to-noise ratio and also led to background removal. The results are shown in Figure 4.21 (b). The spectrum is easy to analyse and 8 prominent Raman bands can be identified. The bands observed at 430 cm^{-1} and 589 cm^{-1} can be assigned to vibrations of phosphate groups (ν_4) of the hydroxyapatite lattice. The most prominent band observed at 961 cm^{-1}, is also due to the phosphate (ν_1). A weak intensity band observed in the region, 857 cm^{-1}, can be

assigned to either carbonate frequency or to the C – C stretch of proline and hydroxyproline.[259] Vibrations of bone proteins are responsible for the bands at 1249 cm^{-1}, 1455 cm^{-1} and 1667 cm^{-1}. The assignment was in close agreement with values reported previously.[259,289,290]

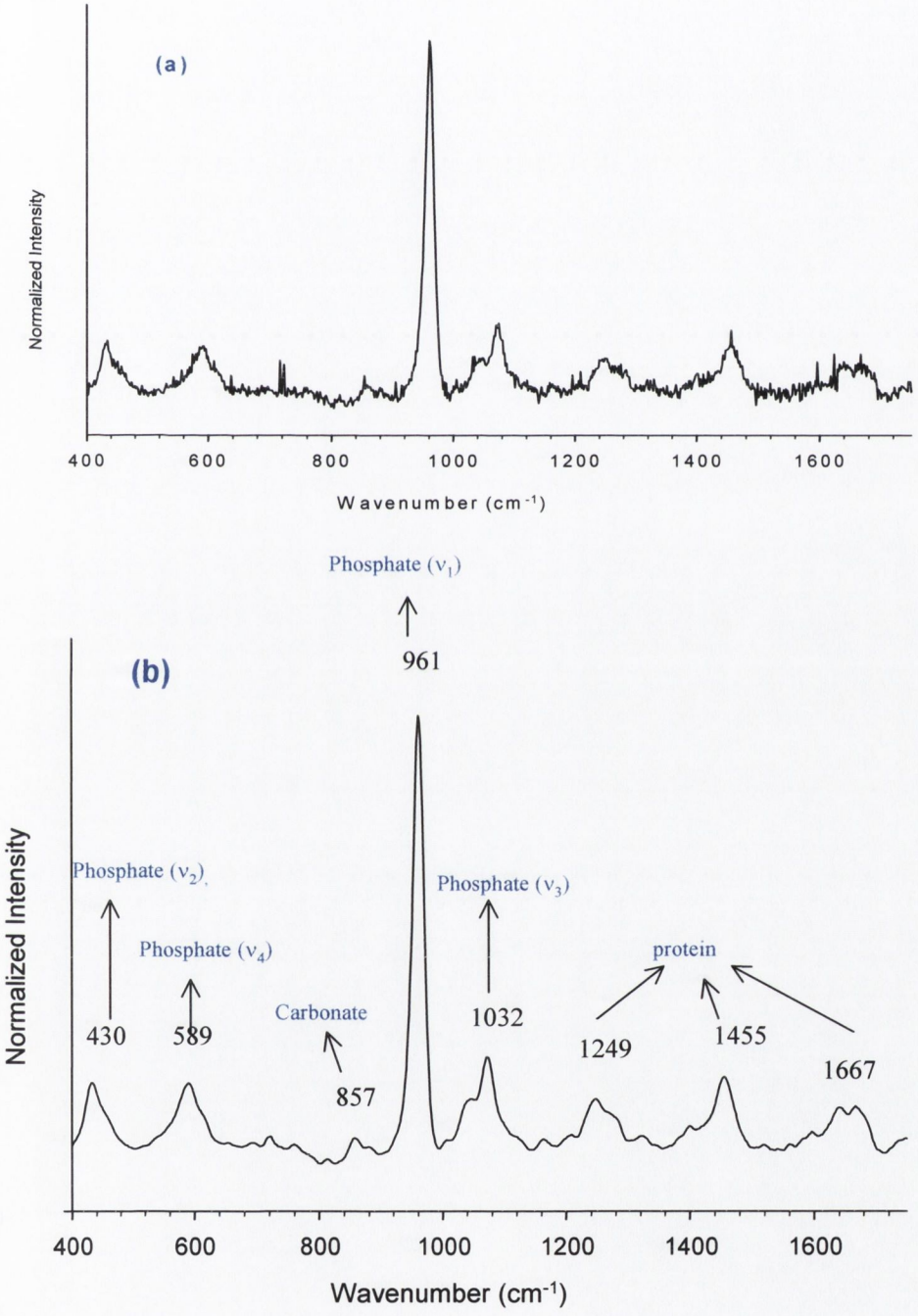

Figure 4.21 ***Raman spectra of unscratched and unlabelled bone. (a) raw Raman spectrum; (b) corrected Raman spectra.***

Next the scratched surface of the bone was scanned and, after data processing, the clean spectrum obtained is shown in Figure 4.22. The spectrum is almost identical to that shown in Figure 4.21 except that there are distinct changes in the bands in the region 1000-1100 cm^{-1}. Two separate bands can be observed in this region (1032 cm^{-1} and 1046 cm^{-1}). These bands are assigned to the phosphate of the hydroxyapatite lattice. These changes may be attributed to the breakage of the phosphate bonds in the hydroxyapatite lattice during scratch generation. Degradation studies carried out on collagen proteins have demonstrated extensive perturbation in the amide bonds observed at 1250 $cm^{-1}$and 1660 cm^{-1}.[291] However, in the present case, no changes were observed in the 1200-1600 cm^{-1} range indicating that collagen proteins are intact during scratch generation. Perhaps a higher load is needed to induce disorder in collagen.

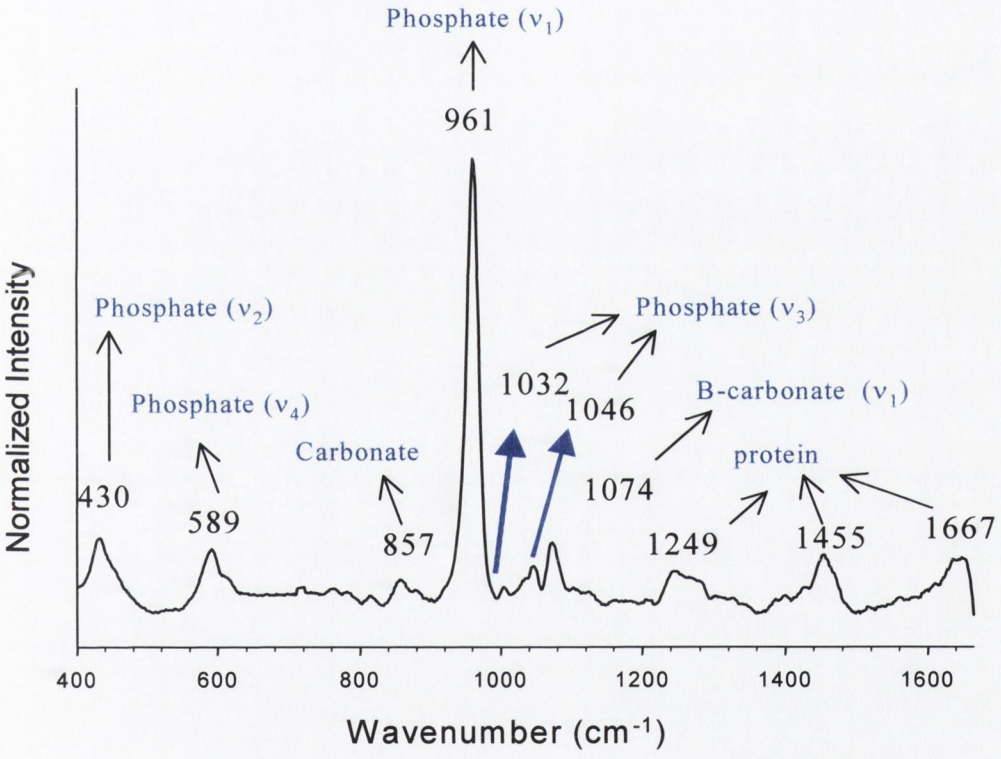

Figure 4.22 ***Corrected Raman spectrum of the scratched region of bone.***

4.6.4 Evaluation of Raman imaging studies of calcium crimson, calcium orange and rose Bengal labelled bone

Interesting results were obtained when the bone specimens were labelled with calcium crimson, calcium orange and rose Bengal. For all three dyes, the scratched region and the

surrounding unscratched surfaces, were scanned and analysed. The Raman spectra of the unscratched surface were identical to that shown in Figure 4.21(b). For the scratched region, spectra were analysed in the region 800-1900 cm^{-1}, as the region 400-800 cm^{-1} was difficult to analyse due to high signal-to-noise ratio and background noise. By restricting the spectral region it was possible to improve the signal-to-noise ratio and interpretable spectra could be obtained. Morris *et al.* have analysed a similar region of microdamage detection in labelled bone using basic fuchsine.[259] The Raman spectrum of the scratch labelled with calcium crimson is depicted in Figure 4.23. A broad phosphate band centred at 1001 cm^{-1} was observed. The bands in the region 1180-1400 cm^{-1} can be assigned to the amide vibration of collagen proteins and also to the aromatic region of the dye. The amide and $-CH_2$ stretching was clearly represented by the bands observed in 1450-1680 cm^{-1} region. The most striking and high intensity band is centred at 1735 cm^{-1}, which is most likely due to the carbonyl groups of the calcium crimson.

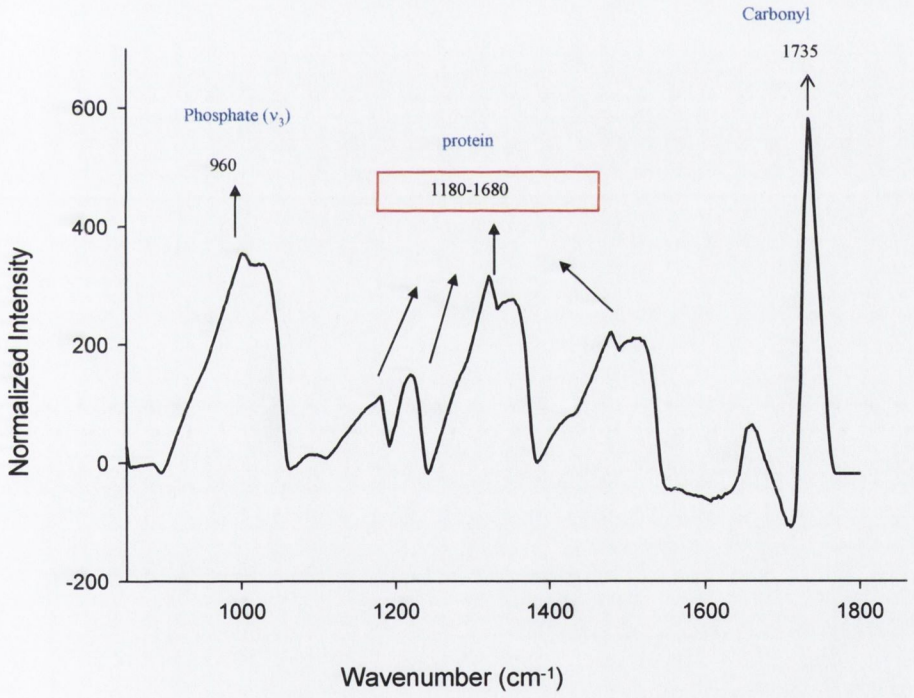

Figure 4.23 ***Corrected Raman spectrum of the bone scratch labelled with calcium crimson.***

The spectrum for calcium orange is depicted in Figure 4.24. The phosphate band (961 cm^{-1}) was similar to that observed in the unlabelled bone sample. In addition the usual amide and CH_2 stretching vibrations of collagen protein was also observed. A band at 1741 cm^{-1} is most likely due to the carbonyl groups as in the case of calcium crimson.

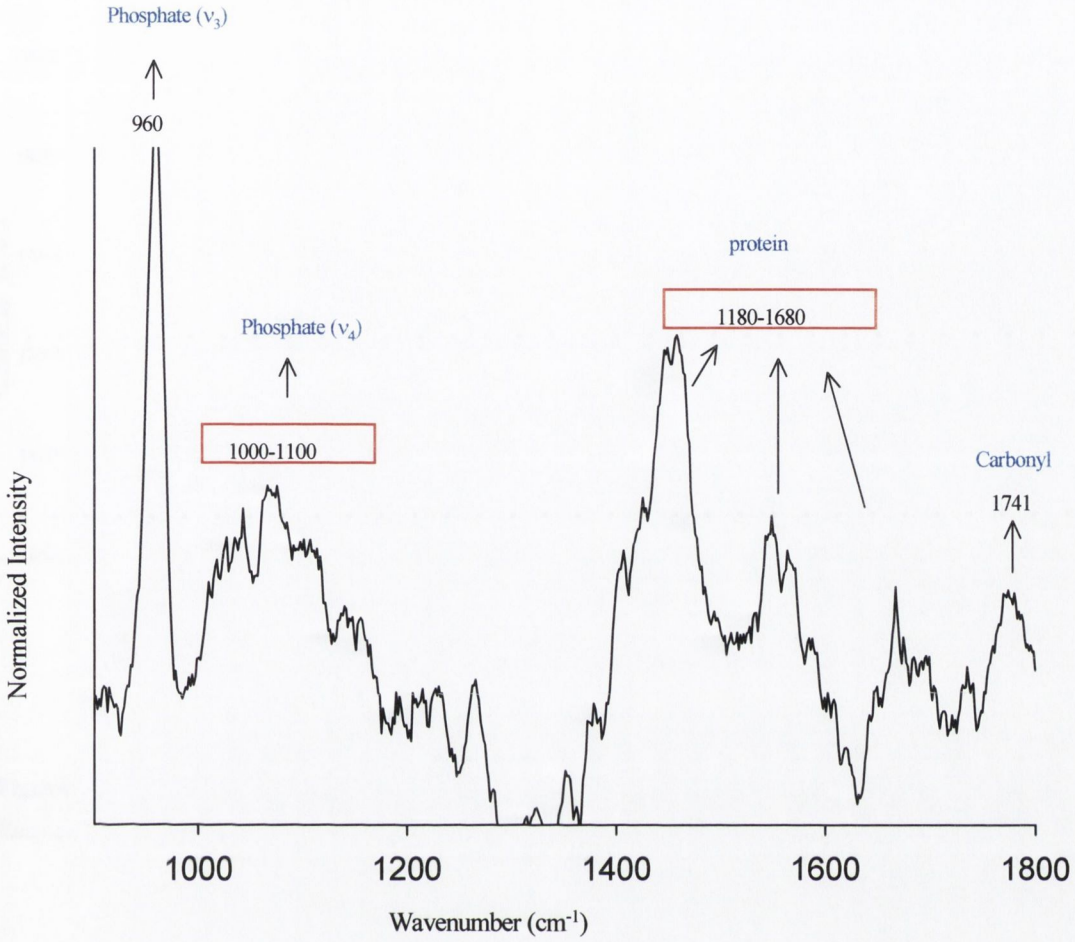

Figure 4.24 Corrected *Raman spectrum of the bone scratch labelled with calcium orange.*

Due to the high fluorescence of the rose Bengal the Raman spectrum of the scratch and the surrounding regions was difficult to analyse. A raw spectrum obtained from the scratched region is shown in Figure 4.25. The region from 800-1800 cm^{-1} is dominated by the background fluorescence form the rose Bengal dye. The spectrum obtained after the processing of the data is shown in Figure 4.26. The high signal-to-noise ratio and background noise, make the interpretation of Raman bands almost impossible. This behaviour of organic pigments is a well known phenomenon in Raman spectroscopy.[292] The most likely reason may be the presence of pigment impurities and the higher energy absorption of the dye at 514 nm l excitation.

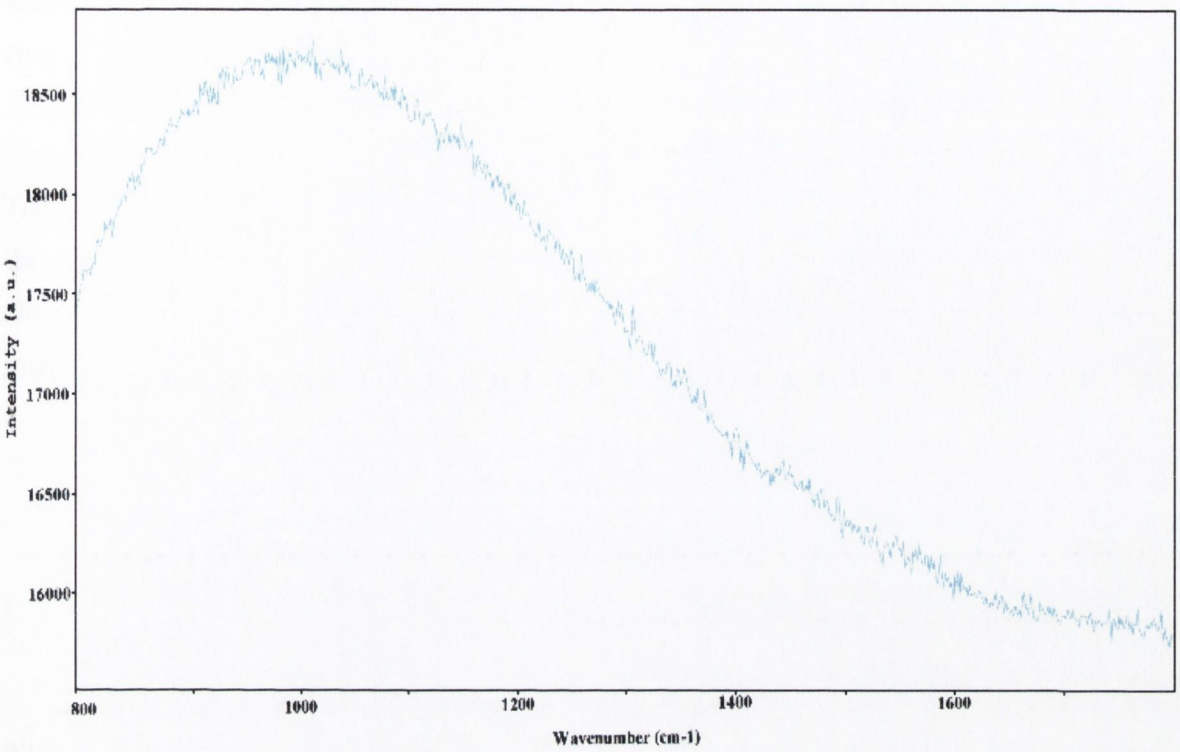

Figure 4.25 ***Raman spectrum of the bone labelled with rose Bengal. Note the high background fluorescence.***

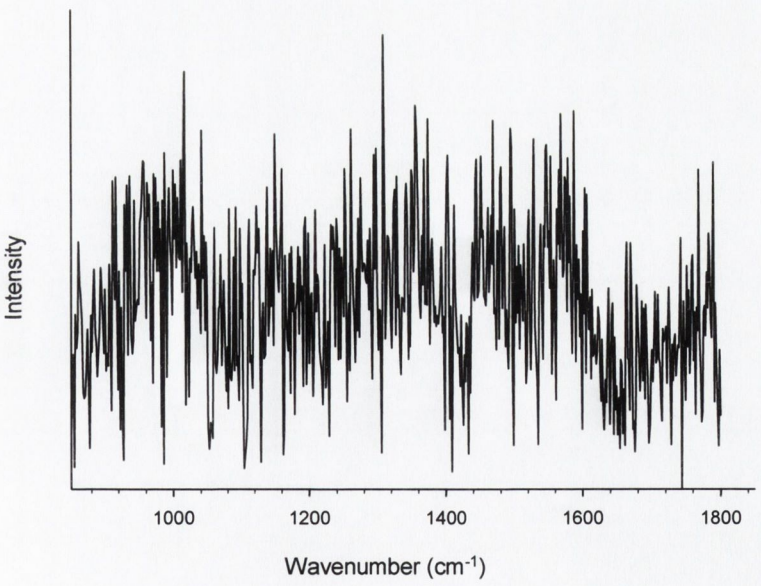

Figure 4.26 ***Corrected Raman spectrum after data processing. The signal-to-noise ratio and background is still high preventing interpretation.***

4.6.5 Evaluation of Raman imaging studies of calcium crimson, calcium orange and rose Bengal

In order to further understand this process it was decided to scan the dyes alone so that comparison could be made between the unlabelled dyes and dyes labelling the scratch. The comparison between the carbonyl group vibrations frequency of the pristine dye with the dye labelled scratches could give vital information about the mechanism of binding. However, two main difficulties were encountered while scanning the dyes for Raman imaging:

- background fluorescence from the dyes was very high.
- charring of the dyes was observed, which might be due to heat damage caused by the focussed laser beam.

All these factors prevented the acquisition of the Raman spectra of these dyes. The high energy from the laser is the probable reason for the above-mentioned drawbacks. Perhaps a laser of higher wavelength such as 785 nm and 1038 nm might prove useful for acquiring the Raman spectra of dyes.

4.7 Scanning electron microscopy (SEM) and Energy dispersive X-ray analysis (EDXA) in bone

Histological methods and Raman spectroscopy demonstrated that dyes are able to specifically label the scratch. In order to further investigate these findings and also to observe the morphological characteristics and chemical composition of the scratch, it was decided to perform SEM and energy dispersive X-ray analysis (EDXA) of unscratched and scratched bone as well as bone labelled with dyes. The aims were two fold:

- to ascertain if there is any chemical difference in the region of a scratch compared to surrounding regions of bone
- to observe the morphological changes when the scratch is labelled with dye.

The dye chosen for the labelling of bone samples was rose Bengal as the iodine atoms can be observed in the EDX spectrum and it will be possible to distinguish the labelled scratch from the surrounding hydroxyapatite matrix.

4.7.1 Bone- SEM and EDX studies using rose Bengal

The protocol used for EDX studies was similar to that used in Raman imaging studies and is shown in Table 4.9. All SEM micrograph were obtained with a dual stage SEM with associated EDX. Samples were coated with gold to achieve optimal imaging results or used as it is for EDX analysis. Studies were carried at Centre for Microscopy and Analysis, Trinity College.

Studies were conducted using unscratched, scratched and rose Bengal labelled bone specimens. A SEM of the unscratched sample is shown in Figure 4.27. The chemical composition analysis was performed using EDXA. Due to the highly composite nature of the bone matrix, two different regions were selected for elemental analysis.

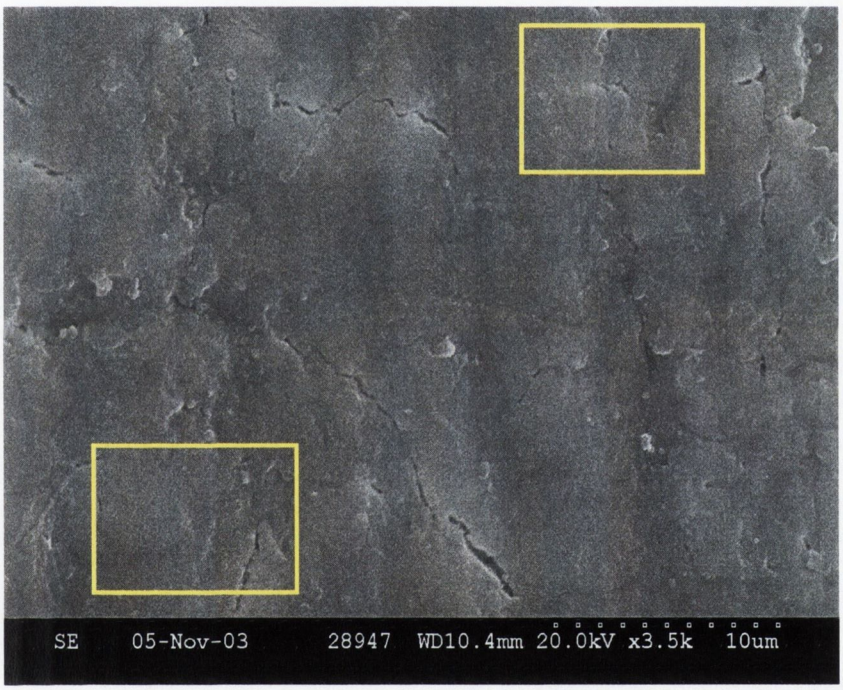

Figure 4.27 ***Scanning electron micrograph of bone. Two different regions (marked by yellow rectangle) were selected for elemental composition by EDXA.***

The EDX spectra showed that the major elements present in bones are calcium, phosphorous and oxygen along with trace amounts of sodium, magnesium and phosphorous (Figure 4.28). Additionally, the elemental composition of both chosen regions was almost identical. This result demonstrates that the bone exhibits chemical uniformity.

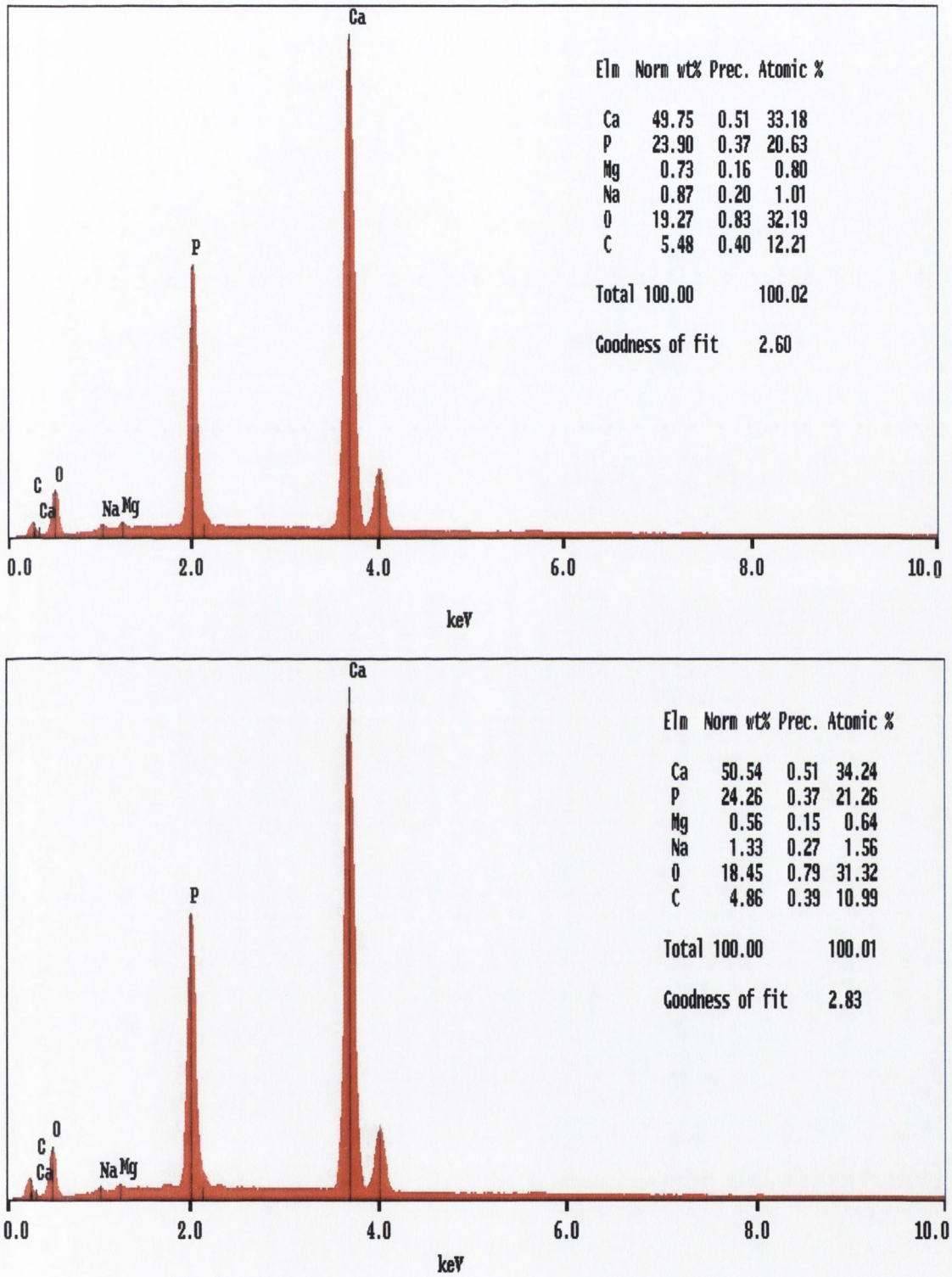

Figure 4.28 ***Elemental composition of two regions of bone marked b yellow boxes in Figure 4.27. Insert shows the percentage of the elements. Note that elemental composition is almost identical in both regions.***

In order to investigate the chemical changes induced by scratch generation, EDX of the scratched bone samples were conducted. The SEM and elemental composition of the scratch is shown in Figure 4.29 and 4.30 respectively.

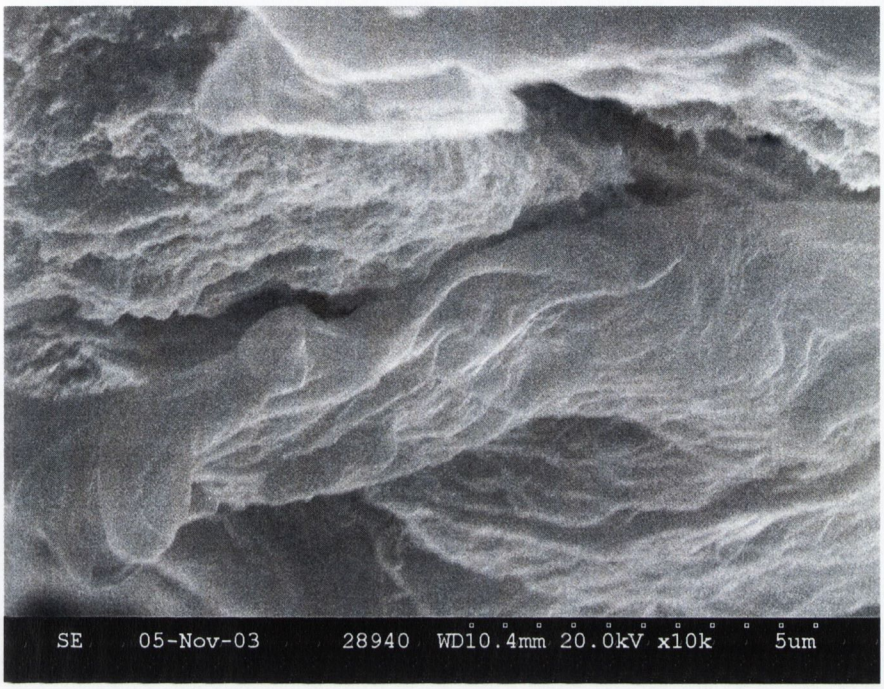

Figure 4.29 *Scanning electron micrograph of scratched region of bone.*

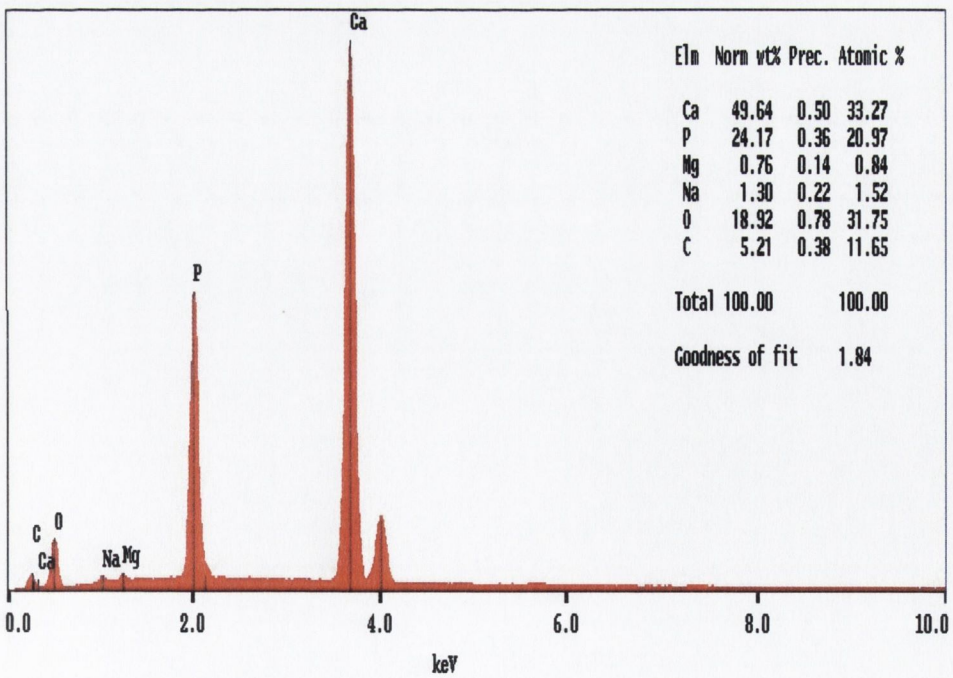

Figure 4.30 *Elemental composition of two regions of bone*

The elemental composition of the scratch is almost identical with the surrounding bone matrix. The scanning electron micrograph demonstrates the morphology of the damaged lattice. It shows the highly porous nature of the area generated by the breaks in the hydroxyapatite lattice. Rose Bengal stained bone samples provided interesting results. The SEM of the scratch area labelled with rose Bengal is depicted in Figure 4.31. The crystals of the rose Bengal are clearly visible in the scratch. No crystals are detected in the surrounding matrix. It can be postulated that the porous and void nature of the broken lattice in the scratch induces crystallisation of the dye.

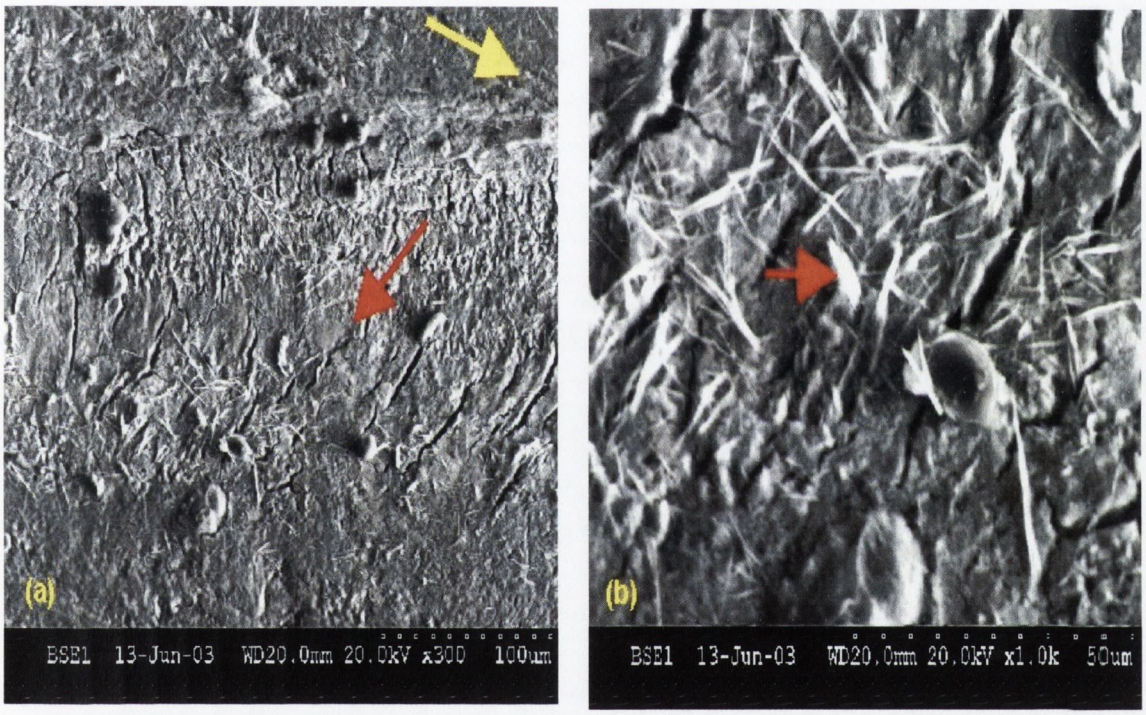

Figure 4.31 ***Scanning electron micrograph of scratched bone labelled with rose Bengal (a) low resolution and (b) high resolution. Red arrow shows the rose Bengal crystallised in the scratch area. Yellow arrow shows the area surrounding scratch.***

The EDX analysis showed in Figure 4.32 shows the presence of iodine in the scratch, This is further supporting the presence of rose Bengal in the scratch.

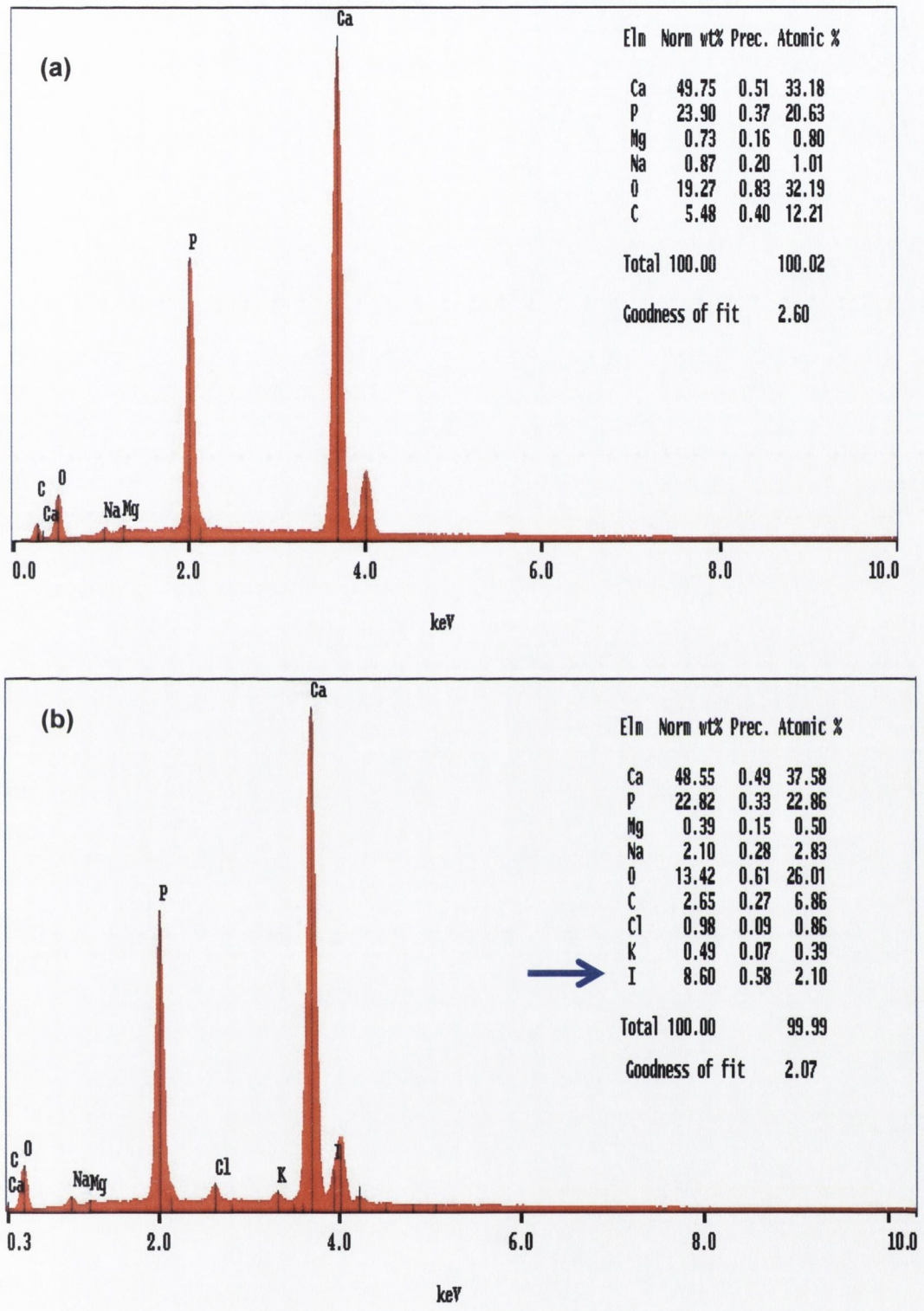

Figure 4.32 ***Elemental composition of (a) surrounding area and (b) scratched area of bone labelled with the rose Bengal; The blue arrow in (b) shows the iodine composition in the scratch region.***

4.8 Conclusions and future work

This chapter presents in detail a critical investigation of microdamage in bone using histological methods. To evaluate the histological findings two independent techniques, Raman spectroscopy and SEM-coupled EDXA were explored. Initially analysis was conducted on earlier dyes (**135**, **136** and **138**) to estimate their Ca^{2+} chelating affinity at physiological pH using fluorescent spectroscopy. These PET based dyes showed negligible fluorescent response on Ca^{2+} titration indicating that the fluorescence was already switched '*on*' due to protonation. However, the selective labelling of scratches observed by Lee *et al*[265] and O'Brien *et al*[267,268] needed some explanation. To explore the labelling further, a set of well known physiologically pH independent, PET based Ca^{2+} indicators (**140**, **141** and **142**) were selected to label the scratch. These dyes are essentially nonfluorescent unless bound to calcium. The dyes labelled the scratch selectively from the surrounding bone matrix. To further explore the labelling, a series of dyes (**92**, **93** and **125**) that showed no chelating affinity towards Ca^{2+} and hence no fluorescence response was used to test the scratch. Again selective fluorescence response was observed from the scratch.

It was possible to understand the difference between the scratched and unscratched surfaces of the bone in terms of lattice vibrations using Raman spectroscopy. The dyes were specifically labelling the scratch rather than the surrounding regions of the bone. Bone is a composite material consisting of minerals such as impure hydroxyapatite containing constituents such as carbonates, citrates, magnesium fluoride and strontium incorporated into the crystal lattice. Generation of a scratch breaks this mineral lattice and generates lattice vacancies for bound elements such as calcium that will be able to bind suitable receptor functionalities. Also due to the porous nature of the scratch, as demonstrated in scanning electron micrograph (Figure 4.29), it is possible to incorporate molecules. Rose Bengal provided definite proof for this hypothesis. The dye contains only a carboxylate group and no specific binding sites. The scratch test conducted demonstrated the ability of rose Bengal to label the scratch. Further proof was obtained from SEM and EDX analysis of a rose Bengal labelled scratch showing the selective crystallisation of dye in the scratch. It demonstrates that even suitable ionic interactions can be exploited for selective scratch labelling. Therefore the site specificity of dyes **135**, **136** and **138** is most likely due to ionic interactions with the broken lattice or the inclusion inside the porous structure generated in the scratch.

The selective labelling of dyes **140**, **141** and **142** is probably either due to their chelation at the free Ca^{2+} vacant sites generated during scratching or the inhibition of PET

process *via* interaction with the porous lattice. The same reasoning can be envisaged for dyes **92** and **93**. In future atomic force microscopy (AFM) and extended X-ray absorption fine structure (EXAFS) can be used to understand selectivity and to determine the binding mode and geometry adapted by the dye in the scratch.

Chapter - 5

Novel Water Soluble Iodinated Contrast Agents

5.1. Introduction

The concept of 'imaging in medicine' based on contrast media emerged after the discovery of X-rays by Rőentgen in 1895.[293] In medical diagnosis, contrast can be used to distinguish an organ or part of the body, *via* opacification or visualisation, thus providing important structural information. Gradually, contrast agents based on magnetic resonance and ultrasound are beginning to emerge.[294] Today imaging or contrast agents are essential parts of radiology and routinely used in modern medicine.[294] Depending on the basis of the principle used, contrast agents available at present can be broadly classified into three main categories as summarised in Table 5.1.[294]

Table 5.1 ***Classification of common types of contrast agents.***[296]

Contrast Agent	Principle	Contrast	Examples
X-ray contrast agent	Absorption of X-rays	High molecular weight atoms (bromine, iodine, metal ions)	Diatrizoate, iopamidol, iohexol, iodixanol
Magnetic resonance imaging contrast (MRI) agent	Perturbation of the magnetic environment of atoms, particularly protons	Paramagnetic atom or group (Gd, Yb, Mn, hyperpolarized noble gas)	Gd-DTPA, Gd-DTPA-BMA, Gd-DOTA, Gadomer-17
Ultrasound contrast agent	Back scatter of electrons; stimulated acoustic emission	Gas (air, perfluorocarbon)	Echovist (glactose+air), sulphur hexafluoride

5.2. X-Ray contrast agents

X-rays are very important in medical diagnoses as one can externally visualize the internal anatomical structures of a patient. There are two types of X-ray contrast agents, which are used frequently:

- metal based X-ray contrast agents such as barium sulphate suspensions that are used strictly for gastrointestinal (GI) tract imaging[295]
- water-soluble iodinated X-ray contrast agents.[133,296]

Even though other metal based contrast agents are becoming increasingly available reports suggest that 80% of diagnostic imaging procedures are X-ray related.[133] Worldwide, iodinated X-ray contrast agent are currently used in approximately 500 million procedure annually.[297] The criteria for a diagnostically useful radiocontrast agent are:

- opacity to X-rays
- high water solubility at high iodine concentration
- low viscosity and low osmolality, similar to those of body fluids
- chemical stability
- biological safety.[298,299]

5.2.1. Historical survey of iodinated contrast agents

The long and rich history of iodinated contrast agents began in 1923 when Osborne and co-workers at the Mayo Clinic observed that either oral or intravenously administered sodium iodide solutions opacified the bladder.[300] This was followed by the introduction of a new class of iodinated contrast agents, based on an organic framework containing one or more iodine atoms (*e.g.* uroselectan and diodone).[301] Modern water-soluble iodinated contrast agents utilise a 1,3,5-triiodobenzene platform, which first appeared as diatrizoic acid or diatrizoate, in 1954.[302] These ionic triiodobenzene monomers were the first generation of X-ray contrast agents developed for general intravascular use, with low toxicity and high water solubility. However, these agents are not completely benign as moderate to severe cardiovascular, anaphylactic and pain reactions may occur with their use.[303] They are not useful for intrathecal injections (directly into the cerebrospinal fluid) or for myelography (spinal cord imaging).[12]

Novel second generation, non-ionic, water-soluble iodinated contrast agents were developed during the 1970s, which had significantly lower osmolality.[298,299] The extent of severe adverse reactions and the degree of pain upon injection were greatly reduced following the widespread adoption of these agents, and they have now largely replaced first-generation agents. Iodinated contrast agents have experienced a significant evolution with a series of new molecular entities replacing a range of old generation products. The historical evolution of contrast agents can be illustrated as shown in Figure 5.1.

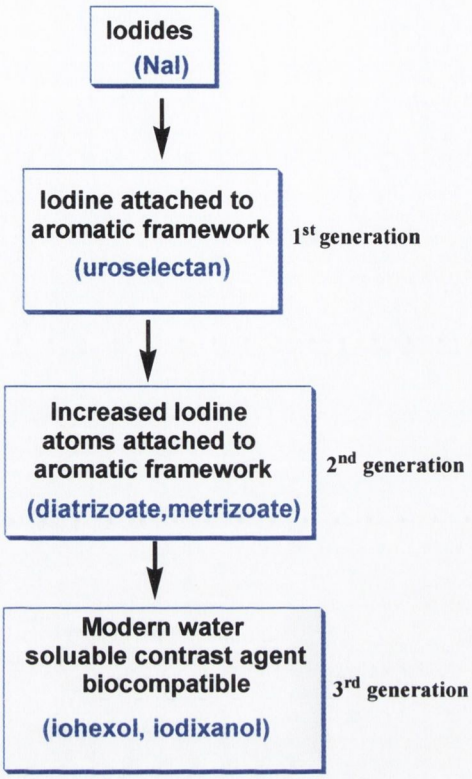

Figure 5.1 ***Historical evolution of X-ray contrast agents from simple inorganic sodium iodide to complex biologically compatible iohexol.***

It is the iodine atoms in these molecules which attenuate X-rays, providing opacification. The carbon, hydrogen, nitrogen and other atoms merely provide a framework or 'carrier' for the iodine atoms.

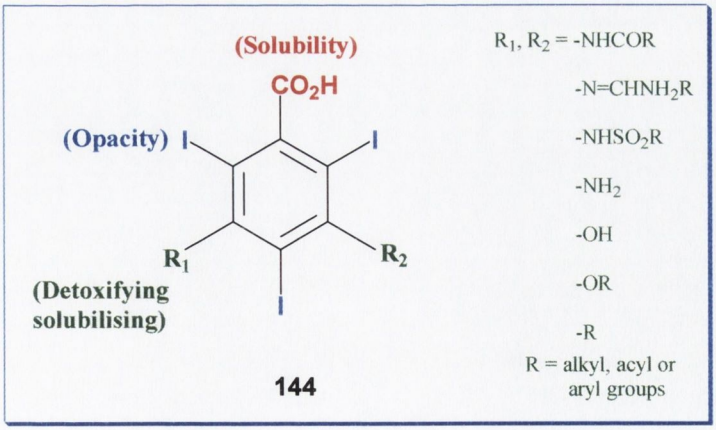

Figure 5.2 ***Essential structural requirements of iodine based contrast agents.***[298]

The structural arrangement of these additional atoms is important in providing stability, non-toxicity, solubility, and concentration in various organs. The general structural requirements for contrast agents are summarised in Figure 5.2.[298,299] Water solubility can be greatly increased by the formation of a salt with a suitable cation such as sodium or *N*-methylglucamine (meglumine).[299] The introduction of *N*-acetoxy or *N*-methylcarbamyl functionality on the aromatic skeleton also greatly improves both water solubility and biological safety.[299] All presently available agents are based exclusively on the trioiodebenzene system, either with one ring (monomers) or two rings (dimers). Present day iodinated contrast agents can be divided into four separate classes based on their aromatic platform as well as charge.[133,298,299,304] Representatives of each class are depicted in Figure 5.3.

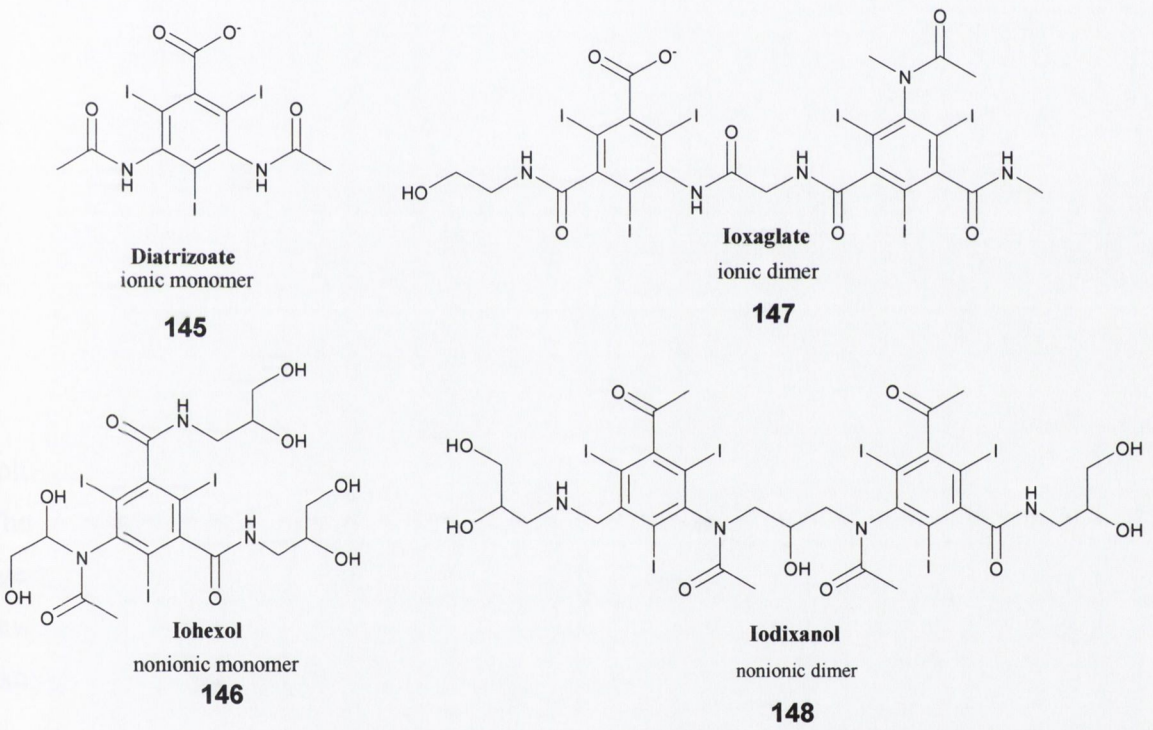

Figure 5.3 ***Representatives of modern iodinated contrast agent based on number of iodinated benzene rings and charge.***[133]

Currently various research groups are focussing on the design of safe, organ-specific, stable, highly water-soluble and low osmolality contrast agents. Ranganathan *et al.* have developed contrast agents **149** and **150** by improving on the design of a known nonionic iodinated contrast agent, iohexol (**146**).[305] These contrast agents are based on the

oxazolidin-2-one moiety that imparts higher stability to the molecule at physiological pH range. Also, due to their amphiphilic nature, the degree of self-association in aqueous solution would lead to lower osmolality. Studies have shown that these agents are hydrolytically more stable in aqueous solutions and their osmolality is approximately 34% lower than the structurally related analog iohexol. Clinical studies have shown that these compounds lengthen blood coagulation time, a property desirable in a contrast medium.[306]

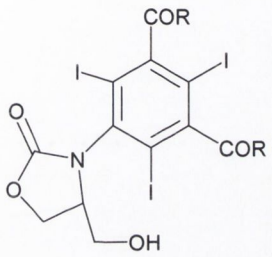

149: R = $NHCH_2CH(OH)CH_2OH$

150: R = $NHCH(CH_2OH)_2$

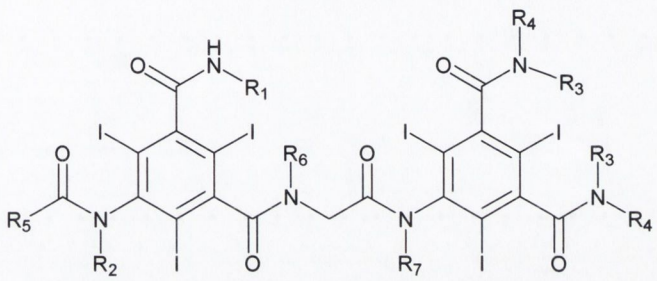

151: R_1 = $CH_2CHOHCH_2OH$
R_2, R_3 = $CH(CH_2OH)CHOHCH_2OH$
R_5 = CH_2OCH_3
R_6, R_7 = CH_3

152: R_1, R_4 = $CH_2CHOHCH_2OH$
R_2, R_3 = H
R_5 = CH_2O
R_6, R_7 = CH_3

Böhle *et al.*[307] further developed contrast agents **151**and **152** that exhibit good water solubility and stability. These compounds also possessed lower osmolality than iohexol. The water solubility of **151** was in the acceptable range (>80%, *w/v*) while the contrast agent **152** had poor water solubility. According to the authors, this behaviour may be to due several chirality centres in **152**, preventing the formation of soluble hydrates. However, extremely low water solubility prevented their clinical use.

Rongved *et al.*[308] have reported the synthesis and kinetics of biocompatible X-ray contrast agents **153** and **154** in which the 2,4,6-triiodobenzene derivative is linked to an amino acid moiety such as glycine and β-alanine with starch microspheres as carriers (Figure 5.4). The attachment of these contrast agents to the starch microparticles greatly increased their solubility in lipid media rendering them specific for imaging the reticuloendothelial system, particularly the liver and spleen. The hydrolytic cleavage by liver enzymes would result in rapid degradation and hence fast elimination of these contrast agents from the body.

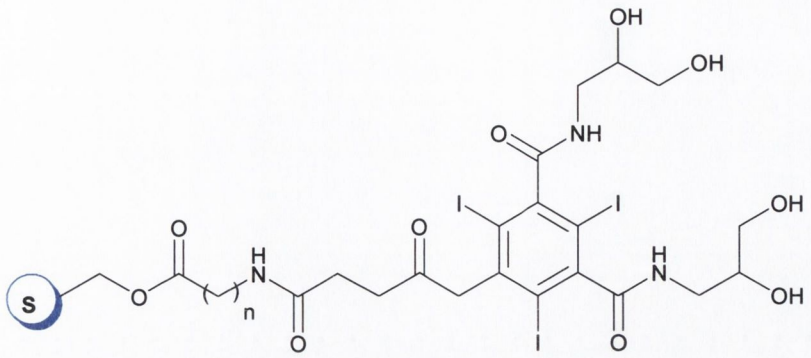

153: n = 1
154: n = 2

Figure 5.4 ***Structure of contrast agent 153 and 154 linked to starch particles. S= starch microparticles.***

Shalem *et al.*[309] have reported the synthesis of amido and peptide based iodinated contrast agents **155-157** for specific internal organs of the body such as the liver and bilary tract. These compounds contain both phosphonic acid and peptide moieties. The peptide moiety could affect the selective affinity towards specific tissues, whereas phosphonic acid enhances the ability of the contrast agent to reach targeted tissues.

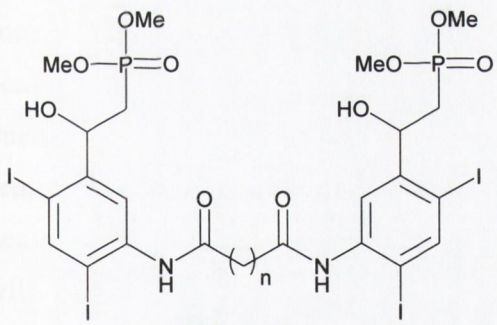

155: n = 0
156: n = 1

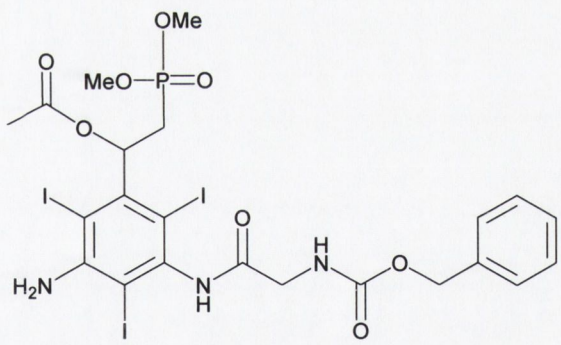

157

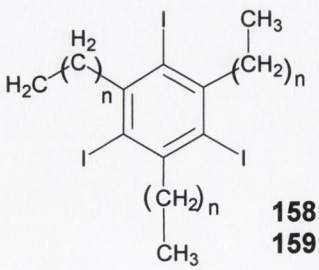

158: n = 6
159: n = 4

Estep *et al.*[310] have developed lipophilic X-ray contrast agents **158** and **159** specifically for gastrointestinal imaging. The flexibility of the long alkyl chain, efficiently offset the inherent crystallinity of a tri-iodobenzene framework. These compounds are free flowing oils, used as oil-in-water emulsions demonstrating excellent mucosal coating and optimal radiodensity. They offered improved physical stability *in vivo* compared to $BaSO_4$ suspensions. Compound **158,** in particular showed promising results in animal studies, as it was minimally absorbed from the gastrointestinal tract, was resistant to metabolism and its safety was considerable following oral and intrapertioneal administration.

5.3. Motivation for the present work

Although iodinated contrast agents have been developed for the vascular, gastrointestinal and nervous systems[308-310] none have been made specifically to characterise bone damage. The problem with bones is their inherent contrast due to the crystalline hydroxyapaptite and organic matrix. Thus it is difficult to distinguish the contrast agent from the surrounding bone matrix. One way of approaching this problem is to increase the degree of opacity at the damage site.

It is synthetically challenging and stimulating to approach this problem of detecting microdamage in bones using iodine based contrast agents. To increase the concentration of contrast agent selectively at the microdamage site, it should possess the specific ability to penetrate the bone matrix and incorporate into the free lattice, where the weak ionic interaction with the lattice can provide additional modes of binding. These factors can probably increase the concentration of contrast agent specifically at microdamage sites and hence it could be possible to distinguish the damaged sites of bone by X-ray imaging. This will provide a non-invasive method of detecting and quantifying microdamage. This chapter will deal with preliminary stages in this direction. Two main objective of this project are:

- synthesis and characterisation of the novel site specific iodine based contrast agents
- evaluation of these contrast agents by using micro-computed tomography (μ-CT). μ-CT measurements will give qualitative and quantitative information about the contrast of these dyes and their potential for clinical application.

5.4. Synthesis and characterisation of iodinated contrast agents

The main features of the iodinated-contrast agents have already been described (Figure 5.2). Based on these principles, the synthesis of contrast agents **160-163** as their sodium salts is proposed. These agents consist of phenyliminodiacetate chelator linked *via* an amide linkage to a triiodo benzene skeleton. In **160** only one phenyliminodiacetate unit is attached to the iodinated aromatic ring, while **161** has two chelator units attached *meta* to each other. The dimer **162** contains six iodine atoms and four chelator units in *meta* configuration.

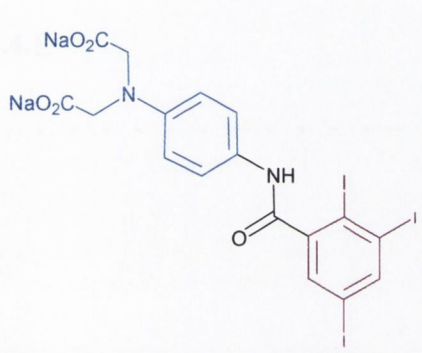

160

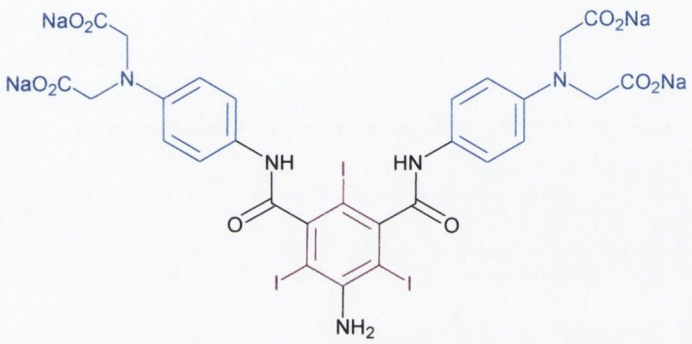

161

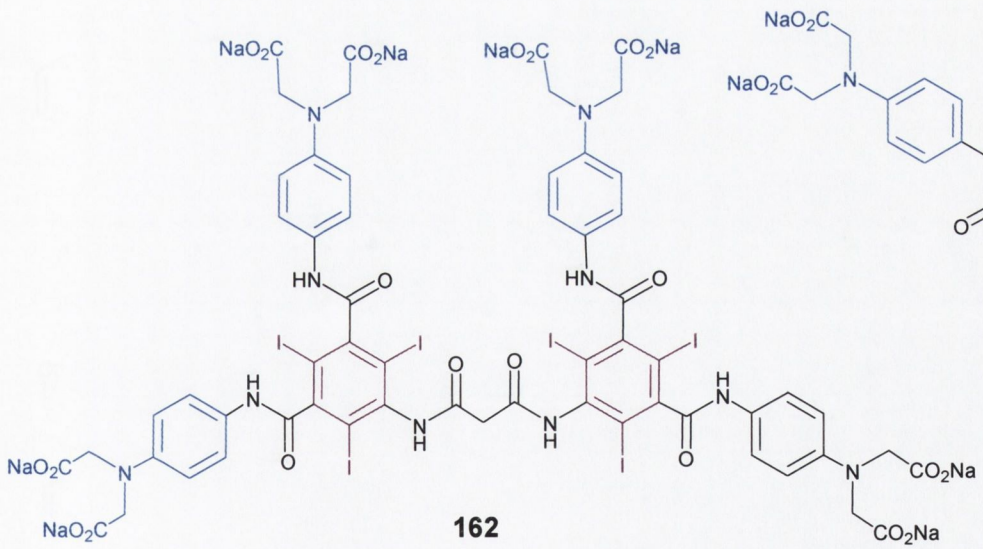

162

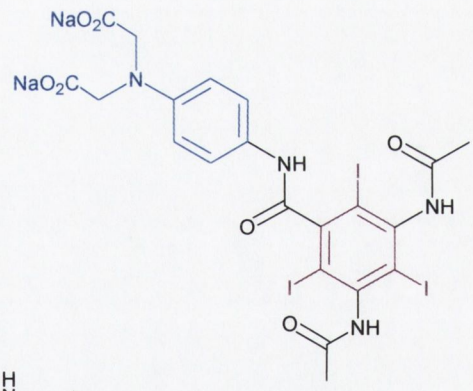

163

The advantage of these contrast agents is their high water-solubility as their sodium salts. Traditionally the water solubility is conferred by the introduction of hydroxyalkyl functionalities (Figure 5.3). Introduction of such groups is synthetically lengthy and cumbersome. Also the presence of hydroxyl groups leads hydrogen bonding providing highly viscous solutions.[311] This limits their *in vivo* use, as low viscosity solutions are

needed for the fast release of contrast agents from the capillary beds into the main blood stream, and also for rapid injection rates.[312] It was proposed to incorporate solubilising groups (*e.g.* amide and acetate) that will render them safe, highly soluble, less viscous and well tolerated by the body. The other important criteria are how fast and efficient these contrast agents are eliminated from the excretory system of the body. The faster their elimination the less they accumulate in the body thus minimising side effects. It is believed that carboxyl groups will facilitate the elimination of the molecules from the excretory system *via* decarboxylation catalysed by enzymes in liver.

5.4.1. Design, synthesis and characterisation of contrast agent 160

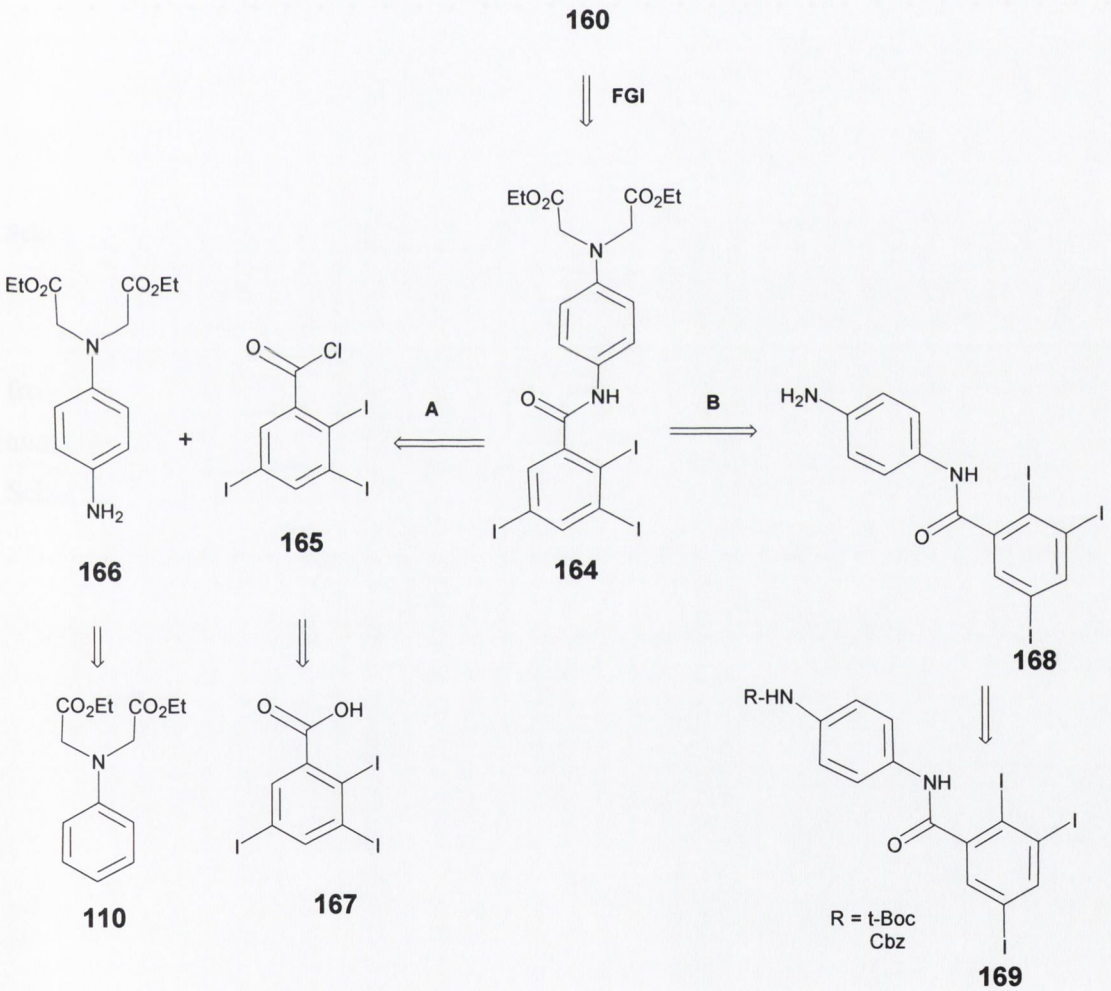

Scheme 5.1 ***Retrosynthetic strategy for 160; FGI = functional group interconversion.***

As discussed earlier **160** is a monomeric contrast agent based on a 2,3,5-triiodobenzene framework. Retrosynthetic analysis shows that **160** can be made in high yields from the alkaline hydrolysis of the intermediate ester **164**. The ester in turn can be synthesised in two different pathways (**A** and **B**, Scheme 5.1). However, the synthetic pathway **A** gives high overall yield statistically and is preferred. The intermediate 2,3,5-triiodobenzoyl chloride was synthesised from the commercially available **167** using thionyl chloride as chlorinating agent (Scheme 5.2).[313]

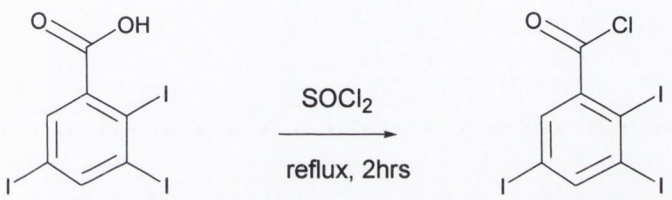

167 **165**

Scheme 5.2 ***Synthesis of 2,3,5-triiodobenzoyl chloride, 165.***

The reaction proceeded smoothly with a high yield (85%) of **165**, after recrystallization from chloroform-hexane (1:1, *v/v*) mixture. ^{1}H-NMR, ^{13}C-NMR, IR, ESMS and elemental analysis confirmed the structure of the acid chloride. Synthesis of **166** is illustrated in Scheme 5.3.

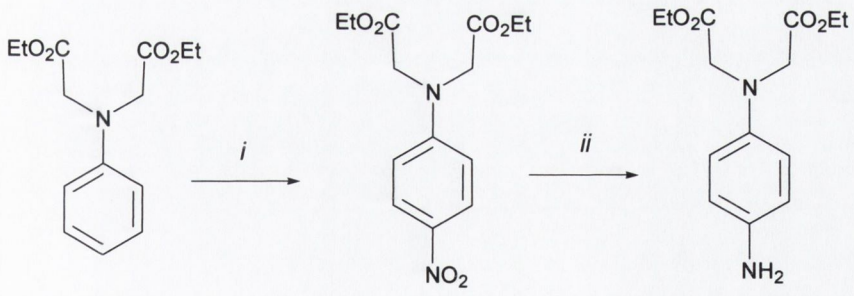

110 **170** **166**

Scheme 5.3 ***Synthesis of 166. Reagents and conditions: (i) HNO_3 (70%), CH_3COOH, 0^0C, 15 minutes; (ii) H_2, Pd-C (10%), 1 atm, 15 minutes.***

The synthesis of **110** has been reported in Chapter 2 (Scheme 2.7). The nitration of **110** was modified from a literature procedure.[314] In the reported method, fuming nitric acid (88%) in acetic acid, and less reaction time (few minutes) was used for the nitration of the related system (methyl esters instead of ethyl). However, use of such concentrated acid resulted in charring and consequently low yield (20%) of **170**. Switching to 70% nitric acid and increasing the reaction time to 15 minutes, followed by recrystallization of the crude product from 2-propanol dramatically improved the yield of **170** (76%). It is most likely that the use of harsh conditions (88% HNO_3) resulted in the oxidation of aromatic system as the $-N(CH_2CO_2Et)_2$ groups make **110** electron rich and thus susceptible to oxidation. Hydrogenation using Palladised charcoal proceeded smoothly to give **166** in quantitative yields. Both **170** and **166** were characterised by ^{1}H-NMR, ^{13}C-NMR, IR, ESMS and elemental analysis.

Condensation of **166** with the acid chloride **165** was straightforward resulting in the high yields (80%) of **164** after purification by silica flash column chromatography using ethylacetate:hexane (2:5, *v/v*) as eluant. The alkaline hydrolysis of **164** in MeOH:H_2O (10:1, *v/v*) mixture resulted in the target compound **160** (Scheme 5.4).

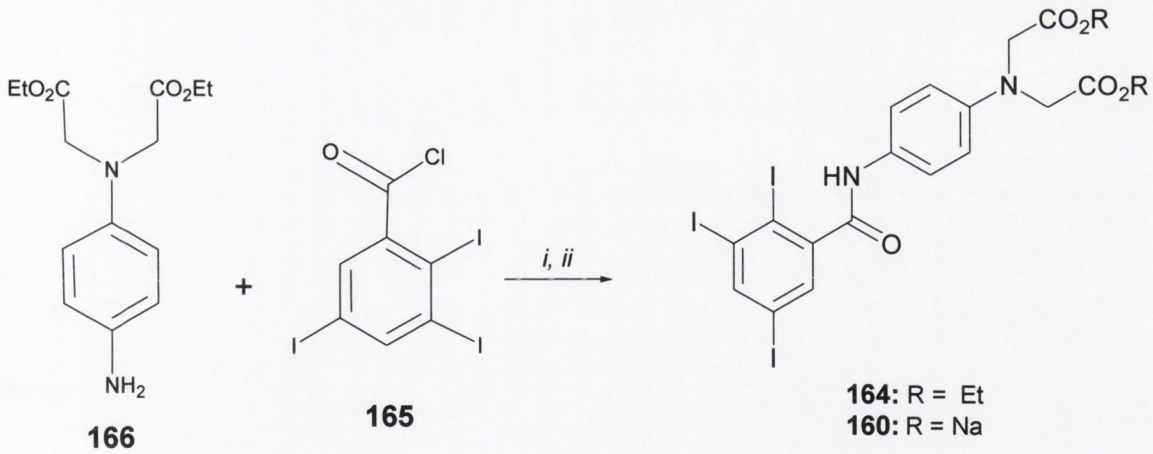

Scheme 5.4 ***Synthesis of 164 and 165. Reagents and conditions: (i) THF, NEt_3, reflux, 8 hours; (ii) NaOH, MeOH-H_2O, reflux, 2 hours.***

The purification of **160** was initially achieved by precipitation at –10°C. However the product was impure and low in yield (32%). The procedure was modified to increase both the yield and purity. Upon completion of hydrolysis the reaction mixture was evaporated

and the residue was dissolved in a minimal amount of distilled water. This solution was then diluted with methanol, heated to boiling and activated charcoal was added. The solution was kept at room temperature for 2 days. The solution was then filtered and evaporated to dryness. The residue was again diluted with a minimal amount of water. This aqueous solution was added dropwise to a stirred ethanol to precipitate **160**. This purification method removed all the coloured impurities and improved the yield dramatically (92%). ^{1}H-NMR, ^{13}C-NMR, IR, ESMS and elemental analysis established the structure of ester **164** and sodium derivate **160**.

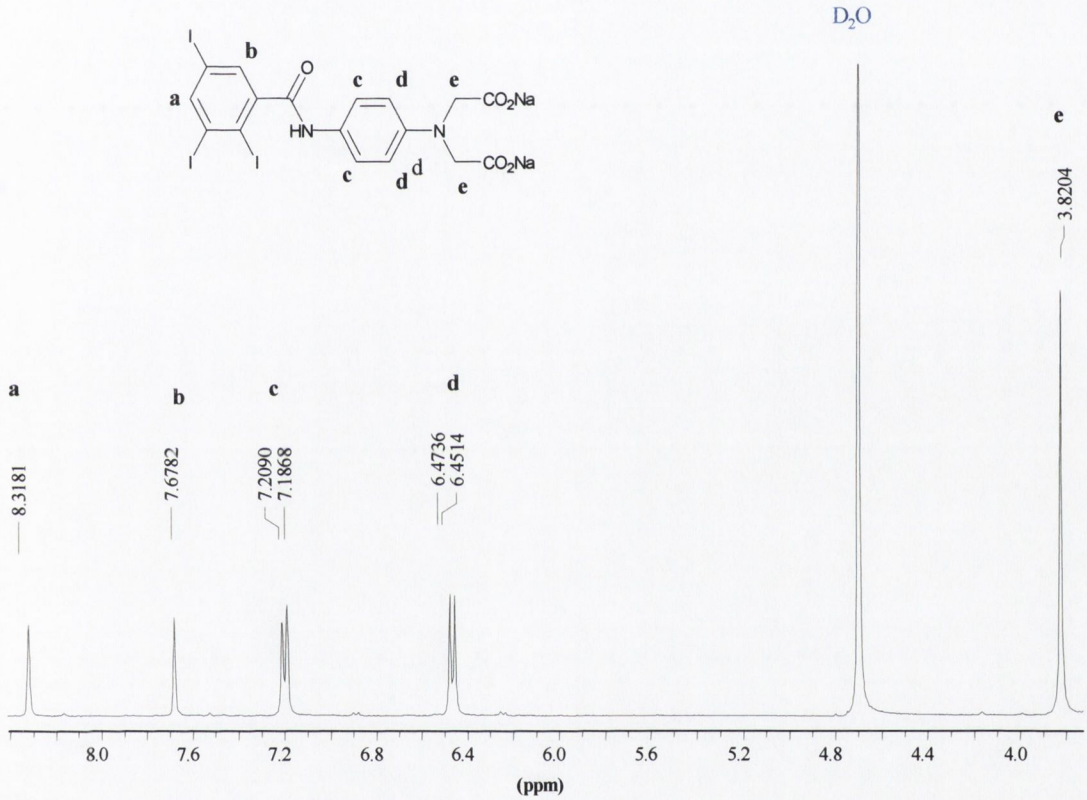

Figure 5.5 ***^{1}H-NMR of 160 (D_2O, 400 MHz).***

The ^{1}H-NMR spectrum of the **160** is illustrated in Figure 5.5. The phenyl protons **c** and **d** appeared as doublets at δ 6.46 and δ 7.20 respectively. The two singlets observed at δ 8.34 and δ 7.68 correspond to **a** and **b** respectively. The methylene groups of the –N(CH_2CO_2Na) moiety showed up as singlet at δ 3.82. In the IR spectra of **160,** the carbonyl stretching frequency was observed at 1690 cm^{-1}. ESMS peak was observed at 767 mass units (M+H_2O).

5. 4.2. Design, synthesis and characterisation of contrast agent 161

The synthesis of **161** is based on the same design strategy developed for **160** and is outlined in Scheme 5.5. The positioning of two phenyliminodiacetate moieties in *meta* configuration would result in ionic interaction with the unsaturated lattice sites in damaged bone. Furthermore, the primary aromatic amine was not functionalised with acetoxy or other similar *N*-alkyl or aryl groups for two main reasons:

- the amine group can be attached to a fluorescent tag such as 4-aminonaphthalimide or fluorescein moiety. Such a dual functionalised molecule can act both as iodinated contrast agent and histological stain. It is envisaged that by using these fluorescent iodinated molecules one can validate μ-CT imaging studies with histology.
- the other advantage is that more iodinated aromatic rings can be attached using amino groups leading to the formation of dimers or trimers with a higher iodine concentration, improving biological and pharmacological stability.

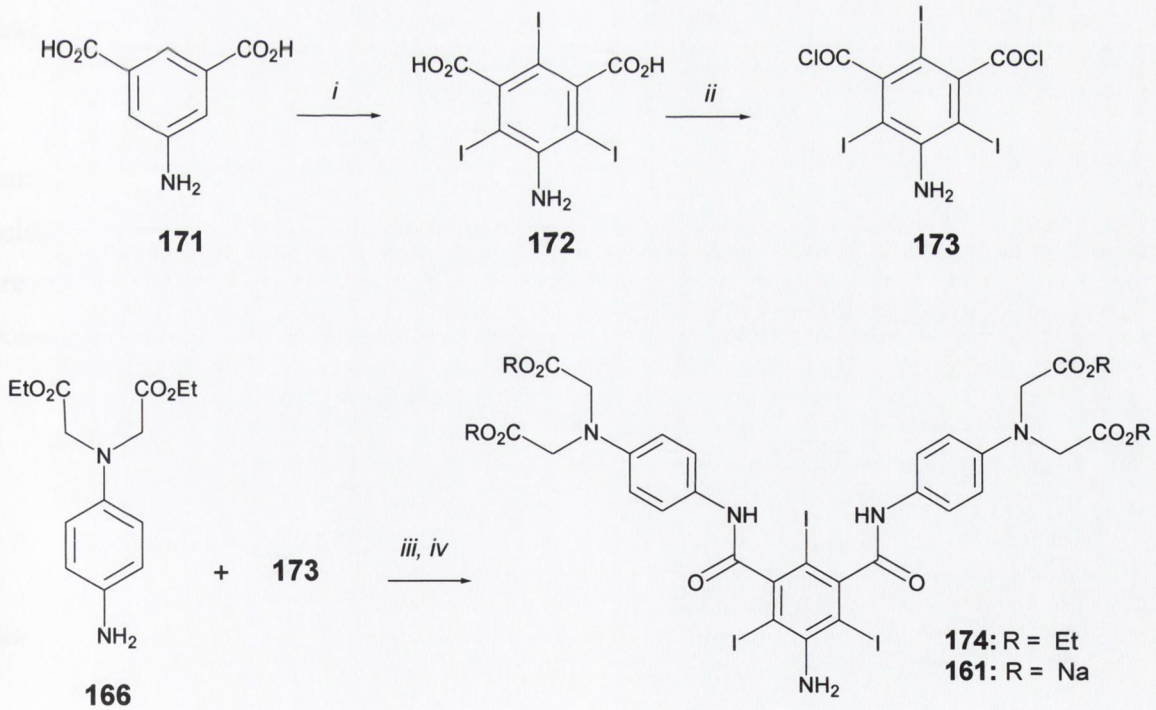

Scheme 5.5. Synthesis of 174 and 161. Reagents and conditions: (i) $KICl_2$-H_2O, 24 hours; (ii) $SOCl_2$, reflux, 6 hours; (iii) DMA, NEt_3, 24 hours; (iv) NaOH, MeOH-H_2O, reflux, 3 hours.

It is feasible to use 5-aminoisophthalic acid **171** as the starting material for the synthesis of **161**, as it consists of two carboxyl groups *meta* to each other. The synthetic protocol followed is shown in Scheme 5.5. In the initial step, the method developed by Larsen was utilised to incorporate three iodine atoms in **171** using $KICl_2$-H_2O in neutral conditions.[315] $KICl_2$ was generated *in situ* by combining potassium chloride (KCl) and iodine mono chloride (ICl). Several issues related to the success of this synthetic plan deserve comment. The iodination step is critical for obtaining the pure and high yield of intermediate compounds. Two different methodologies were explored before identifying the above conditions. The first method was the use of iodine monochloride in hydrochloric acid solution. In these conditions ICI is stabilised by complexation with hydrochloric acid (Scheme 5.6).[316] The water decomposes the iodine monochloride with the release of iodine, which acts as an electrophile for aromatic substitution.[315]

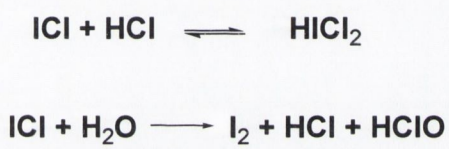

Scheme 5.6 ***Complexation and decomposion of iodine monochloride.***

However, the disadvantage of this system is that conditions are acidic. This is particularly undesirable for compounds containing basic groups such as amines. The highly acidic conditions lead to the oxidation of amines giving highly coloured impurities, which are difficult to remove. Thus the complexation of the iodine monochloride with sodium or potassium chloride was favoured (Scheme 5.7).[317]

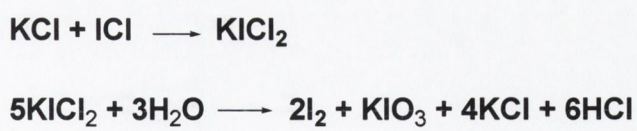

Scheme 5.7 ***Chemical reaction involved during iodination by KCl-HCl-H_2O system.***

Under these conditions the amino group is unprotonated and the carboxyl group exists as a carboxylate anion thus increasing the reactivity of the aromatic system towards electrophilic substitution. The purification of **172** is essential for the success of the

subsequent reactions. The crude product of the iodination was converted to its potassium salt by addition of 1 M KOH and the resulting solution was decolourised with activated charcoal at 70-80^{0}C for 30 minutes with stirring followed by filtering. This procedure was repeated 3-4 times. For complete decolourisation, the solution was kept over charcoal overnight and then filtered. The salt was acidified with concentrated hydrochloric acid to yield **172**. The conversion of 5-amino-2,4,6- triodoisophthalic acid (**172**) to bis-acid chloride **173** was accomplished using freshly distilled thionyl chloride. The spectral data of **172** and **173** was in close agreement with the reported values. Condensation of **173** and **166** in dimethylacetamide (DMA), using triethylamine as base, resulted in **174** (80%). The crude ester **174** was purified by recrystallization from ethanol. Alkaline hydrolysis of ester **174** resulted in almost quantitative yield of **161**. The acetate **161** was purified in a similar manner as described for **160**.

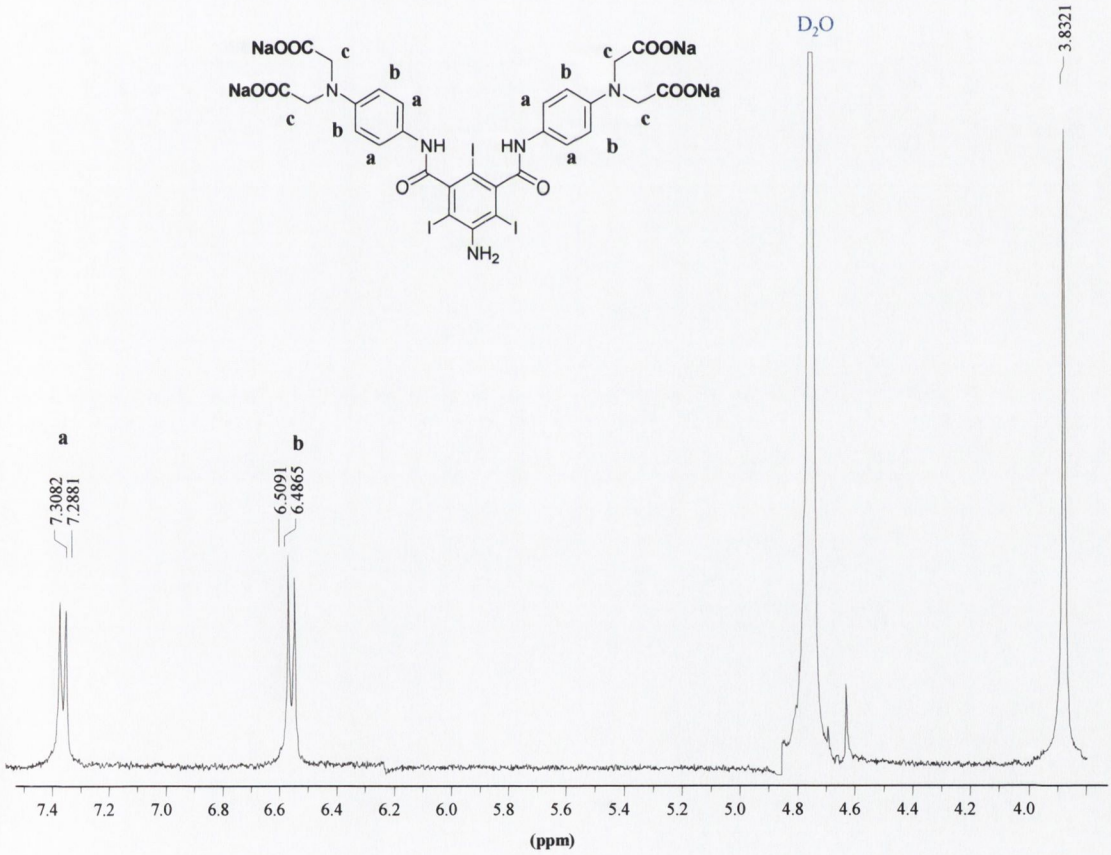

Figure 5.6 ***^{1}H-NMR of 161 (D_2O, 400MHz).***

Both **174** and **161** were characterised by ^{1}H-NMR, ^{13}C-NMR, IR, ESMS and elemental analysis. ^{1}H-NMR spectrum of the **161** (as shown in Figure 5.6) was simple. The phenyl protons resonance **a** and **b** was observed as doublets at δ 6.49 and δ 7.29 respectively. A signal at δ 3.83 was assigned to methylene protons of the –N(CH_2CO_2Na) group. The ^{13}C-NMR spectrum was also simple with peaks at δ 170.83 and δ 178.95 corresponding to the carbonyl group of amide and carboxylate functionality respectively. A IR peak observed at 1600 $cm^{-1}$was assigned to carbonyl stretching frequency. ESMS peak at 1082 mass units ($M+Na^+$, 90%) was observed for **161.**

5.4.3. Design, synthesis and characterisation of contrast agent 162

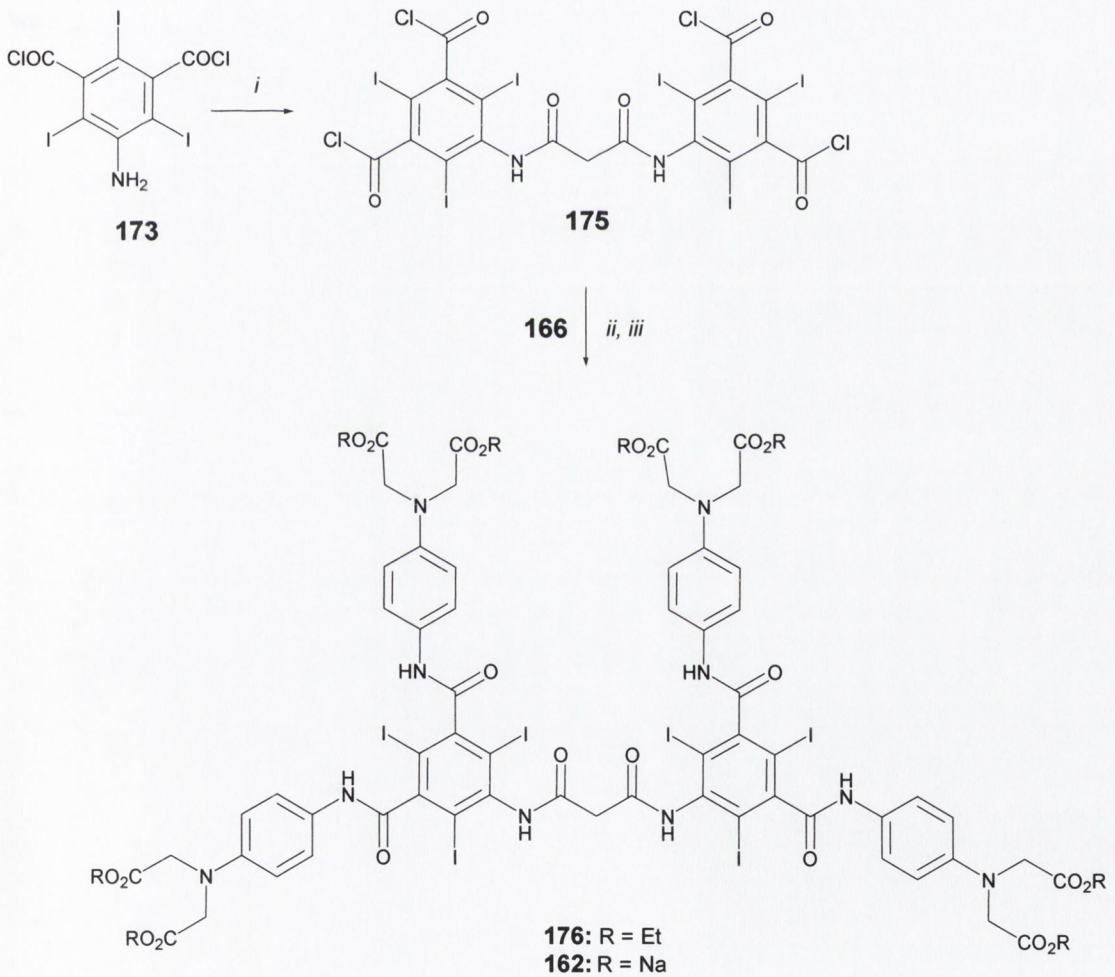

Scheme 5.8 ***Synthesis of 162 and 176. Reagents and conditions: (i) Malonyl dichloride THF, reflux, 6 hours; (ii) $SOCl_2$, reflux, 6 hours; (iii) DMA, NEt_3, 24 hours; (iv) NaOH, MeOH-H_2O, reflux, 3 hours.***

The synthetic protocol illustrated in Scheme 5.8 was used for the synthesis of **162**. The 5-amino-2,4,6-triiodobenzenedicarbonyl dichloride **173** was dimerised using malonyl dichloride.[318] The steric crowding of the bulky iodine atoms hindered the polymerisation of **173** and **175** was obtained as the major product. Ranganathan *et al.* and Wharton and Wilson have reported similar observations.[305,319] The ^{1}H-NMR and ^{13}C-NMR spectra of **175** was in full agreement with the reported values.[319] The condensation of **175** with 5 equivalents of **166** in DMA, using triethylamine as base, resulted in the formation of ester **176**. The progress of the reaction was followed by TLC using ethyl acetate:hexane (3:2, *v/v*) as solvent system. It was discovered that keeping the reaction mixture at 30^{0}C and 24 hours was the optimum temperature and time for the completion of the reaction. The purification of the ester by recrystallization from ethanol resulted in pure **176** (80%). The subsequent basic hydrolysis of **176** in MeOH-H_2O afforded the target molecule **162,** which was purified in a similar manner described for **161**.

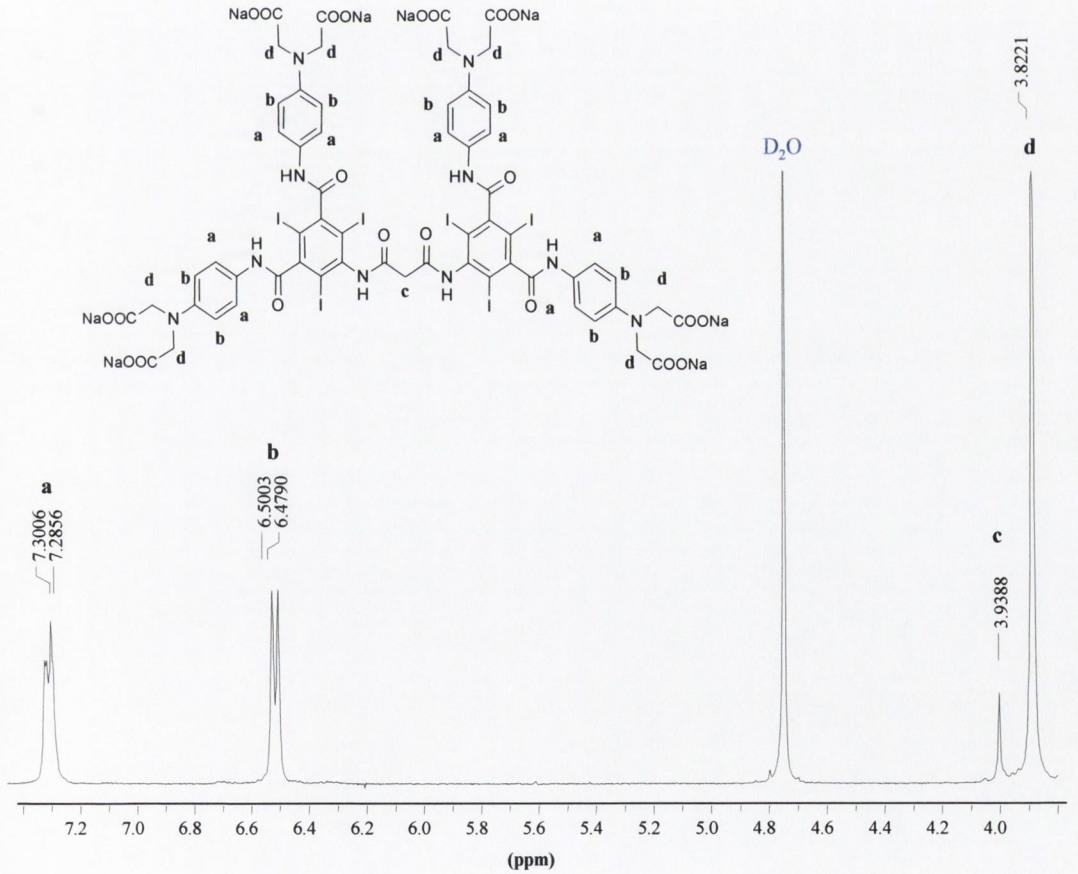

Figure 5.7 ***^{1}H-NMR of 162 (D_2O, 400MHz).***

The ^{1}H-NMR spectrum of **162** (Figure 5.7) was simple enough to interpret showing only the predicted proton signals. The phenyl protons **a** (close to –CONH- group) showed slight degree of splitting and appeared as unsymmetrical doublets at δ 7.30, while protons **b** were observed as distinct doublets at δ 6.49. A singlet at δ 3.93 was assigned to methylene group **c**. The singlet at δ 3.82 was attributed to the methylene protons of –N(CH_2CO_2Na) groups.

5.4.4 NMR analysis of 161 and 162

The hexasubsituted benzene compounds have been studied extensively for the phenomenon of conformational equilibrium analysis.[305,320] As all the positions in the benzene ring are substituted, these compounds are sterically congested leading to atropisomerism. Bradmante and Vittadini have done comprehensive NMR studies on steric effects of these crowded molecules.[320] According to the authors, the isomerism can be originated due to the lack of rotation around four main types of bonds

- Ar-CO bond
- Aryl-N bond
- CO-N bond of isophthalimide moiety
- N-CO bond of amide moiety.

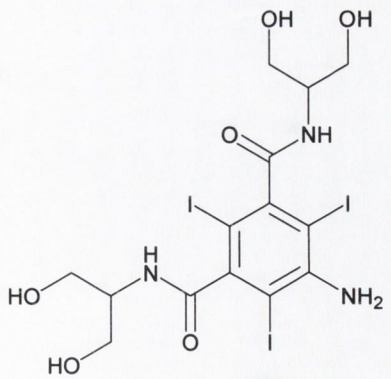

177

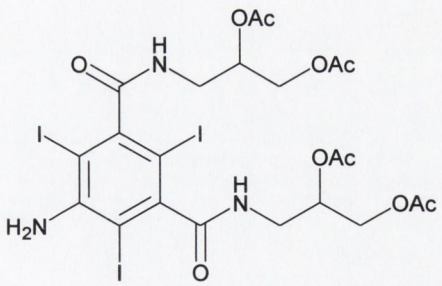

178

This type of isomerism has been reported in contrast agents **177** and **178**.[320,321] In **177** carbon spectrum in DMSO-d_6 showed two signals at δ 168.02 and δ 167.80, which were assigned to carbonyl functionality of two amide groups. In the ^{1}H-NMR the –NH protons

of these amide groups were observed as doublets at δ 8.0 and δ 7.43 in DMSO-d_6. This was interpreted as a result of restricted rotation of Ar-CO bonds. Ranganathan *et al.* have observed similar phenomenon for **178** in which the -NH protons appear as pair of quartet.[321] ^{13}C-NMR spectrum also indicated non-equivalence of the carbon atoms. This was explained due to the lack of free rotation around Ar-CO bond and as a result existing as rotamers. However in contrast agents **160**, **161** and **162**, the ^{13}C-NMR and ^{1}H-NMR exhibited simple splitting patterns with all the carbonyl functionality of the amide group being equivalent. Also the aromatic and methylene protons of the phenyliminodiacetate chelator unit were equivalent. The corresponding esters also exhibited similar spectral patterns. It indicates that the molecules exist as a single isomer. The probable explanation for this could be the effect of stabilisation of one isomer induced by extended conjugation. Similar observations were made in natural products with extended conjugation such as biphyscion.[322]

5.4.5 Attempted synthesis of 163

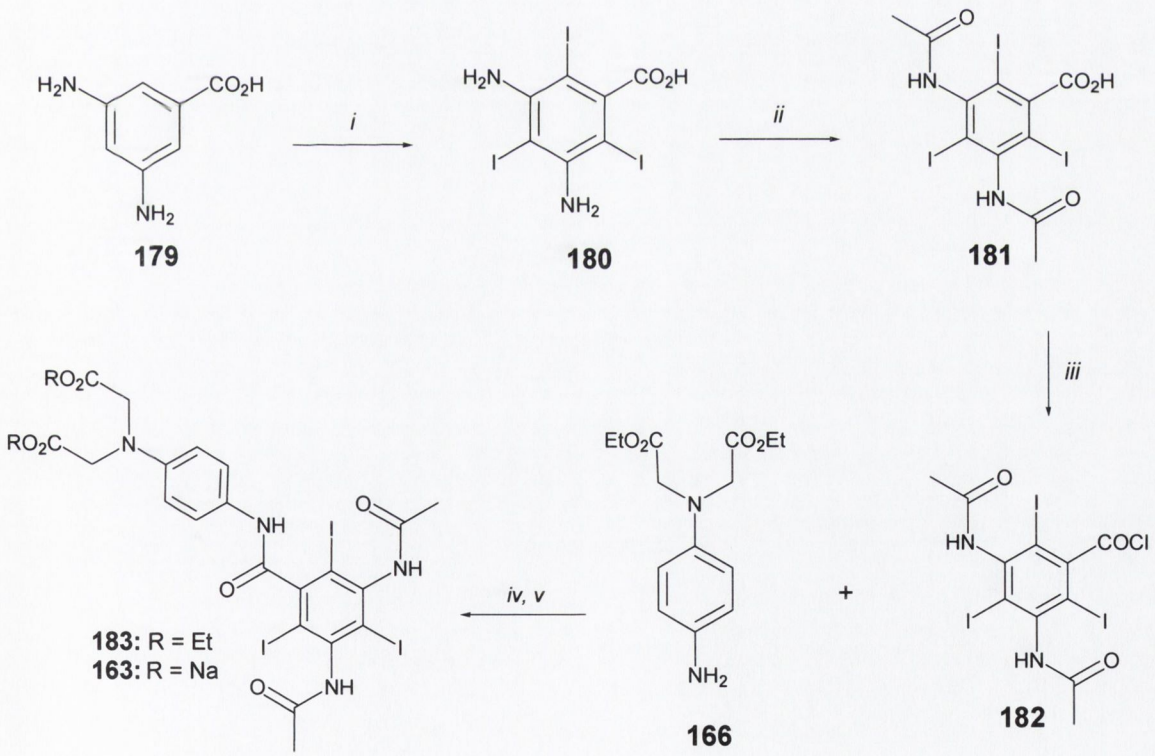

Scheme 5.9 ***Attempted Synthesis of 163 and 183. Reagents and conditions: (i) $KICl_2$-H_2O, 24 hours; (ii) $(CH_3CO_2)_2O$, H_2SO_4, 30 minutes; (iii) $SOCl_2$, reflux, 3 hours; (iv) DMA, NEt_3, 24 hours.***

The synthetic protocol followed for **163** is shown in Scheme 5.9. The iodination of the **179** using $KICl_2$-H_2O followed by purification as described for **172** resulted formation of **180** (65%).[37] Acetylation of **180** was achieved by suspending the amine in acetic anhydride in the presence of a small amount of concentrated sulphuric acid.[298,315] Acetylation was completed in 30 minutes to give crude diacetylated **181**. The product was purified to remove coloured impurities. The crude product was dissolved in 1M NaOH and precipitated as an ammonium salt by addition of ammonium chloride. Upon acidification with concentrated HCl, the free acid **181** was obtained. The chlorination of **181** was effected by using freshly distilled $SOCl_2$. The progress of the reaction was monitoring by ESMS. It was found that 3 hours was the optimal time for the completion of the reaction and to obtain maximum yield of the product **182**. The mass spectrum showed only the peaks corresponding to the sodium complex of the desired product **182** as shown in Figure 5.8.

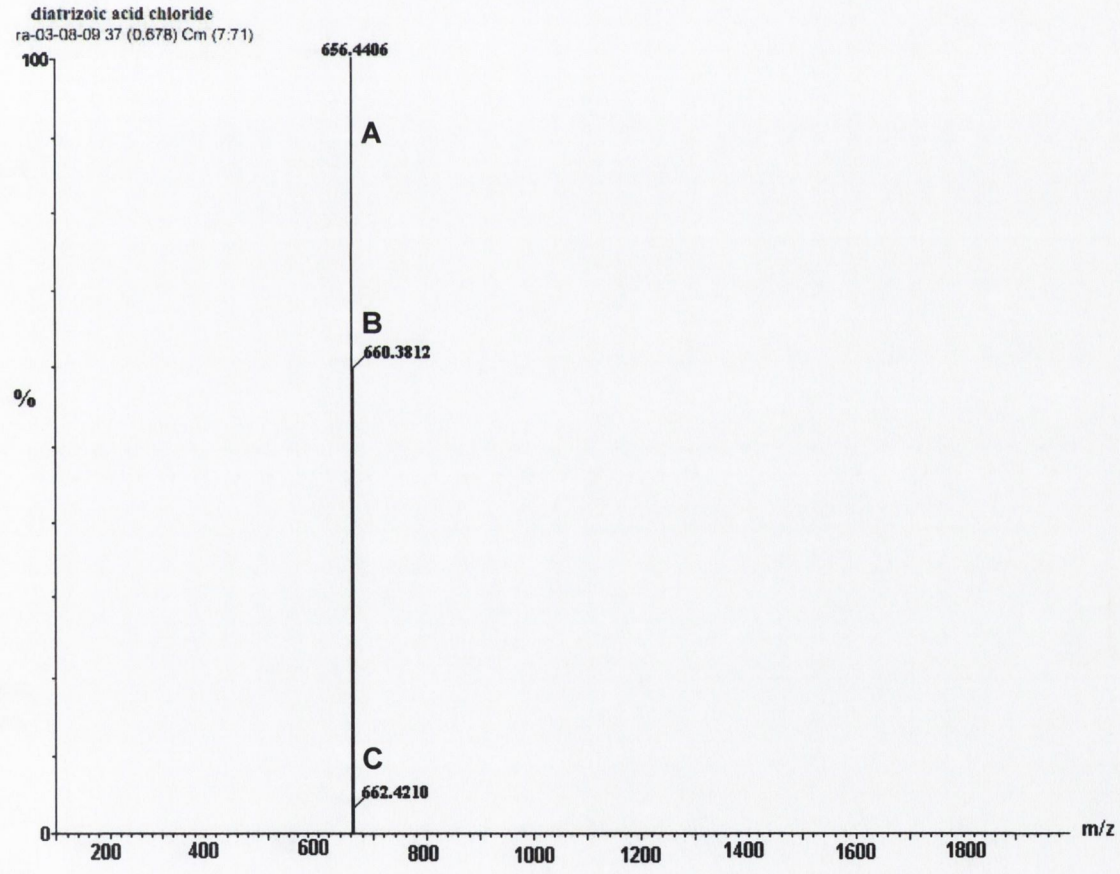

Figure 5.8 ***ESMS of reaction mixture after 3 hours of progress of reaction. A = M+Na, B and C correspond to the isotopic pattern observed due to iodine and chlorine atoms.***

Compounds **180**, **181** and **182** were characterised by ^{1}H-NMR, ^{13}C-NMR, IR, ESMS and elemental analysis.

The final step of condensation of **182** with **166** proved difficult. Condensation was attempted in DMA as described for **174**, but reaction was unsuccessful and only starting material was recovered. Alternate strategies were attempted without success as outlined in Scheme 5.10.

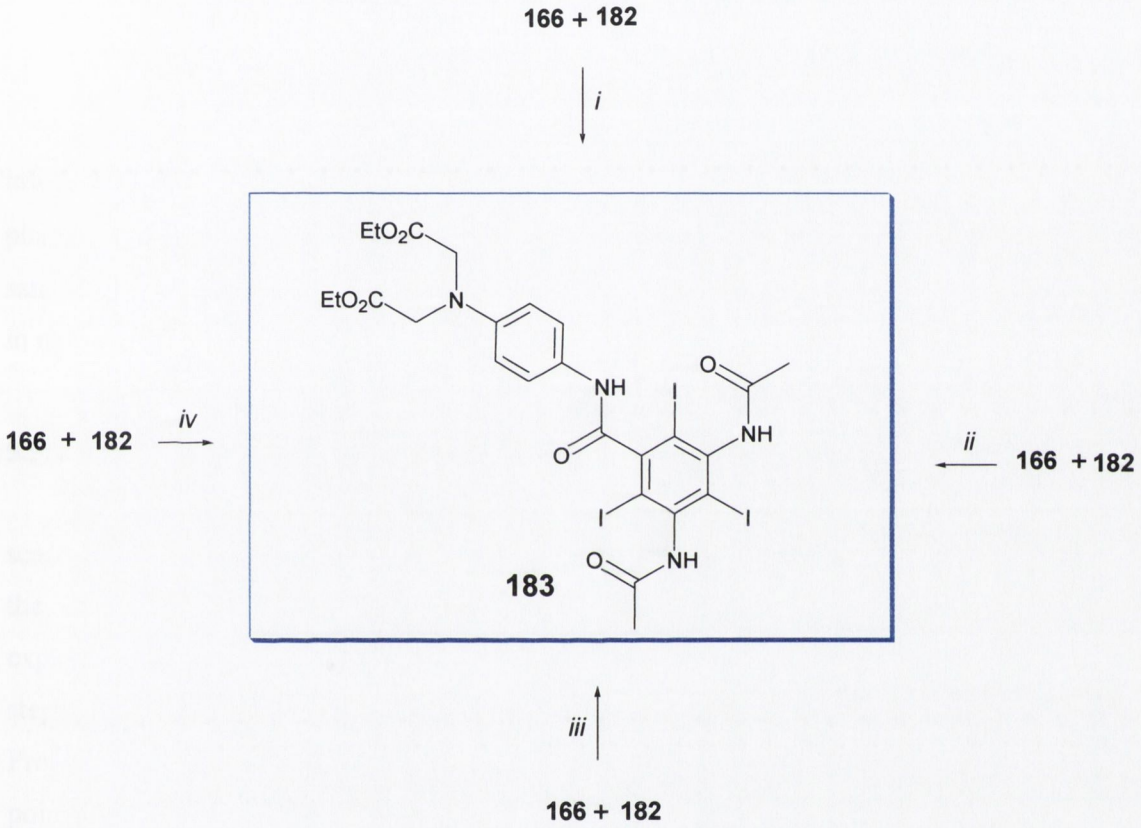

Scheme 5.10 ***Unsuccessful attempts for synthesis of 183. Reagents and conditions: (i) DMA, NEt_3, 48 hours, 2 days, (ii) HMPT, NEt_3; (iii) DMF, NEt_3, 24 hours; (iv) THF, NEt_3, 12 hours, 24 hours.***

At this stage no explanation for the observed failure of these reactions, although it can be postulated that due to the presence of two *N*-acetyl groups and iodine atoms, the attack of the primary aromatic amine is sterically unfavourable. The synthesis of **163** was not attempted further and it was decided to proceed with the preliminary imaging studied of the contrast agents **160-162.**

5. 5 Preliminary evaluation of contrast agents 160, 161 and 162

The next stage was to assess these contrast agents for μ-CT imaging, with the following objectives in mind:

- to obtain qualitative and quantitative information about contrast
- to visualize the internal structure of bone
- to determine the optimal concentration of 160-162 for clinical use.

For this purpose, the qualitative and quantitative studies were carried out to get information about the contrast of the agents **161**, **162** and **163**, in both solid and solution phase. This was accomplished by using a μ-CT imaging system. μ-CT is based on the same theoretical principle as employed in conventional Computed Tomographic (CT) used in radiology.

5.5.1 Computed Tomography

The introduction of CT in the 1970s revolutionised the field of radiology.[323] In a CT scanner a collimated X-ray beam is directed on the object. When the X-ray passes through the object, its intensity decreases depending on the degree of absorption or attenuation as explained in Chapter 1. The X-rays project upon the object at different angles *e.g.* in 1^0 steps, and thus there are a large numbers of projections, *e.g.* 360 for a full rotation. Projections have to be made from all the directions of the object so as to get as many data points as possible. The attenuation values for each projection are stored in a computer, and the CT images are reconstructed from the stored data. The computers store a large amount of data from a selected region of the body. This allows for the accurate reconstruction of the object image. The finite numbers of attenuation values corresponding with the scanned object are organised as intensities called image matrix.[324] The translation of these attenuation values into various analogous grey levels creates a visual image of the scanned object. As the absorptive power varies within the object, this leads to different grey levels of the pixels and hence it is possible to identify the internal architecture of the object. The size of the image matrix, i.e. the number of calculated picture elements, is selectable by the operator. The matrix size influences the image resolution.[324]

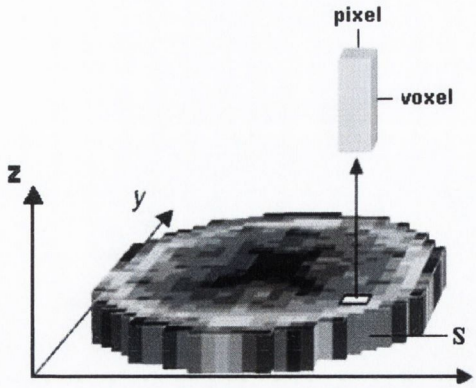

Figure 5.9 ***Schematic illustration of a CT scan with a given slice thickness, demonstrating the concept of two-dimensional picture elements or "pixels" and their associated volume elements or "voxels".***[325]

In order to understand how images are scanned in a CT, it is useful to visualize the human body as built up of a finite number of discrete slices and volume elements (Figure 5.9). Each single slice scan, aims to determine the composition of one transverse cross-section. This respective slice or section is a composition of discrete cubic volume elements. The value attributed to each volume element is displayed in one picture element in the digital image matrix. The picture element of the image matrix is known as "*pixel*" (*pi*cture *el*ement) and the numerical information contained in each pixel is a CT number, or Hounsfield unit (HU). Based on the slice thickness, the pixel also represents a volume element which is determined by slice thickness, matrix size and diameter of the scanning field. Under these conditions, a picture element also represents a "*compressed*" volume element or "*voxel*".[325]

The pixel size depends on the field of view (FOV), the area covered by the image. The size of the image matrix and the FOV determines the spatial resolution of the CT image.[326] Modern CT images can have a resolution of 0.3 mm voxel size.[327] Recent advances in the field of photonics such as the availability of charge-coupled devices (CCD) as well as high-performance computers have made it possible to obtain high resolution images down to 4 μm voxel. Such type of CT systems that are capable of volumetric CT analysis with isotropic spacing (pixel size identical to the slice thickness) of less than 100 μm are defined as μ-CT systems.[328] μ-CT system also differs from the CT systems, in the fact that it is the specimen, mounted on a turntable, which rotates, rather than the source/detector system. μ-CT can employ microfocus an X-ray tubes or a synchrotron-based X-ray source. The latter systems are capable of much higher resolution.[329] In the present study, X-ray tube based μ-

CT was utilised for imaging studies. The μ-CT studies were conducted at the Free University, Berlin where a state-of-the art 'cone-beam' μ-CT system is operating.[338] The key components of the system are:

- a microfocus X-ray tube with 5 μm focus diameter, 50 kV accelerating voltage, 50 μA target load.
- a two-dimensional CCD device square detector with $(512)^3$ elements of $(19\ \mu m)^2$ size each, 3:1 magnifying fibre-optic taper, phosphor plate and a Peltier liquid cooling which can provide a temperature of -40^0C to improve the signal-to-noise ratio in a 16-bit dynamic range.
- a flexible fully motorised positioning system
- software for raw data acquisition, volume reconstruction, simulation, and image analysis.

The schematic representation of the μ-CT employed in the imaging studies is depicted Figure 5.10.[327,328]

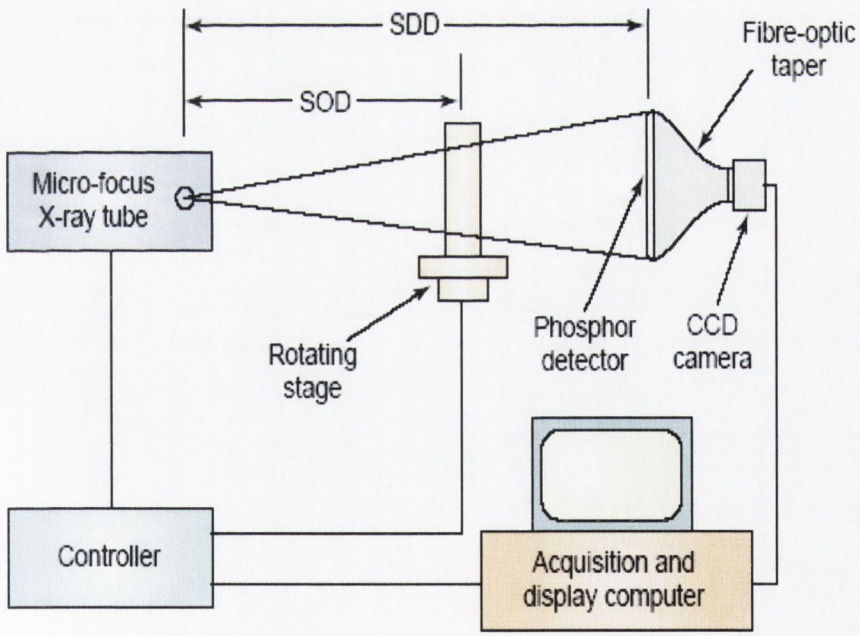

Figure 5.10 ***Schematic representation of μ-CT scanner. The source-to- object distance (SOD) and source-to-detector distance (SDD) is ~ 20 cm and 90 cm respectively.***[327]

The tube and the detector in μ-CT system remain fixed and the object is rotated. A phosphor detector, coupled to CCD by a fibre-optic taper, which reduces the size of the image, acquires X-ray projections. The acquisition of projections is performed in cone geometry. During acquisition, a computer controls the X-ray tube and the specimen table, obtaining X-ray projections at each half degree angle position. The axis of rotation (AOR) is oriented vertically and the object can be vertically translated during acquisition (Figure 5.11).

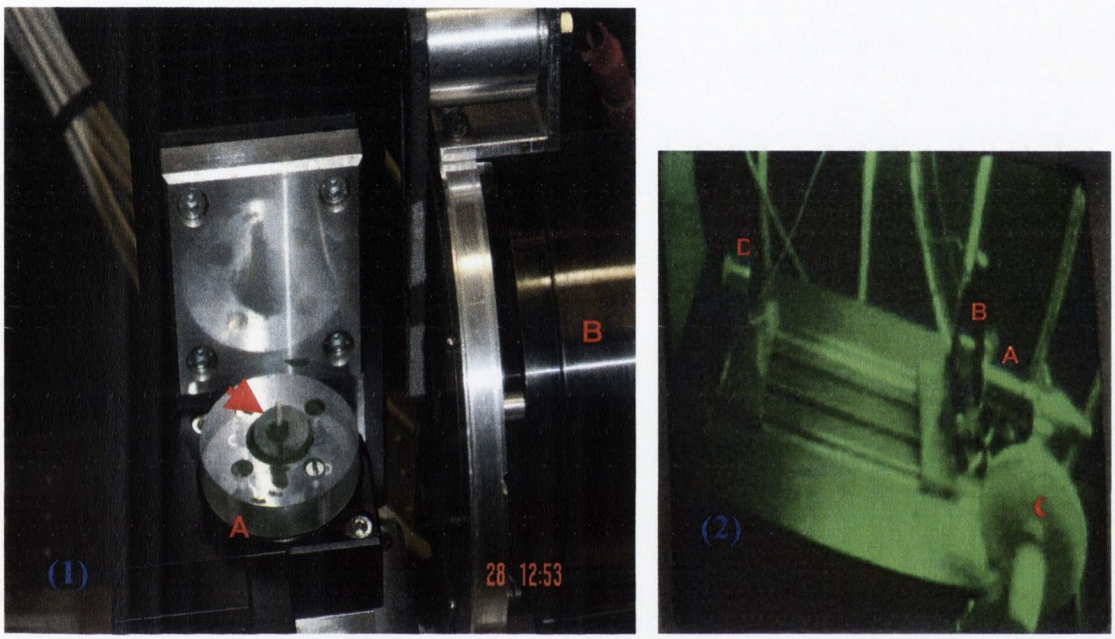

Figure 5.11 ***(1) Close-up of the micro-CT system used in the present study. Note bone specimen (red arrow) mounted on the examination table (A). B = X-ray tube. (2) μ-CT scanner in actual operation. A = X-ray tube, B = turntable on which the specimen is mounted, C = cooling provided by fan, D = Detector.***

Two different approaches were employed for μ-CT imaging of bone specimens:

- the surface of the bone samples were wetted with water and the powdered contrast agent was applied
- a scratch of 5 mm was made on the bone surface and the scratched surface immersed in 10^{-3} M aqueous solution of agents under vacuum overnight and scanned.

5.5.2. Evaluation of 160, 161 and 162 in powder form

Bovine tibia were used in the μ-CT imaging studies. The soft tissue was removed from all bones and they were stored at -20^0C until required. Longitudinal sections of cortical bones with dimensions of 2x2 mm from the mid-diaphysis were cut into 1 cm beams using a band saw and polished using emery paper (grade 400). All machining was carried out in wet conditions and the bones were not allowed to dry at any time. After machining the specimens were stored at -20^0C prior to CT imaging. The sample was mounted on the examination table and rotated 180 degrees and a total of 360 projections were recorded. At 5 seconds exposure time for each projection the entire scanning lasted 1.0 hour. The data stored in the computer was analysed and reconstructed using the Amira software.[330] The reconstruction lasted approximately 1.5 hours. By manipulating 3D data-sets, it was possible to observe the canals, osteons and resorption cavities in bones. The smallest volume element (voxel) achieved was 4 μm and the images were reconstructed using a Shep-Logan filtered modified Feldkamp algorithm.[331] The X-ray absorption value for each and every point in space is reconstructed. The different absorption values (CT number or Hounsfield value) result in a 2D or 3D image of the scanned object. Reconstruction of images along sagittal (2-D plane going from the left to the right side through the specimen), coronal (2D plane going from the front to the back of the specimen) and transaxial planes (2D plane going from the top to the bottom of the specimen) were made possible using Amira visualisation software. As discussed earlier, the two and three-dimensional representation of the image is given in terms of pixel and voxel respectively.

All the contrast agents **160-162** were able to provide good contrast from the surrounding bone matrix as powdered substances. A 2D sagittal reconstruction was performed in order to evaluate the contrast ability of the agents, in comparison to the surrounding bone matrix. Contrast agent **160** was applied to the right side of the bone specimen as shown in the red box in the sagittal reconstruction in Figure 5.12 A. There is no contrast agent on the left-hand side (blue box). Both bone and contrast agent appear white however the agent appears to be more bright due to its higher X-ray absorption power and hence it is distinct from the bone surface. A 3D transparent section was reconstructed to further illustrate the contrast (Figure 5.12 B). It was possible to distinguish the internal architecture of the bone from the contrast agent **160** in the transparent reconstructed section. As can be seen from the Figure 5.12 B, Haversian canals and resorption cavities are clearly distinguished by the contrast provided by **160**

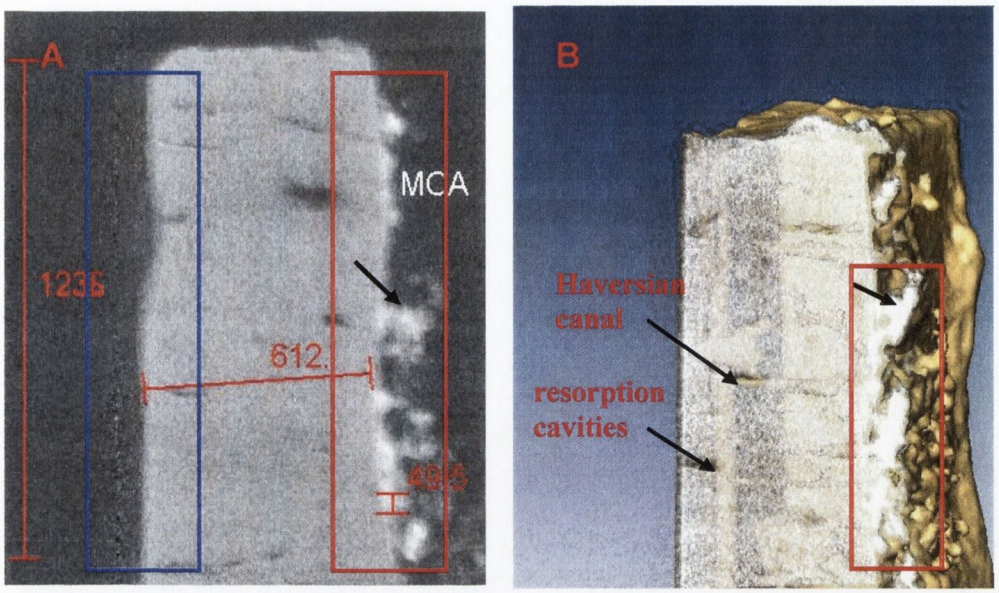

Figure 5.12 ***(A) Two dimensional (B) three dimensional sagittal section of a cortical bone specimen labelled with contrast agent 160. The white powder on bone edges is marked by black arrow). Bar is in μm.***

Both contrast agents **161** and **162** also provided similar results when applied as powder (Figure 5.13 and 5.14). Reconstructed 2D sagittal and transparent 3D images clearly shows that contrast agents are able to absorb X-ray more effectively than the bone thus providing good contrast from bone matrix.

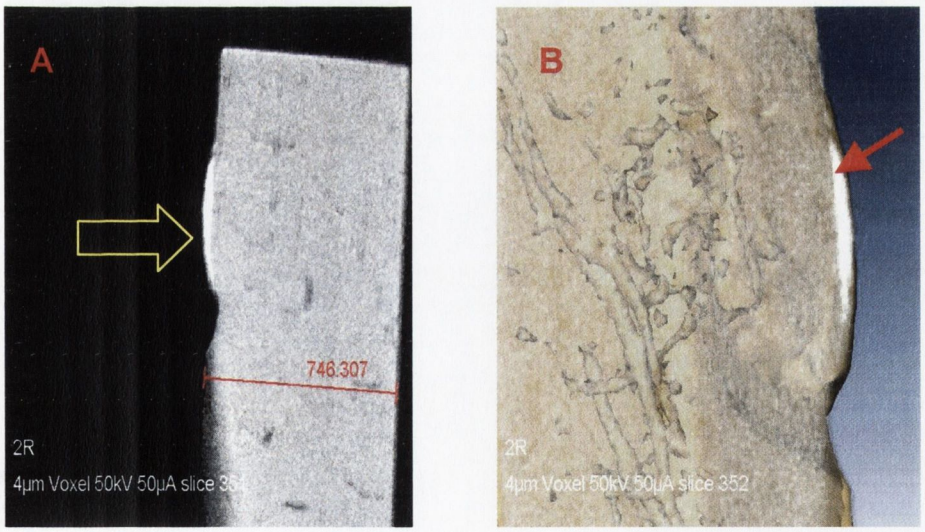

Figure 5.13 (A) Two dimensional sagittal and (B) transparent three dimensional (sagittal) reconstruction of a bone sample labelled with contrast agent 161. Bar is in μm.

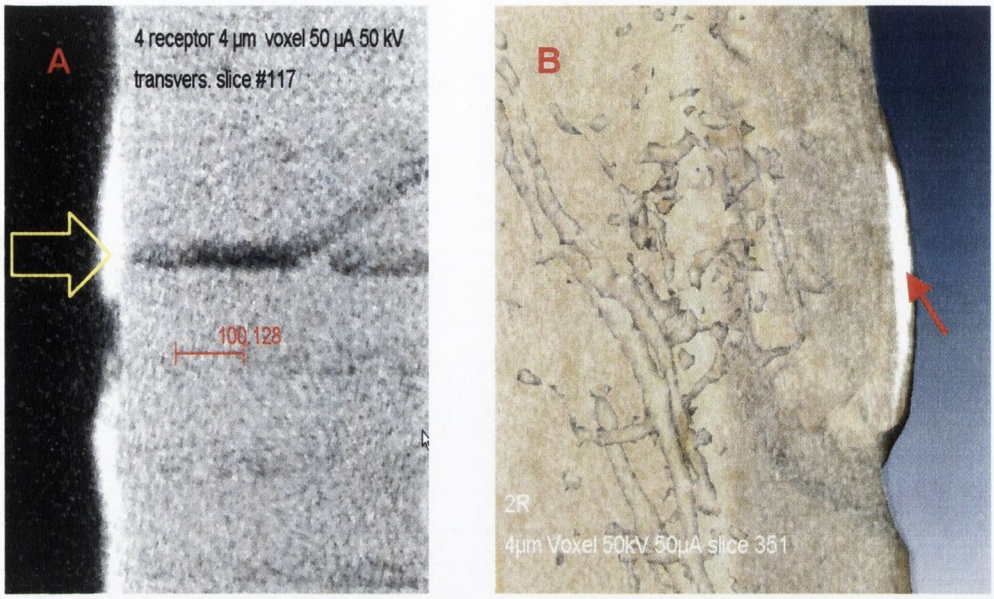

Figure 5.14 *(A) Two dimensional sagittal reconstruction of cortical bone labelled with 162 (arrow). The scale in the bar is in microns; (B). Transparent Three dimensional reconstruction of the same cortical bone specimen labelled with 162 (arrow)*

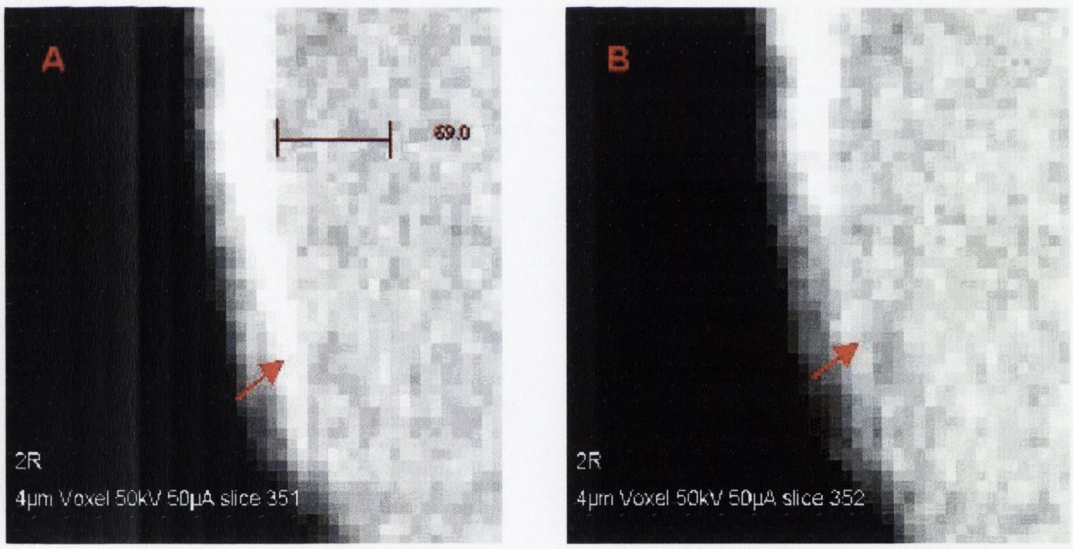

Figure 5.15 *Two dimensional sagittal reconstruction at higher magnifications to determine the thickness of 161 for obtaining the best contrast from the surrounding bone matrix. The difference between the A and B is one slice which corresponds to 4 µm. The red bar given is in pixels.*

In order to determine and quantify the thickness of the agent required to provide observable contrast under the present set of operating conditions the image visualisation was performed at higher magnification. The results are shown in Figure 5.15, as sagittal reconstruction for the bone specimen labelled with contrast agent **160**. As can be seen in Figure 5.15(A), the contrast agent is clearly distinct from the bone (at the red arrow region), while it is not possible to distinguish between bone and the contrast agent in that particular region (marked by red arrow in Figure 5.15 (B)). The difference between the two pictures (A and B) is about one pixel that equals to 4 μm. From these observations, it can be concluded that contrast agent **161** need to form a layer of 4 μm thickness to provide the best possible contrast.

Similar results were obtained for **162** and **163**. The transparent three dimensional sagittal reconstruction also supported the observation that contrast agent thickness of 4μm is required for observing visible contrast from the surrounding bone matrix. The results are shown in Figure 5.16 for bone specimens labelled with contrast agent **163**.

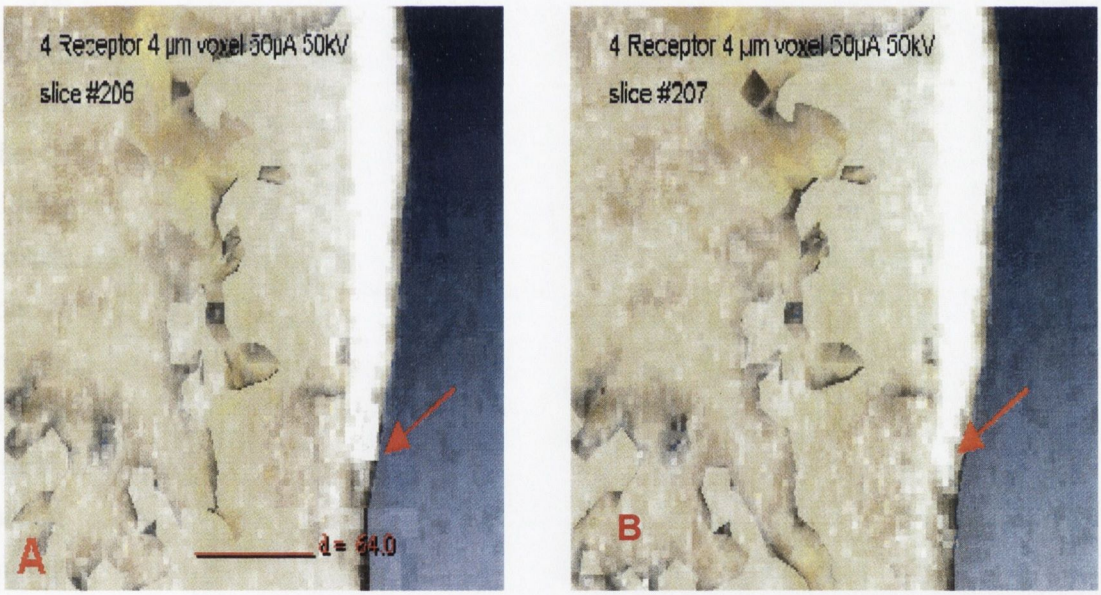

Figure 5.16 ***Three dimensional sagittal reconstruction at higher magnifications to determine the thickness of the 163 for obtaining the best contrast from the surrounding bone matrix. The difference between the A and B is one slice which corresponds to 4 μm. The red bar given in the figure is in pixels.***

5.5.3 Evaluation of 160, 161 and 162 in solution

After performing qualitative studies with the powdered agents, the next stage was to label scratches with the aqueous solutions of the contrast agents **160-162.** The imaging studies have been conducted using 10^{-3} M aqueous solution of the contrast agent **160** and **161.** Bovine tibia was used for the imaging studies. The methodology employed for the μ-CT imaging studies is shown in Table 5.2

Table 5.2 ***protocol used for μ-CT imaging***

Methodology employed for μ-CT imaging studies
• 5 mm straight line scratched on the surface of bone sample using a compass • bone specimens were immersed in a vial containing 10^{-3} M solution of the contrast agent and placed under vacuum (50 mm Hg) overnight • specimens were then analysed using μ-CT

The μ-CT studies were performed in a similar manner as described for powder. From the bone specimen labelled with **160,** the scratch is visible but the background contrast for both the scratch depth and surrounding bone matrix is almost overlapping (Figure 5.17). The difference of the contrast between bone and contrast agent cannot be differentiated. Although there is some blurring in the scratch region, the most likely reason for this may be the beam hardening effect. The beam hardening effect arises as X-ray photons striking the bone surface have different energy so the photons of lower energy are absorbed with higher probability than that of higher energy (Chapter 1, Section 1.4). As a result, the attenuation of X-ray is not homogenous and is dependent upon the energy of radiation, the type of object used in imaging, and the direction of projection. The consequence of all these factors introduces variations in the average energy of the X-ray spectrum when they impinge on thick objects such as bone. In terms of the quality of the image the beam hardening results in light 'hyperdense' zones, which can be easily mistaken for the contrast difference between two different regions. Therefore it cannot be determined if the higher absorption value is due to the contrast agent or the beam hardening. Beam hardening is considered as a type of artefact. It is difficult to correct the beam hardening effects for dense tissues such as bone. The transparent reconstruction (Figure 5.18) was also

performed but unfortunately, it was not possible to distinguish the contrast between bone and contrast agent.

Figure 5.17 Three dimensional axial reconstruction of the bone immersed in an aqueous solution of 160. Scratch can be seen on the left side (yellow arrow). The top of the axial plane shows a vessel canal (red arrow) within the bone tissue.

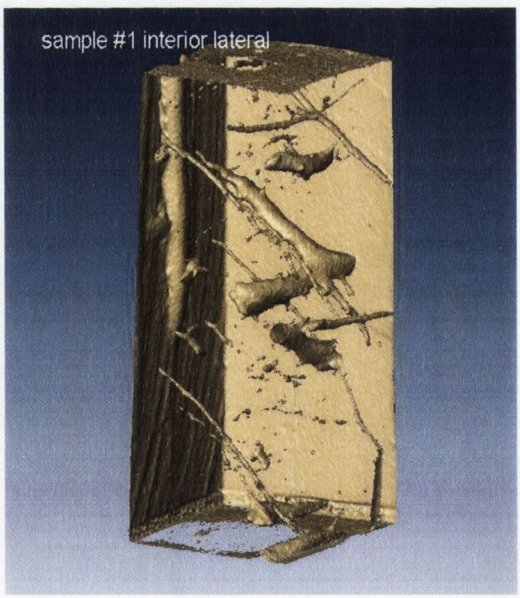

Figure 5.18 Transparent reconstruction (lateral view) of cortical bone immersed in the aqueous solution of 161.

5.6 Conclusions

Three novel iodinated contrast agents **160**, **161** and **162** based on triiodobenzene framework have been synthesised and evaluated for application as agents for non invasive technique for detecting and quantifying microdamage in bone. All the three contrast agents exhibited good water solubility and stability. NMR characterisation of these contrast agent confirmed that they exist as single isomer as result of extended conjugation. This is advantageous as the existence of isomerism adversely affects the desired physiochemical properties such as water solubility, chemical stability and osmolality.[299] It was hypothesised that the presence of chelating phenyliminodiacetate receptor could impart increased affinity for damaged lattice in the area of microdamage. Preliminary imaging studies of these contrast agents on bovine cortical bone specimens, using cone-beam μ-CT, demonstrated that agents in powder form are able to provide good contrast from the surrounding bone matrix. 3D image analysis revealed a radiopaque dye thickness of 4 μm is required for visualisation of contrast. Solution phase studies of these contrast agent was difficult due to beam hardening effect.

Chapter- 6

Experimental

6.1 Materials and methods

All chemicals were purchased form Aldrich, Sigma or Lancaster and were used as such, unless otherwise stated. All anhydrous solvents were either purchased in sure seal bottle or dried by standard procedures, as specified in standard textbook; *Purification of Laboratory Chemicals, 4th edition, ISBN 0-7506-3761-7* by Armarego, W.L.F.; Perrin, D.D. Deutrated solvents were dried over 3-A^0 molecular sieves prior to use. All untreated solvents used were of GPR grade.

Flash-column chromatography was performed using silica gel-60 (230-400 mesh). Thin-layer chromatography (TLC) analysis was performed on Merck Kiesegel F254 silica gel-60 plates and viewed by UV light, or developed with ninhydrin dip or iodine chamber. Melting points were determined using Electrothermal 9100 heating ramp apparatus and are uncorrected. Nuclear magnetic spectra were recorded using Bruker DPX 400 spectrometers with the corresponding deuterated solvent as noted. Tetramethylsilane (TMS) was used as an internal reference standard. ^{1}H-NMR were recorded at 400 MHz. ^{13}C-NMR spectra were recorded at 100 MHz. The chemical shifts are expressed in parts per million (δ or ppm) relative to the residue non-deuterated solvent peak. Chemical shifts are reported as the δ value, followed by the number of protons *e.g.* 1H, splitting pattern *e.g.* doublet, coupling constant (where applicable) *e.g.* J = 8.2 Hz, and assignment of protons *e.g.* Ar-H in brackets. A doublet splitting pattern is represented as **d**, a double doublet as **dd**, a singlet as **s**, a multiplet as **m**, a quartet as **q**, a quintet as **quin** and a broad singlet as **brs**. Infrared spectra were recorded on Mattson Genesis II FTIR spectrophotometer equipped with a Gateway 200 4DX2-66 workstations. Solid samples were dispersed in KBr and recorded as clear pressed discs, while oils were analysed using NaCl plates.

Histological test on bone samples were conducted using bovine tibia. The details are described in Chapter 4 (Section 4.5.3). The epifluorescence experiments were conduced using Nikon microscope and images analysed with Lucia software. Raman Imaging studies were carried out in Dublin Institute of Technology (DIT), Ireland and details are described in Chapter 4 (Section 4.6.2). The micro-CT experiments were conducted at the Free University, Berlin and details are described in Chapter 5 (Section 5.5.1).

The UV absorption measurements were recoded at 20-25 ^{0}C using an Shimadzu diode array spectrophotometer. The fluorescence spectra were recorded on a Varian spectrofluorimeter. The details are described in Chapter 2 (Section 2.6).

6.2 Chapter 2-experimental procedures

Synthesis of *N*-(ethyl)-4-{[((4–aminomethyl)-phenyl)-ethoxycarbonylmethyl-amino)]-acetic acid, sodium salt} -1,8-naphthalimide (92)

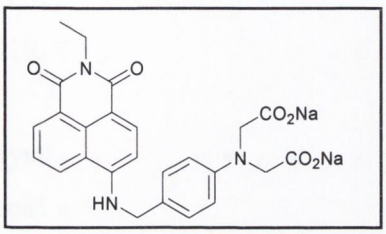

To a solution of *N*-(ethyl)-4-{[((4–aminomethyl)-phenyl)-ethoxycarbonylmethyl-amino)]-acetic acid ethyl ester}-1,8-naphthalimide (**94**) (1.43 g, 2.76 mmol) in dry ethanol (50 mL) was added NaOH (0.300g, 7.5 mmol) in 1 mL of water. The resulting solution was refluxed for 2 hours. Upon cooling, the product was obtained as yellow solid (1.33 g, 95 %). m. p = 310 ^{0}C (decomp.). MS(ES$^+$)*m/z:*= 506 $(M+H)^+$. Anal. calcd for $C_{25}H_{21}N_3Na_2O_6.2H_2O$:C, 55.46, H, 4.65 ; N, 7.76 . Found: C, 55.29; H, 4.23; N, 7.72. ^{1}H-NMR (400MHz, D_2O): δ, 1.09 (t, 3H, *J* = 7.0Hz), 3.75-3.79 (m, 6H), 4.28 (d, 2H), 6.24 (d, 2H, *J* = 8.8Hz), 7.11 (t, 1H, *J* = 7.6Hz), 7.22 (d, 2H, *J* = 8.2Hz), 7.58 (d, 1H, *J* = 8.8Hz), 7.69 (d, 1H, *J* = 8.2 Hz), 7.81 (d, 1H, *J* = 7.6Hz). ^{13}C-NMR (400MHz, D_2O): δ, 179.06, 164.31, 163.28, 158.55, 149.69, 147.69, 133.50, 129.84, 128.70, 124.20, 122.93, 118.79, 117.80, 111.13, 105.52, 55.21, 45.69, 34.94, 11.99. IR (ν_{max}, KBr, cm-^{1}): 3525, 3382, 2875, 1685, 1634, 1547, 1560, 1435, 1394, 1368, 1350, 1314, 1249, 1179, 1130, 1106, 1063, 979, 911, 877, 821, 769, 756, 705, 587.

Synthesis of *N*-(ethyl)-4-{[((4–aminoethyl)-phenyl)-ethoxycarbonylmethyl-amino)]-acetic acid, sodium salt} -1,8-naphthalimide (93)

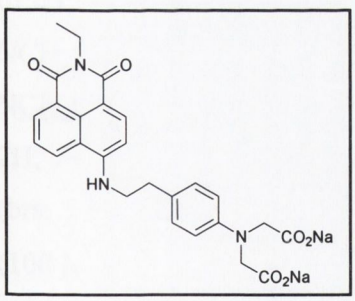

To a solution of (N-(ethyl)-4-{[(4-aminoethyl-phenyl)-ethoxycarbonylmethyl-amino)-acetic acid ethyl ester}-1,8-naphthalimide (**117**) (1.43 g, 2.76 mmol) in dry ethanol (50 mL) was added NaOH (0.30 g, 7.5 mmol) in 1 mL of water. The resulting solution was refluxed for 2 hours. Upon cooling, the product was obtained as yellow solid (1.33 g, 95 %). m.p = 320 ^{0}C (decomp.). MS (ES^+) *m/z* = 520 $(M+H)^+$. Anal. calcd for $C_{26}H_{23}N_3Na_2O_6.2H_2O$: C, 55.46, H, 4.65 ; N,7.76. Found: C, 55.29; H, 4.23; N, 7.72. ^{1}H-NMR (400 MHz, D_2O): δ, 1.09 (t, 3H, *J* = 7.3Hz, $NCH_2\underline{CH3}$), 2.76-2.79 (m, 2H, $\underline{CH_2}$) 3.29-3.33 (m, 2H, CH_2) 3.71-3.79 (m, 6H, $N\underline{CH_2}CH_3$, $N\underline{CH_2}CO_2Na$), 6.16 (d, 2H, *J* = 8.8 Hz, Ar-$\underline{H}$), 6.44 (d, 2H, *J* = 8.0Hz, Ar-$\underline{H}$), 6.98 (t, 1H, *J*

= 8.1Hz, Ar-H), 7.08 (d, 2H, *J* = 8.0Hz, Ar-H), 7.47-7.53 (m, 2H, Ar-H), 7.70 (d, 1H, *J* = 8.2 Hz, Ar-H). ^{13}C-NMR (100 MHz, D_2O): δ, 179.24, 164.23, 163.20, 149.68, 149.87, 133.49, 129.85, 129.07, 126.98, 125.94, 122.83, 118.78, 117.68, 111.29, 105.22, 102.94, 55.24, 43.79, 34.86, 32.68, 32.37, 11.96. IR (ν_{max}, KBr, cm-^{1}): 3374, 2933, 1906, 1854, 1680, 1638, 1546, 1519.51, 1524, 1435, 1399, 1351,1311, 1253, 1188, 1110, 1066, 978, 919, 879, 811 772, 759, 700, 580.

Synthesis of (*N*-(ethyl)-4-{[(4-aminomethyl-phenyl)-ethoxycarbonylmethyl-amino)-acetic acid ethyl ester}-1,8-naphthalimide (94)

To a solution of *N*-ethyl-4-(4-aminomethyl-phenylamine)-1,8-naphthalimide (**99**) (1.5 g, 4.34 mmol) in dry DMF (50 mL) was added K_2CO_3 (1.67 g, 9.46 mmol) and KI (1.57 g, 9.46 mmol) under argon atmosphere. The resulting solution was stirred at room temperature, and ethyl bromoacetate (1.57 g, 9.46 mmol) was slowly added *via* a syringe. The resulting mixture was heated at 90 ^{0}C overnight. After completion of the reaction (by TLC) the solvent was evaporated under reduced pressure. The residue was extracted with chloroform (30 mL) and the organic phase was washed with 1M HCl, water and brine. The product was then dried over sodium sulphate, and evaporated to dryness. The solid was then recrystallised (ethanol) to afford **94** (2.02 g, 90 %) as light yellow solid. m. p = 180–182 ^{0}C. MS (ES^+) *m/z* = 518 $(M+H)^+$. Anal. Calcd for $C_{29}H_{31}N_3O_6$: C, 67.30; H, 6.04; N, 8.12. Found: C, 67.03; H, 6.02; N, 7.91. ^{1}H-NMR (400 MHz, DMSO-d_6): δ, 1.16 (m, 9H, $NCH_2\underline{CH_3}$, $NCH_2CO_2CH_2\underline{CH_3}$), 4.01-4.11 (m, 6H, $N\underline{CH_2}CH_3$, $NCH_2CO_2\underline{CH_2}CH_3$), 4.15 (s, 4H, $N\underline{CH_2}CO_2CH_2CH_3$), 6.5 (d, 2H, *J* = 8.0Hz, Ar-H), 6.67 (d, 1H, *J* = 8.5Hz, Ar-H) 7.21 (d, 2H, *J*= 8.0 Hz, Ar-H), 7.69 (t, 1H, *J* = 8.0Hz, Ar-H), 8.17 (d, 1H, *J* = 8.0Hz, Ar-H), 8.37 (brs, 1H, NH), 8.44 (d, 1H *J* = 7.0 Hz, Ar-H), 8.73(d, 1H *J* = 8.0 Hz, Ar-H). ^{13}C-NMR (100 MHz, DMSO-d_6): δ, 170.54, 163.55, 162.69, 150.44, 146.84, 133.98, 130.65, 129.32, 128.52, 127.94, 126.53, 124.42, 121.89, 120.89, 111.86, 107.84, 104.56, 60.40, 52.66, 45.35, 34.26, 14.08, 13.30. IR (ν_{max}, KBr, cm^{-1}): 3386, 2974, 2929, 1747, 1727.36, 1685, 1616, 1590, 1573, 1541, 1523, 1450, 1397, 1367, 1251, 1183, 1102, 1027, 819, 801, 771, 760, 605, 585.

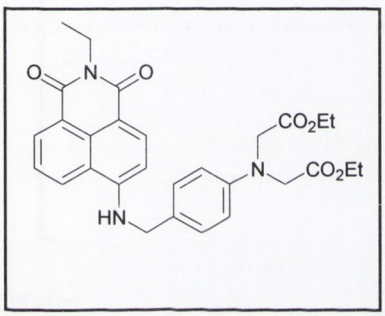

Attempted Synthesis of [(4-Bromomethyl-phenyl)-ethoxycarbonylmethyl-amino]-acetic acid ethyl ester(96)

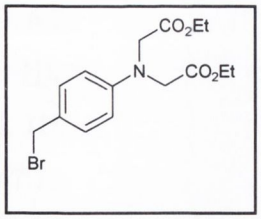

(Ethoxycarbonylmethyl-p-tolyl-amino)-acetic acid ethyl ester (**103**) was reacted under different conditions to obtain **96** as described in Table 2.1. However, the desired product was never obtained.

Synthesis of *N*-ethyl-4-amino-1,8-naphthalimide (97)

4-bromo-1,8-naphthalic anhydride (1.5 g, 5.42 mmol) was dissolved in of 1,4-dioxane (50mL) at room temperature and ethylamine (0.35 g, 6.49 mmol) was added. The solution was refluxed under stirring. After 2 hours, when the reaction was complete (monitored by TLC), the solution was poured into water and resulting product **97** was filtered off and washed with water and dried (1.66 g, 85 %). Upon recrystallization (ethanol) pure **97** was obtained as white lustrous solid. m.p = 162-164 ^{0}C (lit. 160-161 ^{0}C). ^{1}H-NMR (400 MHz, $CDCl_3$): δ, 1.35 (t, 3H, *J* = 7.0 Hz, $NCH_2\underline{CH_3}$), 4.23-4.29(q, 2H, *J* = 7.0 Hz, $N\underline{CH_2}CH_3$), 7.85(t, 1H, *J* = 7.5 Hz, Ar-H), 8.05 (d, 1H, *J* = 7.5 Hz, Ar-H) 8.42 (d, 1H, *J* = 7.5 Hz, Ar-H), 8.58 (d, 1H, *J* = 7.5 Hz, Ar-H), 8.61 (d, 1H, *J* = 7.5 Hz, Ar-H). ^{13}C (100 MHz, $CDCl_3$): δ, 162.97, 132.77, 131.51, 130.72, 130.62, 130.15, 129.75, 128.52, 127.61, 122.70, 121.85, 35.20, 12.80.

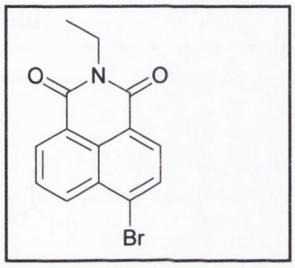

Synthesis of *N*-ethyl-4-(4-aminomethyl-phenylamine)-1,8-naphthalimide (99):

N-ethyl-4-bromo-1,8-naphthalic anhydride (**99**)(1.5 g, 4.93 mmol) was heated with stirring at 130^{0}C under an inert atmosphere. After 10 minutes an excess of a 4-amino benzylamine (3.01 g, 24.65 mmol) was added *via* a syringe. The reaction mixture was kept stirring for 30 minutes. After the completion of the reaction (TLC), water (20 ml) was added when a yellow solid precipitated. The yellow solid was isolated and subsequently dried under vacuum and upon recrystallization (ethanol) **99** was obtained as light fluffy yellow needles (1.48 g, 85 %). m. p = 198-200 ^{0}C. MS (ES^+) *m/ z*= 346 $(M+H)^+$. Anal. calcd for $C_{21}H_{19}N_3O_2$: C, 73.03; H, 5.54; N, 12.17. Found: C, 72.76; H, 5.63; N, 12.06. ^{1}H-NMR

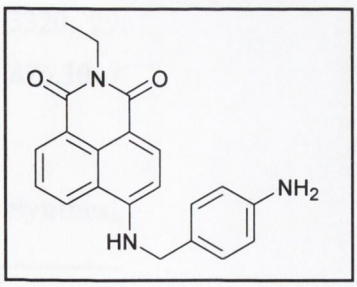

(400 MHz, DMSO-d_6): δ, 1.17 (t, 3H, J = 7.0 Hz, $NCH_2\underline{CH_3}$), 4.04 (q, 2H, J = 7.0 Hz, $N\underline{CH_2}CH_3$), 4.54 (d, 2H, J = 5.2 z, $\underline{CH_2}$) 4.95(brs, 2H, $\underline{NH_2}$), 6.54 (d, 2H, J = 8.0 Hz, Ar-$\underline{H}$), 6.70 (d, 1H, J = 8.5 Hz, Ar-$\underline{H}$), 7.07 (d, 2H, J = 8.0 Hz, Ar-$\underline{H}$), 7.68 (t, 1H, J = 7.5 Hz, Ar-$\underline{H}$), 8.18 (d, 1H, J = 8.5, Ar-$\underline{H}$), 8.42 (brs, 1H, $\underline{NH}$), 8.43(d, 1H, J = 8.5 Hz, Ar-$\underline{H}$), 8.74 (d, 1H, J = 8.5 Hz, Ar-$\underline{H}$). ^{13}C-NMR (100 MHz, DMSO-d_6): δ, 163.53, 162.673, 150.54, 147.70, 133.92, 130.54, 129.37, 128.52, 127.93, 124.93, 124.27, 121.95, 120.26, 107.81, 104.51, 45.86, 34.21, 13.29. IR (ν_{max}, KBr,cm^{-1}): 3358, 2974, 2931, 2108, 1679, 1639, 1579, 1536, 1390, 1346, 1248, 1181, 1101, 1066, 910, 876.30, 773, 757, 694, 581.

Synthesis of (Ethoxycarbonylmethyl-p-tolyl-amino)-acetic acid ethyl ester (103)

p-Toludine (1.3 g, 12.14 mmol) was dissolved in acetonitrile (100 mL), under argon. To this were added K_2HPO_4 (4.31g, 24.8mmol) and KI (4.11 g, 24.5 mmol). The mixture was stirred for 10 minutes and ethyl bromo acetate (4.05 g, 24.8mmol) was added *via* a syringe. The mixture was then refluxed for 24 hours. After completion of the reaction, the inorganic solids were filtered off and solvent evaporated to dryness. The residue was extracted with chloroform and washed with HCl (1M), $NaHCO_3$ followed by saturated aqueous NaCl solution. The resulting organic solution was dried over $MgSO_4$ and the solvent was evaporated to give **103** (3.10 g, 90 %) as dark brown liquid. MS m/z = (ES$^+$) 280 $(M+H)^+$. Anal. Calcd for $C_{15}H_{21}N_2O_4.H_2O$: C, 60.59; H, 7.80; N, 4.7. Found: C, 59.96; H, 7.31; N, 4.5. ^{1}H-NMR (400 MHz, $CDCl_3$): δ, 1.29, (t, 6H, J = 7.0 Hz, $NCH_2CO_2CH_2\underline{CH_3}$), 2.26 (s, 3H, $\underline{CH_3}$), 4.13 (s, 4H, $N\underline{CH_2}CO_2CH_2CH_3$), 4.23 (q, 4H, J = 7.0 Hz, $NCH_2CO_2\underline{CH_2}CH_3$), 6.57(d, 2H, J = 8.5 Hz, Ar-$\underline{H}$), 7.01-7.28(d, 2H, J= 8.5 Hz, Ar-$\underline{H}$). ^{13}C-NMR (100 MHz, $CDCl_3$): δ, 170.59, 145.33, 129.30, 127.08, 112.36, 60.52, 53.26, 19.76, 13.71. IR (ν_{max}, NaCl, cm^{-1}): 3335, 3320, 2980, 2108, 1765, 1639, 1579, 1536, 1390, 1346, 1248, 1181, 1115, 1086, 910, 876.30, 773, 757.

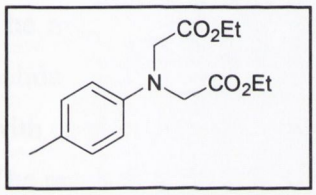

Synthesis of *O*-tetrahydropyranyl-4-aminobenzyl alcohol (107)

O-tetrahydropyranyl-4-nitrobenzyl alcohol (**106**) (5.0g, 2.109 mmol) was dissolved in methanol (50 ml). To this Pd-C (10%, 50 mg) was added .The mixture was hydrogenated at 1 atm for 60

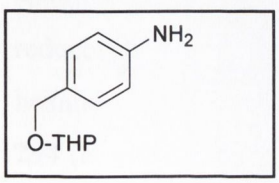

minutes. After the reaction was complete (monitored by TLC), the catalyst was removed *via* filtration and the solvent was evaporated to yield **107** as oily liquid (4.1g, 95%). Mass spectra (ES^+) m/z = 208 $(M+H)^+$. HRMS (ES^+) *m/z* Calcd for $C_{12}H_{17}NO_2$ (M^+) 207.1265; Found 207.1258. ^{1}H-NMR (400 MHz, $CDCl_3$): δ 1.50-1.56 (m, 6H), 3.53-3.58 (m, 1H), 3.92-3.93 (m, 1H), 4.39 (1/2 Abq, 1H), 4.69-4.70 (m, 1H), 6.7 (d, 2H), 7.18 (d, 2H).

Synthesis of (Ethoxycarbonylmethyl-phenyl-amino)-acetic acid ethyl ester (110)

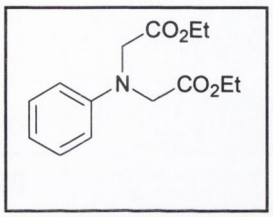

Aniline (2.5 g, 26.85 mmol) was dissolved in 100 mL of acetonitrile under argon. To this K_2HPO_4 (11.8 g, 67.12 mmol) and KI (11.1 g, 67.12 mmol) were added while stirring. The mixture was kept stirring for 10 minutes and ethyl bromoacetate (10.31 g, 61.75 mmol) was added *via* a syringe. The mixture was refluxed for 24 hours. After completion of the reaction, the inorganic solids were filtered off and the solvent evaporated to dryness. The residue was extracted with chloroform and washed with dil. HCl, $NaHCO_3$, and saturated NaCl aqueous solution. The resulting organic portion was dried over $MgSO_4$ and solvent evaporated to yield **110** as dark brown liquid (7.6 g, 90%). HRMS (ES^+) Calcd for $C_{14}H_{19}NO_4$ (M^+) 265.1314; Found 265.1310. ^{1}H-NMR (400 MHz, $CDCl_3$): δ, 1.29 (t, 6H, J = 7.0, $NCH_2CO_2CH_2\underline{CH_3}$), 4.13 (s, 4H, $N\underline{CH_2}CO_2CH_2CH_3$), 4.19-4.25 (q, 4H, J = 7.0 Hz, $NCH_2CO_2\underline{CH_2}CH_3$), 6.64 (d, 2H, J = 8.5 Hz, Ar-<u>H</u>), 6.80 (t, 1H, J = 7.5 Hz, Ar-<u>H</u>), 7.24 (t, 2H, J = 7.5 Hz, Ar-<u>H</u>).

Synthesis of [Ethoxycarbonylmethyl-(4-formyl-phenyl)-amino]-acetic acid ethyl ester (111)

(Ethoxycarbonylmethyl-phenyl-amino)-acetic acid ethyl ester (**110**) (1.12 g, 4.05 mmol)

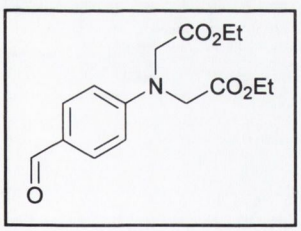

was dissolved in o-dichlorobenzene (50 mL) with stirring under argon. To this dry DMF (0.77 g, 10.5 mmol) and $POCl_3$ (0.8 g, 5.3 mmol) was added. The temp was increased to 90^{0}C and heating was continued overnight. After cooling to room temperature, the solvent was removed under reduced pressure and the residue was extracted with CH_2Cl_2 and washed with 2 M HCl (50 ml), NaCl solution and water respectively. After drying over Na_2SO_4, the solvent was removed under reduced pressure. The residue was purified by flash chromatography using ethyl acetate-hexane (1:2) as eluant to yield **111** as dark brown liquid (0.74 g, 60 %). MS (ES^+) *m/z* = 294 $(M+H)^+$. Anal. Calcd for $C_{15}H_{19}NO_5$: C, 61.42; H, 6.53; N, 4.78. Found: C, 60.89; H,

6.20; N, 4.66. ^{1}H-NMR (400 MHz, $CDCl_3$): δ, 1.32 (t, 6H, *J* = 7.0 Hz, $NCH_2CO_2CH_2\underline{CH_3}$), 4.22 (s, 4H, $N\underline{CH_2}CO_2CH_2CH_3$), 4.26 (q, 4H, *J*= 7.0 Hz, $NCH_2CO_2\underline{CH_2}CH_3$), 6.69 (d, 2H, *J* = 9.0 Hz, Ar-<u>H</u>), 7.76 (d, 2H, *J* = 8.5 Hz, Ar-<u>H</u>), 9.98 (s, 1H, <u>CHO</u>). ^{13}C-NMR (100MHz, $CDCl_3$): δ, 189.92, 169.23, 152.14, 131.50, 130.07, 126.94, 111.38, 61.09, 13.72.

Synthesis of [Ethoxycarbonylmethyl-(4-hydroxymethyl-phenyl)-amino]-acetic acid ethyl ester (112)

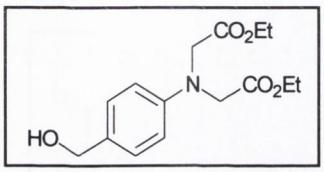

[Ethoxycarbonylmethyl-(4-formyl-phenyl)-amino]-acetic acid ethyl ester (**111**) (0.5 g, 1.71 mmol) was dissolved in methanol (20mL) with stirring at -5^{0}C. $NaBH_4$ (0.9 g, 2.22 mmol) was added portion wise and the solution kept stirring for 20 minutes. After the completion of the reaction (as monitored by the disappearance of the starting material by TLC), the reaction was quenched with 10 mL of water. The resulting solution was extracted with ethyl acetate (3 × 15ml). After drying over anhydrous Na_2SO_4 the solvent was removed under reduced pressure. The residue was purified by flash chromatography using ethyl acetate –hexane (1:2) as eluant to give **112** as dark oil (0.44 g, 85 %). MS (ES^+) *m/z* = 314 ($M+H_2O^+$). HRMS (ES^+) *m/z:* Calcd for $C_{15}H_{21}NO_5$ (M^+) 295.1420; Found 295.1416. ^{1}H-NMR (400 MHz, $CDCl_3$): δ, 1.30 (t, 6H, *J* = 7.0Hz, $NCH_2CO_2CH_2\underline{CH_3}$), 4.15 (s, 4H, $N\underline{CH_2}CO_2CH_2CH_3$), 4.24 (q, 4H, *J* = 7.0Hz, $NCH_2CO_2\underline{CH_2}CH_3$), 4.57 (s, 2H), 6.63 (d, 2H, *J* = 8.5Hz, Ar-<u>H</u>), 7.24 (d, 2H, *J* = 8.5Hz, Ar-<u>H</u>). ^{13}C-NMR (100 MHz, $CDCl_3$): δ, 170.30, 147.15, 130.23, 128.22, 112.15, 64.72, 61.08, 53.14, 13.74. IR (ν_{max}, NaCl, cm^{-1}): 3338, 3345, 3200, 2900, 2109, 1767, 1693, 1528, 1390, 1336, 1248, 1005, 920, 835, 820, 732, 756, 600, 589.

Synthesis of [Ethoxycarbonylmethyl-(4-hydroxymethyl-phenyl)-amino]-acetic acid ethyl ester (113)

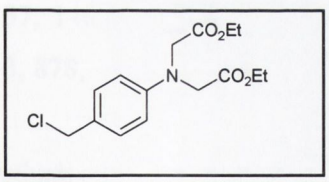

Ethoxycarbonylmethyl-(4-hydroxymethyl-phenyl)-amino]-acetic acid ethyl ester (**112**) (0.5 g, 1.59 mmol) was dissolved in 1,4-dioxane (30 mL) and $SOCl_2$ (1.89g, 1.59 mmol) was added and the solution kept for refluxing. After the completion of the reaction, the solvent was evaporated under reduced pressure and residue titrated with hexane, when **113** was obtained as yellow solid (0.40 g, 80 %). MS (ES^+) *m/z* = 314 ($M+H_2O^+$). HRMS (ES^+) *m/z:* Calcd for $C_{15}H_{21}NO_5$ (M^+) 313.1081; Found 313.1021. ^{1}H-NMR (400 MHz, $CDCl_3$): δ, 1.30 (t, 6H, *J* = 7.0Hz, $NCH_2CO_2CH_2\underline{CH_3}$), 4.16 (s, 4H, $N\underline{CH_2}CO_2CH_2CH_3$), 4.24 (q, 4H, *J* = 7.0Hz,

$NCH_2CO_2\underline{CH_2}CH_3$), 4.56 (s, 2H), 6.63 (d, 2H, *J* = 8.5Hz, Ar-H), 7.27 (d, 2H, *J* = 8.5Hz, Ar-H). ^{13}C-NMR (100 MHz, $CDCl_3$): δ, 170.20, 146.15, 130.22, 129.22, 112.15, 63.72, 62.08, 54.14, 13.72. IR (ν_{max}, NaCl, cm^{-1}): 3318, 3200, 2700, 2109, 1765, 1689, 1598, 1490, 1236, 1218, 1015, 930, 845, 732, 756, 650, 589.

Synthesis of *N*-ethyl-4-(4-aminoethyl-phenyl amine)-1,8-naphthalimide (116)

N-ethyl-4-bromo-1,8-naphthalic anhydride (1.5 g, 4.93 mmol) was heated with stirring at 130 ^{0}C under an argon atmosphere. After 10 minutes 4-ethylaminobenzylamine (3.01 g, 24.65 mmol) was added *via* syringe. The reaction mixture was kept stirring for 30 minutes. After the completion of the reaction (TLC), water (20 mL) was added when a yellow solid began precipitation. The yellow solid was dried under vacuum and upon recrystallization (2-propanol) **116** was obtained as light fluffy yellow needles (1.45 g, 80 %). m.p = 200 – 202 ^{0}C. MS (ES^+) *m/z* = 360 $(M+H)^+$. Anal. Calcd for $C_{22}H_{21}N_3O_2$: C, 73.52; H, 5.89; N, 11.69; Found: C, 72.76; H, 5.63; N, 12.06. ^{1}H-NMR(400 MHz, DMSO-d_6): δ, 1.17 (t, 3H, *J* = 7.0 Hz, $NCH_2\underline{CH_3}$), 2.81-2.84 (t, 2H, *J* = 8.2Hz, $\underline{CH_2}$), 3.45-3.54 (m, 2H, $\underline{CH_2}$), 4.04 (q, 2H, *J* = 7.0Hz, $N\underline{CH_2}CH_3$), 4.89 (d, 2H, *J* = 5.2 Hz,), 6.51 (d, 2H, *J* = 8.2Hz, Ar-H), 6.83 (d, 1H, *J* = 8.8Hz, Ar-H), 6.83 (d, 2H, *J*=8.2Hz, Ar-H), 7.68 (t, 1H, *J* = 8.2 Hz, Ar-H), 7.84 (brs, NH), 8.28 (d, 1H, *J* = 8.2, Ar-H), 8.44 (d, 1H, *J* = 7.5 Hz, Ar-H), 8.66 (d, 1H, *J* = 8.2Hz, Ar-H). ^{13}C-NMR (100 MHz, DMSO-d_6): δ, 163.53, 162.69, , 150.42, 146.94, 134.24, 130.58, 129.38, 129.16, 125.94, 124.22, 121.87, 121.88, 120.09, 114.01, 107.59, 103.87, 45.01, 34.25, 33.35, 13.32; IR (ν_{max}, KBr, cm^{-1}): 3424, 3348, 2981, 2934, 2889, 2679, 1904, 1850, 1680, 1639, 1579, 1537, 1465, 1450, 1432, 1396, 1365, 1347, 1302, 1276, 1178, 1150, 1108, 1070, 1011, 913, 878, 769, 756, 654, 596.

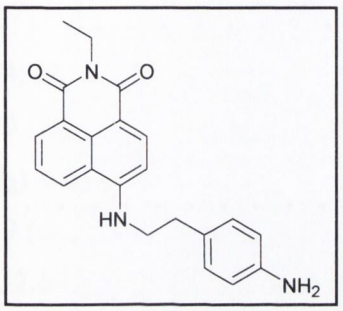

Synthesis of *N* - (ethyl) - 4 - {[(4 - aminoethyl - phenyl)-ethoxycarbonylmethyl - amino)] -acetic acid ethyl ester} -1,8-naphthalimide (117)

To a solution of *N*-ethyl-4-(4-aminoethyl-phenyl amine)-1,8-naphthalimide (**116**) (1.5 g, 4.2 mmol) in dry DMF (50ml), K_2CO_3 (1.30 g, 9.24 mmol) and KI (1.52 g, 9.24) were added under an inert atmosphere. The resulting solution was stirred at room temperature, and then ethyl bromoacetate (1.56 g, 9.24 mmol) was slowly added *via* a syringe. The

resulting mixture was heated at 90 ^{0}C overnight. After the completion of the reaction (by TLC) the solvent was evaporated under reduced pressure. The residue was extracted with chloroform and the organic phase was washed with 1M HCl, water and brine, dried over sodium sulphate, and evaporated to dryness. The residue was recrystallised (ethanol) to afford **117** (2.01 g, 90%) as light yellow solid. m.p = 195-197 ^{0}C. MS (ES^+) *m/z:* 532 $(MH)^+$. Anal. Calcd for $C_{30}H_{33}N_3O_6$: C, 67.30; H, 6.04; N, 8.12. Found: C, 66.42; H, 5.98; N, 7.74. ^{1}H-NMR(400 MHz, DMSO-d_6): δ, 1.16-1.20 (m, 9H, $NCH_2\underline{CH_3}$, $NCH_2CO_2CH_2\underline{CH_3}$), 2.87-2.89 (m, 2H, $\underline{CH_2}$), 3.52-3.54 (m, 2H, $\underline{CH_2}$) 4.04-4.13 (m, 6H, $N\underline{CH_2}CH_3$, $NCH_2CO_2\underline{CH_2}CH_3$), 4.17 (s, 4H, $N\underline{CH_2}CO_2CH_2CH_3$), 6.49 (d, 2H, J = 8.5Hz, Ar-$\underline{H}$), 6.84 (d, 1H, J = 9.0 Hz, Ar-$\underline{H}$) 7.13 (d, 2H, J = 8.5 Hz, Ar-H), 7.67 (t, 1H, J = 8.0 Hz), 7.85 (brs, 1H, $\underline{NH}$) 8.27 (d, 1H, J = 8.5 Hz), 8.44 (d, 1H J = 7.0Hz), 8.66 (d, 1H J = 8.5 Hz). ^{13}C-NMR (100 MHz, DMSO-d_6): δ, 170.61, 163.54, 162.71, 150.41, 146.26, 134.25, 130.60, 129.40, 129.34, 128.52, 127.58, 124.26, 121.89, 120.13, 111.90, 107.69,103.94, 60.35, 52.75, 44.84, 34.25, 32.89, 14.12, 13.32. IR (ν_{max}, KBr, cm^{-1}): 3378, 2974, 2929, 1753, 1731, 1686, 1581, 1543, 1524, 1430, 1395, 1367, 1296, 1181, 1103, 1062, 972, 911, 808, 770, 758; 655, 587.

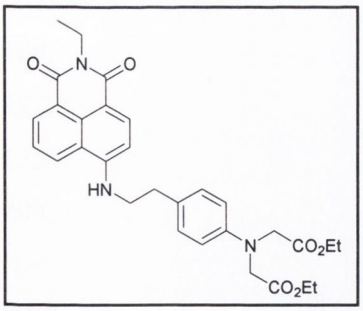

6.3 Chapter 3 Experimental procedures

Synthesis of[(4-Anthracen-9-ylmethyl-phenyl)-ethoxycarbonylmethyl-amino]-acetic acid potassium salt (125)

[(4-Anthracen-9-ylmethyl-phenyl)-ethoxycarbonylmethyl-amino]-acetic acid ethyl ester (**128**) (1 g, 2.19 mmol) was dissolved in methanol (20 mL) while stirring. To this was added aqueous KOH (1mL, 3 M). The mixture was refluxed for 2 hours. After cooling to room temperature, the reaction mixture was kept in the fridge, where the potassium salt precipitated. The resulting solution was filtered and precipitate dried in vacuum to afford **125** as pale yellow solid (0.96 g, 95 %). m. p = 340 ^{0}C (decomp.). MS(ES^+) *m/z* = 476 $(MH)^+$. Anal. Calcd for $C_{25}H_{19}K_2NO_4.2H_2O$: C, 58.69; H, 4.53, N, 2.74. Found: 57.80; H, 4.33; N, 2.56. ^{1}H-NMR (400 MHz, D_2O): δ, 3.67 (s, 4H, $N\underline{CH_2}CO_2K$), 4.65 (s, 2H, $\underline{CH_2}$), 6.20 (d, 2H, J = 8.5 Hz, Ar-$\underline{H}$), 6.82 (d, 2H, J = 8.53

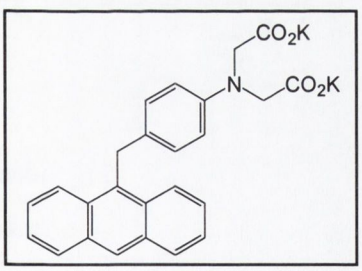

Hz, Ar-H), 7.36-7.38 (m, 4H, Ar-H), 7.91 (d, 2H, J = 5.5 Hz, Ar-H), 8.12 (d, 2H, J = 6.0 Hz, Ar-H), 8.30 (s, 1H, Ar-H). ^{13}C-NMR (100 MHz, D_2O): δ, 177.61, 144.74, 131.10, 129.26, 127.61, 126.89, 126.68, 126.55, 124.06, 123.95, 123.20, 122.57, 109.48, 53.54, 29.22. IR (ν_{max}, KBr, cm^{-1}): 3400, 2877, 2844, 1964, 1915, 1723, 1660, 1500, 1445, 1336, 1256, 1186, 519, 535, 564, 601, 618, 656, 697, 758, 790, 819, 852, 1158, 1100, 987, 955, 903, 884.

Synthesis of [(4-{10-[4-(Bis-ethoxycarbonylmethyl-amino)-benzyl]-anthracen-9-ylmethyl}-phenyl)-ethoxycarbonylmethyl-amino]-acetic acid potassium salt (126)

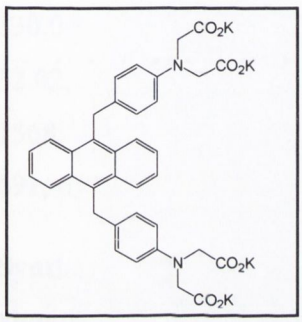

[(4-{10-[4-(Bis-ethoxycarbonylmethyl-amino)-benzyl]-anthracen-9-ylmethyl}-phenyl)-ethoxycarbonylmethyl-amino]-acetic acid ethyl ester (**130**) (1 g, 1.36 mmol) was dissolved in methanol (20 mL) while stirring. To this aqueous KOH (2mL, 3M) was added. The mixture was refluxed for 2 hours. After cooling to room temperature the mixture was kept in the fridge, where the potassium salt precipitated out. The resulting solution was filtered and precipitate dried in vacuum to afford **126** as pale yellow solid (0.95 g, 90 %). m.p = 320 ^{0}C (decomp.). MS(ES^+) m/z = 773 $(M+H)^+$. Anal. Calcd for $C_{36}H_{28}K_4N_2O_8.3H_2O$: C, 52.28; H, 4.14; N, 3.39. Found: C, 52.46; H, 4.02; N, 3.23. ^{1}H-NMR (400 MHz, D_2O): δ, 3.70 (s, 8H, NCH_2CO_2K), 4.86 (s, 4H, CH_2), 6.28 (d, 4H, J=6.1Hz, Ar-H), 6.91 (d, 4H, J=6.1Hz, Ar-H), 7.42-7.45 (m, 4H, Ar-H), 8.29-8.31 (m, 4H, Ar-H). ^{13}C-NMR (100 MHz, D_2O): δ, 179.22, 146.34, 129.27, 128.41, 128.15, 125.23, 124.95, 111.11, 55.11, 45.30, 31.13. IR (ν_{max}, KBr, cm^{-1}): 3450, 3006, 2005, 1851, 1660, 1574, 1515, 1446, 1404, 1320, 1209, 1043, 1029, 976, 913, 820, 790, 746, 706, 601.

Synthesis of [(4-Anthracen-9-ylmethyl-phenyl)-ethoxycarbonylmethyl-amino]-acetic acid ethyl ester (128)

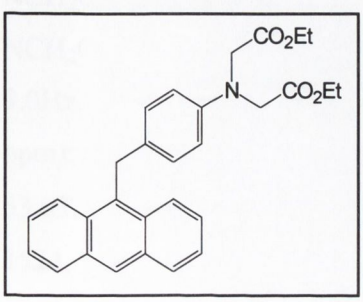

9-Chloromethylanthracene (1.5 g, 6.64 mmol) and phenyliminodi-acetic acid diethyl ester (**110**) (1.76 g, 6.64 mmol) and $AlCl_3$ (0.91 g, 6.64 mmol) were dissolved in dry $CHCl_3$ (50 mL) at –5 ^{0}C. The solution was refluxed overnight. After the reaction was complete, (monitoring

by TLC) the solution was cooled and washed with three 100 ml portions of water. The organic portion was dried over $MgSO_4$. After evaporation of the solvent, crude product was subjected to column chromatography using ethyl acetate:hexane (2:3) as eluant to yield pure **128** (1.89 g, 70 %) as light yellow thick liquid. m.p = 140-142 ^{0}C. MS (ES^+) *m/z* = 456 $(MH)^+$. Anal. Calcd for $C_{29}H_{29}NO_4$: C, 76.46; H, 6.42; N, 3.07. Found: C, 76.18; H, 6.28; N, 3.07. ^{1}H-NMR (400 MHz, $CDCl_3$): δ, 1.25 (t, 6H, *J* = 7.0 Hz, $NH_2CH_2CO_2CH_2\underline{CH_3}$), 4.07 (s, 4H, $N\underline{CH_2}CO_2CH_2CH_3$), 4.18 (q, 4H, *J* = 7.0 Hz, $N\underline{CH_2}CO_2CH_2CH_3$), 4.92 (s, 2H, $\underline{CH_2}$), 6.47 (d, 2H *J* = 8.5 Hz, Ar-H), 6.98 (d, 2H, *J* = 8.5 Hz, Ar-H), 7.45-7.48 (m, 4H, Ar-H), 8.03-8.05 (m, 2H, Ar-H), 8.22-8.25 (m, 2H, Ar-H), 8.43 (s, 1H, Ar-H). ^{13}C-NMR (100 MHz, $CDCl_3$): δ, 170.50, 145.68, 132.03, 130.12, 130.04, 131.24, 128.57, 128.45, 125.82, 125.26, 124.54, 124.40, 112.26, 60.53, 53.06, 32.02, 13.72. IR (ν_{max}, NaCl, cm^{-1}): 3345, 2977, 1895, 1931, 1854, 1765, 1676, 1615, 1568, 1521, 1480, 1447, 1386, 1355, 1334, 1274, 1177, 1065, 970, 879, 820, 786, 728, 691, 650, 635, 602, 570, 538, 517.

Synthesis of [(4-{10-[4-(Bis-ethoxycarbonylmethyl-amino)-benzyl]-anthracen-9-ylmethyl}-phenyl)-ethoxycarbonylmethyl-amino]-acetic acid ethyl ester (130)

9,10-bischloromethyl anthracene (1.0 g, 3.63 mmol), phenyliminodi-acetic acid diethyl ester (**110**) (1.93 g, 7.26 mmol) and $AlCl_3$ (0.96 g, 7.26 mmol) were dissolved in dry $CHCl_3$ (50 mL) at -5 ^{0}C. The solution was refluxed under stirring overnight (12 h). After the reaction was complete, (monitored by TLC) the solution was cooled and washed with three 100 ml portions of water. The organic portion was dried over $MgSO_4$. After evaporation of the solvent, crude product was subjected to column chromatography and yielded pure **110** (1.56 g, 58%) as light yellow solid. m.p = 120-122 ^{0}C. MS (ES^+) *m/z* =:733 $(MH)^+$. Anal. Calcd for $C_{44}H_{48}N_2O_8$: C, 72.11; H, 6.60; N, 3.82. Found: C, 72.26; H, 6.45; N, 3.69. ^{1}H-NMR (400 MHz, $CDCl_3$): δ 1.27 (t, 12H, *J* = 7.6 Hz, $NCH_2CO_2CH_2\underline{CH_3}$), 4.09 (s, 8H, $N\underline{CH_2}CO_2CH_2CH_3$), 4.19 (q, 8H, *J* = 7.0Hz, $NCH_2CO_2\underline{CH_2}CH_3$), 4.95 (s, 4H, $\underline{CH_2}$), 6.50 (d, 4H, *J* = 9.0Hz, Ar-H), 7.01 (d, 4H, *J* = 9.0Hz, Ar-H), 7.44 (m, 4H, Ar-H), 8.27 (m, 4H, Ar-H). ^{13}C-NMR (100 MHz, $CDCl_3$, ppm): δ, 170.52, 145.68, 131.35, 130.25, 130.00, 128.49, 125.19, 124.79, 112.29, 60.54, 53.07, 32.30, 13.74. IR (ν_{max}, KBr, cm^{-1}): 3450, 2979, 1895, 1931, 1859, 1734, 1616, 1568, 1524, 1448, 1371, 1030, 969, 865, 812, 781, 763, 655, 601, 573, 543, 506.

Synthesis of 9, 10-bis cholromethyl anthracene (129)

Paraformaldehyde (4.3g. 48 mmol) and glacial acetic acid (63 mL) were mixed thoroughly to form white slurry. HCl gas was bubbled through a glass frit into a stirred suspension until the solution became clear (about 4 min). Anthracene (9.9 g, 55 mmol) and more glacial acetic acid (63 mL) were added to the flask under stirring. The reaction was stirred at 60 ^{0}C under nitrogen for 20 hours and then poured over ice. The resulting bright yellow solid yielded (14.0 g, 92 %) of **129**. m.p= 276-278 ^{o}C (lit. 277 ^{0}C). Upon recrystallization in toluene bright yellow needles of pure **129** was formed. MS (ES^+) *m/z* = 275 (MH^+). ^{1}H-NMR (400 MHz, DMSO-*d*$_6$): δ, 5.63 (s, 4H, CH2), 7.67-7.69 (dd, 4H, J_1, J_2 = 3.4 Hz, Ar-H), 8.40-8.42 (dd, 4H, J_1, J_2 = 3.4 Hz, Ar-H). ^{13}C-NMR (100 MHz, DMSO-*d6*): δ, 130.68, 129.21, 126.76, 124.73, 40.13.

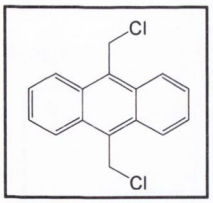

6.4 Chapter 5 Experimental

Synthesis of{Ethoxycarbonylmethyl-[4-(2,3,5-triiodo-benzoylamino)-phenyl]-amino}-acetic acid sodium salt (160)

{Ethoxycarbonylmethyl-[4-(2,3,5-triiodo-benzoylamino)-phenyl]-amino}-acetic acid ethyl ester (**164**) (1.5 g, 1.97 mmol) was dissolved in methanol (20 mL). To this was added NaOH (2 mL, 3 M) and the resulting solution refluxed for 2 hours. The solution became clear after 1 hour and at the end of 2 hour, a thick cloudy mixture was obtained. Addition of ethanol resulted in the precipitation of white solid. Ethanol was continuously added till no more precipitation was observed. The resulting precipitate were collected and dried under vacuum to afford **160** (1.40, 95%) as yellow solid. MS (ES^+) *m/z* = 767 ($M+H_2O$). Anal. Calcd for $C_{17}H_{11}I_3N_2Na_2O_5.H_2O$: C, 26.59; H, 1.71; N, 3.65; Found: C, 26.67; H, 1.52; N, 3.48. ^{13}H-NMR (400 MHz, $CDCl_3$): δ, 3.82 (s, 4H, NCH_2CO_2Na) 6.46 (d, 2H, *J* = 8.9 Hz, Ar-H), 7.2 (d, 2H, *J* = 8.9Hz, Ar-H), 7.68 (s, 1H, Ar-H), 8.32 (s, 1H, CONH). ^{13}C-NMR (100 MHz, D_2O): δ, 178.89, 168.66, 147.35, 146.65, 144.43, 134.40, 124.36, 123.56, 118.86, 112.24, 105.92, 94.00, 55.22. IR (νmax, KBr, cm^{-1}): 3587, 3379, 3099, 1690, 1520, 1477, 1418, 1319, 1269, 1247, 1171, 1125, 1098, 975, 894, 865, 819, 729, 703, 612, 525.

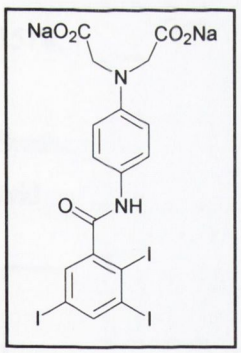

Synthesis of 4-amino- N,N-bis(2,4,6-triiodo) bis phenylimino acetic acid sodium salt 161

4-amino-N,N-bis(2,4,6-triiodo) bis phenylimino acetic acid diethyl ester (**174**) (2.5 g, 2.31 mmol) was dissolved in methanol (20 mL). To this was added KOH (2 ml, 6M) and the resulting solution refluxed for 3 hours. A clear solution was obtained after 1.5 hours and no precipitation was noticed after 3 hours. At this point the reaction was stopped and about 90% of solvent was evaporated under reduced pressure. To the remaining solution on addition of ethanol, precipitation was observed. The addition of ethanol was continued till no more precipitates were formed. The precipitates were collected and dried under vacuum to afford **161** as white solid (2.27 g, 93 %). MS (ES^+) m/z = 1106 $(M+Na)^+$. Anal. Calcd for $C_{28}H_{20}I_3N_5Na_4O_{10}.6H_2O$; C, 28.81; H, 2.76; N, 6.00; Found: C, 28.11; H, 2.22; N, 5.6. ^{1}H-NMR (400 MHz, D_2O): δ, 3.83 (s, 8H, NCH_2CO_2Na), 6.5 (d, 2H, J = 9.0Hz, Ar-H), 7.3 (d, 2H, J = 9.0Hz, Ar-H). ^{13}C-NMR (100 MHz, D_2O): δ, 178.95, 170.83, 170.77, 147.96, 147.25, 147.21, 146.87, 123.72, 123.55, 111.17, 79.53, 72.56, 55.18. IR (ν_{max}, KBr, cm^{-1}): 3548, 3279, 3199, 1677, 1620, 1577, 1518, 1319, 1209, 1107, 1001, 975, 864, 805, 729, 713, 610, 565.

Synthesis of *N,N*-bis(2,4,6-triiodo-3,5-benzenedichlorocarbonyl)-malonamide tetra phenylimino acetic acid sodium salt (162).

N,N-bis(2,4,6-triiodo-3,5-benzenedichlorocarbonyl)-malonamide tetra phenylimino acetic acid ethyl ester (**176**) (2.7 g, 1.21 mmol) was dissolved in methanol (20 mL). To this was added NaOH (3 mL, 6 M) and the resulting solution refluxed for 3 hours. A clear solution was obtained after 2 hours and no precipitation was noticed after 3 hours. At this point the reaction was stopped and about 90 % of solvent was evaporated under reduced pressure. To the remaining solution, on addition of ethanol, precipitation was observed. The addition of ethanol was continued till no more precipitates were formed. The

precipitates were collected and dried under vacuum to afford **162** as dull white solid (2.43g, 92%). m. p = 400 ^{0}C (decomp.). Anal. Calcd for $C_{59}H_{40}I_6N_{10}Na_8O_{22}.8H_2O$: C, 30.41; H, 2.42; N, 6.01; Found: C, 27.55; H, 2.05; N, 5.28 ^{1}H-NMR (400 MHz, D_2O): δ, 3.93 (s, 16H, NH$\underline{CH_2}CO_2Na$), 3.82 (s, 2H, $\underline{CH_2}$), 6.49 (d, 8H, J = 8.5Hz, Ar-$\underline{H}$). ^{1}C-NMR (100 MHz, D_2O): δ, 178.95, 170.38, 170.29, 147.96, 146.90, 123.81, 123.63, 111.22, 95.31, 56.96, 55.20, 53.94, 16.36. IR (ν_{max}, KBr, cm^{-1}): 3239, 1671, 1518, 1404, 1308, 1183, 976, 909, 820, 610.

Synthesis of {Ethoxycarbonylmethyl-[4-(2,3,5-triiodo-benzoylamino)-phenyl]-amino}-acetic acid ethyl ester (164)

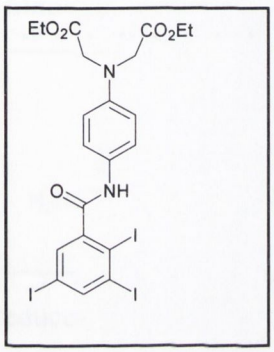

2,3,5-triodobenzoyl chloride (0.5 g, 0.96 mmol) was dissolved in anhydrous Tetrahydrofuran (20 mL) under argon with stirring. To this was added tetrahydrofuran (10 mL) solution of **110** (0.27 g, 0.96 mmol) *via* syringe. Dry triethylamine (0.15g, 0.20 mL, 1.2 mmol) was added to this stirred mixture and the resulting solution was kept refluxing. After the completion of the reaction (monitored by TLC) the THF was evaporated under reduced pressure and the residue extracted with chloroform. The chloroform layer was washed with HCl (1M), $NaHCO_3$ and brine. The organic layer was dried over $MgSO_4$ and solvent evaporated off to afford puffy white solid which on flash-column chromatography afford **164** as white solid (0.67 g, 90 %). m.p = 174-176 ^{0}C. MS (ES^+) *m/z* = 762 $(MH)^+$. Anal. Calcd for $C_{21}H_{21}I_3N_2O_5$: C, 33.10; H, 2.78; N, 3.68; Found: C, 33.40; H, 2.81; N, 3.51. ^{13}H-NMR (400 MHz, DMSO-d_6): δ, 1.20 (t, 6H, *J*=7.0Hz, $NHCH_2CO_2CH_2\underline{CH_3}$), 4.12 (q, 4H, *J*=7.0Hz, $NHCH_2CO_2\underline{CH_2}CH_3$), 4.18 (s, 4H, $NH\underline{CH_2}CO_2CH_2CH_3$) 7.44 (d, 2H, *J*=9.0Hz, Ar-$\underline{H}$), 7.69 (d, 2H, *J*=9.0Hz, Ar-$\underline{H}$), 8.31(d, 1H, *J*=2.0Hz, Ar-$\underline{H}$), 10.19(s, 1H, $CO\underline{NH}$). ^{13}C-NMR (100 MHz, DMSO-d_6): δ, 170.52, 165.73, 147.51, 146.06, 144.55, 134.50, 129.19, 121.02, 111.96, 113.30, 107.94, 95.51, 60.39, 52.81,14.14. IR (KBr, cm^{-1}): 3261, 2977, 1638, 1595, 1520, 1410, 1324, 1261, 1186, 1024, 974, 910, 866, 816, 765, 716, 513, 567.

Synthesis of 2, 3,5-TriodoBenzoyl chloride (165)[314]

2,3,5-Triiodobenzoic acid (1.5g, 3mmol) was dissolved in benzene (100 mL) with stirring. To this was slowly added freshly distilled excess $SOCl_2$ (20 mL) *via* syringe. The solution

was refluxed for 2 hours. After the completion of the reaction (monitored by ESMS), the

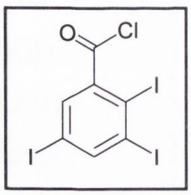

solvent was evaporated under reduced pressure. The crude solid obtained was recrystallized form ethyl acetate: hexane mixture (1:1) to afford **165** (1.32 g, 85 %) as off-white solid. MS (ES^+) *m/z* = 542 $(MNa)^+$. Anal. Calcd for $C_7H_2ClI_3O$: C, 16.22; H, 0.39; Found: C, 16.67; H, 0.31. ^{1}H-NMR (400 MHz, $CDCl_3$) δ 7.91 (d, 1H, *J* = 2.0Hz, Ar-H), 8.39 (d, 1H, *J* = 2.0Hz, Ar-H); ^{13}C-NMR (100 MHz, $CDCl_3$): δ, 165.92, 149.54, 143.93, 136.61, 113.65, 104.72 93.12.

Synthesis of [(4-Amino-phenyl)-ethoxycarbonylmethyl-amino]-acetic acid ethyl ester(166)

[Ethoxycarbonylmethyl-(4-nitro-phenyl)-amino]-acetic acid ethyl ester (**170**) (1.0 g, 3.22

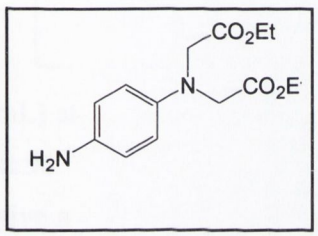

mmol) was dissolved in methanol (50 mL). To this was added Pd-C (10% w/w, 0.07 g). The mixture was hydrogenated at 1 atm for 15 minutes. After the reaction was complete (as shown by the disappearance of the starting material in TLC), the catalyst was filtered off and the solvent evaporated under reduced pressure to yield **166** (0.85g, 95%) as brown liquid. MS (ES^+) *m/z* = 281 $(MH)^+$. Anal. Calcd for $C_{14}H_{20}N_2O_4$: C, 59.99; H, 7.19; N, 9.99. Found: C, 59.25; H, 7.03; N, 9.84 ^{1}H NMR (400 MHz, $CDCl_3$): δ, 1.28 (t, 6H, J=6.8Hz, $NCH_2CO_2CH_2\underline{CH_3}$), 4.09 (s, 4H, $N\underline{CH_2}CO_2CH_2CH_3$), 4.18-4.23 (q, 4H, J=6.8Hz, $NCH_2CO_2\underline{CH_2}CH_3$), 6.57 (d, 2H, J=8.9Hz, Ar-H), 6.66 (d, 2H, J=8.9Hz, Ar-H); ^{13}C-NMR (100MHz, $CDCl_3$): δ, 170.88, 140.94, 138.02, 116.26, 114.54, 60.49, 53.68,13.79; IR (NaCl, cm^{-1}): 3330, 2981, 2930, 2355, 1733, 1616, 1519, 1448, 1412, 1347, 1255, 1188, 1097, 1025, 974, 918, 817, 729, 521.

Synthesis of [Ethoxycarbonylmethyl-(4-nitro-phenyl)-amino]-acetic acid ethyl ester(170)

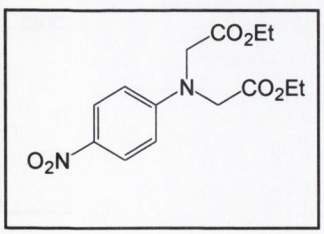

52 (6g, 22.72mmol) in 50 ml of acetic acid treated, with stirring at 0^0C, with 3 mL of HNO_3. After 15 minutes, the reaction mixture was poured over ice yielding **170** as crude green solid. Upon recrystallisation (ethanol) **170** was obtained as yellow brown needles. (5.28 g, 76 %). m.p = 160-162 ^{0}C MS (ES^+) *m/z* = 310 (M^+). Anal. Calcd for $C_{14}H_{18}N_2O_6$: C, 54.19; H, 5.85; N, 9.03. Found: C, 54.12; H, 5.85; N, 8.98.^{1}H-NMR (400 MHz, $CDCl_3$, ppm): δ 1.30 (t, 6H, *J*=7.0Hz, $NHCH_2CO_2CH_2\underline{CH_3}$), 4.21 (s, 4H, $NH\underline{CH_2}CO_2CH_2CH_3$) 4.27(q, 4H, *J*=7.0Hz,

$NHCH_2CO_2\underline{CH_2}CH_3$) 6.6 (d, 2H, *J*=9.5Hz, Ar-H), 8.13 (d, 2H, *J*=9.5Hz, Ar-H). ^{13}C-NMR (100 MHz, $CDCl_3$): δ, 13.74, 53.00, 61.29, 110.82, 125.55, 138.52, 152.23, 168.86. IR (KBr, cm^{-1}); 3474, 3121, 3098, 2976, 2908, 2696, 2614, 2426, 2231, 1918, 1893, 1751, 1591, 1516, 1420, 1272, 1117, 1026, 961, 918, 871, 828, 757, 736, 696, 632, 586, 535, 559.72.

Synthesis of 5-Amino-2,4,6-triiodo-isophthalic acid (172)[319]

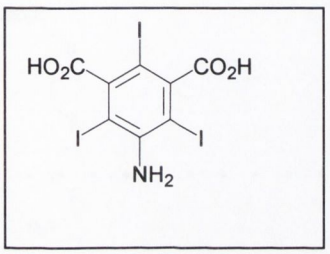

ICl (9.8 g, 100 mmol) was added to a solution of KCl (7.2 g 9.70 mmol) in H_2O (100 mL) and stirred at room temperature for 5 min. The mixture was filtered to remove insoluble material, and this orange solution of $KICl_2$ was added *via* addition funnel over 1 hour to a stirring slurry of 5-aminoisophthalic acid (3.32 g. 1.80 mmol) in H_2O (110 mL) at 55^0 C. After complete addition, mixture was stirred at 60 ^{0}C for 24 hours and then at 90 ^{0}C for 1 hour. On cooling, the tanned product was dissolved in minimal 1M KOH to give a clear-browns solution, which was treated repeatedly with activated charcoal (0.5 g) at 40–50 ^{0}C for 30 minutes. The product was then precipitated with concentrated HCl with stirring until no further precipitation was observed, allowed to stand for several hours, then filtered and dried at 100 ^{0}C under vacuum to obtained **172** as yellow solid (3.68 g, 75 %). m.p = 260 ^{0}C (decomp.). MS (ES^+), *m/z* = 559 ($M+H^+$). Anal. Calcd for $C_8H_4I_3NO_4.H_2O$: C, 16.66; H, 1.05; N, 2.43. Found: C, 16.86; H, 0.78; N, 2.16. ^{13}C-NMR (400 MHz, DMSO-*d6*): δ, 170.11, 148.91, 147.78, 77.93, 70.62. IR (ν_{max}, KBr, cm^{-1}): 3629, 3442, 3378, 3305, 2894, 2600, 1785, 1600, 1367, 1290, 1009, 987, 867, 765.

Synthesis of 5-Amino-2,4,6-triiodo-isophthaloyl dichloride(173)[319]

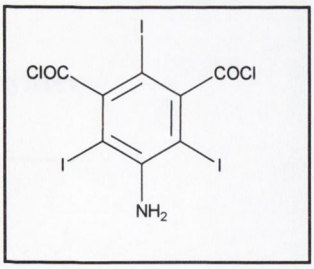

5-Amino-2,4,6-triiodo-isophthalic acid (**172**) (2.6 g, 4.7 mmol) was dissolved in freshly distilled $SOCl_2$(50 mL) and refluxed for 6 h. After the completion of reaction (ESMS), $SOCl_2$ was then removed under reduced pressure, when yellow solid was obtained. This was dispersed in EtOAc (50 mL) and stirred for 30 minutes. EtOAc was removed under reduced pressure to give a dark yellow solid which on recrystallization from ethylacetate:hexane (2:1) offered **173** as yellow solid (2.42 g, 85%). m.p = 240 (decomp.).

MS (ES^+), *m/z* = 619 $(M+Na)^+$. ^{13}C-NMR (400 MHz, acetone-*d6*): δ, 170.01, 150.82, 150.30, 77.02, 64.82. Anal. Calcd for $C_8H_2Cl_2I_3NO_2$ C, 16.13; H, 0.34; N, 2.45. Found: C, 16.13; H, 0.34; N, 2.35.

Synthesis of 4-amino- N,N-bis(2,4,6-triiodo) bis phenylimino acetic acid sodium salt (174)

5-Amino-2,4,6-triiodo-isophthaloyl dichloride(173) (1.5g, 2.5 mmol) was dissolved in anhydrous dimethylacetamide (35 mL) under argon atmosphere with stirring. To this was added dimethylacetamide (15 mL) solution of **166** (1.43 g, 5.11 mmol) via a syringe Dry triethylamine (0.51 g, 0.68 mL, 2.4 mmol) was added to this stirred mixture and the resulting solution was stirred at room temperature for 24 hours. After the completion of the reaction (monitored by TLC) the dimethylacetamide was vacuum distilled and the residue extracted with chloroform. The chloroform layer was washed with HCl (1M), $NaHCO_3$ and brine. The organic layer was dried over $MgSO_4$ and solvent evaporated to afford fluffy white solid which on flash-column chromatography and recrystallization (Ethanol) afford **174** as white solid (2.3 g, 85 %)m.p = 187-189 ^{0}C. MS (ES^+) m/z = 1083 $(M+H)^+$. Anal. Calcd for $C_{36}H_{40}I_3N_5O_{10}.2C_2H_5OH$ C, 40.87; H, 4.46; N, 5.96. Found: C, 40.83; H, 4.13; N, 6.46.^{13}H-NMR (400MHz, DMSO-d_6, ppm): δ 1.20 (t, 24H, *J*=6.5Hz), 4.14 (q, 16H, *J*=6.5Hz), 4.20 (s, 4H, 16H) 6.56 (d, 8H, *J*=7.5Hz), 7.69 (m, 8H), 10.27-10.43 (m, 6H, -NH). ^{13}C-NMR (100MHz, DMSO-d_6, ppm): δ, 170.53, 165.73, 147.51, 146.06, 144.55, 14.14, 134.50, 129.19, 121.02, 113.30, 111.96, 107.94, 95.51, 60.39, 52.81, 14.14. IR (ν_{max}, KBr, cm^{-1}): 3233, 2962, 1745, 1640,1590, 1066, 1024, 976, 815, 730, 645.

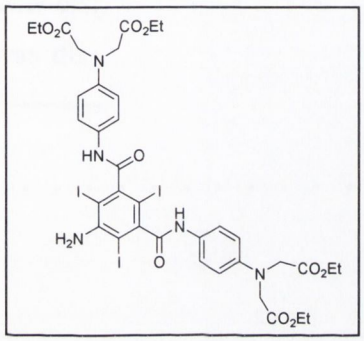

Synthesis of *N,N*-bis(2,4,6-triiodo-3,5-benzenedichlorocarbonyl)-malonamide (175)[319]

5-Amino-2,4,6-triiodo-isophthaloyl dichloride 2.5.7 g, 4.3mmol) was dissolved anhydrous THF (30 mol) and brought to reflux under rgon. To the solution was added Malonyl dichloride (0.2.0 mL, 2.1 mmol) dropwise via syringe and solution refluxed for 6 h in an inert atomsphre. After the completion of

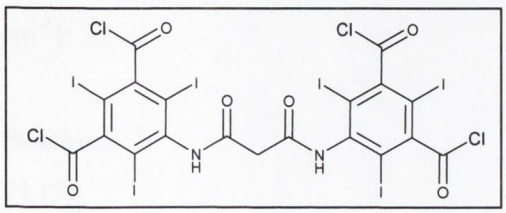

reaction (TLC) solvent was evaporated off under pressure and residue triturated with hexane to obtain pure **175** (2.10g, 75%). ^{1}H NMR (400 MHz, acetone-d6): δ 3.85 (s, 2H, $\underline{CH_2}$, 10.01(brs, 2H, $\underline{NH}$). ^{13}C-NMR (400 MHz, acetone-*d6*): 169.92, 166.10, 151.83, 146.20, 98.32, 83.24, 43.01.

Synthesis of *N,N*-bis(2,4,6-triiodo-3,5-benzenedichlorocarbonyl)-malonamide tetra phenyliminodietyl diester. (176)

N,N-bis(2,4,6-triiodo-3,5-benzenedichlorocarbonyl)-malonamide **(175)** (1.09g, 0.86mmol) was dissolved in anhydrous dimethylacetamide (20 mL) under argon atomosphere with stirring. To this was added dimethylacetamide (15 mL) solution of 110 (1.052 g, 3.75 mmol) *via* syringe. Dry Triethylamine (0.38 g, 0.51 mL, 3.75 mmol) was added to this stirred mixture and the resulting solution was stirred at room temperature for 24 hours. After the completion of the reaction (monitored by TLC) the dimethylacetamide was vacuum distilled and the residue extracted with chloroform. The chloroform layer was washed with HCl (1M), $NaHCO_3$ and brine. The organic layer was dried over $MgSO_4$ and solvent evaporated to afford pluffy white solid which on flash-column chromatography and recrystallization (ethanol) afford **176** as white solid (1.19 g, 80 %). Mass spectra (ES^+) 1117 ($M^+/2$) Calcd for $C_{75}H_{80}I_6N_{10}O_{22}$: C, 40.31; H, 3.61; N, 6.27; Found: C, 40.78; H, 3.98; N, 6.41.^{1}H-NMR (400 MHz, DMSO-d_6): δ, 1.20 (t, 24H, J = 7.0Hz, $NHCH_2CO_2CH_2\underline{CH_3}$), 4.12 (q, 8H, J = 7.0 Hz, $NHCH_2CO_2\underline{CH_2}CH_3$), 4.19 (s, 8H, $NH\underline{CH_2}CO_2CH_2CH_3$), 6.55 (d, 4H, J = 8.5Hz, Ar-$\underline{H}$), 7.43-7.46 (m, 4H, Ar-$\underline{H}$), 10.24 (brs, 2H, -CO$\underline{NH}$). ^{13}C-NMR (100 MHz, DMSO-d_6): δ, 170.55, 167.08, 150.06, 144.54, 142.75, 129.28, 129.24, 121.03, 121.06, 112.01, 111.98, 91.04, 60.40, 52.85, 14.15. IR (ν_{max}, KBr, cm^{-1}): 3243, 2982, 1735, 1650,1530, 1186, 1024, 970, 815.

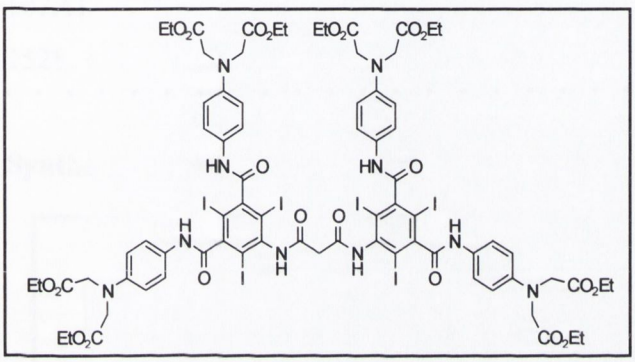

Synthesis of 2,4,6-Triiodo-3, 5-diacetamidobenzoicacid (181)

74 (5g, 9.6mmol) was dissolved in acetic anhydride (9.2g, 90.1 mmol). To this was added few drops of Conc.H_2SO_4. After heating on steam-bath for 30 minutes, the mixture was

poured over ice-cooled water when 75 separated as dark-brown solid. Crude solid was

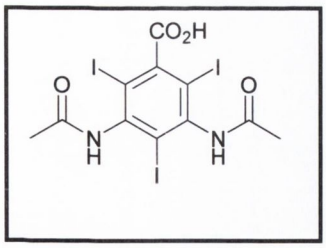

treated with sat. NH_4Cl (10 mL) and solution treated with activated carbon (1g) and filtered. The resulting ammonium salt solution was carefully hydrolysed with hydrochloric acid to yield 75 as dull grey solid (5.219g, 90%). MS (ES^+) m/z = 636 $(M+Na)^+$. Anal. Calcd for $C_{11}H_9I_3N_2O_4.2H_2O$: C, 20.33; H, 2.02; N, 4.31; Found: C, 20.31; H, 1.64; N, 4.13. ^1H NMR (400 MHz, DMSO-d6): δ, 2.02 (s, 6H, CH_3), 9.95 (s, 1H, -NH), 10.04 (s, 1H, -NH), 13.94 (bs, 1H, -COOH). ^{13}C NMR (100 MHz, $CDCl_3$) δ, 169.67, 167.81, 167.56, 148.75, 144.24, 144.22, 107.58, 107.41, 96.59, 23.02, 22.98 ; IR (ν_{max}, KBr, cm^{-1}): 3389, 3200, 2342.63, 2343, 1882, 1672, 1528, 1366, 1279, 1251, 977, 786, 709, 504, 666.

Synthesis of 2,4,6-Triiodo-3,5-diacetamidobenzoylchloride (182) :

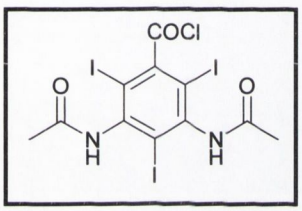

3,5-diaminobenzoic acid (6g, 41.54 mmol) was dissolved in water (20 mL) and Con. HCl (32%, 10mL) with vigorous stirring .To this was added a solution of ICl (21g, 129.23 mmol) in Con.HCl (32%, 21mL). The stirring was continued for 30 minutes, resulting in dark-brown solid, which was filtered and dried under vacuum. Crude solid was treated with saturated NH_4Cl (20 mL) and the solution treated with activated carbon (1g) and filtered. The resulting ammonium salt was carefully hydrolysed with hydrochloric acid to yield **182** as dull white solid (15.1 g, 71%). MS (ES^+) *m/z* = 654 $(MNa)^+$. Anal. Calcd for $C_{11}H_8ClI_3N_2O_2$. C, 20.89; H, 1.28; N, 4.43. Found: C, 20.69; H, 0.87; N, 3.80.^1H NMR (400 MHz, DMSO-d6) δ 2.04 (s, 6H, $NHCO\underline{CH_3}$), 10.09 (s, 1H, -$\underline{NH}COCH_3$), 10.16 (s, 1H, $\underline{NH}COCH_3$); ^{13}C-NMR (100 MHz, $CDCl_3$): δ, 167.92, 167.70, 149.03, 145.02, 111.02, 95.13, 22.98, 22.9; IR (ν_{max}, KBr, cm^{-1}): 3242, 3007, 2058, 1889, 1675, 1498, 1345, 1299, 1007, 850, 782, 650.

References

1. Desiraju, G. R. *Nature* **2000**, *408*, 407.
2. Lehn, J. -M. *Supramolecular Chemistry: Concepts and Perspective, VCH, Weinheim* **1995**.
3. Desiraju, G. R. *Nature* **2001**, *412*, 397.
4. de Silva, A. P.; Fox, D. B.; Moody, T. S.;Weir, S. M. *Pure Appl. Chem.* **2001**, *73*, 503.
5. (a) de Silva, A. P.; McClenaghan, N. D. *Chem. Eur. J.* **2002**, *8*, 493. (b) Gunnlaugsson, T.; MacDonail, D. A.; Parker, D. *Chem. Commun.* **2000**, 93. (c) Irie, M.; Fukaminato, T.; Takatoshi, S.; Naoto, T.; Kawai, T. *Nature* **2002**, *420*, 759.
6. Ozinskas, A, J. In *Topics in Fluorescence Spectroscopy, Volume 4, Probe Design and Chemical Senisng*, Lakowics, J. R., Ed.; Plenum Press, New York **1994**, 449.
7. Morrison, L. E. *Anal. Biochem.* **1988**, *174*, 101.
8. Kraut, J. *Science* **1988**, *242*, 533.
9. Hamilton, A. D. *J. Chem. Edu.* **1990**, *67*, 821.
10. Fischer, E. *Ber. Dr. Chem. Ges.* **1894**, *27*, 2985.
11. Jee, W. S. S. In *Bone Mechanics Handbook, ISBN 0-8493-9117-2*, Cowin, S. C., Ed.; CRC Press, Boca Raton, Florida, USA **2001**.
12. (a) Czarnik, A. W, Ed.; *Fluorescent Chemosensors of Ion and Molecular Recognition, ACS. Symp. Ser.*, American Chemical Society: Washington DC **1993**. (b) Valeur, B. In *Topics in Fluorescence Spectroscopy, Volume 4, Probe Design and Chemical Sensing*, Lakowics, J. R., Ed.; Plenum Press, New York **1994**,21.
13. Beer, P. D.; Gale, P. A. *Angew. Chem. Int. Ed.* **2001**, *40*, 486.
14. Rurack, K.; Resch-Genger, U. *Chem. Soc. Rev.* **2002**, *31*, 116.
15. Smith, R. V.; Nessen, M. A. *J. Pharm. Sci.* **1971**, *60*, 907.
16. Wolfbeis, O. S. *Fibre Optic Chemical Sensors and Biosensors, Volume 1&2,* CRC Press, Boca Raton, Florida **1991**.
17. Lavigne, J. J.; Anslyn, E. V. *Angew. Chem. Int. Ed.* **2001**, *40*, 3118.
18. (a) Yoon, J. -Y.; Czarnik, A. W. *J. Am. Chem. Soc.* **1992**, *114*, 5874. (b) Czarnik, A. W. *Accts. Chem. Res.* **1994**, *27*, 302. (c) Czarnik, A. W. *Nature* **1998,** *394*, 417.

19. (a) Bryan, A. J.; de Silva, A. P.; de Silva, S. A.; Rupasinghe, R. A. D. D.; Sandanayake, K. R. A. S. *Biosensors*, **1989**, *14*, 169. (b) de Silva, A. P.; Gunnlaugsson, T.; Rice, T. E. *Analyst* **1996**, *121*, 1759. (c) Barbarella, G. *Chem. Eur. J.* **2002**, *8*, 5073.
20. Bissel, R. A.; de Silva, A. P.; Gunaratne, H. Q. N.; Lynch, P. L. M.; McCoy, C. P.; Maguire, G. E. M.; Sandanayake, K. R. A. S. *Top. Curr. Chem.* **1993**, 223.
21. Valeur, B.; Leray, I. *Coordination. Chem. Rev.* **2000**, *205*, 3.
22. http:// www.s4ms.com/chem_chemosensor.htm.
23. (a) Bissel, R. A.; de Silva, A. P.; Gunaratne, H. Q. N.; Lynch, P. L. M.; McCoy, C. P.; Maguire, G. E. M.; Sandanayake, K. R. A. S. *Chem. Soc. Rev.* **1992**, 187. (b) Granda-Valdes, M.; Badia, R.; Pina-Luis1, G.; Diaz-Garcia, M. E. *Quimica Analitica.* **2000**, *19 (Suppl. 1)*, 38.
24. Weller, A. *Pure Appl. Chem.* **1968**, *16*, 115.
25. Rehm. D. *Isr. J. Chem.* **1970**, *8*, 259.
26. de Silva, A. P.; Gunaratne, H. Q. N.; Gunnlaugsson, T.; Huxley, A. J. M.; McCoy, C. P.; Rademacher, J. T. and Rice, T. E. *Chem. Rev.* **1997**, *97*, 1515.
27. de Silva, A. P.; Rupasinghe, A. D.D. *J. Chem. Soc., Chem. Commun.* **1985**, 1669.
28. Czarnik, A. W.; Desvergne, J.-P., Eds.; *Chemosensors for Ion and Molecular Recognition, Kluwer, Dordrecht,* The Netherlands, **1997**.
29. Snowden, T. S.; Anslyn, E. V. *Curr. Opin. Chem. Biol.* **1999**, *3*, 740.
30. Martínez-Máñez, R.; Sancenón, F. *Chem. Rev.* **2003**, *103*, 4419.
31. Christianson, D. W.; Lipscomb, W.N. *Acc. Chem. Res.* **1989**, *22*, 62.
32. Puglisi, J. D.; Chen, L.; Frankel, A. D.; Williamson, J. R. *Proc. Nat. Acad. Sci. USA* **1993**, *90*, 3680.
33. Moss, B. *Chem. Ind.* **1996**, 407.
34. Glidewell, C. *Chem. Br.* **1990**, *26*, 137.
35. de Silva, A. P.; de Silva, S. A. *J. Chem. Soc., Chem. Commu.* **1986**, 1709.
36. de Silva, A. P.; Sandanayake,; Samankumara, K. R. S. *Tetrahedron Lett.* **1991**, *32*, 421.
37. Kastenholtz, F.; Grell, E.; Bats, J. W.; Qninkert, G.; Brand, K.; Lanig, H.; Schneider, F. W.; *J. Fluoresc.* **1994**, *4*, 243.

38. deSilva, A. P.; Gunaratne, H. Q. N.; Sandanayake, K. R. S. *Tetrahedron Lett.* **1990**, *31*, 5193.

39. Fages, F.; Desvergne, J–P.; Bouas-Laurent, H. *J. Am. Chem. Soc,* **1989**, *111*, 96.

40. Fages, F.; Desvergne, J–P.; Bouas-Laurent, H.; Marsau, P.; Lehn, J. -M.; Kotzyba-Hibert, F.; Albrecht-Gary, A. -M.; Al-Joubbeh, M. *J. Am. Chem. Soc.* **1989**, *111*, 8672.

41. Ji, F–F.; Dabestant, R.; Brown, G. M.; Hettich, L. R. *J. Chem. Soc. Perkin Trans. 2*, **2001**, 585.

42. Gunnlaugsson, T.; Nieuwenhuyzen, M.; Richard, L.; Thoss, V. *J. Chem. Soc., Perkin Trans. 2* **2002**, 141.

43. Gunnlaugsson, T.; Bichell, B.; Nolan, C. *Tetrahedron Lett.* **2002**, *43*, 4989.

44. Kim, J. S.; Shon, O. J.; Rim, J. A.; Kim, S. K.; Yoon, J. *J. Org. Chem.* **2002**, *67*, 2348.

45. He, H.; Mortellaro, M. A.; Leiner, M. J. P.; Young, S. T.; Fraatz, R. J; Tusa, J. K. *Anal.Chem.* **2003**, *75*, 549.

46. He, H.; Mortellaro, M. A.; Leiner, M. J. P.; Fraatz, R. J; Tusa, J. K. *J. Am. Chem. Soc.* **2003**, *125*, 1468.

47. Minta, A.; Kao, J. P. Y.; Tsien, R. Y. *J. Biol. Chem.* **1989**, *264,* 8171.

48. de Silva, A. P.; Gunaratne, H. Q. N.; Kane, T. M.; Maguire, E. M. *Chem. Lett.* **1995**, 125.

49. Valeur, B. In *Topics in Fluorescence Spectroscopy, Vol. 4: Probe Design and Chemical Sensing*, Lakowicz, J. R., Eds.; Plenum Press, New York. **1994**, 22.

50. Liepour, F.; Deligeorgiev, T. G.; Veneti, Z.; Savakis, C.; Katerinopoulos, H. E. *Cell Calcium.* **2002**, *31*, 221.

51. Haugland, R. P. *Handbook of Fluorescent Probes and Research Products, 9th edition,* Molecular Probes, Inc., Eugene, USA. **2002**

52. (a) Fabbrizzi, L.; Lichelli, M.; Pallavicini, P.; Peroti, A.; Taglietti, A.; Sachi, D. *Angew. Chem. Int. Ed. Engl.* **1994**, *33*, 1975. (b) Fabbrizzi, L.; Lichelli, M.; Pallavicini, P.; Peroti, A.; Taglietti, A.; Sachi, D. *Chem Eur. J.* **1996**, *2*, 167.

53. Fabbrizzi, L.; Lichelli, M.; Pallavicini, P.; Taglietti, A. *Inorg. Chem.* **1996**, *35*, 1733.

54. Sasaki, D. Y.; Shnek, D. R.; Pack, D. W.; Arnold, F. H. *Angew. Chem. Int. Ed. Engl.* **1995**, *34*, 905.

55. Dujols, V.; Ford, F.; Czarnik, A. W. *J. Am. Chem. Soc.* **1997**, *119*, 7386.
56. Kumar, S.; Pramilla; Kaur, S. *Tetrahedron Lett.* **2002**, *43*, 1097.
57. Kaur, S.; Kumar, S. *Chem. Commun.* **2002**, 2840.
58. Pallavicini, P.; Amendola, V.; Massera, C.; Etienne, M.; Tagoetto, A. *Chem. Commun.* **2002**, 2452.
59. Kang, J.; Choi, M.; Kwon, J. Y.; Lee, E. Y.; Yoon, J. *J. Org. Chem.* **2002**, *67*, 4384.
60. Grabchev, I.; Chovelon, J. -M.; Qian, X. *J. Photchem. Photobiol. Part A: Chem.* **2003**, *158*, 37.
61. Zheng, Y.; Cao, X.; Orbulescu, J.; Konka, V.; Andreopoulos, F. M.; Pham, S. M.; Leblanc, R. M. *Anal. Chem.* **2003**, *75*, 1706.
62. Arman, S. A. V.; Czarnik, A. W. *J. Am.Chem. Soc.* **1990**, *112*, 5376.
63. Gunnlaugsson, T.; Davis, A. P.; Glynn, M. *Chem. Commun.* **2001**, 2556.
64. Gunnlaugsson T.; Davis, A. P.; Glynn, M. *Org. Lett.* **2002**, *4*, 2449.
65. Valeur, B.; Bourson, J.; Pouget, J. In: *Fluorescent Chemosensors for Ion and Molecular Recognition*, ACS Symposium Series 538. Czarnik, A. W.; Ed.; Washington, D. C. **1993**, Chapter 3.
66. Valeur, B.; Bourson, J.; Pouget, J. In: *Fluorescent Chemosensors for Ion and Molecular Recognition*, ACS Symposium Series 538. Czarnik, A. W.; Ed.; Washington, D. C. **1993**, Chapter 2.
67. Letard, J. F.; Lapouyade, R.; Rettig, W. *Pure Appl. Chem.* **1993**, *65*, 1705.
68. Tsein, R. Y. *Biochemistry* **1980**, *19*, 2396.
69. (a) Grynkiewica, G.; Poenie, M.; Tsein, R. Y. *J. Biol. Chem.* **1985**, *260*, 3440. (b) Tsein, R. Y. *Methods Cell Biol.* **1989**, *30*, 127.
70. Smith, G. A.; Hesketh, T. R.; Metcalfe, J. C. *Biochem. J.* **1988**, *250*, 227.
71. Yang, J. -S.; Lin, C. -S.; Whang, C. -Y. *Org. Lett.* **2001**, *3*, 889.
72. Collado, D.; Perez-Inestrosa, E. P.; Suau, R.; Desvergne, J. -P.; Bouas-Laurent, H. *Org. Lett.* **2002**, *4*, 855.
73. Chen, C. -T.; Huang, W. -P. *J. Am. Chem. Soc.* **2002**, *124*, 6246.
74. Parker, D.; Williams, J. A. G. *J. Chem. Soc., Dalton Trans.* **1996**, 3613.
75. Jüstel, T.; Nikol, H.; Ronda, C. *Angew. Chem. Int. Ed.* **1998**, *37*, 3084.
76. Rudzinski, C. M.; Engebreston, D. S.; Hartmann, W. K.; Nocera, D.G. *J. Phys. Chem. A* **1998**, *102*, 7442.

77. Grigg, R.; Holmes, J. M.; Jones, S. K.; Norbert, W. D. J. A. *J. Chem. Soc., Chem. Commun.* **1994**, 185.

78. Cotton, F. A.; Wilkinson, G. *Advanced Inorganic Chemistry, 5th ed., ISBN 0-471-84997-9,* John Wiley & Sons, New York **1988**, 955.

79. Richardson, F. S. *Inorg. Chem.* **1984**, *23*, 4607.

80. Parker, D. *Coord. Chem. Rev.* **2000**, *205*, 109.

81. de Silva, A. P.; Fox, D. B., Huxley, A. J. M.; McClenaghan, N. D.; Roiron, J. *Coord. Chem. Rev.* **1999**, *185-186*, 297.

82. Saha, A. L.; Kross, K.; Kloszewski, E. D.; Upson, D. A.; Toner, J. L.; Snow, R. A.; Black. C. D. V.; Desai, V.C. *J. Am. Chem. Soc.* **1993**, *115*, 11032.

83. deSilva, A. P.; Gunaratne, H. Q. N.; Rice, T.E. *Angew. Chem. Int. Ed.* **1996**, *35*, 2116de Silva, A. P.; Gunaratne, H. Q. N, Rice, T. E.; Stewart, S. *Chem. Commun.* **1997**, 1891.

84. (a) Gunnlaugsson, T.; MacDónaill, D. A.; Parker, D. *Chem. Commun.* **2000**, 93. (b) Gunnlaugsson, T.; MacDónaill, D. A.; Parker, D. *J. Am. Chem. Soc.* **2001**, *123*, 12866. (c) Gunnlaugsson, T. *Tetrahedron Lett.* **2001**, *42*, 8901.

85. Gunnlaugsson, T.; Harte, A. J.; Leonard, J. P.; Nieuwenhuyzen, M. *Chem. Commun.* **2002**, 2134.

86. Gunnlaugsson, T.; Leonard, J. P. *Chem. Commun.* **2003**, *19*, 2424.

87. McFarland, S. A.; Finney, N. S. *J. Am. Chem. Soc.* **2001**, *124*, 1178.

88. Ajayaghosh, A.; Arunkumar, E.; Daub, J. *Angew. Chem. Int. Ed.* **2002**, *41*, 1766.

89. (a) Beer, P. D.; Szemes, F.; Balzanni, V.; Sala, C. M.; Drew, M. G. B.; Dent, S. W.; Maestri, M. *J. Am. Chem. Soc.* **1997**, *119*, 11864. (b) Beer, P. D.; Hayes, E. J. *Coord. Chem. Rev.* **2003**, *240*, 167.

90. Jee, W. S. S. In *Orthopaedics, Principle of Basic and Clinical Science*, Bronner, F.; Worrell, R.V., Eds.; Boca Raton, Florida **1999**, Chapter 1.

91. Jee, W. S. S. In *A Textbook of Histology;* Weiss, L., Ed.; Urban Schwarzenberg, Baltimore **1988**, Chapter 7.

92. Martini, F. H.; Ober, W. C.; Garrison, C. W.; Welch, K.; Hutchings, R. T. *Fudamentals of Anatomy and Physiology, 5th edition, ISBN 0-13-017292-8*, New Jersey, Prentice Hall **2001**, Chapter 6.

93. Frost, H. M. *Introduction to a New Skeletal Physiology, Vol. I and II*; Pajaro Group, Pueblo, **1995**.

94. Baron, R. In *Primer on the Metabolic Bone Disease and Disorder or Mineral Metabolism*, 4th ed., Favus, M. J., Ed,: Lippincott/Williams & Wilkins, Philadelphia. **1999**, Chapter 1.
95. Gehron-Robey, P.; Boskey, A. L. In *Osteoporosis*, Marcus, F.; Feldman, D.; Kelsey, J.; Eds.; Academic Press, San Diego **1996**, Chapter 4.
96. Lian, J. B.; Stein, G. S. In *Osteoporosis*, Marcus, F.; Feldman, D.; Kelsey, J.; Eds.; Academic Press, San Diego **1996**, Chapter 2.
97. Gorski, J. P. *Crit. Rev. Oral. Biol.* **1998**, *9*, 201.
98. Khosla, S.; Kleerekoper, M.; In *Primer on the Metabolic Bone Diseases and Disorders of Mineral Metabolism*, 4th ed., Favus, M. J., Ed,; Lippincott/Williams & Wilkins, Philadelphia **1999**, Chapter 2.
99. Miller, S. C.; Jee, W. S. S. *Calcif. Tissue Int.* **1992**, *41*, 1.
100. Dobnig, H.; Turner, R. *Endocrinology.* **1995**, *136*, 3632.
101. Jee, W. S. S.; Ma, Y.F. *Bone* **1997**, *21*, 297.
102. (a) Frost, H. M. In *Paediatric Osteology*, Schönau, E., Ed.; Elsevier, Amsterdam, **1996**, 3.(b) Frost, H. M. *Bone Modelling and Skeletal Modelling errors*, Charles C Thomas, Springfield, **1973**.
103. Frost, H. M. *Anat. Rec.* **1990**, *226*, 403.
104. Burr, D. B.; Martin, R. B.; Schaffler, M. B.; Radin, E. L. *J. Biomech.* **1985**, *18*, 189.
105. Mundy, F. R. In *Primer on the Metabolic Bone Diseases and Disorders of Mineral Metabolism*, 4th ed., Favus, M. J., Ed,: Lippincott/Williams & Wilkins, Philadelphia **1999**, Chapter 4.
106. Barnes, G. L.; Kostenuik, P. L.; Gerstenfield, L. C.; Einhorn, T. A.; *J. Bone Mineral Res.* **1999**, *14*, 1805.
107. Parfitt, A. M. *Metabolism* **1976**, *25*, 909.
108. Parfitt, A. M. In *Osteoporosis*, Marcus, F.; Feldman, D.; Kelsey, J.; Eds.; Academic Press, San Diego, **1996**, Chapter 12.
109. (a) Cowin, S. C. Weinbaum, S.; Zeng, Y. A. *J. Biomech.* **1995**, *28*, 1281.(b) Martin, R. B. *Bone* **2000**, *26*, 1.
110. Marotti, G. *Ital. J. Anat. Embryol.* **1996**, *101*, 25.
111. Frost, H. M. In *Current Concepts of Bone Fragility.*, Uhtoff, H. K., Ed.; Springer-Verlag **1985**, 123.
112. Frost, H. M. *Henry Ford. Hosp. Bull.* **1960**, *8*, 35.

113. Frost, H. M. *Bone Remodelling and its Relationship to Metabolic Bone Diseases*, Springfield, IL, Charles C. Thomas **1973**.

114. Lee, T. C.; Staines, A.; Taylor, D. *J. Anat.* **2002**, 201, 437.

115. Martin, R. B.; Burr, D. B. *Structure, Function and Adaptation of Compact Bone*, Raven Press, New York **1989**.

116. Giladi, M.; Milgrom, C.; Simkiu, A.; Danon, Y. *Am. J. Sports Med.* **1991**, *19*, 647.

117. Burr, D. B.; Martin, R.B.; Schaffler, M. B.; Radin, E. L. *J Biomech.* **1985**, *18*, 189.

118. Martin, R. B. *J. Orthop. Res.* **1995**, *13*, 309.

119. Schiller, A. L. In *Pathology, 2nd ed,* Rubin, E.; Farber, J. L., Eds.; J. B. Lippincott, Philadelphia **1994**.

120. Meurman, K. A. O.; Elfving, s. *Radiology* **1980**, *134*, 483.

121. Daffner, R. H.; Pavlov, H. *Am. J. Roentgen.* **1992**, 159, 245.

122. Zioupos, P. *J. Microsc.* **2001**, *201*, 270.

123. NIH *Consensus Development Panel on Osteoporosis Prevention, Diagnosis and Therapy. J. Am. Med. Assoc.* **2001**, **285**, 785.

124. Schaffler, M. B.; Choi, K.; Milgrom, C. *Bone* **1995**, *17*, 521.

125. Riggs, B. L.; Melton, L. J., III. Bone **1995**, *17 (Suppl.)*, 505S.

126. Melton, L. J.; III. Bone **1996**, *18 (Suppl.)*, 121S.

127. Rodan, G. A.; Martin, T. J. *Science* **2000**, *289*, 785.

128. http/www.kafponline.org/presentation/osetoporosisrpm.ppt.

129. (a) Curry, T. S., III; Downdey, J. E.; Murry, R. C., Jr. *Christensen's Physics of Diagnostic Radiology, 4th ed.*; Lea & Febiger, Philadelphia **1990**. (b) *Medical Imaging Physics, 3rd ed.*; Mosby-Year Book, St. Louis **1992**.

130. Jenkins, R. In *Chemical Analysis, A Series Of Monographs On Analytical Chemistry And Its Applications, Vol.152.;* Winefordner, J. B., Ed.; John-Wiley & Sons, Inc. USA **1999**, Chapter 1.

131. *CRC Handbook of Chemistry and Physics, 66th ed.*; Weast, E.C., Ed.; CRC Press, Boca Raton, FL **1986**, F-170.

132. Jenkins, R. In *Chemical Analysis, A Series Of Monographs On Analytical Chemistry And Its Applications, Vol.152.;* Winefordner, J. B., Ed.; John-Wiley & Sons, Inc. USA **1999**, Chapter. 1

133. Yu, S. –B.; Watson, A. D. *Chem. Rev.* **1999**, *99*, 2353.

134. Hoey, G. B.; Weight, P; Ranks, R. D. In *Organic Compounds as X-ray Contrast media*, Knoefel, P. K. Ed., *Radio Contrast Agent*; Pergamon Press, New York **1971**, Sec. 76, *Volume1*, 23.

135. Takeda, A.; *BioMetals* **2001**, *14*, 343.

136. Vallee, B. L.; Auld. D. S. *Matrix Mettalloproteinases and Inhibitors* **1992**, *Matrix Supplement 1, Stuttgart: Fischer,* 5.

137. Coleman, J. E. *Annu. Rev. Biochem.* **1992**, 897.

138. Vallee, B. L.; Falchuk, K.H.; *Physiol. Rev.* **1993**, *73*, 79.

139. Choi, D. W.; *Annu. Rev. Neurosci.* **1998**, *21*, 347.

140. Chausmer, A. B. *J. Am. Colleg. Nutr.* **1998**, *17*, 109.

141. (a) Formby, B.; Schimid-Formby, F.; Grodsky, G.M. *Diabetes* **1984**, *33*, 229. (b) Grodsky, G.M.; Schimid-Formby, F. *Encocrinology* **1985**, *117*, 704.

142. Wapnir, R. A. *J. Nutr.* **2000**, 1388S-1392S.

143. Prasad, A. S. *Nutrition* **1995**, 93.

144. Berg, J. M.; Shi, Y. *Science* **1996**, *271*, 1081.

145. Vallee, B. L.; Fachuk, K. H. *Phios. Trans. R Soc. Lond. B Biol. Sci.* **1981**, *294*, 185.

146. Fuji, T. *Nature Lond.* **1954**, *174*, 1108.

147. Federickson, C. J.; Moncrieff, D.W. *Biol. Signals* **1994**, *3*, 127.

148. Federickson, C. J. *Int. Rev. Neuobiol.* **1989**, *31*, 145.

149. Federickson, C. J; Bush, A. I. *BioMetals* **2001**, *14*, 353.

150. Weiss, J. H.; Sensi, S. L.; Koj, J. Y. *TiPS* **2000**, *21*, 395.

151. Koi, J. Y.; Choi, D.W.; *Neuroscience* **1994**, *60*, 1049.

152. Sensi, S. L.; Canzoniero, L. M. T.; Yu, S. P.; Ying, S. H.; Koh, J. -Y.; Kerchner, G. A.; Choi, D. W. *J. Neurosci.* **1997**, *17*, 9554.

153. Bush, A. I.; Atwood, C. S.; Huang, X.; Moir, R. D.; Glabe, R. E.; Tanzi. *Eur. Neuropsychopharmacol.* **1996**, *3*, 20 (S-4-2).

154. Bush, A. I.; Pettingel, W. H.; Multhaup, M. D.; Paradis, Vonsatel, J. E.; Gusella, J. E.; Beyreuther, C. L.; Masters, C. L.; Tanzi, R. E. *Science* **1994**, *265*, 16109.

155. Bush, A. I.; Moir, R. D.; Rosenkranz, R. E. *Science* **1995**, *268*, 1921.

156. Bush, A. I.; Multhaup, G.; Moir, R. D.; Williamson, T. G.; Small, D. H.; Rumble, B.; Pollwein, P.; Beyreuther, K.; C. L.; Masters, C. L. *J. Biol. Chem.* **1993**, *268*, 16109.

157. Koh, J. Y.; Suh, S. W.; Gwag, B. J.; He, Y. Y.; Hsu, C.; Choi, D. W. *Science* **1996**, *272*, 1013.

158. Sloviter, R. *Brain Res.* **1985**, *330*, 150.

159. Tønder, N, Johansen, C. J.; Frederickson, G. A.; Zimmer, J.; Diemer, N. H. *Neurosci. Lett.* **1990**, *109*, 247.

160. Guajungco, M. P.; Lees, G. J. *Brain Res.* **1998**, *799*, 118.

161. Auld, D. S. *BioMetals* **2001**, *14*, 271.

162. Vallee, B. L.; Auld, D. S. *Faraday Disuss.* **1992**, *93*, 47.

163. Vallee, B. L.; Auld, D. S. *Biochemistry* **1993**, *32*, 6493.

164. Vallee, B. L.; Auld, D. S. *Acc.Chem. Res.* **1993**, *26*, 543.

165. Auld, D. S. In *Handbook of Proteolytic Enzymes.* Bertini, I.; Sigel, A.; Sigel, H, Eds.; Academic Press, London **2001**, 1326.

166. Iverson, T. M, Alber, B. E.; Kisker, C.; Ferry, J. G. Rees, D. C. *Biochemistry* **2000**, 9222.

167. Papageorgiou, A. C.; Acharya, K. R. *Structure* **1997**, *5*, 991.

168. Thompson, R. B.; Peterson, D.; Mahoney, W.; Cramer, M.; Maliwal, B. P.; Suh, S. W.; Frederickson, C.; Fierke, C.; Herman, P. *J. Neurosci. Method.* **2002**, *118*, 63.

169. Hirano, T.; Kikuchi, K.; Urano, Y.; Higuchi, T.; Nagano, T. *Angew. Chem. Int. Ed.* **2000**, *39*, 1052.

170. Hirano, T.; Kikuchi, K.; Urano, Y.; Higuchi, T.; Nagano, T. *J. Am. Chem. Soc.* **2000**, *122*, 12399.

171. (a) Haugland, R. P. *Handook of Fluorescent Probes and Research*, 9th edition Chemical. Eugene, Oregon: Molecular Probes, Inc. **2002**, 811. (b) http://www.probes.com

172. Burdette, S. C.; Walkup, G. K.; Spingler, B.; Tsien, R. Y.; Lippard, S. J. *J. Am. Chem. Soc.* **2001**, *123*, 7831.

173. Gee, K. R.; Zhou, Z. -L.; Qian, J. -J.; Kenndy, R. *J. Am. Chem. Soc.* **2002**, *124*, 776.

174. Walkup, G. K.; Imperiali, B.; *J. Am. Chem. Soc.* **1996**, *118*, 3053.

175. Godwin, H. A.; Berg, J. M. *J. Am. Chem. Soc.* **1996**, *118*, 6514.

176. Maruyama, S.; Kikuchi, K.; Hirano, T.; Urano, Y.; Nagano, T. *J. Am. Chem. Soc.* **2002**, *124*, 63.

177. Burdette, S. C.; Federickson, C. J.; Bu, W.; Lippard, S. J. *J. Am. Chem. Soc.* **2003**, *125*, 1778.

178. Woodroofe, C. C.; Lippard, S. J. *J. Am. Chem. Soc.* **2003**, 125, 11458.

179. Atkins, P. W. *Physical Chemistry, 6th edition, ISBN 0-19-850102-1,* Oxford University Press, Oxford **1998**, 1947.

180. Guibault, G. C., Ed.; *Practical Fluorescence, 2nd edition*, Marcel Dekker, **1990**.

181. Lakowicz, J. R. *Principles of Fluorescence Spectroscopy, 2nd edition*, Plenum Publishing, **1999**.

182. (a) Rost, F. W. D. *Fluorescence Microscopy, Volume 1*, Cambridge University Press, Cambridge **1992**. (b) Rost, F. W. D. *Fluorescence Microscopy, Volume 2*, Cambridge University Press, Cambridge **1995.**

183. Kelly, L. A.; Rogers, J. E.; Le, T. P. *J. Phys. Chem. A* **2000**, *104*, 6778.

184. Ji, H-F.; Dabestani, R.; Brown, G.M.; Hettich, R. L. *Photochemistry and Photobiology* **1999**, *69*, 513.

185. Gunnlaugsson, T.; McCoy, C.P.; Morrow, R.J.; Phelan, C.; Stomeo, F. *Arkivoc* **2003**, 216.

186. Alexiou, M. S.; Tychopoulos, V.; Ghorbanian, S.; Tyman, J. H. P.; Brown, R. G.; Brittain, P. I. *J. Chem. Soc. Perkin Trans. 2* **1990**, 837.

187. Konstantinova, T.; Spirieva, A.; Petkova, T. *Dyes and Pigments* **2000**, *45*, 125.

188. Romesberg, F. E.; Flanagan, M.E.; Uno, T.; Schultz, P.G. *J. Am. Chem. Soc.* **1998**, *120*, 5160.

189. Tsien, R. Y. *Methods Enzymol.* **1999**, *20*, 224.

190. Brange, J.; Langkjoer, L. *Pharm. Biotechnol* **1993**, *5*, 315.

191. Derewenda, U.; Derewenda, Z.; Dodson, G.; Hubbard, R.; Korber, F. Br. *Med. Bull.* **1989**, *45*, 4.

192. Brader, M. L.; Dunn, M. F. *Trends Biochem. Sci.* **1991**, *16*, 341.

193. Zalewski, P.; Millard, S.; Forbes, I.; Kapaniris, O.; Slavotinke, S.; Betts, W.; Lincoln, S.; Mahadevan, I. *J. Histochem. Cytochem.* **1994**, *42*, 877.

194. Drury, R. A. B.; Wallington, E. A. In *Carletons Histological Technique*, Oxford University Press, Oxford **1980**.

195. Figlewicz, D.; Forhan, S.; Hodgson, A.; Grodsky, G. *Endrocrinology* **1984**, *115*, 877.

196. Lukowiak, B.; Vandewalle, B.; Riachy, R.; Kerr-Conte, J.; Gmyr, V.; Belaich, S.; Lefebvre, J.; Pattou, F. *J. Histochem. Cytochem.* **2001**, *49*, 819.

197. Frausto da Silva, J.J.R.; Williams, R.J. In *The Biological Chemistry of the Elements: The Inorganic Chemistry of Life, 2nd edition, ISBN 0-198508476,* Oxford University Press, Oxford **2001**. (b) *CRC Handbook of Chemistry and Physics, 77th edition,* CRC Press, Inc.; Boca Raton, Florida 1996. (c) Carr, D. S. In *"Cadmium and Cadmium Alloys" Kirk-Othmer Encyclopaedia of Chemical Technology, Volume 4, 4th edition,* John Wiley & Sons, New York **1992**. (d) Morrow, H.; *"Cadmium (Cd),"* *Metals Handbook,* 10th edition, Volume 2, ASM International, Metals Park, Ohio **1990**.

198. (a) *Cadmium and Compounds*, U.S. Environmental Protection Agency **2001**. (b) Cook, M. E.; Morrow, H. *"Anthropogenic Sources of Cadmium in Canada,"* National Workshop on Cadmium Transport Into Plants, Canadian Network of Toxicology Centres, Ottawa, Ontario, Canada **1995**.

199. Marrow, H. *International Cadmium Association, Oral commun.* **2003.**

200. Bak, J.; Jensen, J.; Larsen, M. M.; Pritzl, G.; Scott-Fordsmand, *J. Sci. Total Environ.* **1997**, 179.

201. http://www.cadmium.org

202. (a) Dobson, S. *Cadmium-Environmental Aspects*; World Health Organisation: Geneva. **1992**.(b) Jackson, T.; MacGillivray, A. In *Accounting for Cadmium*, Stockholm Environment Institute, London **1993**.

203. Jones, R.; Lapp, T.; Wallace, D. In *Locating ad Estimating Air Emissions from Sources of Cadmium and Cadmium Compounds*, Institute for the U.S Environment Protection Agency, Office of Air and Radiation, Report EPA-453/R-93-040 **1993**.

204. Van Urk, G.; Marquenie, J. M.; *"Environmental Behaviour of Cadmium: WHO Are at Risk and Why," Heavy Metals in the Environment, Volume 11,* Geneva **1989**, 456.

205. Rydh, C. J.; Svärd, B. *The Science of the Total Environment*, **2003**, *302*, 167.

206. Benjamin, M. W.; Honeyman, B. D. In *Global Biogeochemical Cylces,* Butcher, S. S.; Chalrson, R. J.; Orians, G. H.; Wolfe, G. V.; Eds.; *Academic Press*, London **1992**, 317.

207. Jarup, L.; Berglund, M.; Elinder, Nordberg, G.; Vather, M. *J. Work. Environ. Health* **1998**, *24*, 1.

208. Nordberg, G. F.; Nordberg, M. In *Biological Monitoring of Trace Metals, Volume 151,* Clarksnon, T. W.; Friberg, L.; Nordberg, G. F.; Sager, P. R., Eds.; Plenum Press, New York, **1988**.

209. Friberg, L.; Elinger, C. G.; Kjellström, T. *Cadmium:* World Health Organisation, Geneva, **1992**.

210. (a) Buchet, J. P.; Lauwerys, R.; Roels, H.; Bernard, A.; Bruaux, P.; Claeys, F.; Ducoffre, G.; De Plaen, P.; Staessen, J.; Amery, A.; Linjen, P.; Thijs, L.; Ronda, D.; Sartor, F.; Saint Remy, A.; Nick, L. *Lancet* **1990**, *336*, 699. (b) Gouget, B.; Figard, L.; Carrot, F.; Lemaout, S.; Gobain, R.; Khodja, H. *In Metals Ions in Biology and Medicine, Volume 7*, John Libbey Eurotext **2002**, 138.

211. Nordberg, G. F. *In Effects and Dose-Response Relationships of Toxic Metals*, Elsevier, New York **1976**.

212. Falnoga, I.; Tusek-Znidaric, M.; Horvat, M.; Stegnar, P. *J. Environ. Pathol. Toxicol. Oncol.* **2000**, *19*, 201.

213. (b) Khodja, H.; Avoscan, L.; Carriere, M.; Carrot, F.; Gouget, B. *Nucl. Instr. and Meth. in Phys. Res. B* **2003**, *210*, 359.

214. Nakadaira, H.; Nishi, S. *The Science of the Total Environment* **2003**, *309,* 48.

215. Regunathan, A.; Glesne, D. A.; Wilson, A. K., Song, J.; Nicolae, D.; Flores, T.; Bhattacharyya, M. H. *Toxicology and Applied Pharmacology* **2003**, *191*, 272.

216. Onar, A. N.; Temizer, A. *Analyst* **1987**, *112*, 227.

217. Carmack, G. D.; Evenson, M. A. *Anal. Chem.* **1979**, *51*, 907.

218. Pruszdowska, E.; Carnick, G. R.; Slavin, W. *Clin. Chem.* **1983**, *29*, 477.

219. D'Haese, P.C.; Lamberts, L. V.; Liang, L.; de Vyver, V.; De Broe, M. E. Clin. Chem. **1991**, *37*, 1583.

220. Cerny, E. A.; Bhattacharyya, M. H. *Analytical Biochemistry* **2003**, *314*, 180.

221. Dolan, S. P.; Capar, S. G. *J. Food Composition and Analysis* **2002**, *15*, 593.

222. Huston, M. E.; Akkaya, E. U.; Czarnik, A. W. *J. Am. Chem. Soc.* **1989**, *111*, 8735.

223. Huston M. E.; Engleman, C.; Czarnik, A. W. *J. Am. Chem. Soc.* **1990**, *112*, 7054.

224. Czarnik, A. W. *Acc. Chem. Res.* **1994**, *27*, 302.

225. Czarnik, A. W, Ed.; *Fluorescent Chemosensors of Ion and Molecular Recognition*, Acs Symp. Ser. American Chemical Society: Washington DC, **1993,** 105.

226. Prodi, L.; Montalti, M.; Zaccheroni, N.; Bradshaw, J. S.; Izatt, R. M.; Savage, P. B. *Tetrahedron Lett.* **2001**, *42*, 2941.

227. Choi, M.; Kim, M.; Lee, K. D.; Han, K. N.; Yoon, I. A; Chung, H. J.; Yoon, J. *Organic Lett.* **2001**, *3*, 3455.

228. (a) Bouas-Laurent, H.; Castellan, A.; Daney, M.; Desvergne, J. -P.; Guinand, G.; Marsau, P.; Riffaud, M. -H. *J. Am. Chem. Soc.* **1986**, *108*, 315. (b) Desvergne, J. -P.; Bouas-Laurent, H.; Marsau, P. *Pure & Appl. Chem.* **1992**, *64*, 1231.

229. Chae, M. -Y.; Czarnik, A. W. *J. Am. Chem. Soc.* **1992**, *114*, 9704.

230. Ertaş, N.; Akkaya, E. U.; Ataman, O. Y. *Talanta* **2000**, 51, 693.

231. Terenin, A. N. *Photonica of Dye;* Science: Leningard **1967**.

232. Nijegorodov, N. I.; Downey, W. S. *J. Phy. Chem.* **1994**, *98*, 5639.

233. Fabrizzi, L.; Licchelli, P.; Pallavicini, D.; Sacchi, D.; Taglietti, A. *Analyst* **1996**, *121*, 1763.

234. Armarego, W.L.F.; Perrin, D.D. *Purification of Laboratory Chemicals, 4th edition, ISBN 0-7506-3761-7*, Butterworth-Heinemann, Linacre House, Jordan Hill, Oxford **1997**, 143.

235. Cloninger, M.J.; Whitlock, H.W. *J. Org. Chem.* **1998**, *63*, 6153.

236. Bhattacharyya, K.; Chowdhury, M. *Chem. Rev.* **1993**, 93, 507.

237. Saeva, F.D. *J. Photochem. Photobiol. A-Chem.* **1994**, *78*, 201.

238. Reifsnider, K.L. *In Fatigue of Composite material*, Reifsnider, K. L.; Elsevier, New York. **1991**, 11.

239. Tschantz, P; Rutishauser, E. A. *Ann. Anat. Pathol.* **1967**, *12*, 223.

240. Martin, R. B.; Burr, D. B. *J. Biomech.* **1982**, *15*, 137.

241. Burr, D. B.; Fyhrie, M. R.; Martin, D. P.; Schaffler, R. B.; Turner, C. H.; *J. Bone Miner. Res.* **1997**, *12*, 6.

242. Reifsnider, K.L. *In Fatigue of Composite material*, Reifsnider, K. L.; Elsevier, New York. **1991**, 1.

243. Carter, D. R.; Hayes, W. C. *J. Biomech.* **1976**, *9*, 27.

244. Chamay, A. *J. Biomech.* **1970**, *10*, 325.

245. Fondrk, M.; Bahniuk, E.; Cavy, D. T.; Michaels, C. *J. Biomech.* **1988,** *21*, 623.

246. Jepsen, K. J.; Cavy, D. T. *J. Biomech.* **1997**, *30*, 891.

247. Jepsen, K. J.; Krzypow, D. J.; Dutta Roy, T.; Pizzuto, T. *Trans. Orthop. Res. Soc.* **1999**, *24*, 236.

248. LeMaitre, J. In *A course in Damage Mechanics*, Springer-Verlag, New York. **1992**, 1.

249. Martin, R. B.; Gibson, V. A.; Stover, S. M.; Gibeling, J. C.; Griffin, L. V. *J. Biomech.* **1997**, *30*, 109.

250. Chamay, A.; Tschantz, T. *J. Biomech.* **1972**, *5*, 173.

251. Carter, D. R.; Hayes, W. C.; *J. Biomech.* **1977**, *10,* 325.

252. Hoshwa, S. J.; Cody, D. D.; Saad, A. M.; Fyhrie, D. P.; *J. Biomech.* **1997**, *30*, 323.

253. Keaveny, T. M.; Wachtel, E. F.; Kopperdahl, D. L. *J. Orthop. Res.* **1999**, *17*, 346.

254. Inoue, S.; Sakakida, K.; Yamasita, F.; Inoue, S.; Hirai, T.; Katayama, T.; Hayashibara, M.; In *Progress in Acoustic Emission III, Japanese Society of NDI.* **1988**, 177.

255. Kohn, D. H. *Crit. Rev. Biomed. Eng.* **1995**, *22*, 221.

256. Jonsson, U.; Eriksson, K. *J. Biomech.* **1984**, *55*, 441.

257. Inoue, S.; Sakakida, K.; Yamasita, F.; Kusakabe, T.; Inoue, N. In *Progress in Acoustic Emission III, Japanese Society of NDI.* **1986**, 244.

258. Rajachar, R, M.; Chow, C. E.; Curtis, C. E.; Weissman, N. A.; Kohn, D. H. *In Acoustic Emission: Standards and Technology Updates*, Vahaviolos, S. J., Ed.; ASTM Special Technical Publication, Philadelphia. **1999**,3.

259. (a)Timlin, J. A.; Carden, A.; Morris, M. D.; Rajachar, R, M.; Kohn, D. H. *Anal. Chem.* **2000**, *72*, 2229. (b) Carden, A.; Rajachar, R, M.; Morris, M. D.; Kohn, D. H. *Calcif. Tissue Int.* **2003**, *72*, 166.

260. Forwood, M. R.; Parker, A. W. *Calcif. Tissue. Int.* **1989,** *45*, 47.

261. Burr, D. B.; Stafford, T. *J. Biomech. Eng.* **1999**, *121*, 616.

262. Burr, D. B.; Hooser, M. *Bone* **1995**, *17*, 431.

263. Boyce, B. F.; Byars, J.; McWilliams, S.; Mocan, M. Z.; Elder, H. Y.; Boyle, I. T.; Junor, B. J. R. *Journal of Clinical Pathology.* **1992**, *45*, 502.

264. Lee, T.C.; Myers, E. R.; Hayes, W. C. *J. Anat.* **1998**, *193*, 179.

265. Lee, T.C.; Arthur, T. L.; Gibson, L. J.; Hayes, W. C. *Journal of Orthopaedic Research.* **2000**, *18*, 322.

266. Rahn, B. A. *Zeiss Information* **1977**, *22*, 36.

267. O'Brien, F. J. *Microcracks and the Fatigue Behaviour of Compact Bone, Ph. D Thesis, University of Dublin.* **2000**.

268. O'Brien, F. J.; Taylor, D.; Lee, T. C. *J. Biomeh.* **2002**, *35*, 523.

269. Wänninen, E. In *Indicators*, Bishop, E., Ed.; Pergramon Press, New York **1971**, 231.

270. Huitink, G. M. *Talanta.* **1987**, *34*, 423.

271. Wilkins, D.H.; Hibbs, L.E. *Talanta* **1959**, *2*, 201.

272. Wallach, D. F. H.; Surgenor, D. M.; Soderberg, J.; Delano, E. *Anal. Chem.* **1959**, *31*, 456.

273. Escarilla, A. M. *Talanta* **1966**, *11*, 363.

274. Wallach, D. F. H.; Steck, T. L. *Anal. Chem.* **1963**, *35*, 1035.

275. Tsien, R.Y. *Annu. Rev. Neurosci.* **1989**, *12*, 227.

276. Tsein, R.Y. In: *Fluorescent Chemosensors for Ion and Molecular Recognition*, ACS Symposium Series 538. Czarnik, A. W.; Ed.; Washington, D. C. **1993**, 130.

277. Valeur, B. In *Topics in Fluorescence Spectroscopy, Vol. 4: Probe Design and Chemical Sensing*, Lakowicz, J. R., Eds.; Plenum Press, New York. **1994**, 22.

278. Kuhn, M. A. In: *Fluorescent Chemosensors for Ion and Molecular Recognition*, ACS Symposium Series 538. Czarnik, A. W.; Ed.; Washington, D. C. **1993**, 47.

279. Ramaswami, M.; Krishnan, K. S.; Kelly, R. B. *Neuron* **1994**, *13*, 363.

280. Sinha, S. R.; Patel, S.S.; Saggu, P. *J. Neurosci. Methods* **1995**, *60*, 49.

281. Canepari, M.; Mammano, F. *J. Neurosci. Methods* **1999**, *87*, 1.

282. Erne, P.; Eberhard, M. *Biochem. Biophy. Res. Commun.* **1991**, *180*, 209.

283. Horobin, R. W. In *Conn's Biological Stains, A Handbook of Dyes, Stains and Fluorochromes for Use in Biology and Medicine, 10th edition,*

Horobin, R. W.; Kiernan, J. A., Eds.; BIOS Scientific Publishers Ltd, Oxford **2002**,203

284. (a) Raman, C. V.; Krishnan, K.S. *Nature* **1928**, *121*, 501. (b) Raman, C. V. *Nobel Lecture, December 11* **1930**, 267.
285. Pelletier, M. J. In *Analytical Applications of Raman Spectroscopy, ISBN 0-632-05305-4*. Pelletier, M. J., Ed.; Blackwell Science Ltd., Malden, USA 1999, 1.
286. Malyj, M.; Griffiths, J. E. *Appl. Spectrosc.* **1983**, *37*, 315.
287. Rassat, S. D.; Davis, E. J. *Appl. Spectrosc.* **1994**, *48*, 1498.
288. Chantry, G. W. In *The Raman Effects, Volume 1: Principles.* Anderson, A., Ed.; Marcel Dekker, New York **1979**.
289. Wutheir, R E. *Connect. Tissue Res.* **1989**, *22*, 27.
290. Penel, G.; Leroy, G.; Bres, E. *Appl. Spectrosc.* **1998**, *53*, 312.
291. Paschalis, E. P.; Verdelis, K.; Doty, S. B.; Boskey, A. L.; Mendelsohn, R.; Yamauchi, M. *J. Bone Miner. Res.* **2001**, *16*, 1821.
292. Bell, S. E. J.; Bourguignon, E. S.; O'Grady, A.; Villaumie, J.; Dennis, A. C. *Spectroscopy Europe* **2002**, *14*, 17.
293. (a) Eisenberg, R. L. *Radiology, An Illustrated; Morsby Year Book*, St. Louis, **1992**. (b) Roentgen, W. C. *Sitzungsber. Phys. Med. Ges. Wurzburg.* **1895**, *137*, S132.
294. Krause, W. *Int. J. Neuroradiol.* **1998**, *4*, 296.
295. Bachem, C.; Gunther, H. Z. *Fhr Rontgenkunde* **1910**, *12*, 369.
296. Jeans, J.; Vermereen, P. *Eur. J. Nucl. Med.* **1998**, *25*, 1469.
297. Grainger, R. G. Br. *J. Radiol.* **1982**, *55*, 1.
298. Hoey, G. B.; Weight, P; Ranks, R. D. In *Radiocontrast Agents, Volume 1,* Knoefel, P. K., Ed.; Pergamon Press, New York **1971**, 23.
299. Hoey, G. B.; Smith, K. R. In *Radiocontrast Agents;* Sovak, M., Ed.; Springer-Verlag, Basel **1984**, 23-125.
300. Osborne, E. D.; Sutherland, C. G.; Schul, A. J.; Rowntree, L. G. *J. Am. Med. Asoc.* **1923**, *80*, 368.
301. Swick, M. *Klin. Wochenschr.* **1929**, *8*, 2087.
302. Langecker, H.; Harwart, A.; Junkmann, K. *Naunyn Schmiedebergs Arch. Exp. Pahthol.* **1954**, *222*, 584.